# Exploring non-Hermitian Physics
# in Mechanical Metamaterials

by

## Enrico Martello



A thesis submitted to the
University of Birmingham
for the degree of
DOCTOR OF PHILOSOPHY

# UNIVERSITY OF BIRMINGHAM

## University of Birmingham Research Archive

### e-theses repository

# Abstract

One of the postulates of quantum mechanics demands observables to be real, and as a consequence Hamiltonians, representing the energy of a system, to be Hermitian. In fact, this constraint is unnecessarily strong, since also a non-Hermitian Hamiltonian can feature a real spectrum, for example, in the case that they satisfy *e.g.* both parity and time-reversal ($\mathcal{PT}$) symmetries, as obtained by Bender and Boettcher in 1998. Following the wave of interest towards this topic in the last decades, I will review the consequences of lifting the Hermiticity condition for Hamiltonians described by time-dependent parameters. I will use this to investigate effects related to the adiabatic geometric phase in $\mathcal{PT}$-symmetric non-Hermitian systems. This will be investigated both theoretically, and with our experimental collaborators, in a non-Hermitian dimer model realized by a mechanical metamaterial platform. Metamaterials consist of an arrangement of "meta-atoms", artificially designed units, in this case corresponding to classical harmonic oscillators, whose interactions are then engineered in order to obtain the desired effective Hamiltonian. We will exploit the controllability of this platform to investigate not only the non-Hermitian geometric phase, but then to study the dynamic properties of the interacting so-called Hatano-Nelson dimer, where the interplay of non-Hermiticity and interactions leads to the co-existence of stable and unstable population dynamics. This sets the ground for the final part of this thesis, in which I will theoretically investigate a larger system with three sites with periodic boundary conditions: a triangular plaquette, pierced by a magnetic flux, that might in turn be of interest for the investigation of topological phenomena in the future.

# Contents

# Outline

This thesis consists of 5 main chapters, two of them presented in a publication-style format: in which case the publication is preceded by a short paragraph that clarifies my contribution.

The opening chapter is a brief review aimed at setting the ground for the remainder of this work, and consists of three sections. In Section 1.1 the condition on the Hermiticity of the Hamiltonian is lifted, and its consequences are discussed. Then follows an introduction to two-site models (so-called dimers) and the role of non-Hermiticity is discussed using these minimal models in both the non-interacting and interacting cases.
Finally in Section 1.3 I will introduce the concept of metamaterials, discussing the great novelty and flexibility of this experimental platform. This chapter should be interpreted as a toolbox facilitating reader's understanding of the results presented in Chapters 2 and 3.

The core of this thesis begins with Chapter 2. In Section 2.1 I analytically derive the geometric factor in the case of non-Hermitian Hamiltonians; I will follow the steps of the Hermitian derivation, so to highlight the differences between the two cases. I will then try to formulate the non-Hermitian equivalent of the adiabatic theorem, before moving to the next section, where I check these results in a "numerical experiment". Using a dimer model made non-Hermitian by on-site gain and loss terms, in Section 2.2 I obtain a numerical validation of the expected results. At the same time these results were achieved, my research was scooped and I moved in the direction of finding an actual experimental platform. Together with our collaborators, we realized that the mechanical metamaterial

made of two coupled harmonic oscillator described in Section 2.3 was effectively serving this purpose.

In Chapter 3, the main result of my research is presented in the form of a publication: Yaashnaa Singhal, Enrico Martello, Shraddha Agrawal, Tomoki Ozawa, Hannah Price, and Bryce Gadway. Measuring the adiabatic non-hermitian berry phase in feedback-coupled oscillators. *arXiv preprint arXiv:2205.02700*, 2022. There we inspected the Hatano-Nelson dimer measuring the non-Hermitian geometric factor acquired by the system when its parameters depend on time. We obtained that, as opposed to its Hermitian counterpart, the non-Hermitian geometric factor affects the amplitude also along open paths in parameter space.

Chapter 4 consists of the study of the dynamical features of a dimer model in publication style: Enrico Martello, Yaashnaa Singhal, Bryce Gadway, Tomoki Ozawa, and Hannah M Price. Coexistence of stable and unstable population dynamics in a nonlinear non-hermitian mechanical dimer. *arXiv preprint arXiv:2302.03572*, 2023.
While working at the experimental results obtained with the mechanical metamaterial discussed in Section 2.3, I noticed an interesting coexistence of two dynamical regimes in a non-linear dimer model. We investigated this feature, and found that introducing non-Hermiticity in a dynamical manner the population observes either stable or unstable dynamics, initial conditions holding the balance between one or the other behavior.

Chapter 5 is devoted to the description of the dynamical features of a triangular plaquette, namely a three-site system with periodic boundary conditions, and to the understanding of the interplay between a synthetic magnetic flux and the interactions within the system. I start investigating the symmetries of the model in Section 5.1, before simulating it numerically. The outcome of the numerical simulations is presented in Section 5.2, where I observe three dynamical regimes: two of them being observed also in the dimer case, namely self-trapping and Rabi-like oscillations, and the third can be described as a chiral soliton, that is to say a localized wave packet moving around the plaquette. Lastly, Section 5.3 is intended to set the ground for an experimental proposal

to be performed using the aforementioned mechanical metamaterial.

In the last chapter I give an overview of this work, before discussing future research venues.

# CONTENTS

# Chapter 1

# Theoretical background

When approaching quantum mechanics for the first time, the postulates are one of the early topics tackled [3, 4]. These establish the probabilistic interpretation of the wave function, its time evolution and symmetry and the fact that the expectation values of operators in quantum mechanics *must be real*. Consider *e.g.* the Hamiltonian operator: its eigenvalues are associated with the energy of a system, hence these have to be real.

In Section 1.1 the main focus is on this latter postulate, and I will review why the requirement of Hermiticity of the Hamiltonian is too restrictive when demanding real eigenvalues. In particular, I will illustrate that this constraint can be lifted under the appropriate symmetry conditions and show the consequences of relaxing Hermiticity. As a full review of non-Hermitian quantum mechanics is beyond the scope of this section, the more mathematically-oriented readers are referred to Refs. [5–8] and references therein; in this section the only aim is to make the reader aware of the pitfalls coming with lifting the Hermiticity condition, and to lay the basis for the results presented in Section 2.1.

In Section 1.2, I present a brief review of two-site models (dimers), showing their rich dynamical features and how these can be used to explore the behavior of Hermitian and non-Hermitian physics in both the non-interacting and the interacting case. This will set the ground for the results presented in Section 2.2, where a $2 \times 2$ Hamiltonian is used to numerically investigate the theoretical results, and in Chapters 3 and 4, where two dimer

models are experimentally realized to investigate their dynamical features.

Finally Section 1.3 contains a review of a novel experimental platform: metamaterials. These are obtained arranging together meta-atoms, the building units, with controlled interactions allowing for great control and flexibility of the setup. Focus will then be extended towards metamaterials made of mechanical meta-atoms, as this is the type of platform we used to obtain the experimental results presented in Chapters 3 and 4 and in Appendix B.

## 1.1   Non-Hermitian physics

Two of the postulates of quantum mechanics state that $i$) to any observable in classical mechanics we can associate a linear operator in quantum mechanics, and $ii$) since the eigenvalues represent the outcome of experiments, these have to be real [3,4]; for this reason linear operators are also required to be Hermitian. Hamiltonians describing quantum systems are no exception to this: as their eigenvalues $\varepsilon$ represent the energy of the system, demanding their Hermiticity assures that $\varepsilon \in \mathbb{R}$ [3,4]. Moreover, as the Hamiltonian plays the role of the generator of the dynamics, its Hermiticity is required in order to obtain a unitary time evolution.

In 1998 Bender and Boettcher [9] showed that the Hermiticity requirement is an unnecessarily strong constraint for the Hamiltonian to yield real eigenvalues, since its symmetry with respect to both spatial inversion, parity $\mathcal{P}$, and time-reversal symmetry, $\mathcal{T}$, can be sufficient as we shall review further below. Here:

$$\mathcal{P} : x \rightarrow -x, \qquad \mathcal{T} : i \rightarrow -i;$$

both are reflection operators, $i.e.$ $\mathcal{P}^2 = \mathcal{T}^2 = \mathbb{I}$, and $\mathcal{P}$ is linear, whereas $\mathcal{T}$ has to be anti-linear in order to preserve the canonical commutator [3, 4, 9, 10]. In other words, one can say that if the Hamiltonian commutes with the $\mathcal{PT}$ operator, $[\mathcal{H}, \mathcal{PT}] = 0$, the eigenvalues of the Hamiltonian are real in the common basis as we shall discuss [9, 10].

In fact, $\mathcal{PT}$ symmetry is not the only way to regain a real energy spectrum with a non-Hermitian Hamiltonian [11–13]. In the case of $2 \times 2$ Hamiltonians, in fact, the authors of Ref. [11] show that any Hamiltonian symmetric with respect to an anti-unitary symmetry $\mathbf{S}$ such that $\mathbf{S}^{2k} = 1$, for odd $k$, has real eigenvalues, and in Ref. [13] the author gave a general condition for spectra to be real. The reason why we focus on $\mathcal{PT}$-symmetry is that it is simple to engineer an experiment implementing parity and time reversal symmetries [10, 12].

The study of open quantum systems dates back to studies in the field of nuclear physics, and was initially investigated considering the dynamics of the density operator (Lindblad formalism) or describing the time evolution using a non-Hermitian operator (Feshbach projection), c.f. Refs. [10, 12] and references therein. However, in this thesis I will focus on simulating quantum Hamiltonians with classical systems, in which case the effective non-Hermitian Hamiltonian is sufficient to describe the dynamics of a system. [10, 12]. Thanks to the similarities between the quantum dynamics of a particle and the propagation of classical waves, the investigation of non-Hermitian Hamiltonian has been widely considered in the field of optical structures [10, 14–17], and has later involved other experimental platforms e.g. electrical circuits [18], fluids [19] and mechanical systems [1, 2, 20–22]. Using these platforms, fascinating phenomena like exponential amplification [23, 24] unidirectional invisibility [25], enhanced sensitivity [26, 27] and single mode lasing [28] have been investigated, among many others [10, 12].

I have mentioned that Hermiticity is an unnecessarily strong requirement for a system to display a real spectrum. In the next section, I will review some of the mathematical properties of non-Hermitian Hamiltonian, before focusing on the special case of $\mathcal{PT}$-symmetric systems.

## 1.1.1 Eigenvectors of non-Hermitian Hamiltonians

Let us now review the consequences of lifting the Hermiticity condition for the Hamiltonian of a system. A Hamiltonian $\mathcal{H}$ is Hermitian if it is equal to its Hermitian conjugate,

$\mathcal{H}^\dagger$. One of the consequences of Hermiticity, is that the eigenvalue problem is equivalently solved acting on $\mathcal{H}$ from either the left or the right: solving $\mathcal{H}\,|\psi_n\rangle = \varepsilon_n\,|\psi_n\rangle$ is the same as solving $\langle\psi_n|\,\mathcal{H} = \varepsilon_n\,\langle\psi_n|$, with $|\psi_n\rangle$ being the $n$-th eigenvector of the Hamiltonian $\mathcal{H}$ with eigenenergy $\varepsilon_n$ [3,4]. As soon as the Hermiticity condition is lifted, this result does not hold anymore (in general), so that in this case one has to distinguish between the right and the left eigenvectors [9,12,29]:

$$\mathcal{H}\,|R_n\rangle = \varepsilon_n^R\,|R_n\rangle, \qquad \langle L_n|\,\mathcal{H} = \varepsilon_n^L\,\langle L_n|\,; \tag{1.1}$$

where $|R_n\rangle$ is the $n$-th *right* eigenvector with eigenenergy $\varepsilon_n^R$, and similarly $\langle L_n|$ is the $n$-th *left* eigenvector with eigenvalue $\varepsilon_n^L$. In general $|R_n\rangle \neq \langle L_n|^\dagger$, as is easily seen by taking the Hermitian conjugate of the equation for the left eigenvectors in Eq. 1.1:

$$\mathcal{H}^\dagger\,|L_n\rangle = \varepsilon_n^{L*}\,|L_n\rangle. \tag{1.2}$$

So, the first consequence of dealing with $\mathcal{H} \neq \mathcal{H}^\dagger$, is that we now have two distinct sets of eigenvectors, $\{|R_n\rangle\}$ and $\{|L_n\rangle\}$, one for the Hamiltonian $\mathcal{H}$ and one for its Hermitian conjugate, respectively, with eigenenergies $\varepsilon_n^R$ and $\varepsilon_n^{L*}$ [5,10,12,29].

Let us now turn to the eigenenergies; it is possible to show that these need no $R$ and $L$ labelling, *i.e.* the left eigenvectors have the same eigenvalues as the right eigenvectors: $\varepsilon_n^L = \varepsilon_n^R$. Starting from the eigenvalue equation for the left eigenvectors, Eq. 1.2 can be written as:

$$\det\!\left(\mathcal{H}^\dagger - \varepsilon_n^{L*}\mathbb{I}\right) = 0;$$

since transposing does not affect the determinant and the Hermitian conjugation consists in the transpose of the complex conjugate, it becomes:

$$\det\!\left(\mathcal{H} - \varepsilon_n^L\mathbb{I}\right)^* = \det\!\left(\mathcal{H} - \varepsilon_n^L\mathbb{I}\right) = 0,$$

where it has been taken in account that the complex conjugate of a null quantity is the quantity itself. Similarly, looking at the eigenvalue equation for $|R_n\rangle$:

$$\det\big(\mathcal{H} - \varepsilon_n^R \mathbb{I}\big) = 0.$$

It then follows that the eigenenergies are the same for both sets of eigenvectors $\{|R_n\rangle\}$ and $\{\langle L_n|\}$, as they solve the same equation. Assuming that there is no degeneracy in the spectrum of the Hamiltonian, indexing the energies conveniently we obtain that $\varepsilon_n^L = \varepsilon_n^R \equiv \varepsilon$ [5, 10, 12].

As there are two distinct sets of eigenvectors, it is natural to wonder how does orthogonality work. In general, eigenvectors belonging to each basis are not orthogonal [5], but one can prove that these satisfy another interesting property. Using the results of the eigenvalue problems in Eq. 1.1:

$$\langle L_m|\mathcal{H}|R_n\rangle = \varepsilon_m \langle L_m|R_n\rangle = \varepsilon_n \langle L_m|R_n\rangle ,$$

$$(\varepsilon_m - \varepsilon_n) \langle L_m|R_n\rangle = 0.$$

Assuming again that there is no degeneracy in the spectrum of the Hamiltonian, this relation proves that $\langle L_m|R_n\rangle \propto \delta_{m,n}$. This property goes under the name of *bi-orthogonality*, and it can be shown that $\{|R_n\rangle\}$ and $\{\langle L_n|\}$ form a bi-orthogonal eigenbasis in a finite-dimensional space [5, 12].

The bi-orthogonality has two main implications: one of them will be discussed in more detail in Section 2.1 and relates to the dynamics of the system; the other one concerns the normalization convention that now suffers from an ambiguity, namely $\langle R_n|R_n\rangle = 1$ vs. $\langle L_n|R_n\rangle = 1$. In principle, one can choose to normalize a state using either one of the two, but the latter is preferable as it allows for simplifications in the calculations and for a neater probabilistic interpretation of the eigenvalues of the observables as discussed in Ref. [5]. In order to avoid any issue related to the choice of the normalization, in Section 2.1 I will explicitly keep the normalization factor.

## 1.1.2 $\mathcal{PT}$-symmetry of the Hamiltonian

Having introduced the left and right eigenvectors, we can now briefly review how, under $\mathcal{PT}$-symmetry, a non-Hermitian Hamiltonian can exhibit a real spectrum [12, 29, 30]. To see this, let us consider the eigenvalues equation for the right eigenvectors, and use the $\mathcal{PT}$-symmetry condition $\mathcal{H} = (\mathcal{PT})^{-1}\mathcal{H}(\mathcal{PT})$:

$$(\mathcal{PT})^{-1}\mathcal{H}(\mathcal{PT})\ket{R_n} = \varepsilon_n \ket{R_n};$$

applying the $(\mathcal{PT})$ operator from the left on both sides of this equation and using the fact that time-reversal is anti-linear:

$$\mathcal{H}\mathcal{PT}\ket{R_n} = \varepsilon_n^* \mathcal{PT}\ket{R_n}.$$

This equation compared with the eigenvalues equation for the right eigenvectors in (1.1), says that *if* $\{\ket{R_n}\}$ *is a common basis for both* $\mathcal{H}$ *and* $(\mathcal{PT})$, that is to say if all the eigenstates of the Hamiltonian are also eigenstates of the $(\mathcal{PT})$ operator with eigenvalue $\alpha$, then the eigenenergies are real, $\varepsilon_n = \varepsilon_n^*$:

$$\mathcal{H}\alpha\ket{R_n} = \varepsilon_n^*\alpha\ket{R_n}$$

In this case the $\mathcal{PT}$-symmetry of the Hamiltonian is *unbroken*. Conversely, if no common eigenbasis for $\mathcal{H}$ and $(\mathcal{PT})$ can be found, the symmetry is broken [12, 29, 30]. In the case the symmetry is unbroken the eigenstates associated with real eigenenergies yield $\mathcal{PT}$-symmetric wave functions, namely states that are left unchanged if they are reflected in space and then played backwards in time. The transition from the unbroken to the broken $\mathcal{PT}$-symmetry regime, takes place at the so-called exceptional points, that are the subject of the next section.

### 1.1.3 Exceptional points

This subsection is not intended to be exhaustive; its goal is to make the terminology clear and to prepare the reader for the results presented in Chapter 2. The reader who wants to know more about exceptional points will find it very interesting reading through Refs. [12, 31, 32].

Similar to Hermitian Hamiltonians, non-Hermitian Hamiltonians can also show degeneracy in their spectrum, *i.e.* $\varepsilon_n = \varepsilon_m$ for some $n \neq m$; in which case, one talks about *diabolic points* [12]. However, when the energy spectrum is analytically continued in the complex plane, as can be done for non-Hermitian Hamiltonians, a degeneracy in the eigenvalues can be accompanied by an unusual phenomenon characteristic of the non-Hermitian realm: the coalescence of the eigenvectors, $|R_n\rangle = |R_m\rangle$, $\langle L_n| = \langle L_m|$, that become "self-orthogonal", $\langle L_n|R_m\rangle = 0$ [31–34]. The points at which this phenomenon takes place are referred to as *exceptional points*, and are a distinctive feature of non-Hermitian Hamiltonians [12]. Interestingly, when dealing with $\mathcal{PT}$-symmetric Hamiltonians, exceptional points correspond to the $\mathcal{PT}$-breaking points [31], and at these points systems show anomalous behavior like *e.g.* unidirectional invisibility or enhanced sensitivity [12, 35, 36]. Another interesting fact about exceptional points is that dramatic effects arise also in their neighborhood [12, 31]; this region of parameter space has been inspected using *e.g.* photonics setups [10, 14], that show a good degree of control in that region [12].

In Appendix A I review the well-known analogy between the degeneracy point of the energy spectrum and a fictitious magnetic monopole generating a fictitious magnetic field [4, 37]. Such a parallelism can be drawn also in this case, but this turns out to have a more interesting outcome: exceptional points, in fact, behave as *imaginary* monopoles [38], generating a complex field whose strength grows with the distance from the exceptional point [38, 39]. This result will be relevant in Chapter 3, where we encircle the field generated by such a monopole in parameter space. In order to investigate the role of exceptional points, I will make use of 2-level systems [12]; such minimal models are the subject of next section.

## 1.2   Dimer models

Systems involving a large number of energy levels can often be reduced to analyzing two-level systems [12]. Equivalently, the dynamics of many systems like, *e.g.* Bose-Einstein condensates [40–43] or coupled waveguides [44, 45] can be described, under convenient conditions, by a set of discrete coupled equations, and the simplest non-trivial case is when said system only contains two equations in which case the problem can be solved analytically [46, 47].

In this section I will review this class of minimal models, the so-called *dimers*, in both the Hermitian and the non-Hermitian regimes. In Section 1.2.1 I will review the analytical solution in the Hermitian case for a specific initial condition [46, 47], and I will discuss the Josephson and Rabi oscillations and the transition to the self-trapping regime. These results will serve as a yardstick to interpret the results presented in Chapters 4 and 5, where a 3-level system is discussed. Finally, I will introduce two parametrizations that will prove useful for understanding the physical meaning of the results. Then follows Section 1.2.2 where I introduce non-Hermiticity in a dimer model in two distinct ways: adding on-site gain and loss and making the hopping asymmetric. This will be the starting point for the results presented in Section 2.2 and in Chapters 3 and 4.

### 1.2.1   A minimal Hermitian dimer

A simple example of a Hermitian dimer is given by a Bose-Einstein condensate in a double well potential [40–43]. This can be mathematically described under the two-mode approximation as:

$$\alpha = \alpha_1 \psi_1 + \alpha_2 \psi_2,$$

where $\psi_j, j = 1, 2$ are two functions localized on either one of the two potential wells, and the dynamics of the two components $\alpha_j$ is described by the following non-linear
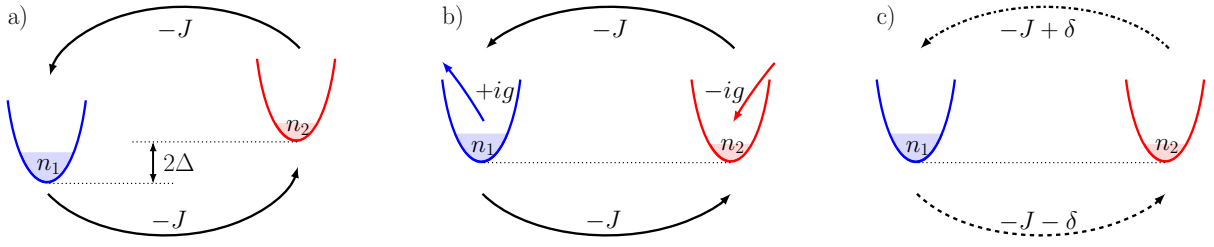
**Figure 1.1:** Cartoons of various dimer models discussed in this and following sections; the shadowed areas are a pictorial representation of the occupation on each well, whereas the black arrows represent the hopping process. *a)*: sketch of the model presented in Eq. 1.4 in the case of $\Delta_1 = \Delta_2 \equiv \Delta$. *b)* sketch of the model in Eq. 1.7 with on-site gain and loss represented by the colored arrows, and $\Delta = 0$ as the dotted line shows. *c)* is the Hatano-Nelson dimer in Eq. 1.8; note the different texture of the arrows representing the hopping process as resembling the different energy cost.

Schrödinger equations [40–43]:

$$i\frac{\partial}{\partial t}\alpha_1(t) = (\Delta_1 + U_1|\alpha_1|^2)\alpha_1(t) - J\alpha_2(t),$$
$$i\frac{\partial}{\partial t}\alpha_2(t) = (\Delta_2 + U_2|\alpha_2|^2)\alpha_2(t) - J\alpha_1(t); \tag{1.3}$$

here $\Delta_j \in \mathbb{R}$ represent the depth of well $j$, $J \in \mathbb{R}$ is the hopping amplitude associated with hopping from one well to the other, $U_j \in \mathbb{R}$ is the strength of the interactions of the atoms within each well, $|\alpha_j|^2 = n_j$ is the number of atoms in well $j$ and $\hbar = 1$.

This system of equations can be cast in the familiar Hamiltonian form:

$$i\boldsymbol{\alpha} = \mathcal{H}\boldsymbol{\alpha}, \qquad \mathcal{H} = \begin{pmatrix} \Delta_1 + U_1 n_1 & -J \\ -J & \Delta_2 + U_2 n_2 \end{pmatrix}. \tag{1.4}$$

A cartoon of this Hamiltonian is sketched in Fig. 1.1a. Without loss of generality, I will consider the interaction values, $U$, the on-site potential, $\Delta$ and the hopping energy, $J$, to be positive.

Note that, had I started talking about coupled waveguides I would have said that $\Delta_j$ is related to the propagation constant, $U_j$ is the strength of Kerr nonlinearity, $\alpha_j$ an electric field amplitude on waveguide $j$ and $J$ a coupling constant (proportional to the inverse of the distance between the waveguides) [15, 24, 48]. Equivalently, I could have started

talking about *e.g.* coupled pendula [21] or exciton polaritons [49] just by assigning the appropriate physical meaning to the matrix elements of $\mathcal{H}$ in Eq. 1.4.

Under the assumption that the two potential wells are not tilted, $\Delta_1 = \Delta_2 = 0$ and that the interaction strength is the same in both wells, $U_1 = U_2 = U$, the two coupled equations in Eq. 1.3 can be solved exactly, if the system is initially in one of the two wells [46, 47]. As the mathematical details can be found in these references, I will only review the final result. Looking at the population imbalance between the two sites, $z = n_1 - n_2$, one finds that its time evolution is obtained solving:

$$\frac{\partial^2 z}{\partial t^2} = \left(-4J^2 - 2JU(\alpha_1\alpha_2^* + \alpha_1^*\alpha_2)_0 + \frac{1}{2}U^2 z_0\right)z(t) - \frac{1}{2}U^2 z(t)^3, \qquad (1.5)$$

where the index 0 means the initial value of the quantity within the brackets, and similarly $z_0 \equiv z(0)$. If the system is initially localized on a single site, *i.e.* initial condition $z_0 = 1$ ($z_0 = -1$ would yield the same result), then $(\alpha_1\alpha_2^* + \alpha_1^*\alpha_2)_0 = 0$, and Eq. 1.5 simplifies to:

$$\frac{\partial^2 z}{\partial t^2} = \left(-4J^2 + \frac{1}{2}U^2\right)z(t) - \frac{1}{2}U^2 z(t)^3. \qquad (1.6)$$

Let us look at the solution to this equation starting from the non-interacting case, $U = 0$. In this case the Hamiltonian (1.4) describes the so-called Josephson junction [50], and Eq. 1.6 has an oscillatory solution. The oscillations of the population imbalance mean that the particles (in the case of a Josephson junction, Cooper pairs [50]) move from one end to the other of the junction, undergoing the so-called Josephson oscillations, *c.f.* Fig. 1.2, where the numerical solution to Eq. 1.6 is plotted for different values of the interaction strength. The observed alternating current in the absence of a potential, is described by the first Josephson equation [41, 47, 50]. When switching on the interactions, Eq. 1.6 still has an oscillating solution. These are the so-called Rabi oscillations, and their period grows larger as $U$ approaches the threshold value $U = 4J$. At the threshold the oscillation period diverges as plotted in Fig. 1.2.

When the interaction strength exceeds the critical value, Eq. (1.6) has a different solution
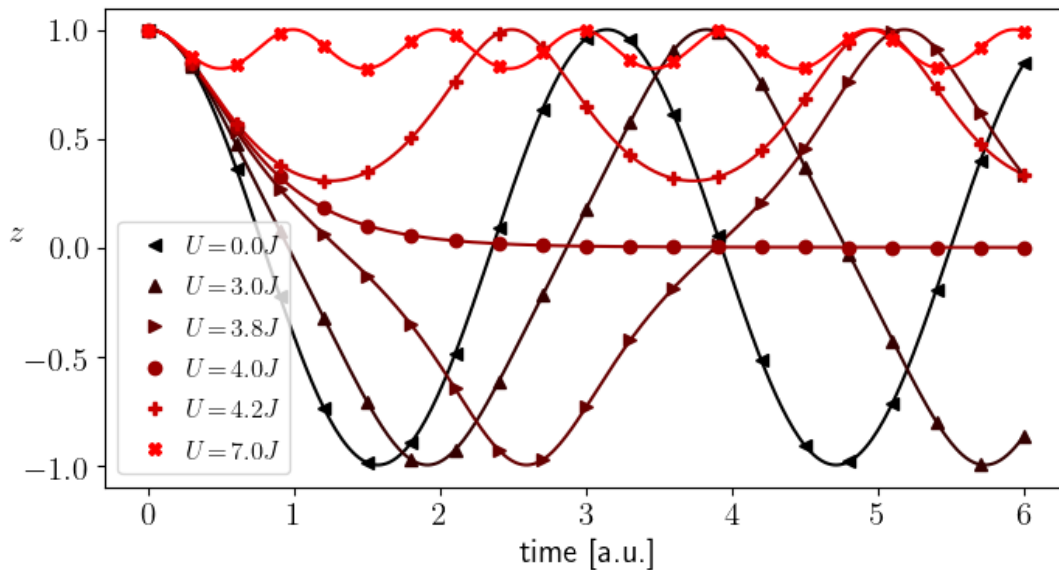
**Figure 1.2:** Numerical solutions to Eq. 1.6 for distinct values of the interaction strength $U$: the lighter the markers the larger the value of $U$ in units of $J$. For $U=0$ Josephson oscillations are observed. Note the period of Rabi oscillations growing larger as $U \to 4J$ (triangles), and that at the critical value the period diverges (bullet). For strong interactions self-trapping is evident and fewer particles tend to leave the initial site (crosses).

that does not change sign [47]. This means that $z(t) > 0$ the whole time, that is to say the initial site is always more populated than the other, as the numerics in Fig. 1.2 show. Moreover, the stronger the interaction grows, the closer the population imbalance is to 1, *c.f.* Fig. 1.2; physically, this means that for $U \gg 4J$, fewer particles move to the other well. This phenomenon is known as self-trapping, and is solely induced by interactions between the particles [40, 41, 47, 49, 51].

These results can also be obtained using two alternative parametrizations of the problem that are both convenient and conventional when describing dimer models as I will now describe in the non-interacting case just for the sake of clarity, but in Refs. [40–43] the interacting case is described. The first one is the "phase space" parametrization, that uses the normalized population imbalance, $\tilde{z} = (n_1 - n_2)/n$ (as done earlier), and the phase between the wave functions in the two wells, $\varphi = \arg \alpha_1/\alpha_2$, to describe the dynamics of

the dimer [40, 41, 49, 51], that in this case becomes:

$$\frac{\partial}{\partial t}\tilde{z} = -2J\sqrt{1-z^2}\sin\varphi$$
$$\frac{\partial}{\partial t}\varphi = 2(\Delta_1 - \Delta_2) + 2\frac{Jz}{\sqrt{1-z^2}}\cos\varphi$$

where I dropped the time dependence of $\tilde{z}$ and $\varphi$ for the sake of notation; note that $\varphi$ is periodic. A numerical solution to this system of equations is shown in the top row of Fig. 1.3. In the $\{\tilde{z}, \varphi\}$ phase space, Rabi-like oscillations are visible as closed trajectories spanning the entire interval of value of $\tilde{z}$ from $-1$ to $1$, whereas self-trapping is observed in the far right panel, and shows up as a trajectory that never crosses the imaginary $\tilde{z}=0$ line.

The second parametrization is performed in terms of the Bloch vector $\mathbf{s}$ whose components are defined as [42, 43]:

$$s_x = \frac{1}{2n}(\alpha_1^*\alpha_2 + \alpha_1\alpha_2^*),$$
$$s_y = \frac{1}{2i\,n}(\alpha_1^*\alpha_2 - \alpha_1\alpha_2^*),$$
$$s_z = \frac{1}{2n}(|\alpha_1|^2 - |\alpha_2|^2),$$

where the factor $1/2$ comes from the condition that $|\mathbf{s}|^2 = 1/4$, so that the head of the Bloch vector lies on the Bloch sphere, a sphere of radius $1/2$, *c.f.* Refs. [42, 43], and again the time dependence of $\alpha_j$ and the components of the Bloch vector are suppressed for the sake of notation. In this parametrization, the dynamics is described by the following set of equations:

$$\frac{\partial}{\partial t}s_x = (\Delta_2 - \Delta_1)s_y,$$
$$\frac{\partial}{\partial t}s_y = -(\Delta_2 - \Delta_1)s_x + 2Js_z,$$
$$\frac{\partial}{\partial t}s_z = -2Js_y.$$

The numerical solution to this set of equations is displayed in Fig. 1.3, and in this case Rabi-like oscillations are the trajectories that wind around the Bloch sphere moving the hemispheres of the Bloch sphere, whereas when the system is self trapped, it walks along

16

trajectories that never cross the equator. As might be expected, the two parametrization are equivalent as can be seen considering that $\varphi = \mathrm{atan}(s_y/s_x)$ and $\tilde{z} = 2s_z$ [2].
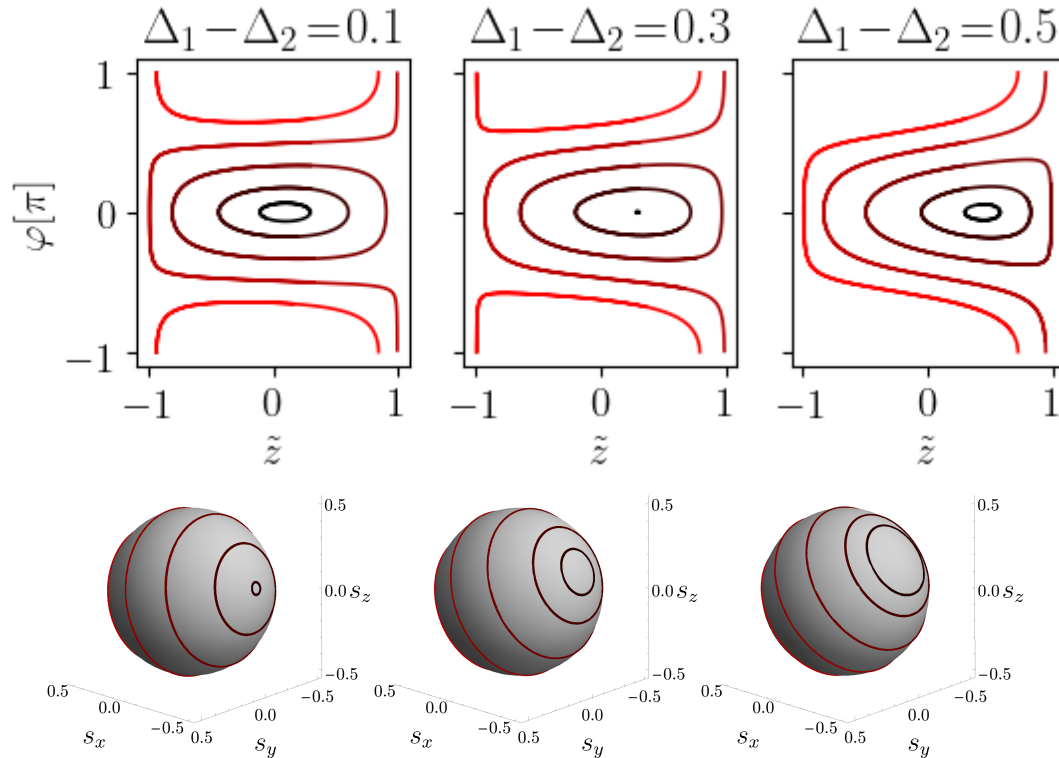


**Figure 1.3:** Plot of the phase space for three different value of $\Delta_1 - \Delta_2$ in the phase space representation (top row) and the Bloch sphere parametrization (bottom row): note that when the system undergoes Rabi-oscillations $z$ oscillates from -1 to 1, whereas the phase spans over an interval of values, and equivalently the trajectories move between the north and the south hemisphere of the Bloch sphere. In the self-trapping regime (far right panel) the wave function is localized on either one of the two sites, and the population imbalance never changes sign, or equivalently, the trajectories never cross the equator of the Bloch sphere.

Now that I have described the Josephson and the Rabi-like oscillations and the self-trapping regime in the Hermitian case, I will add non-Hermiticity to the dimer, to review the known results and highlight the differences.

## 1.2.2 Examples of non-Hermitian dimers

Non-Hermitian effects are ubiquitous, and these can be taken in account in the dimer model either adding on-site gain and loss terms or making the hopping energy asymmetric. The first one is a very common approach in both theory [33, 39, 42, 43, 48, 52] and

experiments $[10, 15, 24]$; the latter, on the other hand, is a two-site version of the well known Hatano-Nelson model $[53–55]$.

**On-site gain and loss**

Consider a system in which gain and loss can be controlled so that one site is fed with atoms (resp. light intensity is amplified in one of the waveguides) at a rate $g$, and the other one leaks atoms (resp. in the other one light is damped) at the same rate. Since gain and loss enter as purely imaginary on-site terms, $\mp ig$ respectively, it is immediate to see that the Hamiltonian

$$\mathcal{H} = \begin{pmatrix} +ig & -J \\ -J & -ig \end{pmatrix},$$

(1.7)

is non-Hermitian yet $\mathcal{PT}$-symmetric $[15, 33, 43, 48]$, since in this case the parity operator $\mathcal{P}$ corresponds to the Pauli matrix $\sigma_x$ and $\mathcal{T}$ is the complex conjugation:

$$\mathcal{H} = \sigma_x \mathcal{H}^* \sigma_x, \qquad \sigma_x = \begin{pmatrix} 0 & 1 \\ 1 & 0 \end{pmatrix}.$$

The eigenvalues of the Hamiltonian in Eq. 1.7 are $\varepsilon_\pm = \pm\sqrt{J^2 - g^2}$, and assuming without loss of generality that both $J, g > 0$, as long as $g < J$, there exist a common eigenbasis for both the Hamiltonian and the $\mathcal{PT}$ operator, and the energy is real, and in the opposite limit $g > J$ the $\mathcal{PT}$-symmetry is broken and the eigenvalues are a complex conjugate pair. Finally, as the Hamiltonian is $\mathcal{PT}$-symmetric, the exceptional point and the $\mathcal{PT}$-breaking correspond $[12, 15, 33, 43, 48]$.

As a review of the results for the dynamics of this model is presented in Section 2.2, I will now include the interactions in this model as follows:

$$\mathcal{H} = \begin{pmatrix} Un_1 + ig & -J \\ -J & Un_2 - ig \end{pmatrix}.$$

As this is a non-linear Hamiltonian, the eigenvalues correspond now to the chemical

potential rather than the energy [43,52]. In Refs. [43,52] the authors perform an extensive study of this system, and obtained that, interestingly, taking in account interactions makes the system break $\mathcal{PT}$-symmetry at a smaller value of the gain and loss rate, namely $g^2 = J^2 - U^2$ [43,52]. Moreover, this relation also says that for $U = J$ no $\mathcal{PT}$-symmetric regime is allowed [43,52].

**Asymmetric hopping: Hatano-Nelson dimer**

Non-Hermiticity can also be introduced into the system in the form of asymmetric hopping; in terms of the Hamiltonian, this means that, assuming there is no on-site potential:

$$\mathcal{H} = \begin{pmatrix} 0 & -J - \delta \\ -J + \delta & 0 \end{pmatrix}, \tag{1.8}$$

where, without loss of generality, I will assume $J, \delta \in \mathbb{R}^+$. This model is sketched in the right-most cartoon of Fig. 1.1, where the different texture of the arrows representing the hopping process resembles the different energy cost.

This Hamiltonian is the two-site version of the well-known Hatano-Nelson model: a $\mathcal{PT}$-symmetric model describing a one-dimensional chain of sites connected via asymmetric hopping [53–55]. In case of open boundary conditions, eigenstates accumulate in a macroscopic number at the ends of the chain, yielding the so-called non-Hermitian skin-effect [7,56,57].

This type of non-Hermiticity has been experimentally investigated in optical setups [58–61] and electrical systems [62–64], and more recently also using mechanical metamaterials [1,2,21].

The main dynamical features of the Hatano-Nelson dimer model are reviewed within the publication in Chapter 4, but I will also briefly review the main results for the non-interacting case here. The spectrum of the Hamiltonian (1.8) is given by $\varepsilon = \sqrt{J^2 - \delta^2}$; this means that the Hamiltonian is in the $\mathcal{PT}$-unbroken symmetry regime as long as $\delta < J$. The dynamics of the system in this regime is characterized by the existence of

two fixed points that behave as *centers* within phase-space: the system oscillates around it along stable orbits [2, 65, 66]. For small values of the asymmetry, these centers are located close to the equilibrium condition $z = 0$, that is to say the system undergoes Rabi-like oscillations, *c.f.* Chapter 4. As $\delta$ grows larger, the centers move away from this equilibrium condition and the system starts showing self-trapping [2].

As soon as the $\mathcal{PT}$-symmetry is broken, the energy becomes purely imaginary and the two centers turn into a pair of stable-unstable points; in this regime, the population grows exponentially and tends to occupy one site rather than the other, that can be interpreted as a two site version of the non-Hermitian skin-effect [2, 7, 56, 57].

Also in this case one can consider adding interactions, either on-site [67] or making the hopping energies depend on the population imbalance [1, 2]. In this latter case:

$$\mathcal{H} = \begin{pmatrix} 0 & -J - gz \\ -J + gz & 0 \end{pmatrix}, \quad z \equiv n_1 - n_2;$$

this model is the subject of Chapter 4, where the outcome of the numerical simulations and the experimental results are presented in publication form, *c.f.* Ref. [2].

## 1.3   Introduction to mechanical metamaterials

I conclude this chapter with a brief overview of mechanical metamaterials, a novel experimental platform whose advantages I will discuss in this section.

When quantum objects like atoms are combined together, new collective properties emerge that depend on the way these are arranged and interact [68]. If instead of atoms, one decides to use artificially generated *meta*-atoms in a custom arrangement, it is possible to generate an exotic *meta*-material characterized by singular phenomena like *e.g.* negative refractive index [69, 70], negative elastic modulus [71, 72] or negative mass density [73].

The choice of the building blocks of metamaterials is arbitrary, as one could use meta-

atoms taken from *e.g.* the photonic [69, 70], acoustic [72] or mechanical [22, 74–77] realm, mainly according to the length scale one wants to act upon. In Chapters 3 and 4 we will take advantage of a metamaterial made of mechanical building units. Mechanical meta-atoms can be as complicated as robotic unit cells [78], or gyroscopes [75], but our collaboration made use of harmonic oscillators and coupling was arranged so to happen without any physical contact, *c.f.* Appendix B [21].

Metamaterials owe much of their success to the fact that the arrangement and the interactions of meta-atoms can be finely tuned, allowing for an overall remarkable control over the metamaterial realized. Along this direction, there has been a huge push because not only have mechanical metamaterials proved themselves to be a valid platform to explore topological phenomena [20, 22, 74–76] but they have as well the potential to be scaled down in size [22, 77], that would allow for scalable real life application of topologically robust phenomena like edge modes [74, 75], light steering and funneling [61, 79], acoustic and vibration insulation, waveguiding and many others [22, 76].

Although these mechanical setups cannot simulate purely quantum effects, the exceptional control displayed by mechanical metamaterials also in reproducing phenomena that in principle break Newton's law [21], could pave the way to the engineering of exotic interactions in non-Hermitian systems, where the exponential behavior following a linear input qualifies this class of materials for sensing applications [26, 27, 76].

# Chapter 2

# Non-Hermitian geometric phase

This chapter is a theoretical introduction to the results presented in Chapter 3. Here the main results are presented at a level half-way between a review and a technical chapter. In order to understand why, a narrative interlude is needed.

At the end of the first year of my PhD, Silberstein et al. [80] published an elegant paper describing the influence of the non-Hermitian Berry connection on the dynamics of a wave packet. By that time, my progress in the study of this question was as presented in Section 2.1 and Section 2.2. Although my work was therefore not original anymore, my results did match those of Silberstein et al.'s. After a few months spent looking for possible experimental platforms to further explore this type of physics, we finally came across a group that was working on the mechanical metamaterial setup that is described in detail in our joint publication included in Appendix B and that I present here in Section 2.3. Our collaboration on this project then led to the work presented in Chapter 3.

In the first section of this chapter, I will derive an analytical form for the geometric Berry phase in the case of a non-Hermitian Hamiltonian, as it constitutes the ground upon which the results in Chapter 3 are obtained. I will formulate it following the same steps as in the Hermitian case [3, 4] in order to better highlight the differences between the two cases. In order to test the results obtained, in Section 2.2 I report the outcome of a "numerical experiment" performed using a dimer model with on-site gain and loss, like

that described in the last chapter. Not only do the results obtained show good agreement between theory and numerics, but these also show the same type of features observed for a Hatano-Nelson dimer in Chapter 3, with the experimental platform described in detail in Section 2.3 that closes this chapter. [1]

## 2.1   Geometric phase

Lifting the Hermiticity condition on the Hamiltonian led to the definition of two sets of eigenvectors, namely the left and the right eigenvectors that together form a basis satisfying the so-called bi-orthogonality relation, *c.f.* Section 1.1. In this section, I will explore the consequences of this non-Hermiticity in the case of Hamiltonians with slowly-varying time-dependent parameters, where the adiabatic evolution of the wave-function is affected by a geometric phase.

As reviewed in Appendix A, the time evolution of a Hamiltonian evolving periodically and adiabatically in parameter space can lead to interesting results. Specifically, the wave function can acquire an observable phase factor known as the *geometric (Berry) phase*, defined as (*c.f.* Eq. A.8):

$$\gamma_n^{\mathrm{H}} = i \oint_{\mathcal{C}} \mathrm{d}\mathbf{P} \cdot \mathcal{A}_n(\mathbf{P}), \quad \mathcal{A}_n(\mathbf{P}) = \langle \phi_n(P) | \boldsymbol{\nabla}_P | \phi_n(P) \rangle, \tag{2.1}$$

where the superscript relates to the fact that this is the geometric phase for the Hermitian case and $\{|\phi_k\rangle\}$ is the set of eigenvectors of the Hermitian Hamiltonian. The fact that it is an *observable* phase factor and that it is *geometrical*, *i.e.* it does not depend on the rate of change of the Hamiltonian (as long as it evolves adiabatically), has attracted interest from scientists working in solid state systems, as well as in many other areas of physics and length scales, see *e.g.* Refs. [81–84] and references therein, since the first time Berry considered the consequences of an adiabatic evolution on a closed loop in parameter

---

[1]The main results in Section 2.1 and Section 2.2 have been presented in their final form also thanks to the help of Tomoki Ozawa, our collaborator, who developed the elegant mathematical formulation.

space [37, 85].

In this section, I will join the group of scientists trying to generalize such a successful and powerful concept to the non-Hermitian realm since a long time [5,80,86–95], going through this process in a pedagogical way, in order to build up the tools needed to understand the results in Section 2.2 and Chapter 3.

The above analytical expression for the geometric Berry phase is obtained making use of the following steps [3, 4] as detailed in Appendix A:

i) writing a generic state in terms of the *instantaneous eigenbasis* and solving the time dependent Schrödinger equation using this as an ansatz;

ii) *projecting* on another basis vector using the *orthogonality relations*;

iii) solving the resulting differential equations under the hypotheses of the *adiabatic theorem*, to obtain the geometric phase acquired by the system.

These steps mainly involve two operations, as emphasized: expanding in terms of the eigenbasis and projecting. As reviewed in Sec. 1.1, these operations have no trivial correspondence in the case of non-Hermitian quantum mechanics, hence the following questions arise naturally:

i) which basis would one choose to expand the generic state? Why would one be a better choice than the other? Should one use the Schrödinger equation for $\mathcal{H}$ or $\mathcal{H}^{\dagger}$?

ii) How does projection work? Why would one choose to project on one basis rather than the other?

iii) Does the adiabatic theorem have an equivalent in non-Hermitian quantum mechanics? Is the geometric phase still an observable?

In order to address these questions and to provide the tools to appreciate the work presented in Chapter 3, I shall now review the derivation of the non-Hermitian geometric phase.

Let us start by writing down a generic state; for the sake of the argument let us expand it as a linear combination of the instantaneous right eigenvectors, $\{|R_n(t)\rangle\}$ of a non-degenerate non-Hermitian Hamiltonian. Using a similar notation as the Hermitian case in Appendix A:

$$\left|\psi^{\mathrm{R}}(t)\right\rangle = \sum_n a_n(t) \frac{|R_n(t)\rangle}{\sqrt{\langle R_n(t)|R_n(t)\rangle}}, \tag{2.2}$$

where $a_n(t)$ is some complex coefficients whose form is to be determined and $|R_n(t)\rangle$ is the $n$-th instantaneous right eigenvector of the system associated with the instantaneous eigenenergy $\varepsilon_n(t)$ and $n$ is an index running over all the eigenvectors.[2] Finally, note that the norm of $|R_n(t)\rangle$ is explicitly written in the denominator (as opposed to what is done in Ref. [88]), in order to avoid any issue related to the choice of the normalization, as discussed in Section 1.1, so that any change in the amplitude of the state is described by the coefficient $a_n(t)$.

As we chose to use the instantaneous right eigenvectors to write down the generic state at time $t$, the most reasonable choice for the Schrödinger equation to substitute this ansatz in, is:

$$\left(i\frac{\partial}{\partial t} - \mathcal{H}(t)\right) \left|\psi^{\mathrm{R}}(t)\right\rangle = 0. \tag{2.3}$$

Had one chosen the left eigenbasis to expand the state, rather than Eq. 2.3, one would choose to solve:

$$\left(i\frac{\partial}{\partial t} - \mathcal{H}^\dagger(t)\right) \left|\psi^{\mathrm{L}}(t)\right\rangle = 0, \tag{2.4}$$

with the ansatz:

$$\left|\psi^{\mathrm{L}}(t)\right\rangle = \sum_n a_n(t) \frac{|L_n(t)\rangle}{\sqrt{\langle L_n(t)|L_n(t)\rangle}},$$

where the symbols have the same meaning as those in Eq. 2.2. Using Eq. 2.2, the eigen-

---

[2]Although in general the coefficients of the expansion $a_n(t)$ might depend on the choice of the basis used for the expansion, for the sake of notation these are not labelled with $R$ or $L$.

value equation in Eq. 2.3 yields:

$$
\sum_n i \frac{1}{\sqrt{\langle R_n(t)|R_n(t)\rangle}} \Bigg[ -i\varepsilon_n(t)a_n(t) \, |R_n(t)\rangle + \dot{a}_n(t) \, |R_n(t)\rangle + a_n(t)\frac{\partial}{\partial t} \, |R_n(t)\rangle
$$
$$
- a_n(t)\frac{1}{2}\frac{\langle R_n(t)|\frac{\partial}{\partial t}|R_n(t)\rangle + \text{c.c.}}{\langle R_n(t)|R_n(t)\rangle} \, |R_n(t)\rangle \Bigg] = 0,
$$

(2.5)

where c.c. stand for the complex conjugate. This equation differs from its Hermitian counterpart Eq. A.2 only because for non-Hermitian Hamiltonians the norm of the eigenstates is not necessarily conserved.[3]

Once the ansatz has been used in the appropriate time dependent Schrödinger equation, the second crossroad is approached in the form of the projection: in the Hermitian case, in fact, projecting on a vector allows to simplify calculations because of the orthogonality relation, see *e.g.* Eq. A.3. Under the same spirit (and following the suggestion in Ref. [5]), it seems reasonable to use the bi-orthogonality of the non-Hermitian bases, $\langle L_m|R_n\rangle \propto \delta_{mn}$. It is understood that projecting on $\langle R_m|$ is possible, but this comes at a cost: calculations become over-complicated, and results are harder to interpret, as they cannot be cast in the form of Eq. 2.7 which will be introduced below.

In the Hermitian case, projecting on the $k$-th eigenvector led to an equation for the coefficient of the expansion $a_k^{\text{H}}$:

$$
\dot{a}_k(t) = a_k(t)\left[ -i\varepsilon_k(t) - \langle \phi_k(t)|\frac{\partial}{\partial t}|\phi_k(t)\rangle \right] + \sum_{n\neq k} a_n(t) \, \langle \phi_k(t)|\frac{\partial}{\partial t}|\phi_n(t)\rangle,
$$

(2.6)

where the symbols have the same meaning as before. In the case that the second term in Eq. 2.6 can be neglected, *i.e.* assuming we are in the condition to apply the adiabatic theorem, this equation can be solved yielding the geometric phase contribution, *c.f.* Appendix A. Turning back to the non-Hermitian case, projecting Eq. 2.5 on $\langle L_m|$ and

---

[3]One could as well start without normalizing the eigenstates as in Ref. [88], namely:

$$
|\psi^{\text{R}}(t)\rangle = \sum_n a_n(t) \, |R_n(t)\rangle,
$$

and normalizing the result afterwards. Although it leads to analogous results [1], we look for encapsulating all the effects related to the geometric phase into the expansion coefficients.

rearranging the terms:

$$\dot{a}_m = a_m(t)\left[-i\varepsilon_m(t) - \frac{\langle L_m(t)|\frac{\partial}{\partial t}|R_m(t)\rangle}{\langle L_m(t)|R_m(t)\rangle} + \frac{1}{2}\frac{\langle R_m(t)|\frac{\partial}{\partial t}|R_m(t)\rangle + \text{c.c.}}{\langle R_m(t)|R_m(t)\rangle}\right] \\ + \sum_{n\neq m} a_n(t)\frac{\langle L_m(t)|\frac{\partial}{\partial t}|R_n(t)\rangle}{\langle L_m(t)|R_m(t)\rangle},$$

(2.7)

where the contribution of the eigenenergy in the first term in the square bracket yields the dynamic *factor*, $e^{i\int \varepsilon_m \, \mathrm{d}t}$, analogously to the Hermitian result. Dynamic factor aside, the similarity between this and Eq. 2.6 is noticeable, in particular when looking at the last term. In a similar fashion as for the Hermitian case, the addends can be rewritten taking the time derivative of the the eigenvalue equation for the right eigenvectors and projecting on $\{\langle L_m|\}$, so that [80,86]:

$$\frac{\langle L_m(t)|\frac{\partial}{\partial t}|R_n(t)\rangle}{\langle L_m(t)|R_m(t)\rangle} = \frac{1}{\varepsilon_n - \varepsilon_m}\frac{\langle L_m(t)|\dot{\mathcal{H}}|R_n(t)\rangle}{\langle L_m(t)|R_m(t)\rangle}.$$

(2.8)

As discussed in Appendix A for the Hermitian case, this term is negligible under the hypotheses of the adiabatic theorem, *i.e.* a slowly varying Hamiltonian, away from degeneracies. However, when considering non-Hermitian Hamiltonians energies are allowed to take complex values; hence the dynamic factor $e^{i\int \varepsilon_m \, \mathrm{d}t}$ contributes with an oscillatory phase modulated by an exponential change, related to $\text{Re}\,\varepsilon_m$ and $\text{Im}\,\varepsilon_m$ respectively. This in turn means that it is not easy to give a formulation of the adiabatic theorem as I now will qualitatively explain considering two extreme conditions [80]: the case in which the imaginary part of the energy dominates the terms in square brackets in Eq. 2.7, and the $\mathcal{PT}$-symmetric case, *c.f.* Section 1.1. Let us start from the former. In this case:

$$|\text{Im}\,\varepsilon_m| \gg \frac{\langle L_m(t)|\frac{\partial}{\partial t}|R_m(t)\rangle}{\langle L_m(t)|R_m(t)\rangle};$$

let us examine first the case in which $|\psi^R\rangle$ is initially in an equal superposition of all the eigenstates. Looking at Eq. 2.2 it is clear that even for a slowly varying Hamiltonian,

the eigenstate whose eigenenergy has the largest imaginary part will rapidly dominate the dynamics; in fact it grows the quickest, outpacing the other eigenstates (resp. decays the slowest, surviving the other eigenstates). This means that after a short time all the amplitudes $a_n(t)$ in Eq. 2.2 can be ignored as they quickly become negligible with respect to $a_M(t)$, with $M$ labeling the dominant state [80]. If the system is initialized in an eigenstate, the story does not change: the terms in Eq. 2.8 regulate the overlap with other eigenstates, and at some later time (the ratio $\langle L_m(t)|\dot{\mathcal{H}}|R_n(t)\rangle/(\varepsilon_n - \varepsilon_m)$ sets the time-scale for how much later) $|R_M\rangle$ will be excited, and it will quickly start dominating the dynamics [80, 86]. Lastly, let us consider the case when $|\psi(0)\rangle = |R_M\rangle$: in this case the overlap with other states can be neglected from the very beginning, as $a_m = 0$, for $m \neq M$, and the adiabatic theorem (as understood from the Hermitian case) holds [80, 86].

Things change if we restrict ourselves to the $\mathcal{PT}$-unbroken region. In this case, in fact, $\varepsilon_n \in \mathbb{R}$, and the adiabatic theorem holds in the Hermitian sense if the system is away from exceptional points; in other words, the adiabatic theorem in the $\mathcal{PT}$-symmetric regime holds if [33, 86]:

$$\langle L_m(t)|\dot{\mathcal{H}}|R_n(t)\rangle \ll \varepsilon_n - \varepsilon_m, \tag{2.9}$$

which is the usual restriction also for a Hermitian Hamiltonian.

Summing up, as long as the energies are allowed to be imaginary, the dynamics will be dominated by the state whose eigenenergy has the largest imaginary part, unless the other terms in (2.7) can compensate for $\text{Im}\,\varepsilon_n$. On the other hand, in the case in which $\mathcal{PT}$-symmetry is unbroken, $i.e.$ energy is real, we have obtained that the adiabatic theorem holds similarly to the Hermitian case. Other regimes require more technicalities that are beyond the scope of this thesis, but more details on the formulation of the adiabatic theorem can be found in Refs. [86–89, 91].

Let us therefore set ourselves in the $\mathcal{PT}$-symmetric regime, so that we can neglect the sum in Eq. 2.8 and focus on the first part of Eq. 2.7. If we now factorize the dynamic factor in the coefficients as $a_m(t) = e^{i \int_0^t \varepsilon_m \, \mathrm{d}\tau} c_m(t)$, parametrizing the time dependence of

the Hamiltonian by $\boldsymbol{\lambda} = (\lambda_1, \lambda_2, \dots)$, Eq. 2.7 turns into:

$$\dot{c}_m(t) = -\frac{\partial \boldsymbol{\lambda}}{\partial t} c_m(t) \left[ \frac{\langle L_m | \nabla_{\boldsymbol{\lambda}} | R_m \rangle}{\langle L_m | R_m \rangle} - \frac{1}{2} \frac{\langle R_m(t) | \nabla_{\boldsymbol{\lambda}} | R_m(t) \rangle + \text{c.c.}}{\langle R_m(t) | R_m(t) \rangle} \right].$$

The quantities in the brackets look like slightly modified copies of the Berry connection given in Eq. 2.1. If we define the following four quantities [1, 80, 92]:

$$\mathcal{A}_{m,j}^{\alpha\beta} = i \frac{\langle \alpha_m(\boldsymbol{\lambda}) | \frac{\partial}{\partial \lambda_j} | \beta_m(\boldsymbol{\lambda}) \rangle}{\langle \alpha_m(\boldsymbol{\lambda}) | \beta_m(\boldsymbol{\lambda}) \rangle}, \quad \alpha, \beta = L \text{ or } R, \tag{2.10}$$

we can see that as soon as Hermiticity is restored, $|R_n\rangle \equiv |L_n\rangle$ and the definitions in Eq. 2.10 collapse on to the definition of the Berry connection in Eq. 2.1. Using the (reasonable) initial condition that at the initial time $c_m(0) = 1$, we obtain that $c_m(t) = e^{i\gamma_m^{\text{G}}(\mathcal{C})}$, where:

$$\gamma_m^{\text{G}}(\mathcal{C}) = \int_{\mathcal{C}} d\boldsymbol{\lambda} \cdot \left( \mathcal{A}_m^{LR}(\boldsymbol{\lambda}) - i \operatorname{Im} \mathcal{A}_m^{RR}(\boldsymbol{\lambda}) \right), \tag{2.11}$$

with $\mathcal{C}$ being the trajectory of the system in parameter space [1]. As opposed to Eq. 2.1, the non-Hermitian geometric factor is now a complex quantity with imaginary part:

$$\operatorname{Im} \gamma_n^{\text{G}}(\mathcal{C}) = \int_{\mathcal{C}} d\boldsymbol{\lambda} \cdot \operatorname{Im}(\mathcal{A}_n^{LR}(\boldsymbol{\lambda}) - \mathcal{A}_n^{RR}(\boldsymbol{\lambda})). \tag{2.12}$$

As soon as Hermiticity is restored $\mathcal{A}_n^{LR} \equiv \mathcal{A}_n^{RR} \equiv \mathcal{A}_n$, and $\operatorname{Im} \gamma_n^{\text{G}}(\mathcal{C}) = 0$. Let us now look at what happens to the Berry connections $\mathcal{A}^{LR}$ and $\mathcal{A}^{RR}$ in Eq. 2.12 under the generalization to the non-Hermitian case of gauge transformation [80, 92]: $|R_n(\boldsymbol{\lambda})\rangle \to r_n(\boldsymbol{\lambda}) |R_n(\boldsymbol{\lambda})\rangle$ and $|L_n(\boldsymbol{\lambda})\rangle \to l_n(\boldsymbol{\lambda}) |L_n(\boldsymbol{\lambda})\rangle$.[4] We obtain:

$$\mathcal{A}^{\alpha R} \to \mathcal{A}^{\alpha R} + i \nabla_{\boldsymbol{\lambda}} \ln r_n(\boldsymbol{\lambda}), \quad \alpha = L \text{ or } R. \tag{2.13}$$

Just like the Hermitian case, Berry connections can be gauged away for a generic path $\mathcal{C}$,

---

[4]In Refs. [80, 92] it is clarified that both $r_n(\boldsymbol{\lambda})$ and $l_n(\boldsymbol{\lambda})$ are two analytic, non-zero functions of the parameter $\boldsymbol{\lambda}$, and that the gauge choice is $l_n(\boldsymbol{\lambda}) = 1/r_n^*(\boldsymbol{\lambda})$ so that the bi-orthogonality holds. However, in the following discussion this latter detail is of no interest, *c.f.* Eq. 2.14.

and so it happens to $\operatorname{Re}\gamma_n^{\mathrm{G}} = \int_{\mathcal{C}} \mathrm{d}\boldsymbol{\lambda} \cdot \operatorname{Re}\boldsymbol{\mathcal{A}}_m^{LR}(\boldsymbol{\lambda})$. However, as opposed to the Hermitian case, combinations of these Berry connections are gauge invariant [1, 80, 92], namely:

$$\delta\boldsymbol{\mathcal{A}}_n^R \equiv \boldsymbol{\mathcal{A}}_n^{LR} - \boldsymbol{\mathcal{A}}_n^{RR}, \tag{2.14}$$

is gauge invariant *for a generic path* $\mathcal{C}$. This means that $\mathcal{C}$ does not need to be closed, the the geometric factor to be an observable, as opposed to the Hermitian case. It is of paramount importance to note that the integrand in the definition of the imaginary part of $\gamma_n^{\mathrm{G}}$ (2.12) is exactly the gauge invariant quantity $\delta\boldsymbol{\mathcal{A}}_n^R$ in Eq. 2.14: we then expect the amplitude of the state to exponentially change during time evolution in parameter space *along a generic path in parameter space* even in the $\mathcal{PT}$-symmetric regime. A detailed discussion on the role of the gauge invariant combination of the Berry connections can be found in Refs. [80, 92] where tha band theory and the wave packet dynamics is discussed in connection with this result.

Note that had we started with expanding the generic state using the vectors of the left eigenbasis $\{|L_n\rangle\}$, we would have obtained for Eqs. 2.13 and 2.14, respectively $\boldsymbol{\mathcal{A}}^{\alpha L} \to \boldsymbol{\mathcal{A}}^{\alpha L} + i\nabla_{\boldsymbol{\lambda}}\ln l_n(\boldsymbol{\lambda})$ and $\delta\boldsymbol{\mathcal{A}}_n^L \equiv \boldsymbol{\mathcal{A}}_n^{RL} - \boldsymbol{\mathcal{A}}_n^{LL}$. The correspondence between $\delta\boldsymbol{\mathcal{A}}_n^L$ and $\delta\boldsymbol{\mathcal{A}}_n^R$ can be derived following Ref. [80].

In the $\mathcal{PT}$-symmetric regime, when the adiabatic theorem holds, it is then possible to explicitly write down the evolution of an eigenstate as:

$$\left|\psi_m^{\mathrm{R}}\right\rangle = \exp\left(-i\int_0^t \varepsilon_m \,\mathrm{d}\tau\right)\exp\left(i\int_{\mathcal{C}} \mathrm{d}\boldsymbol{\lambda}\cdot\left(\boldsymbol{\mathcal{A}}_m^{LR} - i\operatorname{Im}\boldsymbol{\mathcal{A}}_m^{RR}\right)\right)\frac{|R_m\rangle}{\sqrt{\langle R_m|R_m\rangle}},$$

where the explicit time dependence has been hidden for the sake of notation, but it is understood that $\{|R_m\rangle\}$ is the *instantaneous* right eigenbasis, and that the time dependence of the Berry connections is parametrized by $\boldsymbol{\lambda}$, that describes a trajectory $\mathcal{C}$ in parameter space. This formulation makes it easy to explicitly write down the dynamical behavior of the population, $n(t) \equiv \langle\psi^{\mathrm{R}}(t)|\psi^{\mathrm{R}}(t)\rangle$, and will prove itself remarkably useful in the next

section, in fact:

$$n(t) = n(0)\left|e^{i\gamma_m^D}e^{i\gamma_m^G}\right|^2 = n(0)\exp\left\{2\int_0^t \operatorname{Im}\varepsilon_m\,\mathrm{d}\tau - 2\int_{\mathcal{C}}\mathrm{d}\boldsymbol{\lambda}\cdot\operatorname{Im}\delta\boldsymbol{\mathcal{A}}_m^R\right\},$$

and since we are in the $\mathcal{PT}$-symmetric regime:

$$n(t) = n(0)\exp\left\{-2\int_{\mathcal{C}}\mathrm{d}\boldsymbol{\lambda}\cdot\operatorname{Im}\delta\boldsymbol{\mathcal{A}}_m^R\right\}, \tag{2.15}$$

where $n(0)$ is the value of the population at the initial time. This result will be put to a test in the numerical experiment in Section 2.2, but before that I owe the reader answers to the questions posed in the beginning of this section:

i) there is no "better" or "worse" choice when it comes to write a state in terms of the instantaneous eigenbasis. One should only be careful on the choice of the Schrödinger equation to solve with their ansatz, namely Eq. 2.3 or Eq. 2.4 accordingly;

ii) as it is known from Hermitian quantum mechanics, projection is useful in order to select terms in the series expansion. In this case, using the bi-orthogonality relations $\langle L_m|R_n\rangle \propto \delta_{mn}$, allowed for useful simplifications;

iii) it is hard to define the non-Hermitian equivalent of the adiabatic theorem, specially outside of the $\mathcal{PT}$-symmetric regime [86–89, 91], as the dynamics of a non-Hermitian system is exponentially dominated by the state whose eigenenergy has the largest imaginary part. Despite this, we found that the imaginary part of the geometric factor is gauge invariant, causing the norm of the state to change during the time evolution (even in the $\mathcal{PT}$-symmetric case) also along open paths [80].

## 2.2  Our dimer model

Of the two ways of making a dimer model non-Hermitian introduced previously, the first that I studied was using balanced on-site gain and loss, as this model has been widely

explored in both theory and experiments [16, 23, 24, 33, 39, 41–43, 48, 52, 96, 97]. The non-Hermitian Hamiltonian is:

$$\mathcal{H} = \begin{pmatrix} ig & -J \\ -J & -ig \end{pmatrix}, \tag{2.16}$$

where, as described in Section 1.2, $J$ represents the hopping energy and $g$ is the factor accounting for the on-site gain and loss, and without loss of generality, both $J$ and $g$ are real and positive.

The eigenvalues of $\mathcal{H}$ are $\varepsilon_{\pm} = \pm\sqrt{J^2 - g^2} \equiv \pm\varepsilon$, and as long as $g < J$, $\mathcal{PT}$-symmetry is unbroken and $\varepsilon$ is real; left and right eigenvectors are given by:

$$\langle L_{\pm}| = \begin{pmatrix} J, & \pm\varepsilon + ig \end{pmatrix}, \quad |R_{\pm}\rangle = \begin{pmatrix} J \\ \pm\varepsilon + ig \end{pmatrix}, \tag{2.17}$$

up to a normalization constant. Note that as mentioned in Section 1.1, the internal product yields:

$$\langle R_{\pm}|R_{\mp}\rangle = 2g(g \mp i\varepsilon)\langle L_{\pm}|L_{\mp}\rangle \neq 0;$$

$$\langle R_{\pm}|L_{\pm}\rangle = 2\varepsilon(\varepsilon \mp ig) = (\langle L_{\pm}|R_{\pm}\rangle)^*; \tag{2.18}$$

$$\langle R_{\pm}|L_{\mp}\rangle = \langle L_{\pm}|R_{\mp}\rangle = 0.$$

On the other hand, the $\mathcal{PT}$-symmetry of the Hamiltonian is broken if the gain and loss parameter is larger than the hopping energy, $g > J$, in which case the energy is purely imaginary and the eigenvectors in Eq. 2.17 cease to be simultaneous eigenvectors of both $\mathcal{H}$ and the $(\mathcal{PT})$ operator. The $\mathcal{PT}$-breaking point $J = g$ corresponds with the exceptional point, where $\varepsilon = 0$, and the eigenvectors coalesce, causing self-orthogonality $\langle R_{\pm}|L_{\pm}\rangle = 0$, c.f. Ref. [31].

A sketch of the parameter space is plotted in Fig. 2.1, where the $\mathcal{PT}$-broken region, $J < g$ is shadowed.
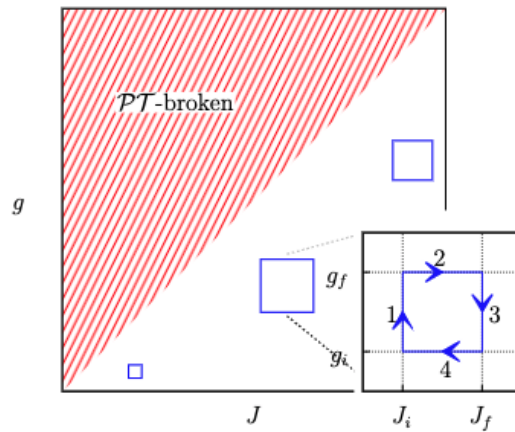
**Figure 2.1:** Sketch of the parameter space; the shaded region is where the $\mathcal{PT}$-symmetry is broken. The square loops represent the trajectories of the system during the time evolution as described in the text; the inset shows the orientation of the loops in the case of clockwise circulation, but the simulations were carried out also for the circulation in opposite direction. Note that the whole evolution takes place in the $\mathcal{PT}$-unbroken region.

Firstly, I investigated the behavior of the system when the Hamiltonian does not change in time to check the code: the goal was to observe the oscillations of the total population accompanied by Rabi-like oscillations for weaker interactions and the exponential growth of the population in the $\mathcal{PT}$-broken regime, as observed *e.g.* in Refs. [43, 48, 52]. After initializing the system in a state given by the superposition of the right eigenstates, namely:

$$\left|\psi^{(R)}\right\rangle = \frac{1}{\sqrt{2}}(|R_-\rangle + |R_+\rangle),$$

I plotted $n = \left\langle\psi^{(R)}\middle|\psi^{(R)}\right\rangle$ to check the behavior of the total population of the system, and the population in each site obtained as the square modulus of the components of $\left|\psi^{(R)}\right\rangle$. The results are plotted in Fig. 2.2, where it is possible to see the solid black line representing $n$ that oscillates only when the non-Hermiticity, $g$, is switched on. The oscillations of the total population have a longer period when the parameters are picked closer to the exceptional point [43, 48, 52]. Together with the oscillation of $n$, $n_1$ (red dash-dotted line) and $n_2$ (blue dashed line) undergo Rabi-like oscillations: particles (or light intensity,...) are exchanged between the two sites, and we note that $n$ grows when the population is on site 1 as this is the one fed with atoms, *c.f.* Eq. 2.16, and decreases when the popu-

lation moves to the lossy site [43, 48, 52]. In the $\mathcal{PT}$-broken regime, energies are purely imaginary, there are no simultaneous eigenstates of $\mathcal{H}$ and the $(\mathcal{PT})$ operator, and the dynamics is dominated by the exponential growth of the population [43, 48, 52, 80].
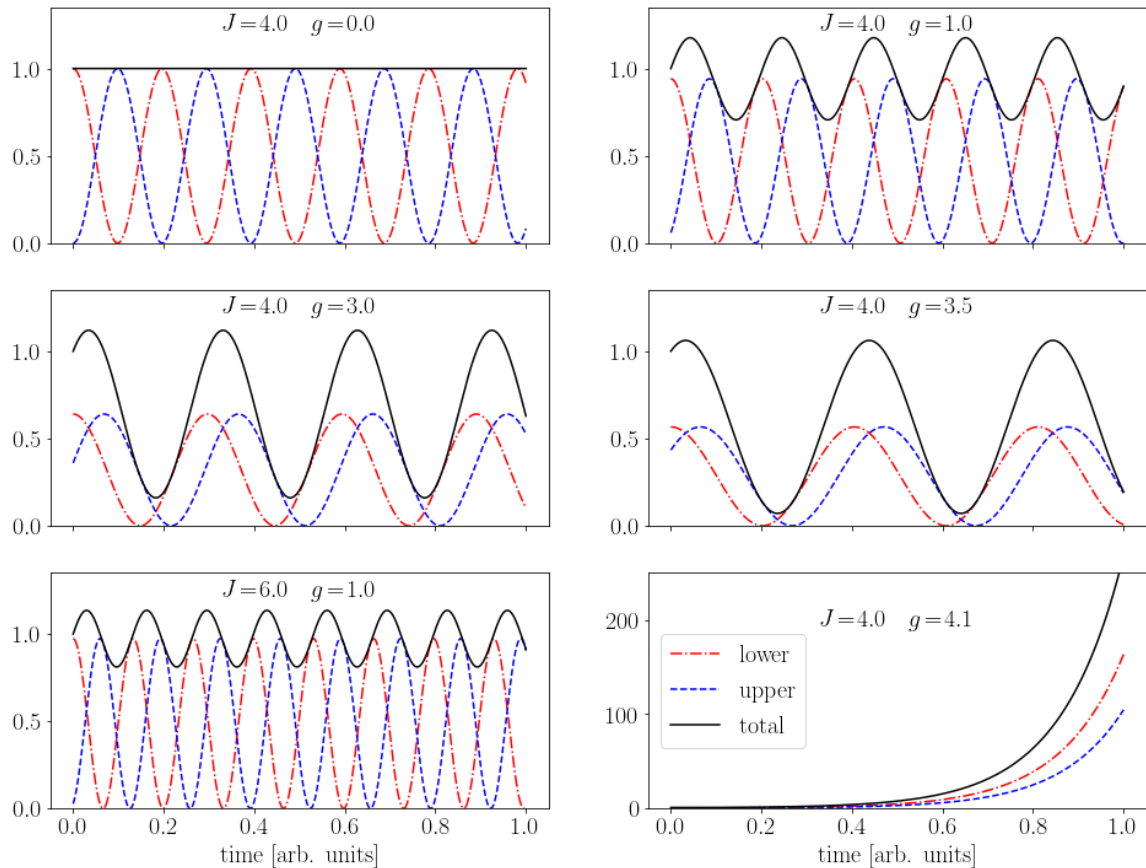


**Figure 2.2:** Plot of the behavior of the population (black solid line) for stationary values of the parameters. Note that the frequency of the oscillations is proportional to the energy gap $2\varepsilon$ between the upper (blue dashed line) and lower (red dash-dotted line) eigenstate, $|R_+\rangle$ and $|R_-\rangle$ respectively.

Once I had verified that the numerics gave the expected result in the stationary case, I made the parameters $g$ and $J$ depend on time. As the goal of this numerical experiment is to check Eq. 2.15, I tuned their time dependence to have the system evolve in the $\mathcal{PT}$-symmetric region of the parameter space, as sketched in Fig. 2.1, in order to avoid any of the issues related to breaking $(\mathcal{PT})$ symmetry.

The time evolution of the parameters was chosen to be cyclic in time, and in order to facilitate both analytical checks and the numerical implementation, I chose the evolution to take place on squares of side-length $\Lambda$, *c.f.* Fig. 2.1: along each side of the square only

| step no. | $J$ | $g$ |
|---|---|---|
| 1 | constant $J_i$ | $g(t) = g_i + \lambda_g(g_f - g_i)\,t$ |
| 2 | $J(t) = J_i + \lambda_J(J_f - J_i)\,t$ | constant $g_f$ |
| 3 | constant $J_f$ | $g(t) = g_f + \lambda_g(g_i - g_f)\,t$ |
| 4 | $J(t) = J_f + \lambda_J(J_i - J_f)\,t$ | constant $g_i$ |

**Table 1:** Scheme of the implementation of the time evolution of the parameters as sketched in Fig. 2.1. The labels $i$ and $f$ refer to the initial and final value taken by the parameters along the side of the square, while $\lambda_g$ and $\lambda_J$ are the linear coefficients tuning the linear dependence on time for $g$ and $J$ respectively, so that the process was adiabatic according to the Hermitian prescription, *c.f.* Eq. 2.9.

one parameter depends linearly on time, as schematically shown in Table 1, hence the Berry connection $\boldsymbol{\mathcal{A}}_\pm^{\alpha,\beta} = (\mathcal{A}_{g,\pm}^{\alpha,\beta}, \mathcal{A}_{J,\pm}^{\alpha,\beta})$ has only one non-zero component.

Starting from an initial value $\tau_0$, time has been discretized considering steps $\delta\tau$ small enough that $[\mathcal{H}(\tau), \mathcal{H}(\tau + \delta\tau)] \approx 0$; under this approximation it was possible to obtain the time evolution as:

$$|R_\pm(t)\rangle = e^{-i \int_0^T \mathcal{H}(\tau)\mathrm{d}\tau} |R_\pm(0)\rangle$$

$$\approx e^{-i\mathcal{H}(\tau_n)\delta\tau} \ldots e^{-i\mathcal{H}(\tau_j)\delta\tau} \ldots e^{-i\mathcal{H}(\tau_1)\delta\tau} |R_\pm(0)\rangle$$

where $\tau_j = \tau_0 + j\delta\tau$, $j$ is an integer and $T$ is the total time of the evolution. At each time step, I evaluated the population by taking $n_\pm(t) = \langle R_\pm(t)|R_\pm(t)\rangle$ and normalizing it with respect to its initial value, yielding the left-hand side of:

$$\frac{n_\pm(t)}{n_\pm(0)} = \exp\left\{-2\,\mathrm{Im}\,\gamma_\pm^\mathrm{G}\right\}. \tag{2.19}$$

As for its right-hand side, it is obtained starting with the evaluation of $\mathcal{A}_\pm^{\alpha\beta}$ considering the following results. Along the vertical segments of the square loops in the inset of Fig. 2.1, only $g$ changes starting from $g_i$ as $g = g_i + \lambda_g t$, straightforward calculations yield:

$$\mathcal{A}_{g,\pm}^{RR} = \pm\lambda_g \frac{1}{2\varepsilon}; \qquad \mathcal{A}_{g,\pm}^{RL} = -\lambda_g \frac{\pm\varepsilon + ig}{2\varepsilon^2};$$

$$\mathcal{A}_{g,\pm}^{LR} = \lambda_g \frac{\pm\varepsilon - ig}{2\varepsilon^2}; \qquad \mathcal{A}_{g,\pm}^{LL} = \mp\lambda_g \frac{1}{2\varepsilon}; \tag{2.20}$$

analogously along the horizontal segments of the loop, where $J$ changes from its initial

value $J_i$ as $J = J_i + \lambda_J t$:

$$\mathcal{A}_{J,\pm}^{RR} = \pm i\lambda_J \frac{\pm 2\varepsilon + ig}{2J\varepsilon}; \qquad \mathcal{A}_{J,\pm}^{RL} = i\lambda_J \frac{1}{2J} \left( 2 + \frac{g^2}{\varepsilon^2} \mp i\frac{g}{\varepsilon} \right)$$

$$\mathcal{A}_{J,\pm}^{LR} = i\lambda_J \frac{1}{2J} \left( 2 + \frac{g^2}{\varepsilon^2} \pm i\frac{g}{\varepsilon} \right); \qquad \mathcal{A}_{J,\pm}^{LL} = \pm i\lambda_J \frac{\pm 2\varepsilon - ig}{2J\varepsilon}. \tag{2.21}$$

In both cases the final time of the evolution is chosen suitably so that $g_f = g_i + \Lambda$ and similarly $J_f = J_i + \Lambda$. Finally, evaluating the gauge invariant quantities connected to these Berry connections as in Eq. 2.14, it is easily found that:

$$\delta\mathcal{A}_g^R = -i\lambda_g \frac{g}{2\,\varepsilon^2} = \delta\mathcal{A}_g^L, \qquad \delta\mathcal{A}_J^R = i\lambda_J \frac{1}{2J} \frac{g^2}{\varepsilon^2} = \delta\mathcal{A}_J^L, \tag{2.22}$$

where the subscripts $g$ and $J$ label the component of the Berry connections along the homologous direction in parameter space, and the $\pm$ label does not enter because there is no difference for the system initialized into either of the two eigenstates. It is also interesting to note that, $\delta\boldsymbol{\mathcal{A}}^R$ yields the same results as $\delta\boldsymbol{\mathcal{A}}^L$, and that in this specific case both components are purely imaginary.
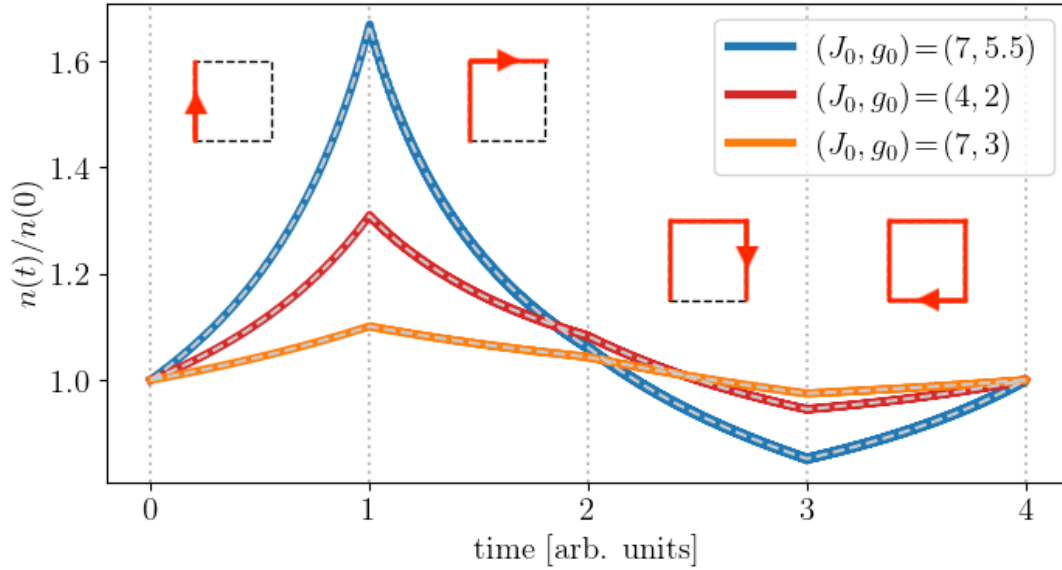
**Figure 2.3:** Plot of the population (thick coloured line) of the system during the time evolution along the square loop of side $\Lambda = 1$ sketched in the small insets, in the counter clockwise direction; the lighter dashed line represents the right-hand side of Eq. 2.19, namely the geometric factor. The legend specifies the value of the parameters at the initial time, corresponding to the bottom-left corner of the loop. Vertical lines represent the time at which the corner of the square is reached; the cartoons highlight the path walked by the system in parameter space. Either plotting the result for the upper or the lower right (resp. left) eigenstates, yields the same result.

The results of the numerical simulations are plotted in Fig. 2.3. The data are simulated for $\Lambda = 1$ meaning that the square has side of unitary length. Time is in arbitrary units with the integer values shown corresponding to the time taken to reach the various corners of the square; the cartoons inside the plot area highlight the segment where the time evolution is taking place. The colored lines represent the behavior of the population $n(t)/n(0)$ when the system moves along square loops in parameter space, starting at the three distinct set of values $(J_0, g_0)$ specified in the legend; note that these values specify the coordinates of the bottom-left corner of the square. On top of the thick colored lines, the dashed line represents the exponential of the geometric factor, *i.e.* the right-hand side of Eq. 2.19. This has been numerically evaluated integrating Eqs. 2.22 along path $\mathcal{C}$ in parameter space.

The first thing to appreciate is the exact overlapping of the norm $n(t)/n(0)$ with $e^{-2\,\mathrm{Im}\,\gamma^{\mathrm{G}}}$, that proves Eq. 2.19. Secondly, we observe that as the system approaches the

exceptional point $n$ grows and conversely shrinks as it moves away from it, as we will show in Chapter 3 [1]. Moreover, the closer the system gets to the $\mathcal{PT}$-breaking line, the larger the growth of the population. We finally comment on the fact that the population goes back to its initial value at the end of the evolution [1, 33, 38]. In the first place, this is a consequence of the fact that the phase is geometric, as the phase accumulated only depends on the position of the contour in parameter space. Secondly, this is related to the concept of magnetic monopole already mentioned in Section 1.1.3. Following Ref. [38], in fact, it is possible to write down the field generated by the fictitious monopole:

$$\boldsymbol{\Omega}_{\pm} = \mp i \, \frac{1}{2 \left( J^2 - g^2 \right)^{3/2}} \begin{pmatrix} -J \\ 0 \\ g \end{pmatrix},$$

corresponding to the field generated by a one-sheet complex hyperbolic magnetic monopole. As the trajectory in parameter space does not encircle it, as opposed to what we did in Chapter 3, the non-Hermitian flux encircled by the loop is zero [1, 33].

The numerical simulations were also performed in the opposite direction along the same loop; the results are plotted in Fig. 2.4, showing a mirror image of the case in which the evolution followed a counter-clockwise path in Fig. 2.3. All of the features observed in the case of counterclockwise evolution, appear also in this case. This specular behavior proves (again) that the phase accumulated is actually geometric [1].
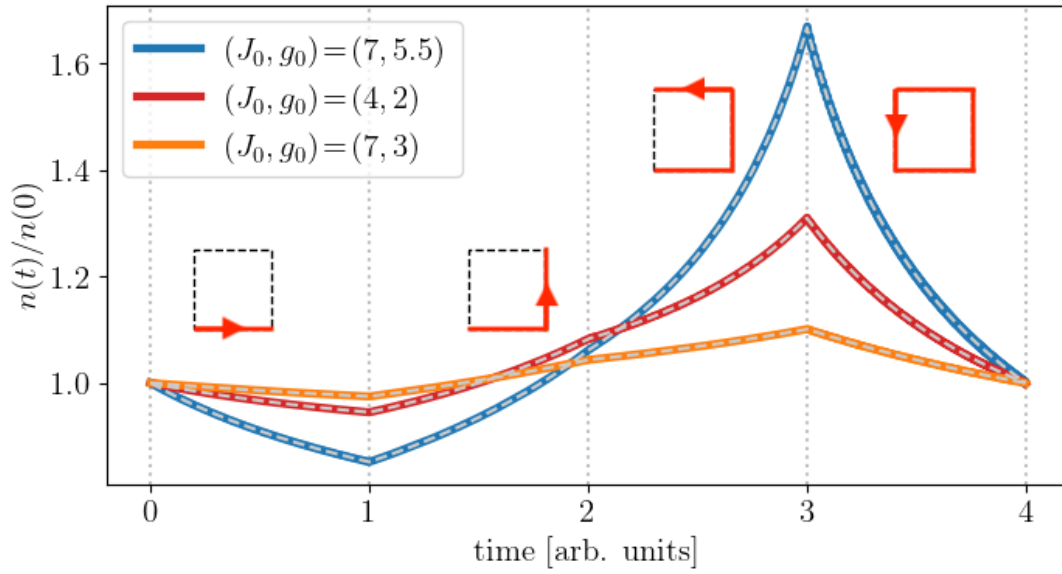
**Figure 2.4:** Plot analogous to Fig. 2.3 but in the case the evolution takes place in the clockwise direction along the loops sketched in the small insets. Note that the dynamics are specular with respect to the previous case.

Finally, I investigated the behavior of the system along larger loops. The results are plotted in Fig. 2.5, where the evolution goes in the counterclockwise direction; the dashed lines represent the oscillations of $n$ for smaller loops, $\Lambda = 1$, whereas the solid lines represent the case of larger loops, $\Lambda = 2$. Lines with the same color represent loops starting at the same point. As expected [1], larger loops lead the system closer to the $\mathcal{PT}$-breaking line where the population grows more quickly, hence the higher peaks.
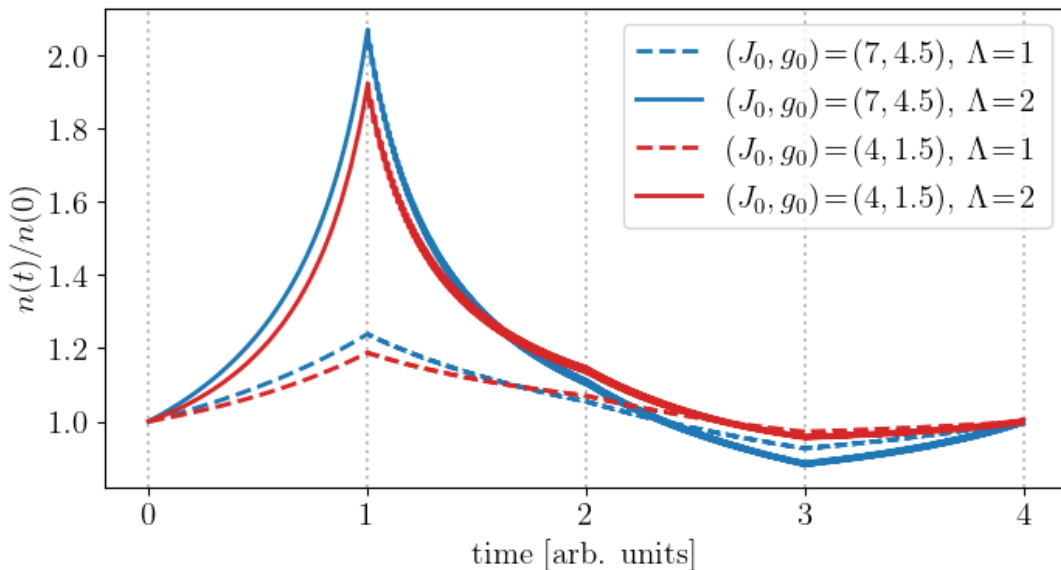
**Figure 2.5:** Plot of the population evolution over time, for loops walked in the counter-clockwise direction. Color encodes the initial value of the parameters; dashed lines are obtained for squared loops with side of length $\Lambda=1$, whereas solid lines are for the case of loops with side of length $\Lambda=1$. Note the tiny wiggles near the peaks for the longer loops, related to numerical instabilities arising close to the $\mathcal{PT}$-breaking line.

## 2.3 Coupled Harmonic Oscillators

At the time my research was scooped, this was the state of my project: a theory matching with a numerical experiment. After checking that my theoretical results were matching also with those in Ref. [80], we decided to move towards an *actual* experimental platform and we started collaborating with a group of experimentalists working on the development of a mechanical metamaterial made of coupled harmonic oscillators. In this section, I will briefly introduce this set-up, but more details can be found in our preprint [21] included as Appendix B. Note that we chose to study the effect of the adiabatic non-Hermitian geometric factor, not in the above dimer with onsite gain and loss, but instead in a Hatano-Nelson dimer [53–55], i.e. the dimer in which non-Hermiticity comes from asymmetry in the hopping energy described in Section 1.2. This was because not only this is a model that scales up to an interesting one-dimensional topological system [7], but is also challenging to realize by other physical means, showing the advantages of our set-up.
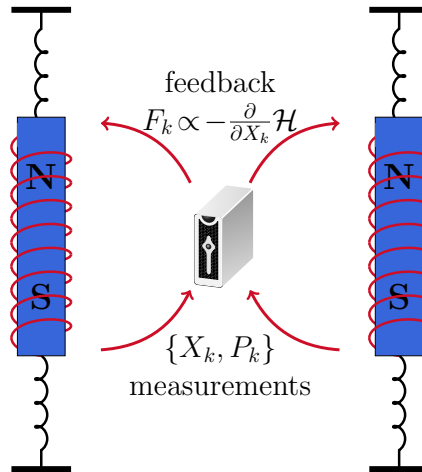
**Figure 2.6:** Sketch of the setup: the harmonic oscillators (in blue) move vertically and are coupled via a contactless feedback that is generated by modulating the current running through the solenoid (in red). Adapted from Ref. [2].

In the last part of this section I will therefore specifically show how this dimer model was realized using two coupled harmonic oscillators; the outcome of the experiment is the subject of the publication-style Chapter 4.

The experimental setup is sketched in Fig. 2.6: it consists of a pair of (almost) identical harmonic oscillators [21], however here I will keep the formalism as generic as possible so that it can be easily extended to any number $N$ of oscillators. Each of the oscillators is made of a mass attached to springs that constrain the motion along the vertical direction, and an accelerometer connected to a computer; this allows for a real time measurement of the acceleration $a(t)$ and the simultaneous computation of its numerical derivative, the jerk $j(t) = \partial a(t)/\partial t$. Feedback is implemented as follows: to each mass is connected a rigid rod ending with a magnet that, during the oscillations, moves inside a solenoid. Controlling the current running through its coils, it is possible to apply a force to the magnet, allowing for a *contactless* feedback [21].

Let us start considering the measurement of the acceleration and the computation of its time derivative. For a harmonic oscillator, their dynamics is described by:

$$\frac{\mathrm{d}a_k}{\mathrm{d}t} = j_k \quad \text{and} \quad \frac{\mathrm{d}j_k}{\mathrm{d}t} = -\omega^2 a_k;$$

these resemble the equations of motion for the position and momentum of a harmonic oscillator with mass $m = 1$ oscillating at frequency $\omega$. For this reason, one can consider the pair $(a_k, j_k)$ for oscillator $k$ as proxies for its position and momentum $(X_k, P_k)$, so that this equation can be written as:

$$\dot{X}_k = P_k \quad \text{and} \quad \dot{P}_k = -\omega^2 X_k, \tag{2.23}$$

where the dot represent the time derivative. Measuring $X$ and $P$ we can build quantities that are analogues of tight binding Hamiltonians quantities, $e.g.$ the proxy for the energy $\tilde{E} \propto (\omega X^2 + P^2/\omega)/2$ (whose analogue is the particle probability density) and the proxy for the phase $\tilde{\phi}_j = \arg(X_j + iP_j)$ of each oscillator (the phase of the evolving wave function) [21]. These measurements are used to engineer a feedback $F$, that is then applied to the oscillators.

In the absence of external feedback, $F_k$, we define the following complex quantities [21, 98, 99]:

$$\alpha_k \equiv \sqrt{\frac{\omega}{2}} X_k + i\sqrt{\frac{1}{2\omega}} P_k, \qquad \alpha_k^* \equiv \sqrt{\frac{\omega}{2}} X_k - i\sqrt{\frac{1}{2\omega}} P_k, \tag{2.24}$$

whose dynamics is described by $\dot{\alpha}_k = -i\omega\alpha_k$ and its complex conjugate $\dot{\alpha}_k^* = i\omega\alpha_k^*$. These quantities have also a physical meaning: the square modulus $|\alpha_k|^2$ corresponds to the energy of oscillator $k$, whereas $\arg \alpha_k$ represents its oscillation phase [21, 99].

Including the effects of an external feedback applied to oscillator $k$, $F_k$, means turning the equation for $\dot{P}_k$ in Eq. 2.23 into $\dot{P}_k = -\omega^2 X_k + F_k$. The full equations of motion for the variables $\alpha_k$ then become [21, 99]:

$$\dot{\alpha}_k = -i\omega\alpha_k + i\sqrt{\frac{1}{2\omega}} F_k, \tag{2.25}$$

and its complex conjugate describes the dynamics of $\alpha_k^*$. Since in this setup the feedback is computed as a function of the measured quantities $X_1, \ldots, X_N, P_1, \ldots, P_N$, with $N$ being the total number of oscillators, it is possible to express $F_k$ as a function of

$(\alpha_1, \ldots, \alpha_N, \alpha_1^*, \ldots, \alpha_N^*)$.

It is clear that as long as no feedback is applied, Eq. 2.25 has an oscillatory solution $\alpha_k \sim e^{-i\omega t}$, and analogously its complex conjugate oscillates as $\alpha_k^* \sim e^{+i\omega t}$. As soon as $F_k$ is switched on, the time dependence of the complex variable is still given approximately by $\alpha_k(t) \sim e^{-i\omega t}$ provided that the following two conditions apply: $i$) that the feedback has small amplitude (weak feedback) and $ii$) that $\omega$ is the largest frequency in the problem. Under these circumstances, when we transform Eq. 2.25 into the frame of reference rotating with frequency $\omega$, we will find that all the "co-rotating" terms proportional to $\alpha_k(t)$ will vary slowly, while terms proportional to $\alpha_k^2$ or "counter-rotating" terms proportional, for example, to $\alpha_k^*(t)$ will be rotating with frequency $\approx \omega$ and $\approx -2\omega$, respectively. Since $\omega$ is large, both terms will average out quickly, hence giving no contribution to the dynamics. This high-frequency limit is known as Rotating Wave Approximation (RWA) and is a common approach in the field of optics [21, 99, 100].

If the conditions for the RWA hold, only terms in the feedback that are $\propto \alpha_k(t)$ contribute, and the equations of motion become [21]:

$$\dot{\alpha}_k = -i\omega\alpha_k + \frac{i}{\sqrt{2\omega}} \sum_j F_{kj}^{\text{RWA}} \alpha_j, \tag{2.26}$$

where $F_{kj}^{\text{RWA}}$ is the part of the feedback applied to the $k$-th oscillator that depends on the $j$-th oscillator, for which we only keep suitable co-rotating terms. As all these co-rotating terms contain one factor of $\alpha_j$, we have factored this out for clarity [21]. To make a connection with quantum dynamics, we need to identify $\alpha_k = \langle \hat{\alpha}_k \rangle$ and $\alpha_k^* = \langle \hat{\alpha}_k^\dagger \rangle$, where $\hat{\alpha}_k$ and $\hat{\alpha}_k^\dagger$ are Bosonic annihilation and creation operators respectively, and $\langle \bullet \rangle$ is the quantum mechanical average with respect to the initial state. We also assume that $F_{kj}^{\text{RWA}} \alpha_k \approx \langle \hat{F}_{kj}^{\text{RWA}} \hat{\alpha}_j \rangle$, where $\hat{F}_{kj}^{\text{RWA}}$ is an operator obtained by replacing all the classical variables $\alpha_k$'s and $\alpha_k^*$'s with $\hat{\alpha}_k$'s and $\hat{\alpha}_k^\dagger$'s. With these identifications and taking $\hbar = 1$, it can then be shown that Eq. 2.26 is equivalent to the mean-field Schrödinger equation

of motion obtained using the following normal-ordered Hamiltonian [21]:

$$\mathcal{H} = \sum_k \omega \hat{\alpha}_k^\dagger \hat{\alpha}_k - \frac{1}{\sqrt{2\omega}} \sum_{k,j} \frac{1}{n_k + 1} \hat{\alpha}_k^\dagger \hat{F}_{kj}^{\mathrm{RWA}} \hat{\alpha}_j, \tag{2.27}$$

where $n_k$ is the number of $\hat{\alpha}_k^\dagger$ operators in $\hat{F}_{kj}^{\mathrm{RWA}}$. Therefore, in order to simulate the quantum dynamics of a particular tight-binding Hamiltonian, we simply need to design and implement suitable feedback terms in our classical system of mechanical oscillators. As shown in Ref. [21], this approach is very general and flexible, and can be applied to an arbitrary number of oscillators.

Here, as an explicative example, I will report how to generate the feedback to simulate the interacting version of the Hatano-Nelson model used in Chapter 4. Starting from the Hamiltonian:

$$\mathcal{H} = \begin{pmatrix} \Delta & -J - gz \\ -J + gz & -\Delta \end{pmatrix}, \quad z \equiv n_1 - n_2,$$

we first calculate the mean-field dynamical equations, which define the classical equations:

$$\dot{\alpha}_k = -i\omega\alpha_k - i \sum_j [\Delta_k \delta_{kj} - (1 - \delta_{kj})(J + gz_{kj})]\alpha_j, \tag{2.28}$$

where $\delta_{kj}$ is the Kronecker delta, $z_{kj} = \langle \hat{z}_{kj} \rangle$ is the mean-field population imbalance between sites $k$ and $j$, and I have used that $z_{kj} = -z_{jk}$. Comparing this with Eq. 2.26, there are three terms that need to be engineered via the feedback to explore this model, namely: (i) on-site energy shifts $\Delta_k$, (ii) reciprocal hopping terms $J$ and (iii) non-reciprocal population-dependent terms tuned by $g$. Feedback-engineering for the first two of these has been demonstrated in Ref. [21], where it was shown that a suitable feedback was of the type $F_k = A_{kj}X_j$. In particular, in order to obtain an alternating onsite shift of energy $\Delta$ on one site and $-\Delta$ on the other and an inter-oscillator coupling of

energy $J$, the parameter $A_{kj}$ has to be [21]:

$$\frac{1}{2\omega} A_{kj} = \begin{cases} (-1)^{k+1} \Delta & \text{for } k = j; \\ zJ & \text{for } k \neq j. \end{cases} \tag{2.29}$$

Finally, the term depending on the population imbalance can be included by applying the following:

$$\begin{aligned} F_k &= B(\omega^2 X_k^2 - P_j^2)X_k \\ &= B\frac{\omega}{2}\left[(\alpha_k^2 + \alpha_k^{*2} + 2\alpha_k\alpha_k^*) + (\alpha_j^2 + \alpha_j^{*2} - 2\alpha_j\alpha_j^*)\right]\frac{1}{\sqrt{2\omega}}(\alpha_k + \alpha_k^*) \\ &\approx \frac{B}{2}\sqrt{\frac{\omega}{2}}(\alpha_k\alpha_k^* - \alpha_j\alpha_j^*)\alpha_k, \end{aligned} \tag{2.30}$$

where the RWA has been used in the last step. In the second equation of this chain, inside the square brackets only terms containing an equal number of $\alpha_k$ and $\alpha_k^*$ will survive, since terms of the type $\alpha_k\alpha_k$ and $\alpha_k^*\alpha_k^*$ rotate with $\approx \omega$ and $-3\omega$ respectively in the co-rotating frame, hence quickly averaging out. It follows, finally, that the feedback to apply to the $k$-th oscillator is:

$$F_{kj}^{\text{RWA}} = \frac{B}{2}\sqrt{\frac{\omega}{2}}(\alpha_k\alpha_k^* - \alpha_j\alpha_j^*).$$

By direct comparison with Eq. 2.28, we find that $B = 4g$. Note that the sign change in the term $gz$ comes naturally from the choice of using the measurement of the acceleration $X$ of the oscillator to which the feedback has to be applied and the jerk $P$ from the other oscillator.

In conclusion, the feedback to apply to the $k$-th oscillator in order to obtain a non-reciprocal hopping between two wells of different depth is:

$$F_k = \sum_j \left[A_{kj}X_j + (1 - \delta_{kj})4g\left(\omega^2 X_k^2 - P_j^2\right)X_k\right],$$

and $A_{kj}$ as in Eq. 2.29.

Having described how to engineer the feedback to apply to each of the oscillators in order to realize the Hatano-Nelson dimer, we can now move to Chapter 3 and then Chapter 4 where the outcome of the experiment are presented in publication style.

# Chapter 3

# Measuring the Adiabatic non-Hermitian Berry Phase

Based on the work I carried out with the collaboration of Hannah Price and Tomoki Ozawa, and that I presented in Chapter 2, we proposed this experiment to the experimental group led by Bryce Gadway. As a joint first author of this paper, together with Hannah Price and Tomoki Ozawa, I dealt with the theoretical aspects presented and with the editing of the manuscript; Yaashnaa Singhal and Bryce Gadway took care of the main writing and collection of the experimental data.

# Measuring the Adiabatic Non-Hermitian Berry Phase in Feedback-Coupled Oscillators

Yaashnaa Singhal,[1, *] Enrico Martello,[2, *] Shraddha Agrawal,[1]
Tomoki Ozawa,[3, †] Hannah Price,[2, ‡] and Bryce Gadway[1, §]

[1]*Department of Physics, University of Illinois at Urbana-Champaign, Urbana, IL 61801-3080, USA*
[2]*School of Physics and Astronomy, University of Birmingham,*
*Edgbaston, Birmingham B15 2TT, United Kingdom*
[3]*Advanced Institute for Materials Research (WPI-AIMR), Tohoku University, Sendai 980-8577, Japan*
(Dated: May 6, 2022)

The geometrical Berry phase is key to understanding the behaviour of quantum states under cyclic adiabatic evolution. When generalised to non-Hermitian systems with gain and loss, the Berry phase can become complex, and should modify not only the phase but also the amplitude of the state. Here, we perform the first experimental measurements of the adiabatic non-Hermitian Berry phase, exploring a minimal two-site $\mathcal{PT}$-symmetric Hamiltonian that is inspired by the Hatano-Nelson model. We realise this non-Hermitian model experimentally by mapping its dynamics to that of a pair of classical oscillators coupled by real-time measurement-based feedback. As we verify experimentally, the adiabatic non-Hermitian Berry phase is a purely geometrical effect that leads to significant amplification and damping of the amplitude also for non-cyclical paths within the parameter space even when all eigenenergies are real. We further observe a non-Hermitian analog of the Aharonov–Bohm solenoid effect, observing amplification and attenuation when encircling a region of broken $\mathcal{PT}$ symmetry that serves as a source of imaginary flux. This experiment demonstrates the importance of geometrical effects that are unique to non-Hermitian systems and paves the way towards the further studies of non-Hermitian and topological physics in synthetic metamaterials.

Geometrical phases play a fundamental role across physics as they emerge from the cyclic adiabatic evolution of a system, and depend only on certain intrinsic geometrical properties within a given parameter space. In quantum mechanics, a key example of this is the Berry phase [1], which can be related, not only to the quantum geometry of eigenstates, but also to important topological invariants, such as the Chern number and winding number [2, 3]. Experimentally, the Berry phase has profound effects on material and transport properties, and it underlies Hall effects, polarization, charge pumping, semiclassical dynamics and many other phenomena [2].

Following its discovery, the Berry phase was generalised to systems with dissipation or gain, in which the Hamiltonian becomes non-Hermitian [4–11]. Interest in such problems has continued to grow, inspired by developments in non-Hermitian experimental platforms, including in photonics [12, 13], mechanics [14–20], electric circuits [21, 22], and cold atoms [23, 24] amongst many others [25–27]. This progress has also been driven by interest in topological systems, in which non-Hermiticity leads to new topological classifications and unusual boundary phenomena [25, 27].

Underlying these effects are fundamental differences between Hermitian and non-Hermitian Hamiltonians; this includes that eigenstates can coalesce and become defective at exceptional points, that the left and right eigenfunctions will typically be different from each other, and that the eigenenergies can become complex [13, 26]. One important consequence of these differences is that the Berry phase will, in general, become complex- instead of real-valued, implying that the amplitude as well as the phase of a state will vary under adiabatic dynam-

ical evolution [4–7, 28–31].

In this paper, we measure the adiabatic non-Hermitian Berry phase, demonstrating how non-Hermiticity leads to gauge-invariant geometrical effects even for non-cyclical paths in parameter space. This goes beyond previous experiments which observed the real part of a Berry phase for closed loops around non-Hermitian exceptional points [32–34]; in those cases, the Berry phase was parametric rather than adiabatic as adiabaticity inevitably breaks down when an exceptional point is dynamically encircled [35–37] and geometrical properties have therefore to be reconstructed from eigenmode measurements. In contrast, here we study a two-site $\mathcal{PT}$-symmetric system, in a regime for which the eigenenergies are real and adiabatic evolution is possible. To realise our model, we employ a mapping between quantum evolution and the classical dynamics of a pair of oscillators coupled with real-time measurement-based feedback [20]. We evolve our system adiabatically and experimentally demonstrate that the imaginary part of the Berry phase leads to significant geometrical amplification and damping, which is intrinsically non-Hermitian.

*Non-Hermitian Berry phase:* Before discussing our experiment, we review the basic theory of non-Hermitian systems [13, 26] to motivate the non-Hermitian Berry phase. Various related definitions exist for this phase [4–11]; here, we introduce a formalism that is motivated by physical observables to concisely include all relevant geometrical effects using Berry connections. This definition has the advantage that its imaginary part is manifestly gauge-invariant and is immediately related to measurements of the population. Detailed derivations are given in the Supplemental Material.

We consider a $N$-component state vector $|\psi(t)\rangle$, which depends on time $t$ and obeys the Schrödinger-type equation $i\partial_t|\psi(t)\rangle = H(\boldsymbol{\lambda})|\psi(t)\rangle$, where the family of $N$-by-$N$ non-Hermitian matrices $H(\boldsymbol{\lambda})$ are parametrized by a set of real parameters $\boldsymbol{\lambda} = (\lambda_1, \lambda_2, \cdots)$. For a given value of $\boldsymbol{\lambda}$, $H(\boldsymbol{\lambda})$ acts as a non-Hermitian Hamiltonian. It has right and left eigenvectors, denoted by $|R_n(\boldsymbol{\lambda})\rangle$ and $\langle L_n(\boldsymbol{\lambda})|$ respectively, which are generally not complex conjugates of each other [13, 26], but which share the same complex eigenvalues $\varepsilon_n(\boldsymbol{\lambda})$, indexed by $n = 1, 2, \cdots, N$. Within the parameter space spanned by $\boldsymbol{\lambda}$, four distinct geometrical Berry connections can then be defined [30, 38]; however, for the non-Hermitian Berry phase, only the following two Berry connections will be relevant:

$$\mathcal{A}_{n,j}^{LR}(\boldsymbol{\lambda}) \equiv i\langle L_n(\boldsymbol{\lambda})|\partial_{\lambda_j}|R_n(\boldsymbol{\lambda})\rangle / \langle L_n(\boldsymbol{\lambda})|R_n(\boldsymbol{\lambda})\rangle, \quad (1)$$

$$\mathcal{A}_{n,j}^{RR}(\boldsymbol{\lambda}) \equiv i\langle R_n(\boldsymbol{\lambda})|\partial_{\lambda_j}|R_n(\boldsymbol{\lambda})\rangle / \langle R_n(\boldsymbol{\lambda})|R_n(\boldsymbol{\lambda})\rangle. \quad (2)$$

Upon a generalized gauge transformation, which multiplies $|R_n(\boldsymbol{\lambda})\rangle$ and $|L_n(\boldsymbol{\lambda})\rangle$ not just by a phase but also by arbitrary and independent nonzero factors, it can be shown that the following combination of the above Berry connections is invariant [30]:

$$\delta\mathcal{A}_{n,j}^{LR-RR}(\boldsymbol{\lambda}) \equiv \mathcal{A}_{n,j}^{LR}(\boldsymbol{\lambda}) - \mathcal{A}_{n,j}^{RR}(\boldsymbol{\lambda}). \quad (3)$$

It is a distinguishing feature of non-Hermitian systems that gauge-independent quantities can be constructed just from a linear combination of Berry connections; in Hermitian quantum mechanics, the different Berry connections coincide and the gauge-invariant combination $\delta\mathcal{A}_{n,i}^{LR-RR}$ is always zero.

We now consider the adiabatic evolution of a state upon changing the parameter $\boldsymbol{\lambda}(t)$ as a function of time $t$ to extract the non-Hermitian counterpart of the Berry phase [4–7, 28–31, 39]. Here, we focus on the situation where all the eigenvalues are real and non-degenerate so that we can apply the adiabatic theorem [40, 41]. Then if the initial state corresponds to the $n$-th right eigenstate, the state at time $t$ can be written as

$$|\psi(t)\rangle = c(t)\frac{|R_n(\boldsymbol{\lambda}(t))\rangle}{\sqrt{\langle R_n(\boldsymbol{\lambda}(t))|R_n(\boldsymbol{\lambda}(t))\rangle}} \quad (4)$$

where $c(t)$ is a complex-valued adiabatic factor that the state acquires as $\boldsymbol{\lambda}(t)$ is varied. In defining $c(t)$, we chose to separate out the denominator, as we are interested in physical observables such as the population $N(t)$, which is then given simply by $N(t) \equiv \langle\psi(t)|\psi(t)\rangle = |c(t)|^2$. We note that the final result is independent of the way the state $|\psi(t)\rangle$ is written as a product of a coefficient $c(t)$ and a basis vector, as explained in detail in Supplemental Material. We formally solve the Schödinger equation $i\partial_t|\psi(t)\rangle = H(\boldsymbol{\lambda}(t))|\psi(t)\rangle = \varepsilon_n(\boldsymbol{\lambda}(t))|\psi(t)\rangle$ by applying $\langle L_n(\boldsymbol{\lambda}(t))|$ from the left, which yields

$$c(t) = c(0)\exp\left[-i\int_0^t dt' \varepsilon_n(\boldsymbol{\lambda}(t')) + i\phi[\mathcal{C}]\right], \quad (5)$$

where the first term in the exponent is the dynamical contribution to the adiabatic factor $c(t)$, whereas the second part is the non-Hermitian Berry phase that we define by

$$\phi[\mathcal{C}] \equiv \int_{\mathcal{C}} d\boldsymbol{\lambda} \cdot \left(\mathcal{A}_n^{LR}(\boldsymbol{\lambda}) - i\text{Im}\mathcal{A}_n^{RR}(\boldsymbol{\lambda})\right), \quad (6)$$

where $\mathcal{A}_n^{LR}(\boldsymbol{\lambda}) = (\mathcal{A}_{n,1}^{LR}(\boldsymbol{\lambda}), \mathcal{A}_{n,2}^{LR}(\boldsymbol{\lambda}), \cdots)$ and similarly for $\mathcal{A}_n^{RR}(\boldsymbol{\lambda})$. The non-Hermitian Berry phase depends on the path $\mathcal{C}$ taken in parameter space and reflects the geometrical structure of the eigenstates, analogous to the well-known Berry phase for Hermitian systems [1, 2]. However, unlike the Hermitian Berry phase, the non-Hermitian Berry phase has both real and imaginary parts. In particular, the imaginary part

$$\text{Im}(\phi[\mathcal{C}]) = \int_{\mathcal{C}} d\boldsymbol{\lambda} \cdot \text{Im}\delta\mathcal{A}_n^{LR-RR}(\boldsymbol{\lambda}), \quad (7)$$

depends solely on the imaginary part of $\delta\mathcal{A}_n^{LR-RR}(\boldsymbol{\lambda}) = (\delta\mathcal{A}_{n,1}^{LR-RR}(\boldsymbol{\lambda}), \delta\mathcal{A}_{n,2}^{LR-RR}(\boldsymbol{\lambda}), \cdots)$, which is the gauge-invariant combination of Berry connections introduced in Eq. (3). Therefore, it is then immediately obvious that the imaginary part of the non-Hermitian Berry phase is gauge independent even when the path $\mathcal{C}$ is not closed [39]. On the other hand, the real part of the Berry phase is gauge invariant only when the path $\mathcal{C}$ forms a closed path, just like in the Hermitian case [2]. When the eigenvalues are all real, the evolution of the population [as depicted in Fig. 1 (a)] is thus determined purely by the imaginary part of the Berry phase as

$$N(t) = |c(t)|^2 = N(0)\exp\left[-2\text{Im}(\phi[\mathcal{C}])\right], \quad (8)$$

which is directly observable in our experiment.

*Experimental set-up:* To experimentally explore the effects of non-Hermitian geometry, we implement the simple two-site model Hamiltonian

$$H = \begin{pmatrix} -\Delta & J + \delta J \\ J - \delta J & \Delta \end{pmatrix}, \quad (9)$$

as depicted in Fig. 1 (b). The elements of $H$ have units of frequency, consistent with the aforementioned Schrödinger-type equation describing the system dynamics. Physically, the real parameters $\Delta$, $J$, and $\delta J$ relate to relevant frequency shifts of ($\Delta$) and hopping rates between ($J \pm \delta J$) the oscillators. This model is inspired by the Hatano-Nelson model for a 1D lattice [42], which has non-reciprocal hoppings between neighbouring lattice sites and which can exhibit nontrivial topology and the non-Hermitian skin effect [27]. The eigenvalues of Eq. 9 are given by $\varepsilon_{\pm} = \pm\sqrt{\Delta^2 + J^2 - \delta J^2}$, which means that the two eigenvalues are both real when $\Delta^2 + J^2 > \delta J^2$, corresponding to the $\mathcal{PT}$-symmetric region. If $\Delta^2 + J^2 = \delta J^2$, the eigenvalues coalesce at an exceptional point; within the parameter space of $(\Delta, J, \delta J)$,
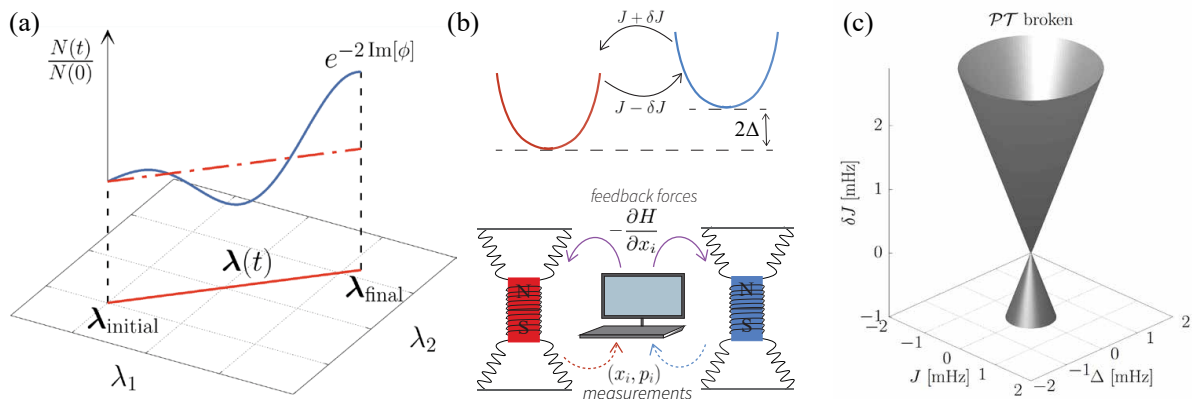
FIG. 1. **Exploration of the non-Hermitian Berry phase in the two-site Hatano-Nelson model.** **(a)** In non-Hermitian systems with $\mathcal{PT}$ symmetry, adiabatic paths in parameter space generically results in amplification or attenuation of the time-dependent population $N(t)$. This results directly from the imaginary portion of the adiabatic non-Hermitian Berry phase $\phi$ acquired by a state along its trajectory. **(b)** Top: The Hatano-Nelson (HN) dimer, a minimal non-Hermitian lattice model with non-reciprocal left/right hopping rates $J \pm \delta J$ and an inter-site frequency imbalance $2\Delta$. Bottom: Implementation of the HN dimer in a mechanical system via measurement-and-feedback. Non-reciprocal coupling between mechanical oscillators, as well as shifts to their resonance frequencies, are realised through applied forces that are responsive to real-time measurements. **(c)** $\mathcal{PT}$ symmetry-breaking phase diagram of the HN dimer. A conical surface of exceptional points in the $J - \delta J - \Delta$ parameter space separates regions of broken and preserved $\mathcal{PT}$ symmetry, respectively lying inside and outside of the conical surface.

the surface of exceptional points corresponds to a double cone, with its apex at the origin [11], as shown in Fig. 1 (c).

The gauge-invariant combinations of the Berry connections within the $\mathcal{PT}$-symmetric region (c.f. Eq. 3) are all purely imaginary, and they diverge as we approach the $\mathcal{PT}$-symmetry breaking transition, where adiabaticity breaks down. (Analytical expressions of the Berry connections and associated Berry curvatures are derived in the Supplemental Material, and can be interpreted in terms of a complex hyperbolic pseudo-magnetic monopole in parameter space [11, 31].) This in turn means that the only non-vanishing part of the non-Hermitian Berry phase (Eq. 6) is purely imaginary and therefore gauge-invariant for any path.

To explore the two-site Hatano-Nelson model, we construct a synthetic mechanical lattice made up of two classical oscillators artificially coupled by real-time feedback measurements, based on our approach reported in Ref. [20]. The essential idea of this scheme is to map the Heisenberg equations for a desired tight-binding quantum Hamiltonian onto Newton's equations of motion for classical oscillators in phase-space within a rotating wave-approximation [43, 44]. As discussed in [20], the use of real-time feedback then means that many two level non-Hermitian Hamiltonian can be realized with this setup. Here, we use self- and cross-feedback between the oscillators to realize the Hamiltonian described in Eq. 9, as depicted at the bottom of Fig. 1 (b). Self-feedback terms proportional to the oscillator positions ($F_i \propto x_i$) allow us to shift their frequencies by $\pm \Delta$ from a nominal starting value of $f_0 \approx 3.05$ Hz. Cross-feedback forces ($F_i \propto x_j$)

allow us to introduce independent left-to-right and right-to-left hopping terms $J \pm \delta J$, with no intrinsic limitation to reciprocal energy exchange. By applying self-feedback terms proportional to the oscillator momenta ($F_i \propto p_i$), we cancel the oscillators' natural damping and explore coherent dynamics for well over 1000 s ($> 3000$ periods). These long timescales are crucial to performing the first explorations of adiabatic response in a non-Hermitian system. Beyond single-body (quadratic, in the operator sense) terms, we additionally apply higher-order feedback to cancel nearly all native quartic nonlinearities. However, small residual nonlinearities remain, serving to, *e.g.*, cap the energy growth in cases of broken $\mathcal{PT}$ symmetry.

*Results:* We first experimentally establish the $\mathcal{PT}$ symmetry-breaking phase diagram of the canonical two-site Hatano–Nelson model, with tunable reciprocal ($J$) and non-reciprocal ($\delta J$) components of the real-valued inter-site hopping, but with no inter-site bias ($\Delta = 0$). In this case, for fixed $J$, an exceptional point and $\mathcal{PT}$ symmetry-breaking phase transition are encountered at $\delta J = J$, as previously demonstrated with this platform by spectral analysis in Ref. [20]. In the full ($J, \delta J$) parameter space, there are two distinct regions of conserved and broken $\mathcal{PT}$ symmetry, denoted by white and grey in Fig. 2 (a). We experimentally determine the exceptional line separating these regions by probing the breakdown of adiabaticity and the rapid onset of energy growth as states cross over into the $\mathcal{PT}$-broken region, as shown in Fig. 2 (b). We prepare eigenmodes of the symmetric double-well for various fixed values of the reciprocal hopping $J$, and then linearly ramp $\delta J$ from 0 to 1.2 $J$ over 400 s. We establish the exceptional points (white
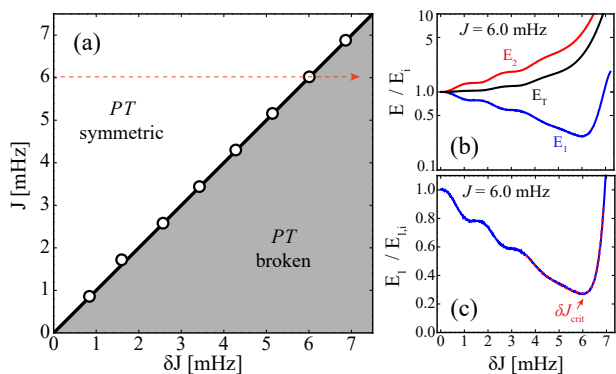
FIG. 2. $\mathcal{PT}$ **symmetry-breaking phase diagram of the unbiased** ($\Delta = 0$) **Hatano–Nelson dimer. (a)** White points mark the experimentally measured exceptional points (EPs). Critical $\delta J$ values for these points are determined by detecting the breakdown of adiabaticity as the EP is crossed. **(b)** Experimental energy dynamics of prepared eigenstates along the ramp of $\delta J$ [dashed red line in (a)] for $J = 6.0$ mHz. The measured energy at site 1 decays (while the site 2 and total energy grow) until the EP is reached at $\delta J \sim J$. Here, we plot the site 1 ($E_1$), site 2 ($E_2$), and total energy ($E_T$) normalized to their respective initial values ($E_i$). **(c)** Crossing of the EP is marked by the onset of growth of the otherwise decaying site 1. The red dashed line is an empirical fit to the data, with the fit minimum defining $\delta J_{\mathrm{crit}}$. Here, we plot the energy in oscillator 1 normalized to its initial value ($E_1/E_{1,i}$).

circles) by determining the instantaneous $\delta J$ values for which there begins to be energy growth at the otherwise decaying first site, as shown in Fig. 2 (c). Here, an observable proportional to the $i^{\mathrm{th}}$ oscillator energy $E_i(t)$ is reconstructed from the measured $x_i$ and $p_i$ signals [20]. We can then associate the oscillators' energy dynamics with relative changes in the macroscopic mechanical energy population $N_i(t) \sim E_i(t)/hf_0$.

We now restrict ourselves to the $\mathcal{PT}$ symmetric region of Fig. 2 (a), exploring the adiabatic gauge invariant non-Hermitian Berry phase acquired (via the energy dynamics of prepared eigenmodes) as we slowly evolve along controlled paths in parameter space. In Fig. 3 (a), we first prepare our system as an eigenmode of the symmetric double well for a fixed reciprocal hopping $J = 6.45$ mHz, and then we smoothly vary the asymmetric hopping as $\delta J(t) = \delta J_{\mathrm{max}} \sin^2(\pi t/T_{\mathrm{ramp}})$ over a time $T_{\mathrm{ramp}} = 500$ s. From the left inset, this corresponds to a closed linear path in parameter space from the black dot at $\delta J = 0$ to one of the colored dots (representing different values of $\delta J_{\mathrm{max}}$), and back. It is seen in Fig. 3 (a) that the total energy increases as the trajectory moves closer to the exceptional line, with the blue ($\delta J_{\mathrm{max}} = 5.16$ mHz) path showing the largest gain. For such a trajectory, the energy in the system is determined by the instantaneous $\delta J$ value, as confirmed by the parametric collapse of the energy vs. $\delta J$ for the blue and yellow curves, shown in

the right inset. To note, slight wiggles in both the data (solid lines) and the numerical simulation curves (dashed lines, which include effects of the finite ramp duration) arise, primarily due to non-adiabatic deviations accumulated near the exceptional line. However, for all curves the total energy returns to near its initial value at the end of the trajectories, consistent with adiabatic evolution along a time-reversed path that encloses zero non-Hermitian flux.

In Fig. 3 (b), we start from the same conditions but now move along closed circular loops by also varying the symmetric hopping term $J$ by a sinusoidal function over a time period of 1000 s. Coordination between the variation of $J$ and $\delta J$ allows us to make either clockwise or counterclockwise paths in parameter space (inset). The energy dynamics curves for the two path directions are essentially (up to small non-adiabatic corrections) mirrored versions of each other with respect to the time midpoint $T_{\mathrm{ramp}}/2$, as the gauge-invariant Berry phase accumulated from the common starting point is again uniquely determined by the instantaneous position in parameter space. This is consistent with the fact that these finite-area paths enclose *zero* non-Hermitian Berry phase. To note, the curves in Fig. 3 (a) and Fig. 3 (b) do exhibit percent level gain and loss over their respective evolution times of 500 and 1000 s, stemming from residual loss and gain terms at the scale of a few $\mu$Hz.

We now explore closed paths in parameter space that enclose a region of broken $\mathcal{PT}$ symmetry, and which correspondingly aquire a finite non-Hermitian Berry phase. We accomplish this by introducing a site-to-site energy bias ($\Delta$). To recall, the exceptional surface in the full ($\Delta, J, \delta J$) parameter space of Eq. 9 corresponds to a double cone with an apex at the origin [11]. As depicted in Fig. 4 (a), this admits closed paths within the $\mathcal{PT}$ symmetric region that enclose areas of broken $\mathcal{PT}$ symmetry. The $\mathcal{PT}$-broken region can, in a sense, serve as a source of non-Hermitian Berry flux, in analogy to the manner in which a magnetic solenoid serves as a source of flux in the canonical Aharonov–Bohm thought experiment [45]. Indeed, our procedure can be viewed as measuring the imaginary Aharonov-Bohm phase in parameter space.

We explore the dynamics of the total energy $E_T$ as we traverse counter-clockwise (CCW) and clockwise (CW) paths in the $J - \Delta$ plane, starting from several fixed values of $\delta J$. We start by preparing eigenmodes of the system with $J = 0$ and then ramp, over 1000 s, about an ellipse in the $J - \Delta$ parameter space as displayed in Fig. 4 (a). As we see from Fig. 4 (b), the dynamics of the total energy are strongly dependent on $\delta J$. In the fully symmetric case, $\delta J = 0$, we find no significant change to the total oscillator energy, as expected from the lack of an enclosed $\mathcal{PT}$-broken region. For increasing values of $\delta J$, we find that the CCW (CW) paths in parameter space lead to an increasing growth (decay) of the energy upon completing one cycle. Fig-
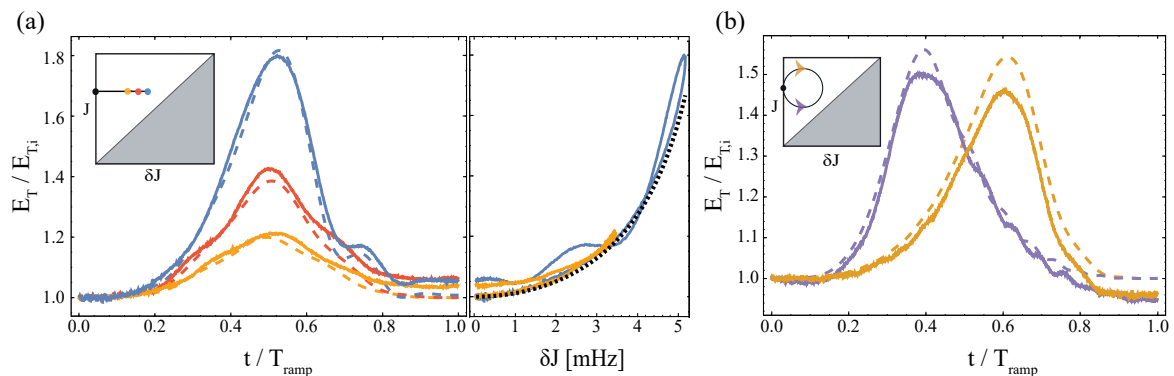
FIG. 3. **Geometric energy amplification and attenuation in the Hatano–Nelson dimer. (a)** Left: Dynamics of the total energy $E_T = E_1 + E_2$ for adiabatic transformations (normalized to its initial value $E_{T,i}$). Inset: path of the adiabatic transformation, for fixed $J = 6.5$ mHz, ramping from $\delta J = 0$ to/from different maximum values of $\delta J_{\max} = 3.4$ mHz (yellow), $\delta J_{\max} = 4.3$ mHz (red), and $\delta J_{\max} = 5.2$ mHz (blue). Right: Plot of the total energy vs. the instantaneous $\delta J$ value, for the yellow and blue paths. The black dotted line shows the expected parametric dependence of $E_T/E_{T,i}$ on $\delta J$ for fully adiabatic evolution under $H$. **(b)** Dynamics of $E_T$ for CW (purple) and CCW (gold) paths as specified by the inset, centered at $(J, \delta J) = (6.5, 2.2)$ mHz and having a radius of 2.2 mHz. The colored dashed lines in the main panels relate to the time-dependent solutions of the Schrödinger-type equation based on evolution under the ideal HN model, including non-adiabatic effects due to the finite ramp durations of $T_{\text{ramp}} = 500$ $s$ for (a) and $T_{\text{ramp}} = 1000$ $s$ for (b).

ure 4 (c) summarizes the $\delta J$-dependence of the measured gain (attenuation) of the total energy experienced upon completing one cycle in the CCW (CW) direction. The near-exponential dependence of the measured gain (attenuation) with $\delta J$ is in qualitative agreement with the expected variation of the acquired non-Hermitian Berry phase for cyclic paths. The non-Hermitian Berry phase accumulated around such paths grows with the size of the $\mathcal{PT}$ broken region, having a form that is nearly proportional to $\delta J$, as presented in the Supplement. For the experimentally traversed path in the CCW (CW) direction, the system picks up a negative (positive) contribution of this imaginary phase, and the state of the oscillators thus experiences a corresponding growth (decay) in its energy. At short times or for small values of the hopping asymmetry $\delta J$, the observed amplification and attenuation are in fair agreement with the analytical form expected based on pure geometric contributions of an imaginary Berry phase. However, clear deviations can be found, most prominently in situations where very large growth of the total energy are expected (CCW orbits for large $\delta J$ values). On physical grounds, deviations from the expected response can be expected for very large oscillator displacements due to natural anharmonicities. We qualitatively capture the observed saturation of growth by comparing to a dynamical evolution that incorporates small but non-negligible (empirical) nonlinear contributions, described further in the Supplement.

*Conclusion:* We have experimentally measured the non-Hermitian Berry phase for adiabatic evolution in a two-site Hatano-Nelson model. We have demonstrated significant geometrical contributions to amplification and damping along both closed and open paths, and shown

that these effects are observable in a synthetic mechanical metamaterial. Going further, we will be able to add different types of nonlinearities to the two-site Hatano-Nelson model, allowing us to explore the interplay of interactions with $\mathcal{PT}$-symmetry [46, 47]. As active mechanical metamaterials are scaled up to larger systems with dozens of oscillators, they will enable controllable explorations of the effects of quantum geometry and topology in non-Hermitian Chern insulators, such as, for example, the anomalous velocity contributions predicted to arise from the non-Hermitian Berry phase [30] and the breakdown of the canonical bulk-boundary correspondence of Hermitian models [48–50].
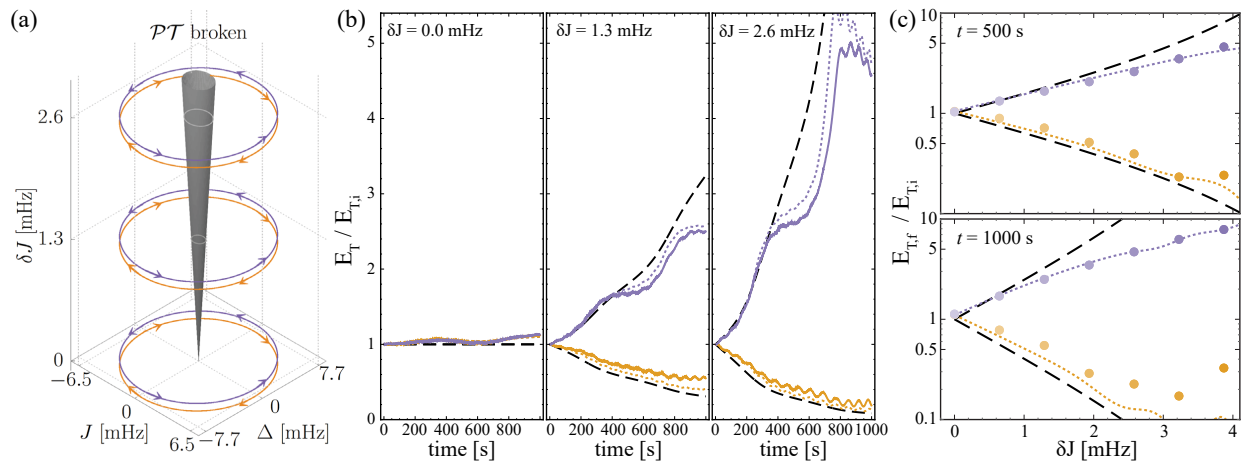
FIG. 4. **Cyclic amplification and attenuation along adiabatic paths enclosing $PT$-broken sources of non-Hermitian Berry phase.** (a) Cartoon depiction of the paths traversed in parameter space. For trajectories in the $J - \Delta$ plane at fixed and finite $\delta J$, the paths enclose a conical $\mathcal{PT}$-broken region that acts as a source of non-Hermitian Berry flux. (b) Dynamics of the total energy $E_T = E_1 + E_2$ for CCW (purple) and CW (gold) paths in the $J - \Delta$ plane as specified in panel (a), shown for three values of the tunneling asymmetry $\delta J$. The solid purple (gold) lines are the measured trajectories from experiment for CCW (CW) paths. The long-dashed and short-dashed lines are theory comparisons, described below. (c) Ratio of the final total energy $E_{T,f}$ to the initial total energy $E_{T,i}$ as a function of the tunneling asymmetry $\delta J$. The upper and lower panels show the energy ratios for one half cycle and one full cycle, respectively. The purple (gold) points are the experimentally measured ratios for the CCW (CW) paths (with error bars smaller than the data points) and the long-dashed and short-dashed lines are theory comparisons. For (b,c), the black long-dashed lines are the analytical predictions (detailed in the Supplement) for the amplification/attenuation under fully adiabatic evolution according to Eq. 9. The dotted lines are the trajectories determined by numerical simulation of the experimental ramping procedure, also incorporating weak nonlinear contributions that serve to capture the saturation observed for large amplification (detailed in the Supplement).

* These authors contributed equally to this work.
† tomoki.ozawa.d8@tohoku.ac.jp
‡ H.Price.2@bham.ac.uk
§ bgadway@illinois.edu

[1] M. V. Berry, Proceedings of the Royal Society of London. A. Mathematical and Physical Sciences **392**, 45 (1984).

[2] D. Xiao, M.-C. Chang, and Q. Niu, Rev. Mod. Phys. **82**, 1959 (2010).

[3] M. Z. Hasan and C. L. Kane, Rev. Mod. Phys. **82**, 3045 (2010).

[4] J. Garrison and E. M. Wright, Physics Letters A **128**, 177 (1988).

[5] G. Dattoli, R. Mignani, and A. Torre, Journal of Physics A: Mathematical and General **23**, 5795 (1990).

[6] F. Keck, H. J. Korsch, and S. Mossmann, Journal of Physics A: Mathematical and General **36**, 2125 (2003).

[7] S.-D. Liang and G.-Y. Huang, Phys. Rev. A **87**, 012118 (2013).

[8] A. Mondragón and E. Hernández, Journal of Physics A: Mathematical and General **29**, 2567 (1996).

[9] M. Berry and M. Dennis, Proceedings of the Royal Society of London. Series A: Mathematical, Physical and Engineering Sciences **459**, 1261 (2003).

[10] M. V. Berry, Czechoslovak journal of physics **54**, 1039 (2004).

[11] A. I. Nesterov and F. A. de la Cruz, Journal of Physics A: Mathematical and Theoretical **41**, 485304 (2008).

[12] A. Guo, G. J. Salamo, D. Duchesne, R. Morandotti, M. Volatier-Ravat, V. Aimez, G. A. Siviloglou, and D. N. Christodoulides, Phys. Rev. Lett. **103**, 093902 (2009).

[13] Ş. K. Özdemir, S. Rotter, F. Nori, and L. Yang, Nature Materials **18**, 783 (2019).

[14] C. Coulais, D. Sounas, and A. Alù, Nature **542**, 461 (2017).

[15] M. Brandenbourger, X. Locsin, E. Lerner, and C. Coulais, Nature Communications **10**, 4608 (2019).

[16] C. Scheibner, W. T. M. Irvine, and V. Vitelli, Phys. Rev. Lett. **125**, 118001 (2020).

[17] C. Scheibner, A. Souslov, D. Banerjee, P. Surowka, W. T. Irvine, and V. Vitelli, Nature Physics **16**, 475 (2020).

[18] D. Zhou and J. Zhang, Physical Review Research **2**, 023173 (2020).

[19] A. Ghatak, M. Brandenbourger, J. van Wezel, and C. Coulais, Proceedings of the National Academy of Sciences (2020), 10.1073/pnas.2010580117.

[20] R. Anandwade, Y. Singhal, S. N. M. Paladugu, E. Martello, M. Castle, S. Agrawal, E. Carlson, C. Battle-McDonald, T. Ozawa, H. M. Price, and B. Gadway, (2021), arXiv:2107.09649 [cond-mat.mes-hall].

[21] Y. Choi, C. Hahn, J. W. Yoon, and S. H. Song, Nature communications **9**, 1 (2018).

[22] T. Helbig, T. Hofmann, S. Imhof, M. Abdelghany, T. Kiessling, L. Molenkamp, C. Lee, A. Szameit, M. Greiter, and R. Thomale, Nature Physics **16**, 747 (2020).

[23] W. Gou, T. Chen, D. Xie, T. Xiao, T.-S. Deng, B. Gadway, W. Yi, and B. Yan, Phys. Rev. Lett. **124**, 070402 (2020).

[24] J. Li, A. K. Harter, J. Liu, L. de Melo, Y. N. Joglekar, and L. Luo, Nature communications **10**, 1 (2019).

[25] C. Coulais, R. Fleury, and J. van Wezel, Nature Physics **17**, 9 (2021).

[26] Y. Ashida, Z. Gong, and M. Ueda, Advances in Physics **69**, 249 (2020).

[27] E. J. Bergholtz, J. C. Budich, and F. K. Kunst, Rev. Mod. Phys. **93**, 015005 (2021).

[28] S. Longhi, Phys. Rev. Lett. **103**, 123601 (2009).

[29] R. Hayward and F. Biancalana, Phys. Rev. A **98**, 053833 (2018).

[30] N. Silberstein, J. Behrends, M. Goldstein, and R. Ilan, Phys. Rev. B **102**, 245147 (2020).

[31] R. Hayward and F. Biancalana, Phys. Rev. A **101**, 043846 (2020).

[32] C. Dembowski, H.-D. Gräf, H. L. Harney, A. Heine, W. D. Heiss, H. Rehfeld, and A. Richter, Phys. Rev. Lett. **86**, 787 (2001).

[33] C. Dembowski, B. Dietz, H.-D. Gräf, H. L. Harney, A. Heine, W. D. Heiss, and A. Richter, Phys. Rev. E **69**, 056216 (2004).

[34] T. Gao, E. Estrecho, K. Bliokh, T. Liew, M. Fraser, S. Brodbeck, M. Kamp, C. Schneider, S. Höfling, Y. Yamamoto, et al., Nature **526**, 554 (2015).

[35] R. Uzdin, A. Mailybaev, and N. Moiseyev, Journal of Physics A: Mathematical and Theoretical **44**, 435302 (2011).

[36] M. Berry, Journal of Optics **13**, 115701 (2011).

[37] J. Doppler, A. A. Mailybaev, J. Böhm, U. Kuhl, A. Girschik, F. Libisch, T. J. Milburn, P. Rabl, N. Moiseyev, and S. Rotter, Nature **537**, 76 (2016).

[38] H. Shen, B. Zhen, and L. Fu, Phys. Rev. Lett. **120**, 146402 (2018).

[39] S. Massar, Phys. Rev. A **54**, 4770 (1996).

[40] G. Nenciu and G. Rasche, Journal of Physics A: Mathematical and General **25**, 5741 (1992).

[41] J. Hoeller, N. Read, and J. Harris, Physical Review A **102**, 032216 (2020).

[42] N. Hatano and D. R. Nelson, Phys. Rev. Lett. **77**, 570 (1996).

[43] G. Salerno, T. Ozawa, H. M. Price, and I. Carusotto, Phys. Rev. B **93**, 085105 (2016).

[44] G. Salerno and I. Carusotto, EPL (Europhysics Letters) **106**, 24002 (2014).

[45] Y. Aharonov and D. Bohm, Phys. Rev. **115**, 485 (1959).

[46] V. V. Konotop, J. Yang, and D. A. Zezyulin, Rev. Mod. Phys. **88**, 035002 (2016).

[47] Y. Lumer, Y. Plotnik, M. C. Rechtsman, and M. Segev, Phys. Rev. Lett. **111**, 263901 (2013).

[48] S. Yao, F. Song, and Z. Wang, Phys. Rev. Lett. **121**, 136802 (2018).

[49] F. K. Kunst, E. Edvardsson, J. C. Budich, and E. J. Bergholtz, Phys. Rev. Lett. **121**, 026808 (2018).

[50] K. Kawabata, K. Shiozaki, and M. Ueda, Phys. Rev. B **98**, 165148 (2018).

# Supplemental Material for "Measuring the Adiabatic Non-Hermitian Berry Phase in Feedback-Coupled Oscillators"

## THEORETICAL BACKGROUND ON NON-HERMITIAN BERRY PHASE

We summarize here details of the theoretical formalism for the non-Hermitian Berry phase.

We consider a family of $N$-by-$N$ matrices $H(\boldsymbol{\lambda})$ parametrized by a set of real parameters $\boldsymbol{\lambda} = (\lambda_1, \lambda_2, \cdots)$. For a given value of $\boldsymbol{\lambda}$, the matrix $H(\boldsymbol{\lambda})$ is generally not Hermitian, and we consider a system which obeys the Schrödinger equation where $H(\boldsymbol{\lambda})$ acts as a non-Hermitian Hamiltonian: $i\partial_t|\psi(t)\rangle = H(\boldsymbol{\lambda})|\psi(t)\rangle$. Here, $|\psi(t)\rangle$ is a time-dependent $N$-component vector, which is an analog of the wavefunction in this non-Hermitian system.

Various properties of the system are characterized by the eigenvectors and eigenvalues of the non-Hermitian Hamiltonian $H(\boldsymbol{\lambda})$. Assuming that the Hamiltonian is diagonalizable, there exist $N$ right eigenvectors $|R_n(\boldsymbol{\lambda})\rangle$ and the same number of left eigenvectors $\langle L_n(\boldsymbol{\lambda})|$ indexed by an integer $n = 1, 2, \cdots, N$, which satisfy $H(\boldsymbol{\lambda})|R_n(\boldsymbol{\lambda})\rangle = \varepsilon_n(\boldsymbol{\lambda})|R_n(\boldsymbol{\lambda})\rangle$ and $\langle L_n(\boldsymbol{\lambda})|H(\boldsymbol{\lambda}) = \varepsilon_n(\boldsymbol{\lambda})\langle L_n(\boldsymbol{\lambda})|$. Here, generally complex eigenvalues $\varepsilon_n(\boldsymbol{\lambda})$ are common for the right and left eigenvectors. Assuming non-degeneracy of energies, namely $\varepsilon_n(\boldsymbol{\lambda}) \neq \varepsilon_{n'}(\boldsymbol{\lambda})$ for $n \neq n'$ for a given value of $\boldsymbol{\lambda}$, left and right eigenvectors of different eigenvalues are orthogonal $\langle L_n(\boldsymbol{\lambda})|R_{n'}(\boldsymbol{\lambda})\rangle = 0$ if $n \neq n'$. There is no *a priori* reason to take a particular normalization for the left and/or right eigenvectors, and thus, upon defining the eigenvectors, there is a freedom to choose an overall multiplicative factor. Physically observable quantities should not depend on this choice of overall factors of the eigenvectors. In other words, we should look for properties which are independent under the following gauge transformations:

$$|R_n(\boldsymbol{\lambda})\rangle \to r_n(\boldsymbol{\lambda})|R_n(\boldsymbol{\lambda})\rangle, \quad |L_n(\boldsymbol{\lambda})\rangle \to l_n(\boldsymbol{\lambda})|L_n(\boldsymbol{\lambda})\rangle, \tag{10}$$

where $r_n(\boldsymbol{\lambda})$ and $l_n(\boldsymbol{\lambda})$ are nonzero complex numbers.

From the analogy with Hermitian quantum mechanics, we define the Berry connection for non-Hermitian systems; however, since the left and the right eigenvectors are different, we need to consider the following four distinct Berry connections [30, 38]:

$$\mathcal{A}_{n,j}^{LR}(\boldsymbol{\lambda}) \equiv i\langle L_n(\boldsymbol{\lambda})|\partial_{\lambda_j}|R_n(\boldsymbol{\lambda})\rangle / \langle L_n(\boldsymbol{\lambda})|R_n(\boldsymbol{\lambda})\rangle, \quad (11)$$

$$\mathcal{A}_{n,j}^{RL}(\boldsymbol{\lambda}) \equiv i\langle R_n(\boldsymbol{\lambda})|\partial_{\lambda_j}|L_n(\boldsymbol{\lambda})\rangle / \langle R_n(\boldsymbol{\lambda})|L_n(\boldsymbol{\lambda})\rangle, \quad (12)$$

$$\mathcal{A}_{n,j}^{RR}(\boldsymbol{\lambda}) \equiv i\langle R_n(\boldsymbol{\lambda})|\partial_{\lambda_j}|R_n(\boldsymbol{\lambda})\rangle / \langle R_n(\boldsymbol{\lambda})|R_n(\boldsymbol{\lambda})\rangle, \quad (13)$$

$$\mathcal{A}_{n,j}^{LL}(\boldsymbol{\lambda}) \equiv i\langle L_n(\boldsymbol{\lambda})|\partial_{\lambda_j}|L_n(\boldsymbol{\lambda})\rangle / \langle L_n(\boldsymbol{\lambda})|L_n(\boldsymbol{\lambda})\rangle. \quad (14)$$

Upon the gauge transformation Eq. (10), these four Berry

connections transform as

$$\mathcal{A}_{n,j}^{LR}(\boldsymbol{\lambda}) \to \mathcal{A}_{n,j}^{LR}(\boldsymbol{\lambda}) + i\partial_{\lambda_j} \ln r_n(\boldsymbol{\lambda}) \tag{15}$$

$$\mathcal{A}_{n,j}^{RL}(\boldsymbol{\lambda}) \to \mathcal{A}_{n,j}^{RL}(\boldsymbol{\lambda}) + i\partial_{\lambda_j} \ln l_n(\boldsymbol{\lambda}) \tag{16}$$

$$\mathcal{A}_{n,j}^{RR}(\boldsymbol{\lambda}) \to \mathcal{A}_{n,j}^{RR}(\boldsymbol{\lambda}) + i\partial_{\lambda_j} \ln r_n(\boldsymbol{\lambda}) \tag{17}$$

$$\mathcal{A}_{n,j}^{LL}(\boldsymbol{\lambda}) \to \mathcal{A}_{n,j}^{LL}(\boldsymbol{\lambda}) + i\partial_{\lambda_j} \ln l_n(\boldsymbol{\lambda}). \tag{18}$$

Thus, each Berry connection is gauge-dependent, namely the Berry connections depend on how one chooses the normalization of the left and right eigenvectors. However, we can construct the following gauge-invariant combinations of the Berry connections [30]:

$$\delta\mathcal{A}_{n,j}^{LR-RR}(\boldsymbol{\lambda}) \equiv \mathcal{A}_{n,j}^{LR}(\boldsymbol{\lambda}) - \mathcal{A}_{n,j}^{RR}(\boldsymbol{\lambda}) \tag{19}$$

$$\delta\mathcal{A}_{n,j}^{RL-LL}(\boldsymbol{\lambda}) \equiv \mathcal{A}_{n,j}^{RL}(\boldsymbol{\lambda}) - \mathcal{A}_{n,j}^{LL}(\boldsymbol{\lambda}). \tag{20}$$

We note that it is a distinguishing feature of non-Hermitian systems that we can construct gauge-independent quantities just from the Berry connections. Since the four Berry connections coincide for Hermitian quantum mechanics, the gauge-invariant combinations $\delta\mathcal{A}_{n,j}^{LR-RR}$ and $\delta\mathcal{A}_{n,j}^{RL-LL}$ are zero when the Hamiltonian is Hermitian. As we see soon, these gauge-independent combinations of Berry connections appear in a properly-defined Berry phase upon adiabatic change of the parameter $\boldsymbol{\lambda}$.

We now consider an adiabatic evolution of a state upon changing the parameter $\boldsymbol{\lambda}(t)$ as a function of time $t$ and study a scaling factor that the state acquires, which is a non-Hermitian counterpart of the Berry phase [4–7, 28–31, 39]. In Hermitian systems, the adiabatic theorem guarantees that, if the change of the parameters is sufficiently slow, the state remains in the original state up to an overall phase factor if the initial state is an energy eigenstate. As mentioned above, one needs to be cautious when applying the adiabatic theorem to non-Hermitian systems; however, we now assume that this theorem can be applied. Starting from a right eigenstate, we consider adiabatic change of the parameter $\boldsymbol{\lambda}(t)$ as the time $t$ changes, and follow how the eigenstate evolves during this process. We take a family of right eigenstates $|R_n(\boldsymbol{\lambda}(t))\rangle$. Assuming that the adiabatic theorem holds, if the initial state is in the $n$-th right eigenstate, the state at time $t$ can be written as

$$|\psi(t)\rangle = c(t)\frac{|R_n(\boldsymbol{\lambda}(t))\rangle}{\sqrt{\langle R_n(\boldsymbol{\lambda}(t))|R_n(\boldsymbol{\lambda}(t))\rangle}} \tag{21}$$

where $c(t)$ is a complex function accounting for the adiabatic factor the state acquires as $\boldsymbol{\lambda}(t)$ is varied. The denominator is introduced so that the change of the intensity of the state $|\psi(t)\rangle$ can be captured by just looking at

the coefficient $c(t)$ because $\langle\psi(t)|\psi(t)\rangle = |c(t)|^2 \equiv N(t)$, where $N(t)$ is the population. In the next section, we show that the final result is independent of how $|\psi(t)\rangle$ is written as a product of the coefficient and a basis vector.

We can formally solve the Schrödinger equation $i\partial_t|\psi(t)\rangle = H(\boldsymbol{\lambda}(t))|\psi(t)\rangle = \varepsilon_n(\boldsymbol{\lambda}(t))|\psi(t)\rangle$ to obtain the Berry phase. We first apply $\langle L_n(\boldsymbol{\lambda}(t))|$ from the left to the Schrödinger equation. Writing the state as Eq.(21), the Schrödinger equation becomes

$$i\langle L_n(\boldsymbol{\lambda}(t))|\frac{\partial}{\partial t}\left(c(t)\frac{|R_n(\boldsymbol{\lambda}(t))\rangle}{\sqrt{\langle R_n(\boldsymbol{\lambda}(t))|R_n(\boldsymbol{\lambda}(t))\rangle}}\right)$$
$$= c(t)\varepsilon_n(\boldsymbol{\lambda}(t))\frac{\langle L_n(\boldsymbol{\lambda}(t))|R_n(\boldsymbol{\lambda}(t))\rangle}{\sqrt{\langle R_n(\boldsymbol{\lambda}(t))|R_n(\boldsymbol{\lambda}(t))\rangle}}. \quad (22)$$

Expanding the time derivative and arranging terms, we obtain the following differential equation for $c(t)$:

$$\frac{\partial c(t)}{\partial t} = c(t)\left[-i\varepsilon_n(\boldsymbol{\lambda}(t)) - \frac{\langle L_n(\boldsymbol{\lambda}(t))|\partial_t|R_n(\boldsymbol{\lambda}(t))\rangle}{\langle L_n(\boldsymbol{\lambda}(t))|R_n(\boldsymbol{\lambda}(t))\rangle}\right.$$
$$\left.+\frac{1}{2}\frac{\langle R_n(\boldsymbol{\lambda}(t))|\partial_t|R_n(\boldsymbol{\lambda}(t))\rangle + c.c.}{\langle R_n(\boldsymbol{\lambda}(t))|R_n(\boldsymbol{\lambda}(t))\rangle}\right], \quad (23)$$

where $c.c.$ stands for complex conjugate of the preceding term. Converting the time derivative in the right-hand side to the derivative in $\boldsymbol{\lambda}$, and using the definition of the Berry connections, Eq.(15)-(18), we obtain

$$\frac{\partial c(t)}{\partial t} = c(t)\left[-i\varepsilon_n(\boldsymbol{\lambda}(t)) + \right.$$
$$\left.+i\frac{\partial\boldsymbol{\lambda}(t)}{\partial t}\cdot\left(\boldsymbol{\mathcal{A}}_n^{LR}(\boldsymbol{\lambda}) - i\text{Im}\boldsymbol{\mathcal{A}}_n^{RR}(\boldsymbol{\lambda})\right)\right], \quad (24)$$

where $\boldsymbol{\mathcal{A}}_n^{LR}(\boldsymbol{\lambda}) = (\mathcal{A}_{n,1}^{LR}(\boldsymbol{\lambda}), \mathcal{A}_{n,2}^{LR}(\boldsymbol{\lambda}), \cdots)$ and similarly for $\boldsymbol{\mathcal{A}}_n^{RR}(\boldsymbol{\lambda})$. Solving this differential equation, we obtain

$$c(t) = c(0)\exp\left[-i\int_0^t dt'\varepsilon_n(\boldsymbol{\lambda}(t')) + \right.$$
$$\left.i\int_{\mathcal{C}}d\boldsymbol{\lambda}\cdot\left(\boldsymbol{\mathcal{A}}_n^{LR}(\boldsymbol{\lambda}) - i\text{Im}\boldsymbol{\mathcal{A}}_n^{RR}(\boldsymbol{\lambda})\right)\right], \quad (25)$$

The first term in the exponent is the dynamical contribution to the adiabatic factor $c(t)$, whereas the second part is the line integral in the parameter space and only depends on the path $\mathcal{C}$, and is thus analogous to the Berry phase, reflecting the geometrical structure of the eigenstates. In analogy with Hermitian quantum mechanics, we define the non-Hermitian Berry phase as a function of the path $\mathcal{C}$ as

$$\phi[\mathcal{C}] = \int_{\mathcal{C}}d\boldsymbol{\lambda}\cdot\left(\boldsymbol{\mathcal{A}}_n^{LR}(\boldsymbol{\lambda}) - i\text{Im}\boldsymbol{\mathcal{A}}_n^{RR}(\boldsymbol{\lambda})\right). \quad (26)$$

Unlike the Hermitian Berry phase, the non-Hermitian Berry phase has both the real and imaginary parts

$$\text{Re}\left(\phi[\mathcal{C}]\right) = \int_{\mathcal{C}}d\boldsymbol{\lambda}\cdot\text{Re}\boldsymbol{\mathcal{A}}_n^{LR}(\boldsymbol{\lambda}), \quad (27)$$

$$\text{Im}\left(\phi[\mathcal{C}]\right) = \int_{\mathcal{C}}d\boldsymbol{\lambda}\cdot\text{Im}\delta\boldsymbol{\mathcal{A}}_n^{LR-RR}(\boldsymbol{\lambda}), \quad (28)$$

where $\delta\boldsymbol{\mathcal{A}}_n^{LR-RR}(\boldsymbol{\lambda}) = (\delta\mathcal{A}_{n,1}^{LR-RR}(\boldsymbol{\lambda}), \delta\mathcal{A}_{n,2}^{LR-RR}(\boldsymbol{\lambda}), \cdots)$ is the gauge-invariant combination of the Berry connections introduced in Eq. (19). Therefore, the imaginary part of the non-Hermitian Berry phase is gauge independent even when the path $\mathcal{C}$ is not closed [39]. On the other hand, the real part of the Berry phase is gauge invariant only when the path $\mathcal{C}$ forms a closed path, just like in the Hermitian case.

An advantage of the above formulation in terms of the Berry connection is also that the geometrical contribution to the time evolution of the population $N(t) = |c(t)|^2$ is manifestly gauge-invariant even for an open path:

$$N(t) = N(0)\exp\left[2\int_0^t dt'\text{Im}\varepsilon_n(\boldsymbol{\lambda}(t')) - 2\text{Im}\left(\phi[\mathcal{C}]\right)\right]. \quad (29)$$

Therefore, when the energy eigenvalue is real during the time evolution and hence $\text{Im}\varepsilon_n(\boldsymbol{\lambda}(t)) = 0$, which is the case we experimentally study in this paper, the population dynamics is solely determined by the imaginary part of the Berry phase. And thus by observing the population dynamics, we can experimentally determine the imaginary part of the Berry phase.

## DIFFERENT DEFINITION OF THE ADIABATIC COEFFICIENT

The observable result of the non-Hermitian Berry phase through the population dynamics, Eq. (29), is insensitive to the way the adiabatic coefficient $c(t)$ is defined. For demonstration, we write, instead of as in Eq. (21), the state vector as

$$|\psi(t)\rangle = \tilde{c}(t)|R_n(\boldsymbol{\lambda}(t))\rangle, \quad (30)$$

which is also a natural definition to take. Applying $\langle L_n(\boldsymbol{\lambda}(t))|$ from left to the Schrödinger equation

$$i\frac{\partial}{\partial t}\{\tilde{c}(t)|R_n(\boldsymbol{\lambda}(t))\rangle\} = \varepsilon_n(\boldsymbol{\lambda}(t))\tilde{c}(t)|R_n(\boldsymbol{\lambda}(t))\rangle, \quad (31)$$

we obtain the differential equation for $\tilde{c}(t)$:

$$\frac{\partial\tilde{c}(t)}{\partial t} = \tilde{c}(t)\left[-i\varepsilon_n(\boldsymbol{\lambda}(t)) - \frac{\langle L_n(\boldsymbol{\lambda}(t))|\partial_t|R_n(\boldsymbol{\lambda}(t))\rangle}{\langle L_n(\boldsymbol{\lambda}(t))|R_n(\boldsymbol{\lambda}(t))\rangle}\right]. \quad (32)$$

Integrating this differential equation, we obtain

$$\tilde{c}(t) = \tilde{c}(0)\exp\left[-i\int_0^t \varepsilon_n(\boldsymbol{\lambda}(t'))dt' + i\int_{\mathcal{C}}\boldsymbol{\mathcal{A}}_n^{LR}(\boldsymbol{\lambda})\cdot d\boldsymbol{\lambda}\right]. \quad (33)$$

On the other hand, the population evolves in time as

$$N(t) = |\tilde{c}(t)|^2\langle R_n(\boldsymbol{\lambda}(t))|R_n(\boldsymbol{\lambda}(t))\rangle. \quad (34)$$

To understand the dynamics, in addition to the time evolution of $\tilde{c}(t)$, we need to understand how $\langle R_n(\boldsymbol{\lambda}(t))|R_n(\boldsymbol{\lambda}(t))\rangle$ evolves in time. By a simple calculation, we can show

$$\frac{\partial}{\partial t}\left\{\langle R_n(\boldsymbol{\lambda}(t))|R_n(\boldsymbol{\lambda}(t))\rangle\right\}$$
$$= \langle R_n(\boldsymbol{\lambda}(t))|R_n(\boldsymbol{\lambda}(t))\rangle 2\frac{\partial\boldsymbol{\lambda}(t)}{\partial t}\mathrm{Im}\left[\boldsymbol{\mathcal{A}}_n^{RR}(\boldsymbol{\lambda})\right]. \quad (35)$$

Integrating this differential equation, we obtain

$$\langle R_n(\boldsymbol{\lambda}(t))|R_n(\boldsymbol{\lambda}(t))\rangle$$
$$= \langle R_n(\boldsymbol{\lambda}(0))|R_n(\boldsymbol{\lambda}(0))\rangle \exp\left[2\int_{\mathcal{C}}\mathrm{Im}\left[\boldsymbol{\mathcal{A}}_n^{RR}(\boldsymbol{\lambda})\right]\cdot d\boldsymbol{\lambda}\right]. \quad (36)$$

Combining Eq.(33) and Eq.(36), time evolution of the population is

$$N(t) = N(0)\exp\left[2\int_0^t\mathrm{Im}\varepsilon_n(\boldsymbol{\lambda}(t'))dt'\right.$$
$$\left. -2\int_{\mathcal{C}}\mathrm{Im}\left[\boldsymbol{\mathcal{A}}_n^{LR}(\boldsymbol{\lambda})-\boldsymbol{\mathcal{A}}_n^{RR}(\boldsymbol{\lambda})\right]\cdot d\boldsymbol{\lambda}\right], \quad (37)$$

which is exactly the same as Eq. (29). Thus, the time evolution of the population is independent of the way the adiabatic coefficient is defined, as expected.

## TWO-SITE HATANO-NELSON MODEL

Here we describe the two-site non-Hermitian model we experimentally realize. The Hamiltonian is

$$H/h = \begin{pmatrix} -\Delta & J+\delta J \\ J-\delta J & \Delta \end{pmatrix}. \quad (38)$$

Here, we take $\Delta$, $J$ and $\delta J$ to be real parameters, relating to relevant frequency shifts of and hopping rates between the oscillators. The eigenvalues of Eq. 38 are given by $\varepsilon_\pm = \pm\sqrt{\Delta^2+J^2-\delta J^2}$, which means that the two eigenvalues are both real when $\Delta^2+J^2 > \delta J^2$, corresponding to the $\mathcal{PT}$-symmetric region. If $\Delta^2+J^2 = \delta J^2$, the eigenvalues coalesce at an exceptional point; within the parameter space of $\boldsymbol{\lambda} = (\Delta, J, \delta J)$, this exceptional point corresponds to a double cone, with its apex at the origin [11], as shown in Fig. 1 (c).

Within the $\mathcal{PT}$-symmetric region, the gauge-invariant combinations of the Berry connections are

$$\delta\mathcal{A}_{\pm,\Delta}^{LR-RR} = i\frac{\delta J}{2}\cdot\frac{\Delta\delta J\pm J\sqrt{\Delta^2+J^2-\delta J^2}}{(\Delta^2+J^2)(\Delta^2+J^2-\delta J^2)} \quad (39)$$

$$\delta\mathcal{A}_{\pm,J}^{LR-RR} = i\frac{\delta J}{2}\cdot\frac{J\delta J\mp\Delta\sqrt{\Delta^2+J^2-\delta J^2}}{(\Delta^2+J^2)(\Delta^2+J^2-\delta J^2)} \quad (40)$$

$$\delta\mathcal{A}_{\pm,\delta J}^{LR-RR} = -i\frac{\delta J}{2}\cdot\frac{1}{\Delta^2+J^2-\delta J^2}, \quad (41)$$

We note that they are all purely imaginary, and that they diverge as we approach the $\mathcal{PT}$-symmetry breaking transition, where adiabaticity breaks down. The associated geometrical Berry curvature $\delta\boldsymbol{\Omega}_\pm^{LR-RR} \equiv \nabla\times\delta\boldsymbol{\mathcal{A}}_\pm^{LR-RR}$, where $\delta\boldsymbol{\mathcal{A}}_\pm^{LR-RR} = (\delta\mathcal{A}_{\pm,\Delta}^{LR-RR},\delta\mathcal{A}_{\pm,J}^{LR-RR},\delta\mathcal{A}_{\pm,\delta J}^{LR-RR})$ is also imaginary and takes the form [11]:

$$\delta\boldsymbol{\Omega}_\pm^{LR-RR} = \frac{\pm i}{2(\Delta^2+J^2-\delta J^2)^{3/2}}(\Delta, J, \delta J), \quad (42)$$

which is analogous to the magnetic field of a one-sheeted complex hyperbolic magnetic monopole. From the above quantities, we are able to analytically calculate the non-Hermitian Berry phase and to predict the consequent amplification and damping of the population.

## NON-HERMITIAN BERRY PHASE FOR PATHS ENCLOSING $PT$-BROKEN REGIME

We provide theoretical analysis of the non-Hermitian Berry phase for the configuration described in Fig. 4 of the main text. The path we take is an ellipse in $\Delta-J$ plane with a fixed value of $\delta J$. For a given value of $\delta J$, the path can be parametrized by a single parameter $\theta$ as

$$\Delta = \Delta_0\cos\theta, \qquad J = J_0\sin\theta, \quad (43)$$

where, in the experiment, $\theta$ depends on time $t$, which varies from 0 to $T$. Time dependence of $\theta(t)$ is such that initially, $\theta(0) = 0$ and at the final time, $\theta(T) = \Theta \leq 2\pi$. Note that the path is not closed unless $\Theta = 2\pi$. In our experiment, $\Delta_0 = 7.5\mathrm{mHz}$ and $J_0 = 6.45\mathrm{mHz}$. We note that the gauge-invariant combinations of Berry connections $\delta\mathcal{A}_{\pm,\Delta}^{LR-RR}$ and $\delta\mathcal{A}_{\pm,J}^{LR-RR}$ are both purely imaginary in $PT$-symmetric region. Thus the imaginary part of the Berry phase along the path $\mathcal{C}$ described by Eq.(43) is

$$\mathrm{Im}[\phi[\mathcal{C}]] = -i\int_{\mathcal{C}}d\boldsymbol{\lambda}\cdot\delta\boldsymbol{\mathcal{A}}_\pm^{LR-RR}(\boldsymbol{\lambda})$$
$$= -i\int_0^\Theta d\theta\left\{\partial_\theta\Delta(\theta)\delta\mathcal{A}_{\pm,\Delta}^{LR-RR}(\theta) + \partial_\theta J(\theta)\delta\mathcal{A}_{\pm,J}^{LR-RR}(\theta)\right\}$$
$$= -i\int_0^\Theta d\theta\left\{-\Delta_0\sin\theta\delta\mathcal{A}_{\pm,\Delta}^{LR-RR}(\theta)\right.$$
$$\left. +J_0\cos\theta\delta\mathcal{A}_{\pm,J}^{LR-RR}(\theta)\right\}. \quad (44)$$

Using expressions (39) and (40), we can perform the integral and obtain

$$\mathrm{Im}[\phi[\mathcal{C}]] = -\frac{1}{4}\log\left\{\frac{(\Delta_0^2-\delta J^2)(\delta_0^2\cos^2\Theta+J_0^2\sin^2\Theta)}{\Delta_0^2(\Delta_0^2\cos^2\Theta+J_0^2\sin^2\Theta-\delta J^2)}\right\}$$
$$\mp\frac{\delta J}{2}\frac{J_0}{\Delta_0\sqrt{\Delta_0^2-\delta J^2}}\Pi\left(1-\frac{J_0^2}{\Delta_0^2};\Theta\left|1-\frac{J_0^2-\delta J^2}{\Delta_0^2-\delta J^2}\right.\right), \quad (45)$$
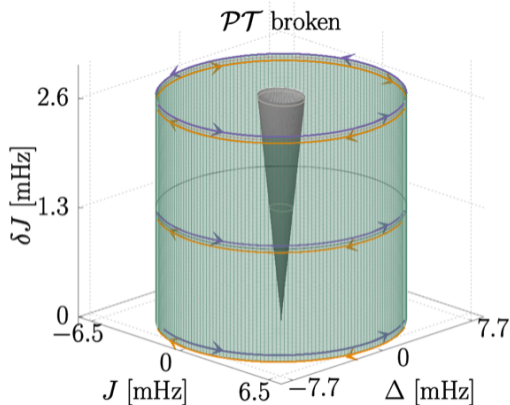
FIG. 5. The cylindrical surface of integral over which the Berry curvature can be defined everywhere continuous. The integral of the Berry curvature over this surface yields the non-Hermitian Berry phase corresponding to the closed elliptical path at a fixed value of $\delta J$.

where $\Pi(n; \phi|k)$ is the incomplete elliptic integral of the third kind defined by

$$\Pi(n; \phi|m) = \int_0^\phi \frac{d\theta}{(1 - n\sin^2\theta)\sqrt{1 - m\sin^2\theta}}. \quad (46)$$

For a closed path with $\Theta = 2\pi$, the real part of the non-Hermitian Berry phase also becomes gauge invariant (up to $2\pi$ multiples of an integer). However, we can show that for the path we consider here, the real part is zero, and thus the non-Hermitian Berry phase for a closed path in our setup is purely imaginary. Furthermore, the first logarithm term in Eq.(45) vanishes for a closed path and the elliptic integral becomes the complete one, yielding

$$\phi[\mathcal{C}]_{\Theta=2\pi} =$$
$$\mp \frac{i2\delta J J_0}{\Delta_0\sqrt{\Delta_0^2 - \delta J^2}} \Pi\left(1 - \frac{J_0^2}{\Delta_0^2}\middle| 1 - \frac{J_0^2 - \delta J^2}{\Delta_0^2 - \delta J^2}\right), \quad (47)$$

where we now have the complete elliptic integral of the third kind defined by

$$\Pi(n|m) = \int_0^{\pi/2} \frac{d\theta}{(1 - n\sin^2\theta)\sqrt{1 - m\sin^2\theta}}. \quad (48)$$

The expressions (45) and (47) are what we used in Fig. 4 of the main text to draw theoretical curves.

So far, we have derived the non-Hermitian Berry phase through the line integral of the Berry connections along the path. For a closed path ($\Theta = 2\pi$) we can obtain the same result using the surface integral of the Berry curvatures as we show below. We can convert the line integral to the surface integral using Stokes' theorem, which is a standard procedure also in Hermitian cases. However, we should be careful that, in the plane determined by a fixed value of $\delta J$ in the parameter space of $\boldsymbol{\lambda} = (\Delta, J, \delta J)$, the interior of the curve $\mathcal{C}$ contains the $PT$-broken region. At the $PT$-breaking transition the eigenstates coalesce and we are no longer able to use the Stokes' theorem, which assumes the involved functions be continuous. We can, however, deform the surface of integral to the cylindrical form, as illustrated in Fig. 5. The surface of the cylinder is entirely contained in the $PT$-symmetric region, and thus Stokes' theorem can be safely applied. The surface to be integrated contains two parts: side and the base. The Berry curvature (42) does not have any component perpendicular to the base of the cylinder at $\delta J = 0$. We then need to consider the surface integral only over the side of the cylinder. The side of the cylinder can be parametrized by $\boldsymbol{\lambda} = (\Delta, J, \delta J) = (\Delta_0 \cos\theta, J_0 \sin\theta, \delta J')$ with parameters $\theta$ and $\delta J'$. Here, $\theta$ varies from 0 to $2\pi$, and $\delta J'$ varies from $\delta J$, which is the initial value, to 0. Then, denoting the unit vector normal to the surface by $\mathbf{n}$ and the surface element by $dS$, the surface integral is

$$\phi[\mathcal{C}]_{\Theta=2\pi} = \int\int \delta\mathbf{\Omega}_{\pm}^{LR-RR} \cdot \mathbf{n}dS$$

$$= \int_0^{2\pi} d\theta \int_{\delta J}^0 d\delta J' \delta\mathbf{\Omega}_{\pm}^{LR-RR} \cdot \left(\frac{\partial\boldsymbol{\lambda}}{\partial\theta} \times \frac{\partial\boldsymbol{\lambda}}{\partial\delta J'}\right) d\theta d\delta J'$$

$$= \int_0^{2\pi} d\theta \int_{\delta J}^0 d\delta J' \frac{\pm i\Delta_0 J_0}{2(\Delta_0^2\cos^2\theta + J_0^2\sin^2\theta - \delta J'^2)^{3/2}}$$

$$= \int_0^{2\pi} d\theta \frac{\mp i\Delta_0 J_0 \delta J}{2(\Delta_0^2\cos^2\theta + J_0^2\sin^2\theta)\sqrt{\Delta_0^2\cos^2\theta + J_0^2\sin^2\theta - \delta J^2}}$$

$$= \mp i\frac{J_0}{\Delta_0} \frac{2\delta J}{\sqrt{\Delta_0^2 - \delta J^2}} \int_0^{\pi/2} d\theta \frac{1}{\left(1 - \left(1 - \frac{J_0^2}{\Delta_0^2}\right)\sin^2\theta\right)\sqrt{1 - \frac{\Delta_0^2 - J_0^2}{\Delta_0^2 - \delta J^2}\sin^2\theta}}$$

$$= \mp i\frac{J_0}{\Delta_0} \frac{2\delta J}{\sqrt{\Delta_0^2 - \delta J^2}} \Pi\left(1 - \frac{J_0^2}{\Delta_0^2}\bigg|\ \frac{\Delta_0^2 - J_0^2}{\Delta_0^2 - \delta J^2}\right), \tag{49}$$

which is exactly the expression Eq.(47). The population increase/decrease due to the imaginary part of the non-Hermitian Berry phase is thus directly related to the imaginary magnetic flux enclosed in the surface defined by the interior of the closed path. The change of population upon adiabatically following a closed path is a manifestation of the Aharonov-Bohm effect with an imaginary magnetic flux.

## DATA ACQUISITION AND ANALYSIS

As described previously in Ref. [20], we acquire real-time proxies of the oscillators' positions based on continuous voltage signals from analog accelerometers attached to each oscillator. We additionally acquire a proxy for the oscillators' momenta based on determining the instantaneous jerk by taking the numerical derivative of acquired acceleration signals. These voltage signals proportional to the acceleration and jerk are normalized to a common scale, and respectively serve as dimensionless proxies for the oscillator positions ($\tilde{x}_i$) and momenta ($\tilde{p}_i$). From the rapidly oscillating (at frequency $f_0$) $\tilde{x}_i$ and $\tilde{p}_i$ signals, we can reconstruct a proxy for the mechanical energy stored in each oscillator $E_i \propto \tilde{x}_i^2 + \tilde{p}_i^2$. Furthermore, the total energy of the two-oscillator dimer can be reconstructed simply as $E_T = E_1 + E_2$.

In Fig. 6, we display the progression of acquired and processed data, relating to the scenario of cyclic attenuation (a) and amplification (b) of energy upon encircling a $PT$-broken region. In both cases, we start with a state initialized by resonantly depositing energy into oscillator 1 while maintaining an inter-oscillator bias (frequency mismatch) $2\Delta$. The first column depicts the paths for CW (gold, row (a)) and CCW (purple, row (b)) trajectories in the model's parameter space. The second column

depicts the $\tilde{x}_i$ position signals for oscillators 1 (red) and 2 (blue). The $\tilde{p}_i$ momentum signals, which are indistinguishable from the $\tilde{x}_i$ signals on this long timescale, are not shown. The third column displays the calculated energies for each oscillator, normalized to the initial total energy. The fourth and final column displays the total mechanical energy in the two-oscillator dimer, normalized to the initial total energy. To note, the data from the final column is the same as that appearing (combined) in the central panel of Fig. 4 (b).

## INFLUENCE OF WEAK NONLINEARITIES

Our experimental implementation involves rather large, few cm-scale displacements from equilibrium of our masses on springs (further details in Ref. [20]). For large displacements, there is a natural increase of the oscillation frequency due to the anharmonicity of the physical springs that appear above and below our oscillating masses. We apply feedback forces to cancel out, to first order, this natural stiffening effect. Specifically, for each oscillator, we apply a nonlinear contribution to the feedback forces of the form $F_i^{NL} = \alpha_i(\tilde{x}_i^2 + \tilde{p}_i^2)\tilde{x}_i$. In general, the control over $\alpha_i$ for such a nonlinear feedback can be used to implement nonlinear interaction terms, as was demonstrated in Ref. [20]. Here, we set $\alpha_i$ for each oscillator so as to cancel their natural quartic nonlinearities.

However, this cancellation is imperfect, and residual and higher-order nonlinearities lead to shifts in the frequencies of the oscillators that become more severe as the mechanical energy in an oscillator grows. In particular, for experiments in which we expect to observe a large increase in the overall mechanical energy due to the accrual of a complex Berry phase, we tend to find less growth than expected. Specifically, for the experiments
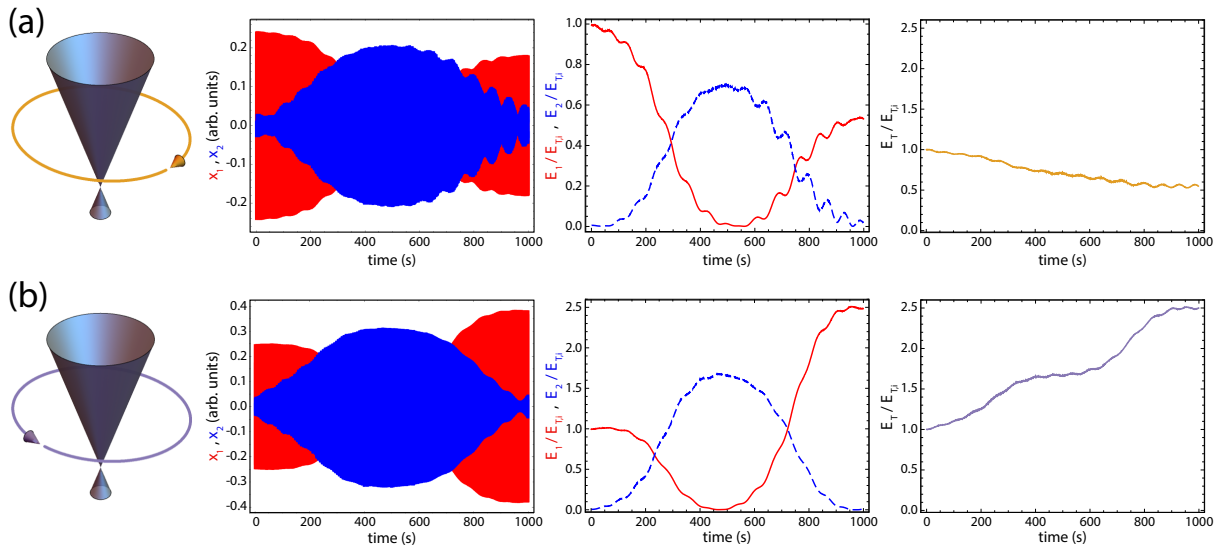
FIG. 6. **Representative primary and processed data, demonstrating how quantities like total energy are derived from the primary acquired signals for the individual oscillators.** Shown for the data as presented in Fig. 4, for $\delta J = 1.3$ mHz and for both directions of encircling. **Row (a):** For CW (gold) trajectories in the $J - \Delta$ plane, the data panels display (from left to right) the progression from position $(\tilde{x}_i)$ signals, to the individual energy signals in each oscillator, to the total energy of the two-oscillator dimer. To note, both the individual and total oscillator energies are normalized to the total energy at time $t = 0$ (start of the encircling process). For the CW trajectory, the total energy is attenuated upon completing one cycle. **Row (b):** Same data progression for the case of CCW (purple) trajectories in the $J - \Delta$ plane. For the CCW trajectory, the total energy is amplified upon completing one cycle.

described in Fig. 4 of the main text involving cyclic amplification along CCW paths encircling the $PT$-broken region, we find reasonable agreement between our experimental data and the analytical theory results in cases in which the total energy remains small ($E_T/E_{T,i} \lesssim 2$, with $E_{T,i}$ being the initial total energy). However, for conditions in which there is larger energy growth, we ob-

serve significant deviations from the expected analytical results. To capture this effect, we also compare our data (for Fig. 4) to numerical simulation curves that incorporate additional nonlinear contributions to the dynamics. Specifically, we compare to dynamical evolution according to the set of coupled equations:

$$\dot{a} = -i[(\omega_0 - \Delta)a + i\Gamma_a a - (J + \delta J)b + \tilde{g}(|a|^2 - 1)a] \tag{50}$$

$$\dot{b} = -i[(\omega_0 + \Delta)b + i\Gamma_b b - (J - \delta J)a + \tilde{g}(|b|^2 - 1)b] \tag{51}$$

The majority of terms are as defined previously in the text, with $\omega_0 = 2\pi f_0$ describing the common bare angular frequency of the two oscillators, $2\Delta$ the angular frequency mismatch imposed between the oscillators, and $J \pm \delta J$ the left-to-right and right-to-left hopping rates. These parameters are evolved according to the state preparation procedure and parameter ramps as described in the context of Fig. 4. Specifically, population is first initialized at site $a$ (corresponding to $a(t = 0) = 1$) in the presence of a large initial detuning of $2\Delta_0$, with $\Delta_0/2\pi = 7.7$ mHz. Then, a purely non-reciprocal hopping of $\delta J$ is smoothly turned on as $\delta J = (\delta J_{\max}/2) \times (1 - \cos(\pi t/T_{\text{prep}}))$ over a preparation

time of $T_{\text{prep}} = 250$ s, with variable final values of $\delta J_{\max}$ as described in the main text. Then, after this preparation stage, encircling orbits in the $J - \Delta$ plane are made as depicted in Fig. 4. Specifically, the coordinates $\Delta$ and $J$ follow their respective forms of $\Delta = \Delta_0 \cos(2\pi t/T_{\text{ramp}})$ and $J = C \times J_0 \sin(2\pi t/T_{\text{ramp}})$, where $T_{\text{ramp}} = 1000$ s, $J_0/2\pi = 6.45$ mHz, and $C = \pm 1$ defines the chirality for CW and CCW parameter trajectories.

The fixed terms $\Gamma_{a,b}$ account for small residual loss/gain at oscillators $a$ and $b$, taking values of $\Gamma_a/2\pi = 10.25$ $\mu$Hz and $\Gamma_a/2\pi = $ -5.75 $\mu$Hz, relating to weak loss and gain terms, respectively. The coefficient of the empirical nonlinear term contains both a real and imaginary

contribution (*i.e.*, $\tilde{g} = \tilde{g}_{\text{re}} + i\tilde{g}_{\text{im}}$), which take respective values of $\tilde{g}_{\text{re}}/2\pi = 1.12$ mHz and $\tilde{g}_{\text{im}}/2\pi = 32.5$ $\mu$Hz. To note, these values ($\Gamma_{a,b}$ and $\tilde{g}$) were determined based on a global optimization of the agreement between theory and experiment (minimization of summed squared residuals) for the full CCW ramp case for all $\delta J$ values.

The complex numbers $a$ and $b$ represent the field coefficients for the two mechanical oscillator modes. By convention these coefficients are normalized as $|a(t)|^2 + |b(t)|^2 = 1$ at time $t = 0$, and as such their squared norms can be compared to the individual normalized (to the total initial energy) oscillator energies as presented in the main text ($E_1/E_{\text{T,i}}$ and $E_2/E_{\text{T,i}}$). As the frequencies and damping/gain of the individual oscillators were separately fine-tuned in experiment under the respective conditions of $|a(t = 0)|^2 = 1$ and $|b(t = 0)|^2 = 1$, the contributions from the empirical nonlinear terms vanish under those conditions. Importantly, the nonlinear contributions to the dynamical evolution become significant when the total energy of either oscillator grows large, reproducing the saturation of cyclic growth as observed in the main text.

# Chapter 4

# Interacting non-Hermitian dimer

As first author of this paper, I was responsible for all the numerical and analytical results, together with the majority of the writing; Hannah Price and Tomoki Ozawa assisted me both in the writing and the directing of the project, Bryce Gadway and Yaashnaa Singhal took care of the experimental sections and collected the data shown.

# Coexistence of stable and unstable population dynamics in a nonlinear non-Hermitian mechanical dimer

Enrico Martello,[1] Yaashnaa Singhal,[2] Bryce Gadway,[2] Tomoki Ozawa,[3] and Hannah M. Price[1]

[1]*School of Physics and Astronomy, University of Birmingham,*
*Edgbaston, Birmingham B15 2TT, United Kingdom*
[2]*Department of Physics, University of Illinois at Urbana-Champaign, Urbana, IL 61801-3080, USA*
[3]*Advanced Institute for Materials Research (WPI-AIMR), Tohoku University, Sendai 980-8577, Japan*
(Dated: February 13, 2023)

Non-Hermitian two-site "dimers" serve as minimal models in which to explore the interplay of gain and loss in dynamical systems. In this paper, we experimentally and theoretically investigate the dynamics of non-Hermitian dimer models with non-reciprocal hoppings between the two sites. We investigate two types of non-Hermitian couplings; one is when asymmetric hoppings are externally introduced, and the other is when the non-reciprocal hoppings depend on the population imbalance between the two sites, thus introducing the non-Hermiticity in a dynamical manner. We engineer the models in our synthetic mechanical set-up comprised of two classical harmonic oscillators coupled by measurement-based feedback. For fixed non-reciprocal hoppings, we observe that, when the strength of these hoppings is increased, there is an expected transition from a $\mathcal{PT}$-symmetric regime, where oscillations in the population are stable and bounded, to a $\mathcal{PT}$-broken regime, where the oscillations are unstable and the population grows/decays exponentially. However, when the non-Hermiticity is dynamically introduced, we also find a third intermediate regime in which these two behaviors coexist, meaning that we can tune from stable to unstable population dynamics by simply changing the initial phase difference between the two sites. As we explain, this behavior can be understood by theoretically exploring the emergent fixed points of a related dimer model in which the non-reciprocal hoppings depends on the *normalized* population imbalance. Our study opens the way for the future exploration of non-Hermitian dynamics and exotic lattice models in synthetic mechanical networks.

## I. INTRODUCTION

In recent decades, systems described by non-Hermitian Hamiltonians have become a topic of great interest since gain and loss can lead to many intriguing effects, including parity-time ($\mathcal{PT}$) symmetry and real energy spectra [1–7], exceptional points [8–11], non-Hermitian geometrical phases [12–20] and new types of topological phenomena [21–28]. This interest has also been driven by recent experimental developments leading to non-Hermitian physics being simulated across a wide-range of platforms such as photonics [11, 29–33], ultracold gases [34–36] and mechanical metamaterials [20, 37–43].

Within this field, significant effort has been devoted to the study of so-called "dimer" models, in which two sites are coupled together in a (non-Hermitian) Hamiltonian that can be represented generally as a $2 \times 2$ matrix. Such models are useful as they serve as minimal systems in which to (often analytically) understand the effects of non-Hermitian terms on dynamical behavior [44–47]. Many of the previous works focused on the dimer models where the non-Hermiticity is introduced and controlled through on-site loss and gain terms (see, *e.g.*, [5–7, 44–50] and references therein), that is, through the diagonal components in the Hamiltonian.

In this paper, we instead explore dynamics of dimer models in which the non-Hermitian effects are introduced by making the hopping between the two sites asymmetric [51]. Such systems are inspired by the Hatano-Nelson (HN) model [52–54], which is a one-dimensional lat-

tice model with asymmetric hoppings between the sites exhibiting the so-called non-Hermitian skin effect [55–57]. Such asymmetric, or non-reciprocal, hoppings are more difficult to experimentally implement than on-site gain and loss. However, there has been significant recent progress in realizing such asymmetric hoppings using setups based on optical systems [58–61], electrical circuits [62–64] and synthetic mechanical metamaterials [20, 65], opening up a possibility to experimentally study such non-Hermitian models.

In this paper, we engineer non-Hermitian dimer models by taking advantage of the flexibility of a mechanical set-up consisting of two coupled harmonic oscillators with measurement-based feedback [65]. As we have previously demonstrated, this approach can be used to simulate near-arbitrary mean-field lattice Hamiltonians, with controllable on-site gain and loss, non-reciprocal couplings and (exotic) synthetic nonlinearities amongst other effects [20, 65]. In addition to its tunability, a key advantage of this set-up is that it provides full access to the dynamics, allowing us to observe the evolution of the system in real time.

Here, we exploit this mechanical set-up to investigate dynamics of Hatano-Nelson dimer models. We first investigate the linear Hatano-Nelson dimer in which the asymmetric hopping is externally fixed [51]. In this linear model we observe that, while in the $\mathcal{PT}$-symmetric regime the trajectories of dynamics show closed stable orbits, in the $\mathcal{PT}$-broken regime the behavior is unstable, with the population exponentially exploding or de-

caying. We fully characterize this behavior in terms of fixed points of motion. Building on the understanding of the linear model, we then explore a nonlinear version of the Hatano-Nelson dimer in which the asymmetric coupling is induced by population imbalance between the two sites. For this model, we again find both a stable regime at low coupling strengths, in which population oscillations are bounded, analogous to the $\mathcal{PT}$-symmetric regime described above, and an unstable regime at high coupling strengths, in which the population grows/decays, similar to the $\mathcal{PT}$-broken regime. However, we also find a new regime at intermediate coupling strengths, where the two types of behavior coexist, allowing us to tune the population dynamics from a stable oscillation to an unstable divergence by simply tuning the initial phase difference between the oscillators. As we discuss, this behavior can be understood by studying the fixed points of a variant of the nonlinear Hatano-Nelson dimer model, which we call the instantaneous Hatano-Nelson dimer model, in which the non-reciprocal coupling depends on the *normalized* population difference between the two sites as introduced below. Our work lays the foundation to exploring dynamics of more exotic lattice Hamiltonians with non-Hermiticity and mean-field interactions.

The paper is structured as follows: in Sec. II we introduce and define the models we explore. We introduce the linear Hatano-Nelson dimer model, nonlinear Hatano-Nelson dimer model, and the instantaneous Hatano-Nelson dimer model that helps elucidate the dynamics of the original nonlinear Hatano-Nelson dimer model. In Sec. III we describe the experimental approach and setup, and the details and parameters chosen. In Sec. IV, we analyze the linear Hatano-Nelson dimer model. We first analytically study the dynamical behavior of the model, and then compare the results with numerically and experimentally obtained dynamics. In Sec. V, we analyze the dynamical behavior of the instantaneous Hatano-Nelson dimer model and discuss the emergence of multiple fixed points and the structure of the transition between the weakly and strongly interacting regimes. In Sec. VI, we finally study the nonlinear Hatano-Nelson dimer model. We give qualitative explanations of the phase diagram using results obtained in previous sections, and discuss the coexistence of different phases in the dynamics from both numerical and experimental approaches. Finally, in Sec. VII, we draw conclusions and discuss the outlook for this work.

## II. MODELS

We experimentally realize two types of non-Hermitian dimer models. The first is the *linear* Hatano-Nelson (HN) dimer model, in which Hermiticity is broken by externally-tuneable non-reciprocal couplings between the two sites. The second is the *nonlinear* HN dimer model, in which the non-reciprocal couplings are instead induced
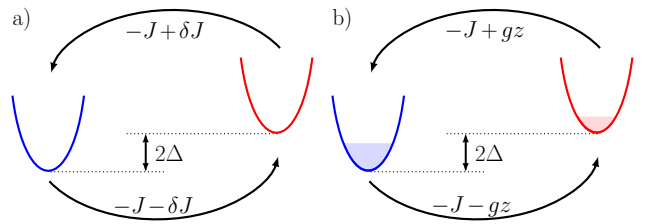


FIG. 1. *a)* Sketch of the Hatano-Nelson dimer as described in Eq. 1 where $\delta J$ is the hopping asymmetry parameter. *b)* Sketch of the dimer with population-dependent hopping asymmetry as described in Eq. 3, where $z$ describes the population imbalance between the two sites and $g$ is a control parameter.

by the population imbalance between the two sites, and hence evolve dynamically, depending on the interparticle interaction strength. In order to obtain analytical understanding of the nonlinear HN dimer model, we also theoretically introduce a variant of the nonlinear HN dimer model in which the non-Hermiticity only depends on the *normalized* population imbalance between the two sites; such a model describes the dynamics of the nonlinear HN dimer model for a short period of time, and thus we call it an *instantaneous* HN dimer model. We shall now introduce the linear, nonlinear, and instantaneous HN dimer model in turn.

### A. Linear Hatano-Nelson Dimer Model

The linear HN dimer model is a model in which two sites are coupled by non-reciprocal hopping amplitudes [28, 51, 66, 67]. By writing the complex-valued wave-function of the two sites as $\boldsymbol{\alpha} = (\alpha_1, \alpha_2)^{\mathrm{T}}$, the dynamics of the linear HN dimer is described by

$$i\dot{\boldsymbol{\alpha}} = \begin{pmatrix} \omega - \Delta & -J - \delta J \\ -J + \delta J & \omega + \Delta \end{pmatrix}\boldsymbol{\alpha}, \qquad (1)$$

where $\omega$ is an overall energy offset and $\Delta$ determines the on-site energy difference between the two sites (with $\hbar = 1$), as shown in Fig. 1 (a). Without loss of generality, from now on we will consider $J$, $\Delta$ and $\delta J$ to be non-negative real values. The coupling between the sites is split into the reciprocal part of the hopping amplitude $-J$ and the non-reciprocal part $\pm\delta J$, the latter being responsible for breaking Hermiticity. This model is the two-site version of the famous Hatano-Nelson model for a one-dimensional chain [52–54] in which all the nearest-neighbor inter-site couplings take the form as in Eq. 1. As a result of the non-reciprocal hopping, the Hatano-Nelson model is topologically nontrivial and exhibit phenomena such as directional transport and the non-Hermitian skin effect in a 1D chain [55–57, 68].

Similar to other two-site non-Hermitian models [44, 69], the linear HN dimer (Eq. 1) exhibits a $\mathcal{PT}$-symmetry breaking transition, in which the eigenstates of the

Hamiltonian coalesce at an exceptional point [1, 2, 70] as the strength of the non-Hermitian terms is increased. The energy eigenvalues, $E_\pm$, of the Hamiltonian, which is the two-by-two matrix in Eq. 1, are [2, 70]:

$$E_\pm = \omega \pm \sqrt{J^2 + \Delta^2 - \delta J^2}. \qquad (2)$$

The spectrum shows qualitatively different behavior depending on the relative strength between $J^2 + \Delta^2$ and $\delta J^2$. The energies are purely real when $J^2 + \Delta^2 > \delta J^2$, corresponding to a weakly non-Hermitian regime called the $\mathcal{PT}$-symmetric regime. When $J^2 + \Delta^2 = \delta J^2$ the two eigenvalues become degenerate, at which point the eigenvectors also coalesce, yielding the exceptional point in the parameter space. When $J^2 + \Delta^2 < \delta J^2$, the energies acquire nonzero imaginary part, which is called the $\mathcal{PT}$-broken regime. The appearance of the imaginary part of eigenenergies indicates that the norm of the wavefunction will not be conserved over time, and the population exponentially grows or decays [28, 51, 66, 67, 71].

### B. Nonlinear Hatano-Nelson Dimer Model

In the linear HN dimer model, the non-Hermiticity was included via a constant off-diagonal contribution $\pm \delta J$. In the nonlinear HN dimer model, the non-Hermiticity is introduced dynamically via the population imbalance between the two sites. The nonlinear HN dimer model is defined by the following equation of motion:

$$i\dot{\boldsymbol{\alpha}} = \begin{pmatrix} \omega - \Delta & -J - gz \\ -J + gz & \omega + \Delta \end{pmatrix} \boldsymbol{\alpha}, \qquad (3)$$

in which the non-reciprocal part of the hopping amplitude is now set by $\pm gz$, where $g$ is the interaction strength and $z \equiv |\alpha_1|^2 - |\alpha_2|^2$ represents the population imbalance between the two sites. A sketch of this model is made in Fig. 1 (b). As $z$ depends on the complex wavefunction, this is no longer a linear model and so does not have linear eigenstates and eigenenergies similar to the linear HN dimer. Understanding the rich behavior of this model is a goal of the current paper. Because of the nonlinearity, it is not possible to obtain a good analytical understanding of the model. In order to approximately understand the dynamics of this model for a short period of time, we introduce the following instantaneous HN dimer model.

### C. Instantaneous Hatano-Nelson Dimer model

The nonlinearity in the nonlinear HN dimer model was in the term $\pm gz$ in the off-diagonal terms. We can rewrite this term as $\pm gn(z/n)$, where $n$ is the norm of the wavefunction. In non-Hermitian models, the norm $n$ generally depends on time, and so do $gn$ and $z/n$. However, as we discuss in more detail in Sec. V, the model

$$i\dot{\boldsymbol{\alpha}} = \begin{pmatrix} \omega - \Delta & -J - \bar{g}z/n \\ -J + \bar{g}z/n & \omega + \Delta \end{pmatrix} \boldsymbol{\alpha}, \qquad (4)$$
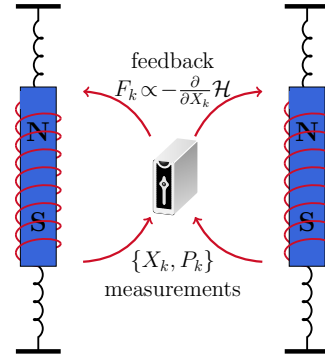


FIG. 2. Sketch of the experimental apparatus used for implementing the described models. We perform real-time measurements of the effective position $X_k$ and momentum $P_k$ variables of our oscillators (labeled by index $k$), which are used to compute real-time feedback forces that are applying magnetically through a voltage-controlled current. The form of the feedback forces used to implement a desired Hamiltonian $\mathcal{H}$ is given simply by the relationship $F_k \propto -\partial \mathcal{H}/\partial X_k$.

which is obtained by replacing $gn$ in the nonlinear HN dimer model by $\bar{g}$, allows description of the dynamics without complication arising from the time-dependence of $n$ if $\bar{g}$ is taken to be a constant value. Physically, we can view the model as describing the dynamics of the nonlinear HN dimer model at time close to $t_0$ if we set $\bar{g} = gn(t_0)$. We thus call the model the instantaneous HN dimer model.

Before moving on to describe the dynamical features of the linear, nonlinear and instantaneous HN dimer models, we briefly explain how the models can be experimentally realized in our system of mechanical oscillators.

### III. EXPERIMENTAL SET-UP

Our experimental setup is described in detail in Ref. [65], and consists of two almost identical oscillators, whose acceleration $a(t)$ and its numerical derivative, the jerk $j(t) = da(t)/dt$, are measured in real time. These measurements can be used to produce a real-time feedback force on each oscillator that allows us to synthetically couple the two oscillators. This procedure enables us to effectively generate a wide variety of two-level tight-binding Hamiltonians. Within the rotating-wave approximation, the Heisenberg's equations of motion for a generic tight-binding Hamiltonian can be mapped onto Newton's equations for the harmonic oscillators. Hence, we can engineer a combination of self and cross feedback [65]: the former is responsible for local on-site terms (e.g. site-dependent potential energy shifts, site-dependent gain or loss, and on-site nonlinear interactions), while the latter introduces off-site terms that allow energy to hop from site to site (e.g., complex hopping, non-reciprocal coupling, and even density-dependent hopping).

Experimentally, feedback forces are implemented by using real-time voltage output signals to control the currents through gradient solenoids surrounding each oscillator. These control signals result in magnetic forces on the oscillators, each of which feature an embedded dipole magnet. The real-time voltage measurement signals relating to acceleration and jerk are normalized to a common scale. Given the simple harmonic nature of our oscillators, these normalized measurement signals $X_k$ and $P_k$, where $k$ is the oscillator index, serve as direct proxies for the oscillators' positions and momenta, $x_k$ and $p_k$. As depicted in Fig. 2, a desired Hamiltonian $\mathcal{H}$ is implemented by feeding back on the oscillators with forces that are true to Hamilton's equation ($dp_k/dt = -\partial\mathcal{H}/\partial x_k$). Hence, feedback forces are of the form $F_k \propto -\partial\mathcal{H}/\partial X_k$. Naturally, site energy shifts are implemented by forces of the form $F_k \propto X_k$, while gain and loss terms are implemented through feedback of the form $F_k \propto P_k$, and so on [65]. Owing to our co-normalization of the $X_k$ and $P_k$ variables, the *relative* magnitude of all the linear terms in our experimentally implemented Hamiltonians are defined simply by the ratio of the applied feedback coefficients. The *absolute* calibration of our feedback forces (*i.e.*, how the control voltage signals generated by our measurement-and-feedback system relate to the actual mHz-scale terms of the implemented Hamiltonian) is performed by investigating the frequency shift of the individual oscillators based on self-feedback forces ($F_k \propto X_k$), as detailed in Ref. [65].

In order to simulate the dynamics as in Eq. 1, we introduce a combination of self-feedback (to cancel natural loss terms and to shift the site energies) and linear cross-feedback (to introduce hopping between sites). To capture nonlinear terms, such as the population-dependent hopping contributions of Eq. 3, we introduce feedback forces of the form $F_{1(2)} \propto g(X_1^2 + P_1^2 - X_2^2 - P_2^2)X_{2(1)}/(X_{1,i}^2 + P_{1,i}^2 + X_{2,i}^2 + P_{1,i}^2)$, where $X_{k,i}$ and $P_{k,i}$ are the initial values taken by the effective position and momentum variables. Through this normalization, these nonlinear terms are governed by the same absolute calibration as the linear terms.

In addition to allowing for implementation of the desired linear and nonlinear HN dimer models, our control over these applied forces enables us to set the initial state of the oscillators for each experiment. Starting with oscillators nominally at rest, we sinusoidally drive the two oscillators at their common resonance frequency of $\sim 3.05$ Hz for several seconds. By controlling the relative strength and phase of these two sinusoidal "initialization" drives, we control the initial amplitudes and phases of the two oscillators (or correspondingly, the initial complex-valued wave-function $\boldsymbol{\alpha}$.

## IV.   LINEAR HN DIMER MODEL

With the experimental setup we just described, we study the dynamical behavior of the linear HN dimer model. To understand the dynamics, we employ two descriptions, one is in the "phase space" of the population imbalance and the phase difference between the two sites, and the other is the Bloch sphere representation. Although the dynamics of linear HN dimer model can be obtained just by looking at the eigenstates of the non-Hermitian Hamiltonian, the description in terms of the phase space and the Bloch sphere gives us intuitive picture for understanding, and will also lay the groundwork for later Sections to understand the dynamics of the nonlinear and instantaneous HN dimer models.

### A.   Dynamical Equations for the linear HN dimer

We rewrite here the equation of motion for the linear HN dimer model, Eq. 1,

$$i\frac{\partial}{\partial t}\begin{pmatrix} \alpha_1 \\ \alpha_2 \end{pmatrix} = \begin{pmatrix} \omega - \Delta & -J - \delta J \\ -J + \delta J & \omega + \Delta \end{pmatrix}\begin{pmatrix} \alpha_1 \\ \alpha_2 \end{pmatrix}. \quad (5)$$

In standard Hermitian quantum mechanics, the overall normalization of the wavefunction is not an observable, and we can assume the wavefunction to be normalized with the overall phase left as a gauge degree of freedom. However, in non-Hermitian quantum mechanics, time evolution is non-unitary in general and the change of norm of the wavefunction over time plays an important role, describing phenomena such as decay and lasing. In our classical experimental setup, all the information of the wavefunction, $\alpha_1$ and $\alpha_2$, can in principle be measured. Following the practice of non-Hermitian quantum mechanics, we consider the norm of the wavefunction to be an observable, but we choose to not consider the overall phase to be significant.

In describing dynamics of two-site (two-level) systems, it is both convenient and conventional to recast the dynamical equations either in terms of "phase space" dynamics [72] or in terms of the Bloch vector [45, 46]. As we shall use both pictures interchangeably, we now briefly introduce each in turn.

In the phase-space picture, we look at the dynamics in the space of phase difference between two sites, $\varphi \equiv \arg(\alpha_1/\alpha_2) \in (-\pi, \pi]$, and the normalized population imbalance between two sites $\tilde{z} \equiv (|\alpha_1|^2 - |\alpha_2|^2)/n$, where $n \equiv |\alpha_1|^2 + |\alpha_2|^2$ is the total population. In the dynamics of two-site Hermitian models, the dynamics is fully characterized in the space of $\{\tilde{z}, \varphi\}$. In non-Hermitian models, however, the overall norm of the wavefunction can change and have significance, the full dynamics is characterized in the space of $\{n, \tilde{z}, \varphi\}$. Equations of motion for $\{n, \tilde{z}, \varphi\}$ can be obtained from Eq. 1 in a straightforward manner, and they are

$$\dot{n} = -2\,\delta J\, n\,\sqrt{1 - \tilde{z}^2}\,\sin\varphi, \quad (6)$$

$$\dot{\tilde{z}} = 2(\tilde{z}\,\delta J - J)\sqrt{1 - \tilde{z}^2}\,\sin\varphi, \quad (7)$$

$$\dot{\varphi} = -2\,\Delta + 2\,\frac{J\tilde{z} - \delta J}{\sqrt{1 - \tilde{z}^2}}\,\cos\varphi. \quad (8)$$

We see that the time evolution of the variables $\tilde{z}$ and $\varphi$ are closed by themselves and does not depend on the total population $n$. As a result, we can consider the dynamics in the restricted 2D phase space $\{\tilde{z}, \varphi\}$; the dynamics of $n$ is separately determined from the information of $\{\tilde{z}, \varphi\}$, as in other non-Hermitian dimer models [45, 46]. Most importantly, when considering the dynamics of $\{\tilde{z}, \varphi\}$, we do not need to worry about the fact that the total population $n$ can change in time, and thus we can analyze the dynamics in $\{\tilde{z}, \varphi\}$ in a way analogous to the Hermitian dimer models.

Secondly, we can alternatively visualize the dynamics by means of the normalized Bloch vector, $\mathbf{s} = (s_x, s_y, s_z)^{\mathrm{T}}$, whose components are defined as:

$$s_x \equiv \frac{1}{2\,n}(\alpha_1^* \alpha_2 + \alpha_1 \alpha_2^*), \qquad (9)$$

$$s_y \equiv \frac{1}{2i\,n}(\alpha_1^* \alpha_2 - \alpha_1 \alpha_2^*), \qquad (10)$$

$$s_z \equiv \frac{1}{2\,n}\left(|\alpha_1|^2 - |\alpha_2|^2\right) = \frac{1}{2}\tilde{z}, \qquad (11)$$

subject to the condition $|\mathbf{s}|^2 = 1/4$, implying that the head of the Bloch vector always lies on the surface of a sphere of radius $1/2$ called the Bloch sphere [45, 46]. As the total population $n$ also changes, the full dynamics is described by the four variables $\{n, s_x, s_y, s_z\}$. We then obtain [51]:

$$\dot{n} = -4\,\delta J\, n\, s_y \qquad (12)$$

$$\dot{s}_x = 2\Delta s_y + 4\,\delta J\, s_x s_y \qquad (13)$$

$$\dot{s}_y = -2\Delta s_x + 2J s_z - \delta J + 4\,\delta J\, s_y^2 \qquad (14)$$

$$\dot{s}_z = -2J s_y + 4\,\delta J\, s_y s_z, \qquad (15)$$

where again we see that the time dependence of the Bloch vector $(s_x, s_y, s_z)$ does not depend on the total population $n$, and thus, upon considering the dynamics of the Bloch vector $(s_x, s_y, s_z)$, we do not need to worry about the time dependence of $n$. We note that since a vector $(s_x, s_y, s_z)$ lies on the surface of a two-dimensional sphere, the dimension of the space the variables $\{n, s_x, s_y, s_z\}$ move is three-dimensional, agreeing with the three-dimensional description in the phase space $\{n, \tilde{z}, \varphi\}$. Naturally, the phase-space and the Bloch-vector equations are fully equivalent, as can be shown by noting that $\varphi = \arctan(s_y/s_x)$ and $\tilde{z} = 2s_z$.

## B. Dynamics of the linear HN dimer

As one increases the non-Hermiticity $\delta J$, the dynamics of the linear HN dimer qualitatively change before and after the $\mathcal{PT}$-symmetry breaking transition at $J^2 + \Delta^2 = \delta J^2$. We first discuss the $\mathcal{PT}$-symmetric region $J^2 + \Delta^2 > \delta J^2$ to show, both theoretically and experimentally, that the dynamics is described by oscillation around two fixed points. We then discuss the $\mathcal{PT}$-broken regime $J^2 + \Delta^2 < \delta J^2$ where the fixed points turn into a source and sink of dynamics.

### 1. $\mathcal{PT}$-symmetric Regime

In the $\mathcal{PT}$-symmetric regime, $J^2 + \Delta^2 > \delta J^2$, where eigenvalues of the Hamiltonian are real, we will show that the dynamics consist of Rabi oscillations between the two sites, which can be seen as closed orbits in phase-space and on the Bloch sphere. We also show that the population can be biased toward one of the two sites; the emergence of population imbalance comes from non-Hermiticity, and its mechanism is different from the self-trapping known in interacting Hermitian Josephson dimers.

To understand the dynamics, we look for *fixed points* of motion, which are obtained by setting the time derivative of the variables to zero. In the non-Hermitian models we analyze in this paper, we find it convenient and useful to look for fixed points of variables other than $n$, leaving possibility for $n$ to change in time. In what follows, when we refer to fixed points, they refer to fixed points in the parameter space of either $\{\tilde{z}, \varphi\}$ in the phase space description or $\{s_x, s_y, s_z\}$ in the Bloch sphere description without including $n$.

In terms of the Bloch-sphere description, the fixed points are thus obtained by setting $\dot{s}_x = \dot{s}_y = \dot{s}_z = 0$ in Eqs. 13, 14 and 15. Looking at the equation for $\dot{s}_z = 0$, one sees that the fixed point should satisfy either $s_y = 0$ or $s_z = J/2\delta J$. The latter solution implies $s_z > 1/2$ in the $\mathcal{PT}$-symmetric region, $J^2 + \Delta^2 > \delta J^2$, which is not compatible with the condition $|\mathbf{s}|^2 = 1/4$ and thus not a valid solution. Therefore, the only fixed points in the $\mathcal{PT}$-symmetric region satisfy $s_y = 0$. Solving the other equations $\dot{s}_x = \dot{s}_y = 0$, we obtain two fixed points:

$$\begin{pmatrix} s_x \\ s_y \\ s_z \end{pmatrix} = \frac{1}{2(J^2 + \Delta^2)} \begin{pmatrix} -\delta J\, \Delta \pm \Omega\, J \\ 0 \\ \delta J\, J \pm \Omega \Delta \end{pmatrix}, \qquad (16)$$

where $\Omega \equiv \sqrt{J^2 + \Delta^2 - \delta J^2} > 0$ in the $\mathcal{PT}$-symmetric regime.

Equivalently, the fixed points can be expressed in terms of the phase-space variables by setting $\dot{\tilde{z}} = \dot{\varphi} = 0$. We find two fixed points,

$$\begin{pmatrix} \tilde{z} \\ \varphi \end{pmatrix} = \left\{ \begin{pmatrix} \frac{\delta J\, J + \Omega \Delta}{J^2 + \Delta^2} \\ 0 \text{ or } \pi \end{pmatrix}, \begin{pmatrix} \frac{\delta J\, J - \Omega \Delta}{J^2 + \Delta^2} \\ \pi \end{pmatrix} \right\}, \qquad (17)$$

In the first fixed point, we should choose $\varphi = 0$ when $\delta J < J$ and $\varphi = \pi$ when $\delta J > J$. This discontinuous change of $\varphi$ may look odd, but this is due to the fact that when $J = \delta J$, the first fixed point becomes $\tilde{z} = 1$, which corresponds to the north pole in the Bloch sphere description. As the fixed point crosses the north pole, the phase angle $\varphi$ changes discontinuously from 0 to $\pi$. Note that there is no discontinuity in the Bloch sphere description.

We now consider dynamics of the system around the fixed points. Dynamics around a fixed point can be understood by looking at the Jacobian matrix, $\mathcal{J}$, of the
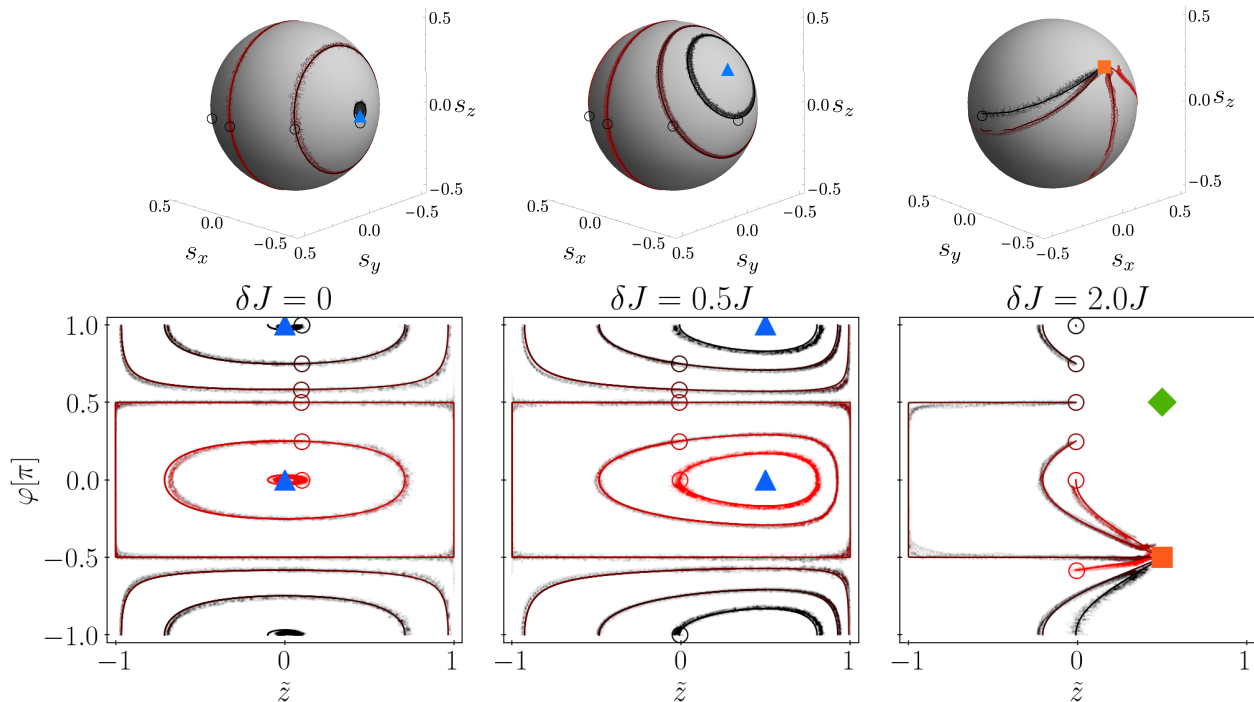
FIG. 3. Numerically and experimentally obtained dynamics of the linear Hatano-Nelson dimer model, with $\Delta = 0$, and three distinct values of $\delta J$ in both the Bloch-sphere representation (top panels) and the phase space representation (bottom panels). Different colors of points represent the different initial conditions, which are highlighted by open circles. Numerical results are in solid lines, whereas experimental data are plotted with (slightly transparent) points. In the $\mathcal{PT}$-symmetric regime the fixed points in Eqs. 16 and 17 are centers (blue triangles), while as soon as the $\mathcal{PT}$-symmetry is broken (panel on the right), one of the points in Eq. 19, or equivalently in Eq. 20, behaves as a source (unstable point, green diamond) and the other as a drain (stable point, orange square).

fixed point. In the phase space $\{\tilde{z}, \varphi\}$ the Jacobian is

$$\mathcal{J} = \begin{pmatrix} \partial_{\tilde{z}}\dot{\tilde{z}} & \partial_{\varphi}\dot{\tilde{z}} \\ \partial_{\tilde{z}}\dot{\varphi} & \partial_{\varphi}\dot{\varphi} \end{pmatrix}. \tag{18}$$

It is known from general theory of dynamical systems that the dynamics around a fixed point is classified according to the eigenvalues of the Jacobian matrix [73–76]. If the real part of the two eigenvalues are both zero, the fixed point acts as a *center* of motion around which the system oscillates. If the real part of the eigenvalues are both positive, the fixed point is called an *unstable* fixed point, and the dynamics flows away from the point. If the real part of the eigenvalues are both negative, the fixed point is called a *stable* fixed point, and the dynamics sinks into the point. If one of the eigenvalues has a positive real part and the other eigenvalue has a negative real part, the fixed point behaves as a *saddle point* of dynamics.

For the fixed points of Eq. 17, the eigenvalues of this Jacobian are a purely imaginary complex conjugate pairs with no real part, indicating that these points behave as centers for the dynamics. This oscillatory behavior is analogous to the Rabi oscillation in coherently coupled two-level quantum systems. Such oscillatory dynamics

is confirmed also experimentally as seen in Fig. 3. Depending on the value of $\delta J$, which is the strength of the non-Hermiticity, the value of $\tilde{z}$ at the fixed points vary, and can even reach the maximum value of $\tilde{z} = 1$. This imbalance of population is a two-site version of the non-Hermitian skin effect known in the extended Hatano-Nelson model with edges, where all the eigenstates are known to be localized on one edge [52–54].

These dynamical features are both numerically and experimentally confirmed, as described in Fig. 3. The left panel describes the Hermitian limit ($\delta J = 0$) of the linear HN dimer model, whereas the central panel is in the $\mathcal{PT}$-symmetric regime and the right panel is the $\mathcal{PT}$-broken regime. Fixed points which serve as centers of dynamics are indicated by blue triangles whereas source and sink are indicated by a green diamond and an orange square, respectively. The roles of fixed points found in dynamics obtained from numerical and experimental means are in accord with what we found above.

So far, we have not looked at the dynamics of $n$. If we insert the fixed points into the equation for $n$, we see $\dot{n} = 0$, indicating that the total population does not change in time on the fixed points. This behavior is expected because the eigenvalues of the Hamiltonian in the $\mathcal{PT}$-symmetric region are both real. However, if we look
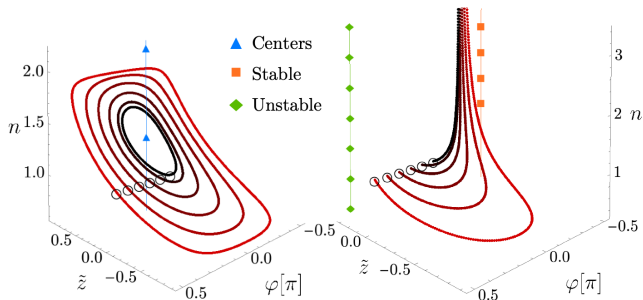
FIG. 4. Numerically calculated phase space dynamics for the linear HN dimer model in the space of $\{n, \tilde{z}, \varphi\}$. Different colors are for different initial conditions, highlighted with open circles. All the fixed points are represented as lines perpendicular to the $\tilde{z} - \varphi$ plane as their coordinates are independent of the population, $n$. Left panel: in the $\mathcal{PT}$-symmetric case ($\delta J = 0.5\,J$ and $\Delta = 0.01\,J$), the fixed points in Eq. 17 (triangles) are centers. Right panel: if the system is not $\mathcal{PT}$-symmetric ($\delta J = 2\,J$ and $\Delta = 0.01\,J$), only points in Eq. 20 are well defined, and appear in pairs of stable (orange squares) and unstable (green diamonds) points.

at the dynamics around the fixed points, the total population $n$ changes in time. In the left panel of Fig. 4, we plot the numerically-calculated dynamics within a region of the 3D phase-space of $\{n, \tilde{z}, \varphi\}$. In the 3D phase-space, the fixed point in the phase space $\{\tilde{z}, \varphi\}$ corresponds to a line perpendicular to the $\tilde{z} - \varphi$ plane. The variation of the population during dynamical evolution even in the $\mathcal{PT}$-symmetric region reflects that the eigenstates are not orthogonal, and their overlap can lead to a change of population during dynamics.

### 2. $\mathcal{PT}$-broken Regime

Approaching to the $\mathcal{PT}$-breaking transition from the $\mathcal{PT}$-symmetric region corresponds to taking $\Omega \to 0$, and the fixed points of the $\mathcal{PT}$-symmetric region in Eq.(16) merge in this limit, giving rise to an exceptional point.

Beyond the $\mathcal{PT}$-breaking transition, $J^2 + \Delta^2 < \delta J^2$, we enter the $\mathcal{PT}$-broken regime where the eigenvalues of the Hamiltonian are no longer real. We again look for fixed points by setting $\dot{s}_x = \dot{s}_y = \dot{s}_z = 0$ in (13), (14), and (15). The fixed point solution with $s_y = 0$ we had in the $\mathcal{PT}$-symmetric region is no longer a valid solution in the $\mathcal{PT}$-broken regime with $J^2 + \Delta^2 < \delta J^2$. Instead, we find two fixed points at

$$\begin{pmatrix} s_x \\ s_y \\ s_z \end{pmatrix} = \frac{1}{2\,\delta J} \begin{pmatrix} -\Delta \\ \pm i\,\Omega \\ J \end{pmatrix}. \quad (19)$$

Equivalently, in the phase-space description, the fixed points are:

$$\begin{pmatrix} \tilde{z} \\ \varphi \end{pmatrix} = \begin{pmatrix} J/\delta J \\ \pm \arccos\left(-\Delta/\sqrt{\delta J^2 - J^2}\right) \end{pmatrix}. \quad (20)$$

The eigenvalues of the Jacobian corresponding to these fixed points are both negative for the fixed point with $\varphi < 0$ and both positive for the fixed point with $\varphi > 0$, which implies that the fixed point at $\varphi < 0$ is a stable fixed point acting as a sink of dynamics, where as the fixed point at $\varphi > 0$ is an unstable fixed point acting as a source. In the linear HN dimer, fixed points are nothing but the eigenstates of the 2-by-2 Hamiltonian; the eigenstate corresponding to the stable fixed point has the eigenvalue whose imaginary part is larger than the other eigenstate. We can physically understand the source/sink nature of these fixed point by noting that, starting from a state which is a superposition of the two eigenstates, the weight of the eigenstate corresponding to the sink will grow because of the larger imaginary part. We note that the total population $n$ at the fixed points is no longer a constant, but rather grows in time. In this sense, the fixed points we found here are not fixed points in the full dynamics taking $n$ into account. As we noted earlier in this paper, we keep this terminology that the fixed points are points where variables other than $n$ are kept constant.

## V. INSTANTANEOUS HN DIMER MODEL

Now we turn to models with nonlinearities. Unlike the linear HN dimer model where the fixed points correspond to the eigenstate of the 2-by-2 Hamiltonian, obtaining the fixed points of dynamics of models with nonlinearity is generally nontrivial. Although the model we experimentally implement is the nonlinear HN model, this model does not allow for a simple description in terms of fixed points. However, as we shall explain, we can obtain the fixed points of the instantaneous HN model, which also contains nonlinearity and thus provides a good approximation to understand the experimentally realized nonlinear HN model. In this section, we give a theoretical description of the dynamics of the instantaneous HN dimer model, which we will use in later Sections to understand the dynamics of nonlinear HN dimer model.

We rewrite here the equation of motion for the instantaneous HN dimer model Eq.(4):

$$i\dot{\boldsymbol{\alpha}} = \begin{pmatrix} \omega - \Delta & -J - \bar{g}\tilde{z} \\ -J + \bar{g}\tilde{z} & \omega + \Delta \end{pmatrix} \boldsymbol{\alpha}, \quad (21)$$

where we used the notation $\tilde{z} = z/n$ we introduced in the previous section. The equations for the phase-space variables $\{n, \tilde{z}, \varphi\}$ are

$$\dot{n} = -2\,\bar{g}\,n\,\tilde{z}\sqrt{1 - \tilde{z}^2}\sin\varphi \quad (22)$$

$$\dot{\tilde{z}} = 2(\bar{g}\,\tilde{z}^2 - J)\sqrt{1 - \tilde{z}^2}\sin\varphi \quad (23)$$

$$\dot{\varphi} = -2\Delta + 2\frac{J - \bar{g}}{\sqrt{1 - \tilde{z}^2}}\tilde{z}\cos\varphi, \quad (24)$$

while the equations for the Bloch sphere variables are:

$$\dot{n} = -8\,\bar{g}n\,s_y s_z \tag{25}$$

$$\dot{s}_x = 2\Delta s_y + 8\,\bar{g}\,s_x s_y s_z \tag{26}$$

$$\dot{s}_y = -2\Delta s_x + 2(J-\bar{g})s_z + 8\,\bar{g}\,s_y^2 s_z \tag{27}$$

$$\dot{s}_z = -2Js_y + 8\,\bar{g}\,s_y s_z^2. \tag{28}$$

Just like the linear HN dimer model, time derivatives of the variables $\tilde{z}$, $\varphi$, $s_x$, $s_y$, and $s_z$ have no $n$ dependence, which implies that we can consider the dynamics in the phase space $\{\tilde{z},\varphi\}$ and on the Bloch sphere $\{s_x, s_y, s_z\}$ independent from how $n$ depends on time. Nonetheless, the instantaneous HN dimer model is not a linear model; indeed the dynamics has $\tilde{z}$ dependence in the 2-by-2 nonlinear Hamiltonian of Eq.(4). The situation should be contrasted with what happens for the nonlinear HN dimer model, whose equations of motions are Eqs. (40-46) in the next section. The nonlinear HN dimer model has explicit $n$ dependence in equations of motion for $\tilde{z}$, $\varphi$, $s_x$, $s_y$, and $s_z$, and a closed description in terms of either $\{\tilde{z},\varphi\}$ or $\{s_x, s_y, s_z\}$ is not allowed, making the analysis more difficult. The dynamics of the instantaneous HN dimer model we explore in this section serves as the basis to understand the dynamics of the nonlinear HN dimer model in the next section.

## A. Dynamics of the instantaneous HN dimer model

As before, we first look for the fixed points of motion. Fixed points, as before, are points determined by $\dot{\tilde{z}} = \dot{\varphi} = 0$ for the phase-space dynamics and $\dot{s}_x = \dot{s}_y = \dot{s}_z = 0$ for the Bloch sphere dynamics, without imposing $\dot{n} = 0$. The fixed points we discuss are, therefore, fixed points in the restricted space in which we do not look at the time evolution of $n$.

From the condition $\dot{s}_z = 0$, we obtain $s_y = 0$ or $s_z^2 = J/(4\bar{g})$. Let us first examine the case $s_y = 0$. From the other two equations, $\dot{s}_x = \dot{s}_y = 0$, we obtain the following two fixed point solutions

$$\begin{pmatrix} s_x \\ s_y \\ s_z \end{pmatrix} = \pm \frac{1}{2\sqrt{(J-\bar{g})^2 + \Delta^2}} \begin{pmatrix} J-\bar{g} \\ 0 \\ \Delta \end{pmatrix}. \tag{29}$$

A striking feature of the instantaneous HN dimer model is that these fixed points are always valid fixed points irrespective of the values of $J$, $\delta J$, and $\Delta$, which is to be contrasted to the linear HN dimer model where the fixed point $s_y = 0$ was valid only in the $\mathcal{PT}$-symmetric region. These fixed points in phase-space description are

$$\begin{pmatrix} \tilde{z} \\ \varphi \end{pmatrix} = \left\{ \begin{pmatrix} \frac{\Delta\,\text{sign}(J-\bar{g})}{\sqrt{(J-\bar{g})^2+\Delta^2}} \\ 0 \end{pmatrix}, \begin{pmatrix} -\frac{\Delta\,\text{sign}(J-\bar{g})}{\sqrt{(J-\bar{g})^2+\Delta^2}} \\ \pi \end{pmatrix} \right\} \tag{30}$$

The sign of the fixed points of $\bar{z}$ depends on $\text{sign}(J-\bar{g})$; this is because when $J = \bar{g}$, the fixed point reaches the north pole in the Bloch sphere description and thus $\varphi$

changes between 0 and $\pi$ around $J = \bar{g}$. Note that there is no discontinuous change in the Bloch sphere representation.

Now we look for the fixed point $s_y \neq 0$. Combining $s_z^2 = J/(4\bar{g})$ with $\dot{s}_x = \dot{s}_y = 0$, we obtain the following additional four fixed points

$$\begin{pmatrix} s_x \\ s_y \\ s_z \end{pmatrix} = \pm \frac{1}{2\sqrt{\bar{g}J}} \begin{pmatrix} -\Delta \\ 0 \\ J \end{pmatrix} \pm \frac{1}{2\sqrt{\bar{g}}} \begin{pmatrix} 0 \\ \sqrt{\bar{g}-g_{\text{T}}} \\ 0 \end{pmatrix}, \tag{31}$$

where the signs of the first and the second terms can be chosen independently, and we defined

$$g_{\text{T}} \equiv \frac{J^2 + \Delta^2}{J}. \tag{32}$$

These additional fixed points with $s_y \neq 0$ are valid fixed points only when $\bar{g} - g_{\text{T}} > 0$. Thus, the instantaneous model behaves qualitatively differently depending on whether $\bar{g} < g_{\text{T}}$ or $\bar{g} > g_{\text{T}}$, where the former has only two fixed points but the latter has six fixed points. We will refer to the case $\bar{g} < g_{\text{T}}$ as the *weak interaction regime* and $\bar{g} > g_{\text{T}}$ as the *strong interaction regime*.

These fixed points with $s_y \neq 0$ in the phase-space description have the following expressions:

$$\begin{pmatrix} \tilde{z} \\ \varphi \end{pmatrix} = \begin{pmatrix} \pm\sqrt{J/\bar{g}} \\ \pm\arccos\left(\frac{\mp\Delta}{\sqrt{J(\bar{g}-J)}}\right) \end{pmatrix}, \tag{33}$$

where the sign of $\tilde{z}$ and the sign inside arccos should be chosen to be opposite, but the sign in front of arccos is independent of the other signs.

We now consider the weak interaction regime $\bar{g} < g_{\text{T}}$ and the strong interaction regime $\bar{g} > g_{\text{T}}$ in turn to inspect the nature of fixed points and dynamics around them.

### 1. Weak interaction regime

In the weak interaction regime $\bar{g} < g_{\text{T}}$, the instantaneous HN dimer model has two fixed points given by Eq. (29). These fixed points satisfy $\dot{n} = 0$, indicating that the total number does not change in time. Thus, the weak interaction regime is a direct analog of the $\mathcal{PT}$-symmetric regime in the linear HN dimer model.

We find that the eigenvalues of the Jacobian of the two fixed points in phase space description are $\lambda_\pm = \pm 2\sqrt{J(\bar{g}-g_{\text{T}})}$ for both fixed points. Since $\bar{g} < g_{\text{T}}$ in the weak interaction regime, $\lambda_\pm$ are complex conjugate pairs, indicating that these fixed points serve as the center of oscillation in the phase space of $\{\bar{z},\varphi\}$, analogous to the fixed points in the $\mathcal{PT}$-symmetric regime in the linear HN dimer model.

In Fig. 5, we plot numerically obtained dynamics of the weak interaction regime. All orbits are closed as expected.

## 2. Strong interaction regime

The strong interaction regime $\bar{g} > g_{\mathrm{T}}$ of the instantaneous HN dimer model behaves differently from the $\mathcal{PT}$-broken regime of the linear HN dimer model. First of all, the two fixed points present in the weak interaction regime $\bar{g} < g_{\mathrm{T}}$ remain as fixed points in the strong interaction regime. The eigenvalues of the Jacobian of these two fixed points are $\lambda_\pm = \pm 2\sqrt{J(\bar{g} - g_{\mathrm{T}})}$, which are now both real and have opposite signs; this indicates that the fixed points now act as saddle points of dynamics in the $\{\tilde{z}, \varphi\}$ phase space.

In addition to the two fixed points inherited from the weak interaction regime, there are four additional fixed points in the strong interaction regime. Calculating the eigenvalues of the Jacobian of these four fixed points, we can group them into two categories.

Among the four additional fixed points, the eigenvalues
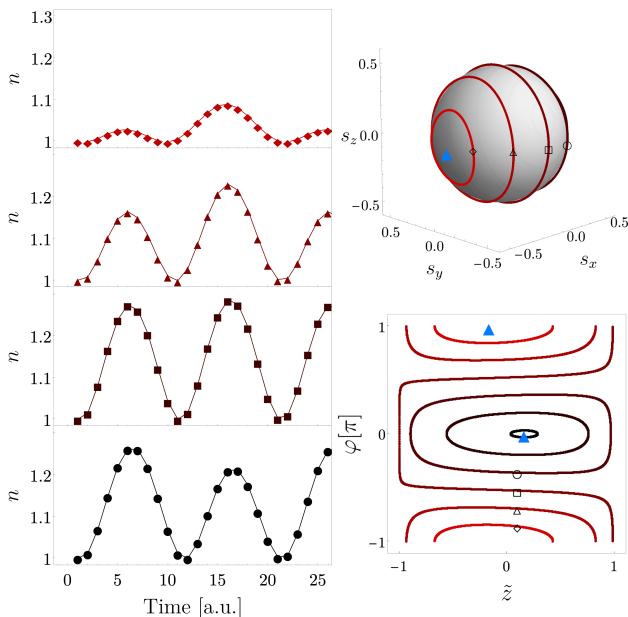


FIG. 5. Numerically obtained dynamics for the instantaneous HN dimer model in the weak interaction regime $\bar{g} = 0.4J < g_{\mathrm{T}}$ with $\Delta = 0.1J$. The panels on the right show the dynamics on the Bloch sphere (top) and in the phase space (bottom) for a set of different initial conditions, as highlighted by the empty markers. The filled triangles in the bottom right plot represent the two fixed points which behave as centers. Rabi-like oscillations are clearly seen as is the shift of the fixed-point centers away from $\tilde{z} = 0$, reflecting the interplay of the non-reciprocal couplings with the on-site energy difference. The behavior of population in time for each of the initial conditions highlighted is plotted in the left panels.

of the Jacobian of the following two fixed points

$$\begin{pmatrix} \tilde{z} \\ \varphi \end{pmatrix} = \begin{pmatrix} \sqrt{J/\bar{g}} \\ \arccos\left(\frac{-\Delta}{\sqrt{J(\bar{g}-J)}}\right) \end{pmatrix}, \begin{pmatrix} -\sqrt{J/\bar{g}} \\ -\arccos\left(\frac{\Delta}{\sqrt{J(\bar{g}-J)}}\right) \end{pmatrix},$$
(34)

are in both cases

$$\lambda = 2\sqrt{J(\bar{g} - g_{\mathrm{T}})} \text{ and } 4\sqrt{J(\bar{g} - g_{\mathrm{T}})}, \quad (35)$$

which are both positive in the strong interaction regime $\bar{g} > g_{\mathrm{T}}$. Therefore, these two fixed points are unstable fixed points which act as sources of dynamics.

On the other hand, the eigenvalues of the Jacobian of the other two fixed points

$$\begin{pmatrix} \tilde{z} \\ \varphi \end{pmatrix} = \begin{pmatrix} \sqrt{J/\bar{g}} \\ -\arccos\left(\frac{-\Delta}{\sqrt{J(\bar{g}-J)}}\right) \end{pmatrix}, \begin{pmatrix} -\sqrt{J/\bar{g}} \\ \arccos\left(\frac{\Delta}{\sqrt{J(\bar{g}-J)}}\right) \end{pmatrix},$$
(36)

are both

$$\lambda = -2\sqrt{J(\bar{g} - g_{\mathrm{T}})} \text{ and } -4\sqrt{J(\bar{g} - g_{\mathrm{T}})}, \quad (37)$$

which are both negative, indicating that these two fixed points are stable fixed points that act as sinks of dynamics. This behavior is confirmed by the numerically obtained dynamics as plotted in Fig. 6.

Calculating the time dependence of the total population at these four fixed points, we find

$$\dot{n} = \pm 2n\sqrt{J(\bar{g} - g_{\mathrm{T}})}, \quad (38)$$

where the positive (negative) sign corresponds to the two stable (unstable) fixed points. This indicates that the total population of the stable fixed points exponentially increases, whereas that of the unstable fixed points exponentially decreases; such behavior is consistent with these stable points acting as sinks and sources of dynamics.

For all these four fixed points, the population imbalance is $|\bar{z}| = \sqrt{J/\bar{g}}$, which indicates that $|\bar{z}| \to 0$ as $\bar{g} \to \infty$. The non-Hermitian localization on one of the two sites becomes smaller and smaller as the interaction $\bar{g}$ becomes larger, which is in stark contrast to the self-trapping phenomenon known in two-site nonlinear Josephson model where the localization becomes stronger as the interaction becomes larger.

## 3. Transition between the weak and strong regimes

We have just seen that, as the interaction $\bar{g}$ increases and crosses $g_{\mathrm{T}}$, the number of fixed points changes from two to six. We now examine this transition.

We first note that such an increase of the number of fixed points beyond two is not possible with any linear dimer model, in which the fixed points are determined by
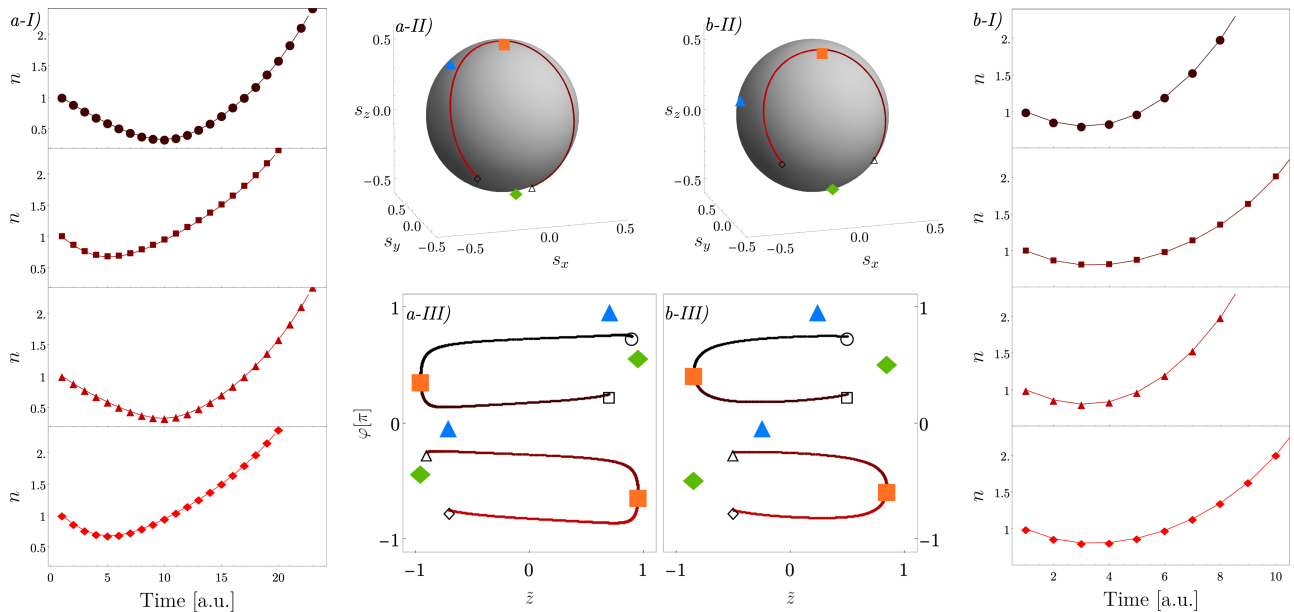
FIG. 6. Numerically obtained dynamics of the instantaneous HN dimer model in the strong interaction regime with $\bar{g} = 1.1\,J > g_T$ ($a$) and $\bar{g} = 1.4\,J$ ($b$), both with $\Delta = 0.1\,J$. In each case, we plot the behavior of the population over time ($a$-$I$ and $b$-$I$), the trajectories on the normalized Bloch sphere ($a$-$II$ and $b$-$II$) and the trajectories in the phase space of $\{\tilde{z}, \varphi\}$ ($a$-$III$ and $b$-$III$). Plots in the phase space and the Bloch sphere are for different initial conditions (marked with open markers); the evolution of the population over time for each initial condition is plotted in $a$-$I$ and $b$-$I$ using the corresponding marker. The saddle (blue triangles), stable (orange squares) and unstable (green diamonds) fixed points are highlighted. Note the trajectories converge towards the stable fixed points, after being slightly bent by the presence of saddle points. As expected, the population diverges quickly as a stable point is approached.

(at most) two eigenstates of the two-by-two Hamiltonian. Therefore, the appearance of six fixed points in the strong regime is an intrinsically nonlinear phenomenon.

Approaching the transition point from the weak regime, each of the two fixed points split into three as one crosses the transition point $\bar{g} = g_T$. During this process, a fixed point on the weak interaction side, which is a center of dynamics, turns into three fixed points which are a saddle point, a stable fixed point, and an unstable fixed point. This process is consistent with the *Poincaré-Hopf index theorem* as we shall explain. On a two-dimensional parameter space, such as the phase space $\{\bar{z}, \varphi\}$ and the surface of the Bloch sphere, the tangent vectors of the dynamics define a vector field. Such a vector field can have singularities, corresponding to the fixed points. For each of these singularities, a topological index called the Poincaré index can be defined, which assigns the value of $-1$ for saddle points and $+1$ for centers, stable, and unstable fixed points. The index theorem states that the sum of the Poincaré indices on the two-dimensional parameter space should be equal to the Euler characteristics of the parameter space [46, 77]. The Euler characteristics of our parameter space, which is a two-dimensional sphere as evident from the Bloch sphere description, is $+2$. In the weak interaction regime, we have two centers as singularities, and thus the sum of the Poincaré indices is $+2$, which is equal to the Euler characteristics as ex-

pected. As one crosses the transition point, a center, which has the Poincaré index of $+1$, turns into a saddle point, a stable point, and an unstable point, whose Poincaré indices are $-1$, $+1$, and $+1$, respectively, conserving the sum of the Poincaré indices. Thus the strong interaction regime also satisfies the index theorem.

## VI. NONLINEAR HN DIMER MODEL

With the understanding of the instantaneous HN dimer model, we can now understand dynamics of the nonlinear HN dimer model, which is the model experimentally implemented.

We rewrite the equations of motion for the nonlinear HN dimer model Eq. (3),

$$i\frac{\partial}{\partial t}\begin{pmatrix} \alpha_1 \\ \alpha_2 \end{pmatrix} = \begin{pmatrix} \omega - \Delta & -J - gz \\ -J + gz & \omega + \Delta \end{pmatrix}\begin{pmatrix} \alpha_1 \\ \alpha_2 \end{pmatrix}. \quad (39)$$

The dynamical equations in the phase-space are

$$\dot{n} = -2\,gn^2\,\tilde{z}\,\sqrt{1 - \tilde{z}^2}\,\sin\varphi, \quad (40)$$

$$\dot{\tilde{z}} = 2\,(gn\,\tilde{z}^2 - J)\,\sqrt{1 - \tilde{z}^2}\,\sin\varphi, \quad (41)$$

$$\dot{\varphi} = -2\,\Delta + 2\,\frac{J - gn}{\sqrt{1 - \tilde{z}^2}}\,\tilde{z}\cos\varphi. \quad (42)$$

and in terms of the Bloch sphere variables, the dynamics obey

$$\dot{n} = -8gn^2 \, s_y s_z, \tag{43}$$

$$\dot{s}_x = 2\Delta s_y + 8gn \, s_x s_y s_z, \tag{44}$$

$$\dot{s}_y = -2\Delta s_x + 2(J - gn)s_z + 8gn \, s_y^2 s_z, \tag{45}$$

$$\dot{s}_z = -2J s_y + 8gn \, s_y s_z^2. \tag{46}$$

We see that the time dependence of $\tilde{z}$, $\varphi$ and $s_x$, $s_y$, $s_z$ depend explicitly on $n$, implying that we can no longer use the two-dimensional phase space $\{\tilde{z}, \varphi\}$ and the surface of the Bloch sphere $\{s_x, s_y, s_z\}$ as a parameter space within which the equations of motion are closed. Instead, we should consider the time dependence of $n$ together with the other variables to understand the dynamics. This explicit $n$ dependence in the equations of motion makes it difficult to analytically approach the dynamics of the nonlinear HN dimer model when the interaction is strong. However, as we shall see, the theory of the instantaneous HN dimer model can provide a good qualitative understanding of what happens in the nonlinear HN dimer model.

## A. Dynamics of the nonlinear HN dimer model

We first look for fixed points of the dynamics. Since replacing $\bar{g}$ in the instantaneous HN dimer model by $gn$ recovers the equations of motion of the nonlinear HN dimer model, the two fixed points in the weak interaction regime and the six fixed points in the strong interaction regime of the instantaneous HN dimer model still satisfy $\dot{\tilde{z}} = \dot{\varphi} = 0$ and $\dot{s}_x = \dot{s}_y = \dot{s}_z = 0$. However, these points are not truly fixed anymore in the parameter space because $n$ can depend on time, and the time dependence of $n$ itself affects the position of the fixed points in the parameter space.

We first note that the two fixed points satisfying $s_y = 0$ are still fixed in the parameter space even in the nonlinear HN dimer model because they obey $\dot{n} = 0$, namely $n$ is time independent. The additional four fixed points are not fixed anymore in the parameter space because $n$ changes in time. The transition between the weak and strong interaction regimes is clear in the case of the instantaneous HN dimer model, given by $\bar{g} = g_T$. On the other hand, in the case of the nonlinear HN dimer model, there appears also a distinctive intermediate interaction regime between the weak and the strong regimes as we shall explain now.

In the nonlinear HN dimer model, one measure of the interaction strength is $gn_0$, where $n_0$ is the total population at the initial time. Replacing $\bar{g}$ by $gn_0$, the two fixed points with $s_y = 0$ of the instantaneous HN dimer model are still the fixed points in the nonlinear HN dimer model. If $gn_0$ is small enough compared to $g_T$, the dynamics we found for the weak interaction regime of the instantaneous HN dimer model applies also to the nonlinear HN dimer model. However, one should remember

that, although the total population $n$ does not change in time exactly at the fixed points, the total population does change during the periodic Rabi oscillation around the fixed points. This implies that even though the system initially satisfies $gn_0 < g_T$, the total population changes and at some time $t$ we may enter the regime with $gn(t) > g_T$ at which the dynamics should be compared to the strong interaction regime of the instantaneous HN dimer model.

We refer to the regime in which $gn(t) < g_T$ holds for any time $t \geq 0$ as the weak interaction regime of the nonlinear HN dimer model. In the weak interaction regime, all the dynamics are described by orbital motion around the two fixed points which serve as the centers of dynamics.

We refer to the regime in which both $gn(t) < g_T$ and $gn(t) > g_T$ happen at some time $t \geq 0$ during the evolution as the *intermediate* interaction regime. In this intermediate interaction regime, which is a unique feature of the nonlinear HN dimer model, there simultaneously exist two types of orbits: one is a closed orbit similar to the weak interaction regime, and the other is a diverging orbit which is reminiscent of the strong interaction regime of the instantaneous HN dimer model.

We finally refer to the regime in which $gn(t) > g_T$ holds for any time $t \geq 0$ as the strong interaction regime, where the dynamics diverges as in the strong interaction regime of the instantaneous HN dimer model. A crucial difference between the strong interaction regime of the instantaneous HN dimer model and the nonlinear dimer model is that, in the latter, the source and the sink of dynamics are no longer fixed points in the space $\{\tilde{z}, \varphi\}$ or $\{s_x, s_y, s_z\}$ because of the change of the total population $n$.

We now examine these three regimes experimentally, and compare them to numerical simulations.

## B. Experimental results and Numerical simulations

Figure 7 shows the dynamics of the nonlinear HN dimer model, experimentally and numerically obtained, for different values of $gn_0$. Firstly, panels with $gn_0 = 0$ and $gn_0 = 0.4\,J$ correspond to the weak interaction regime. We observe Rabi-like oscillations, similar to the ones found in the linear and instantaneous HN dimer models. Secondly, the panel with $gn_0 = 1.1J$ corresponds to the strong interaction regime, where the population of the trajectories diverges over time towards either positive or negative population imbalances, depending on the initial conditions. Finally, in the intermediate interaction regime at $gn_0 = 0.7J$ the two behaviors co-exist, *i.e.*, stable orbits and unstable trajectories are possible, depending on the initial conditions used, i.e. the initial phase difference between the two sites. This co-existence of both regimes is the unique feature of the nonlinear HN dimer model.

We can further see the unique feature of the nonlinear
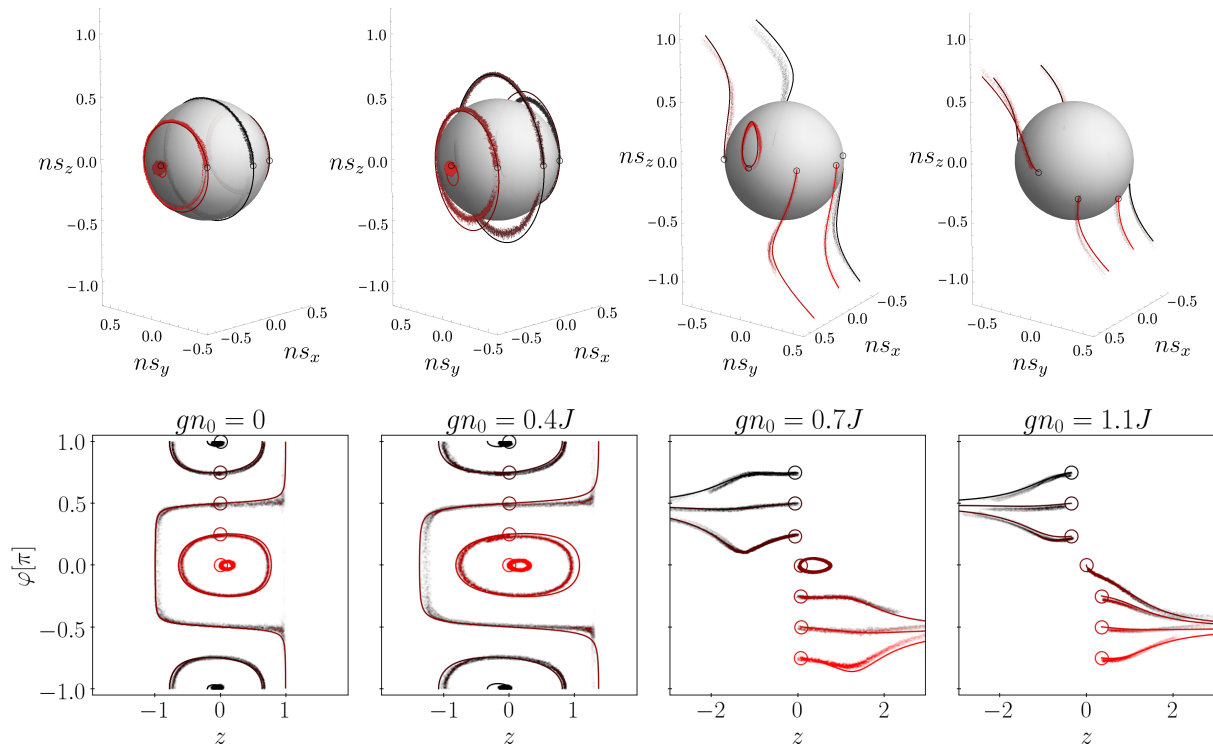
FIG. 7. Comparison between the numerical simulation and the experimental results of dynamics of the nonlinear HN dimer model, for $\Delta = 0.1J$, and four distinct values of $gn_0$ in both the *unnormalized* Bloch-sphere representation (top panels), in which we plot $n\mathbf{s} = n(s_x, s_y, s_z)^{\mathrm{T}}$, and the phase space representation (bottom panels). Numerical results are in solid lines, whereas experimental data are plotted with (slightly transparent) points, open circles represent the initial conditions. We note that the points can leave the surface of the Bloch sphere because the distance from the origin reflects the total population $n$. Three regimes are identified: for zero or small values of $g$ (two panels on the left), Rabi-like oscillations are observed just like in Fig. 3. In the opposite limit of very strong interactions (right-most panel), the system tends towards an asymptotic value of $z$, either positive or negative. In the intermediate regime, $gn_0 = 0.7J$, the two behaviors coexist, depending on the initial conditions.

HN dimer model if we examine the dynamics on the normalized Bloch sphere, as shown in the central panel of Fig. 8. We observe that the trajectories bend in arcs on the sphere, before eventually converging towards points on the equator. This behavior arises because instantaneously the trajectory is attracted towards the stable fixed points of the instantaneous HN dimer model for that particular value of $gn \to \bar{g}$. However, as $n$ keeps growing, the coordinates of the fixed points in the instantaneous HN dimer model also keep changing (see, e.g., Fig. 6), so that the trajectories appear to effectively "chase down" the stable points by following these arcs. Indeed, in the limit that $n \to \infty$, the coordinates on the Bloch sphere of the stable fixed points in the instantaneous HN dimer model become:

$$\begin{pmatrix} s_x \\ s_y \\ s_z \end{pmatrix} \to \begin{pmatrix} 0 \\ \pm 1/2 \\ 0 \end{pmatrix}, \qquad (47)$$

corresponding to the points of convergence on the equator of the normalized Bloch sphere in the experimental

model, e.g., as can be seen in the central panel of Fig. 8. Physically, this corresponds to the modes changing from being localized primarily on one of the two sites at small $\bar{g}$ (and hence small $n$), to being an equal superposition of the two sites as $\bar{g} \to \infty$, as the non-reciprocal coupling term dominates over all other terms in the Hamiltonian.

Of particular note in Fig. 8, two trajectories starting close to each other (black points and red points in the top panels) actually behave very differently: one describes a closed loop around the center (full blue triangle) and its population remains finite, although oscillating, whereas the other about half-way through the loop, diverts and ends up in the basin of attraction of the stable points (full orange squares), where the population diverges exponentially. As in the strong interaction case, note that the trajectories are bent in arcs to "follow" the always changing position of the fixed point in the corresponding instantaneous model.

Another helpful way to visualize this physics is shown in Fig. 9, where we plot arrows corresponding to the tangent vectors of dynamics on each point of the three di-
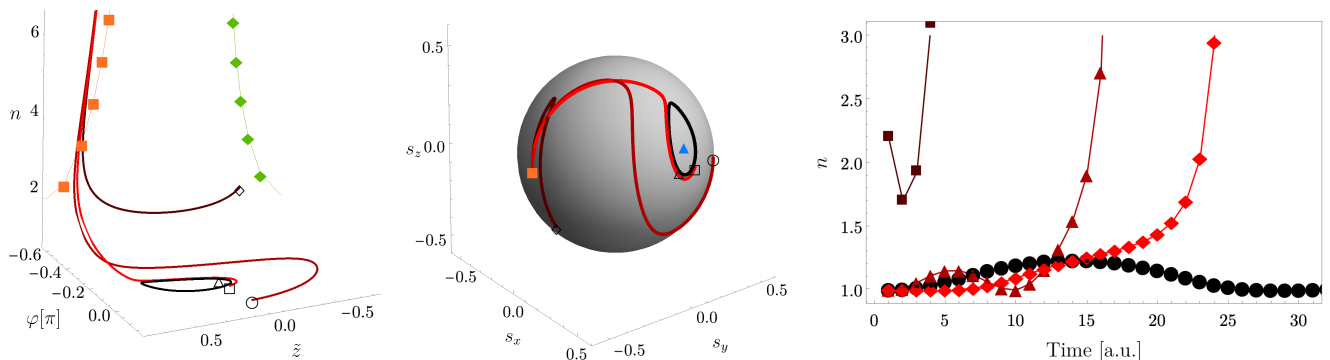
FIG. 8. Numerical dynamics of the population in the phase-space for the nonlinear HN dimer model with $g = 0.7J$ and $\Delta = 0.1\,J$; initial conditions are chosen so to highlight the different behaviors described in the text. The empty markers in the phase space plot and Bloch sphere plot (left and central panel) highlight the initial conditions, while different colors are for trajectories starting from each of the initial conditions; the change of $n$ over time of each set of initial conditions (right panel, corresponding markers and colors) shows an evident decrease of population in the neighborhood of the unstable points (green diamonds). As the system evolves, it is then attracted towards the stable points (orange squares) where $n$ grows exponentially.

mensional phase space. The top panels show the change in behavior of the fixed points on slices of fixed $n$: as long as for some time $t_1$, $gn(t_1) < g_{\mathrm{T}}$, the former are centers (top left panel), whereas as soon as for some later time $t_2$ the condition $gn(t_2) > g_{\mathrm{T}}$ is met, the latter behave like saddles (see top mid and right panels).

In the intermediate regime, in the case of initial conditions close to $\varphi = 0$, the system is pushed by the equations in a closed orbit around the center (top left panel in Fig. 9) and the population oscillates, as shown in Fig. 5. If the initial conditions are not sufficiently close to the fixed point of the blue up-triangle in the top left panel, while moving around the center, the trajectory ends up close enough to the basin of repulsion of unstable points (green diamonds) or to the basin of attraction of the stable points (orange squares).

## VII. CONCLUSIONS AND OUTLOOK

In this paper, we have investigated both theoretically and experimentally the dynamics of two-site models with hopping asymmetry. In a linear model where the hopping asymmetry is externally fixed, we experimentally observed the transition from $\mathcal{PT}$-symmetric to $\mathcal{PT}$-broken regimes as the hopping asymmetry is increased. While all the orbits are closed in the $\mathcal{PT}$-symmetric regime, the population diverges in the $\mathcal{PT}$-broken regime due to the non-Hermiticity from the hopping asymmetry. In a nonlinear model where the hopping asymmetry is dynamically induced by population imbalance between the two sites, we experimentally observed three different regimes in behavior, depending on the initial coupling strength. In the weak and strong regimes, we observe stable population oscillations and exponential growth/decay of the population, respectively, similar to the behavior in the linear model described above. However, in the inter-

mediate regime, we observe a coexistence of these dynamics, meaning that we can tune from stable oscillations to divergent behavior by simply varying the initial phase-difference between the two sites. As we explain, all three different regimes can be understood by studying the emergent fixed points of a closely-related nonlinear model in which the non-reciprocal hopping depends on the normalized population imbalance between the two sites.

In the future, this work opens the way towards the further exploration of non-Hermitian dynamics in more exotic systems. As demonstrated here and in our previous works [20], this mechanical platform can be used to simulate a wide-variety of lattice models, which would not not easy to realize in other systems. Going further, it will be interesting to explore, for example, the addition of other mean-field nonlinear effects [78] as well as extensions to larger systems, *e.g.*, such as non-Hermitian three-site trimer models [79–81] or large lattices with many sites [82], where the interplay of gain and loss with artificial gauge fields and topological phenomena can also be explored [83, 84].
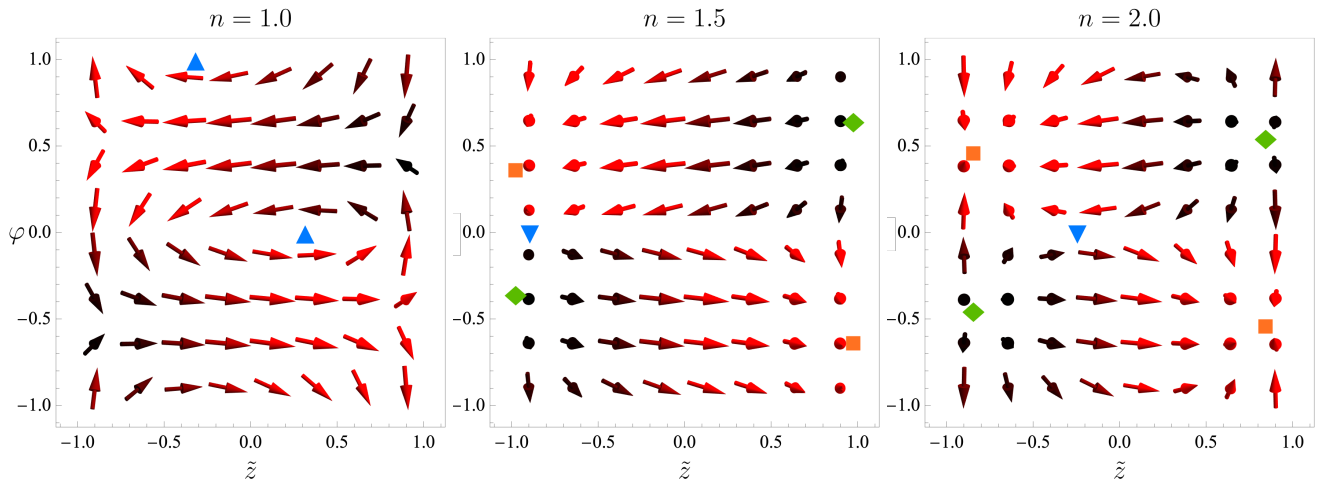
FIG. 9. Plot of slices of the 3D parameter space for the nonlinear HN dimer model when $g = 0.7J$ and $\Delta = 0.1J$. The top panels represent bird-eye plots of different slices of constant $n$ values, while the bottom panels represent slices of constant $\tilde{z}$ as seen from $\tilde{z} = 0$. The centers (blue, up triangles), saddles (blue, down triangles), stable (orange squares) and unstable (green diamonds) points, are those of the instantaneous HN dimer model when $gn \to \bar{g}$. The arrows represent the vector field described by Eqs. 40 to 42, while their color is representative of the tilt along the $n$ direction: black indicates tilting in the negative direction, and red indicates the positive tilting.

[1] C. M. Bender and S. Boettcher, Phys. Rev. Lett. **80**, 5243 (1998).

[2] C. M. Bender, Reports on Progress in Physics **70**, 947 (2007).

[3] S. Longhi, Phys. Rev. Lett. **103**, 123601 (2009).

[4] R. El-Ganainy, K. G. Makris, M. Khajavikhan, Z. H. Musslimani, S. Rotter, and D. N. Christodoulides, Nature Physics **14**, 11 (2018).

[5] A. Guo, G. J. Salamo, D. Duchesne, R. Morandotti, M. Volatier-Ravat, V. Aimez, G. A. Siviloglou, and D. N. Christodoulides, Phys. Rev. Lett. **103**, 093902 (2009).

[6] S. Bittner, B. Dietz, U. Günther, H. L. Harney, M. Miski-Oglu, A. Richter, and F. Schäfer, Phys. Rev. Lett. **108**, 024101 (2012).

[7] J. Schindler, A. Li, M. C. Zheng, F. M. Ellis, and T. Kottos, Phys. Rev. A **84**, 040101 (2011).

[8] C. Dembowski, H.-D. Gräf, H. L. Harney, A. Heine, W. D. Heiss, H. Rehfeld, and A. Richter, Phys. Rev. Lett. **86**, 787 (2001).

[9] C. Dembowski, B. Dietz, H.-D. Gräf, H. L. Harney, A. Heine, W. D. Heiss, and A. Richter, Phys. Rev. E **69**, 056216 (2004).

[10] T. Gao, E. Estrecho, K. Bliokh, T. Liew, M. Fraser, S. Brodbeck, M. Kamp, C. Schneider, S. Höfling, Y. Yamamoto, et al., Nature **526**, 554 (2015).

[11] Ş. K. Özdemir, S. Rotter, F. Nori, and L. Yang, Nature Materials **18**, 783 (2019).

[12] J. Garrison and E. M. Wright, Physics Letters A **128**, 177 (1988).

[13] G. Dattoli, R. Mignani, and A. Torre, Journal of Physics A: Mathematical and General **23**, 5795 (1990).

[14] F. Keck, H. J. Korsch, and S. Mossmann, Journal of Physics A: Mathematical and General **36**, 2125 (2003).

[15] S.-D. Liang and G.-Y. Huang, Phys. Rev. A **87**, 012118 (2013).

[16] A. Mondragón and E. Hernández, Journal of Physics A: Mathematical and General **29**, 2567 (1996).

[17] M. Berry and M. Dennis, Proceedings of the Royal Society of London. Series A: Mathematical, Physical and Engineering Sciences **459**, 1261 (2003).

[18] M. V. Berry, Czechoslovak journal of physics **54**, 1039 (2004).

[19] A. I. Nesterov and F. A. de la Cruz, Journal of Physics A: Mathematical and Theoretical **41**, 485304 (2008).

[20] Y. Singhal, E. Martello, S. Agrawal, T. Ozawa, H. Price, and B. Gadway, arXiv:2205.02700 (2022).

[21] T. E. Lee, Phys. Rev. Lett. **116**, 133903 (2016).

[22] H. Shen, B. Zhen, and L. Fu, Phys. Rev. Lett. **120**, 146402 (2018).

[23] L. Xiao, T. Deng, K. Wang, G. Zhu, Z. Wang, W. Yi, and P. Xue, Nature Physics , 1 (2020).

[24] S. Yao and Z. Wang, Phys. Rev. Lett. **121**, 086803 (2018).

[25] M. G. Silveirinha, Phys. Rev. B **99**, 125155 (2019).

[26] Y. Ashida, Z. Gong, and M. Ueda, Advances in Physics **69**, 249 (2020).

[27] C. Coulais, R. Fleury, and J. van Wezel, Nature Physics **17**, 9 (2021).

[28] E. J. Bergholtz, J. C. Budich, and F. K. Kunst, Rev. Mod. Phys. **93**, 015005 (2021).

[29] A. Guo, G. J. Salamo, D. Duchesne, R. Morandotti, M. Volatier-Ravat, V. Aimez, G. A. Siviloglou, and D. N. Christodoulides, Phys. Rev. Lett. **103**, 093902 (2009).

[30] L. Feng, R. El-Ganainy, and L. Ge, Nature Photonics 11, 752 (2017).

[31] R. El-Ganainy, M. Khajavikhan, D. N. Christodoulides, and S. K. Ozdemir, Communications Physics 2, 1 (2019).

[32] H. Zhao, X. Qiao, T. Wu, B. Midya, S. Longhi, and L. Feng, Science 365, 1163 (2019).

[33] H. Price, Y. Chong, A. Khanikaev, H. Schomerus, L. J. Maczewsky, M. Kremer, M. Heinrich, A. Szameit, O. Zilberberg, Y. Yang, et al., Journal of Physics: Photonics (2022).

[34] W. Gou, T. Chen, D. Xie, T. Xiao, T.-S. Deng, B. Gadway, W. Yi, and B. Yan, Phys. Rev. Lett. 124, 070402 (2020).

[35] J. Li, A. K. Harter, J. Liu, L. de Melo, Y. N. Joglekar, and L. Luo, Nature communications 10, 1 (2019).

[36] Q. Liang, D. Xie, Z. Dong, H. Li, H. Li, B. Gadway, W. Yi, and B. Yan, Physical review letters 129, 070401 (2022).

[37] C. Coulais, D. Sounas, and A. Alù, Nature 542, 461 (2017).

[38] M. Brandenbourger, X. Locsin, E. Lerner, and C. Coulais, Nature Communications 10, 4608 (2019).

[39] C. Scheibner, W. T. M. Irvine, and V. Vitelli, Phys. Rev. Lett. 125, 118001 (2020).

[40] C. Scheibner, A. Souslov, D. Banerjee, P. Surowka, W. T. Irvine, and V. Vitelli, Nature Physics 16, 475 (2020).

[41] D. Zhou and J. Zhang, Physical Review Research 2, 023173 (2020).

[42] A. Ghatak, M. Brandenbourger, J. van Wezel, and C. Coulais, Proceedings of the National Academy of Sciences 117, 29561 (2020).

[43] A. Ghatak, M. Brandenbourger, J. van Wezel, and C. Coulais, Proceedings of the National Academy of Sciences (2020), 10.1073/pnas.2010580117.

[44] E. M. Graefe, U. Günther, H. Korsch, and A. Niederle, Journal of Physics A: Mathematical and Theoretical 41, 255206 (2008).

[45] E. M. Graefe, H. Korsch, and A. Niederle, Physical review letters 101, 150408 (2008).

[46] E.-M. Graefe, H. J. Korsch, and A. E. Niederle, Phys. Rev. A 82, 013629 (2010).

[47] E.-M. Graefe, Journal of Physics A: Mathematical and Theoretical 45, 444015 (2012).

[48] O. Vázquez-Candanedo, J. C. Hernández-Herrejón, F. M. Izrailev, and D. N. Christodoulides, Phys. Rev. A 89, 013832 (2014).

[49] Y. Zhiyenbayev, Y. Kominis, C. Valagiannopoulos, V. Kovanis, and A. Bountis, Physical Review A 100, 043834 (2019).

[50] C. Valagiannopoulos, IEEE Transactions on Antennas and Propagation 70, 5534 (2022).

[51] Y.-P. Wu, G.-Q. Zhang, C.-X. Zhang, J. Xu, and D.-W. Zhang, Frontiers of Physics 17, 1 (2022).

[52] N. Hatano and D. R. Nelson, Phys. Rev. Lett. 77, 570 (1996).

[53] N. Hatano and D. R. Nelson, Phys. Rev. B 56, 8651 (1997).

[54] N. Hatano and D. R. Nelson, Phys. Rev. B 58, 8384 (1998).

[55] E. J. Bergholtz, J. C. Budich, and F. K. Kunst, Rev. Mod. Phys. 93, 015005 (2021).

[56] T. E. Lee, Phys. Rev. Lett. 116, 133903 (2016).

[57] Z. Gong, Y. Ashida, K. Kawabata, K. Takasan, S. Higashikawa, and M. Ueda, Phys. Rev. X 8, 031079 (2018).

[58] B. Peng, Ş. K. Özdemir, F. Lei, F. Monifi, M. Gianfreda, G. L. Long, S. Fan, F. Nori, C. M. Bender, and L. Yang, Nature Physics 10, 394 (2014).

[59] F. Ruesink, M.-A. Miri, A. Alu, and E. Verhagen, Nature communications 7, 1 (2016).

[60] K. Fang, J. Luo, A. Metelmann, M. H. Matheny, F. Marquardt, A. A. Clerk, and O. Painter, Nature Physics 13, 465 (2017).

[61] S. Weidemann, M. Kremer, T. Helbig, T. Hofmann, A. Stegmaier, M. Greiter, R. Thomale, and A. Szameit, Science 368, 311 (2020).

[62] M. Ezawa, Phys. Rev. B 99, 121411 (2019).

[63] M. Ezawa, Phys. Rev. B 100, 165419 (2019).

[64] S. Liu, R. Shao, S. Ma, L. Zhang, O. You, H. Wu, Y. J. Xiang, T. J. Cui, and S. Zhang, Research 2021 (2021).

[65] R. Anandwade, Y. Singhal, S. N. M. Paladugu, E. Martello, M. Castle, S. Agrawal, E. Carlson, C. Battle-McDonald, T. Ozawa, H. M. Price, and B. Gadway, arXiv:2107.09649 (2021).

[66] L. Li, C. H. Lee, S. Mu, and J. Gong, Nature communications 11, 1 (2020).

[67] T. Liu, J. J. He, T. Yoshida, Z.-L. Xiang, and F. Nori, Phys. Rev. B 102, 235151 (2020).

[68] H. Shen, B. Zhen, and L. Fu, Phys. Rev. Lett. 120, 146402 (2018).

[69] M. Hiller, T. Kottos, and A. Ossipov, Phys. Rev. A 73, 063625 (2006).

[70] W. Heiss, Journal of Physics A: Mathematical and Theoretical 45, 444016 (2012).

[71] N. Silberstein, J. Behrends, M. Goldstein, and R. Ilan, Phys. Rev. B 102, 245147 (2020).

[72] S. Raghavan, A. Smerzi, S. Fantoni, and S. R. Shenoy, Phys. Rev. A 59, 620 (1999).

[73] R. C. Hilborn, Chaos and nonlinear dynamics: an introduction for scientists and engineers (Oxford University Press on Demand, 2000).

[74] M. Cencini, F. Cecconi, and A. Vulpiani, Chaos: from simple models to complex systems, Vol. 17 (World Scientific, 2009).

[75] M. S. Chong, A. E. Perry, and B. J. Cantwell, Physics of Fluids A: Fluid Dynamics 2, 765 (1990).

[76] T. Zibold, E. Nicklas, C. Gross, and M. K. Oberthaler, Phys. Rev. Lett. 105, 204101 (2010).

[77] V. Arnol'd, V. Arnold, M. Levi, J. Szücs, and J. Cs, Geometrical Methods in the Theory of Ordinary Differential Equations, Grundlehren der mathematischen Wissenschaften in Einzeldarstellungen mit besonderer Berücksichtigung der Anwendungsgebiete (Springer New York, 1983).

[78] W. N. Faugno and T. Ozawa, Phys. Rev. Lett. 129, 180401 (2022).

[79] R. Franzosi and V. Penna, Phys. Rev. E 67, 046227 (2003).

[80] B. Liu, L.-B. Fu, S.-P. Yang, and J. Liu, Phys. Rev. A 75, 033601 (2007).

[81] T. Lahaye, T. Pfau, and L. Santos, Phys. Rev. Lett. 104, 170404 (2010).

[82] M. Molina and G. Tsironis, Physica D: Nonlinear Phenomena 65, 267 (1993).

[83] T. Ozawa and H. M. Price, Nature Reviews Physics 1, 349 (2019).

[84] T. Keilmann, S. Lanzmich, I. McCulloch, and M. Roncaglia, Nature communications 2, 1 (2011).

# Chapter 5

# From dimer to trimer

In condensed matter, magnetic fields are responsible for the realization of intriguing physical phenomena like *e.g.* the quantum Hall effect [101, 102], the appearance of fractal energy spectra (Hofstadter's butterfly) [103] or anyons, quasi-particles with fractional statistics [104]. Over the decades, there has been a growing interest towards the simulation of such phenomena in charge neutral settings that allow for a fuller exploration of the physics of charged particles in magnetic fields, for example, without disorder. Such attempts have been performed using *e.g.* cold atoms [105], photons [106], or phonons [107].

A minimal model to investigate the physics of magnetic fields is a triangular plaquette, namely a three-site tight-binding chain with periodic boundary conditions. Notwithstanding this has has long been a configuration of interest [46, 106, 108, 109], to my knowledge a systematic study of the interplay between interactions and magnetic flux on the dynamics of particles in this system has not been performed yet. In this chapter I focus on this interplay, inspired by the possibility of generating a tunable magnetic field through a triangular plaquette with on-site interaction using the mechanical metamaterial discussed already in Section 2.3 and in Appendix B.

The chapter is structured as follows. In Section 5.1 I review the Hamiltonian for a trimer starting from the generic case of a charged boson hopping on a one-dimensional chain with periodic boundary conditions. I will then switch to the semiclassical picture,

and discuss the symmetry properties that I will use to check my numerical results, that are presented and discussed in Section 5.2. In the last part, Section 5.3, I propose the implementation of the feedback for generating the Hamiltonian discussed, and investigate some future research avenues for this ongoing work.

## 5.1   The trimer model

In this chapter, I will use the same notation as in the previous ones: $J$ will again represent the hopping energy, $U$ the control parameter of the on-site interaction, and $\alpha_j$ the amplitude of the wave function on site $j$. Moreover, as I will keep the "condensate jargon", again I will refer to $|\alpha_j|^2 = n_j$ as the population on site $j$, and talk about single particles moving around the plaquette; finally, I will take $\hbar = 1$.

Consider a gas of charged boson hopping on a ring made of $M$ discrete sites (namely a one-dimensional chain with periodic boundary conditions); assuming a magnetic flux is pierced through the ring, the quantum system is described by the Hamiltonian (here $\hbar = 1$):

$$\hat{\mathcal{H}} = \sum_{k=1}^{M} \left[ \frac{U}{2} \hat{\alpha}_k^\dagger \hat{\alpha}_k^\dagger \hat{\alpha}_k \hat{\alpha}_k - \frac{J}{2} e^{i\phi/N} \hat{\alpha}_{k+1}^\dagger \hat{\alpha}_k + \text{H.c.} \right],$$

that is the Bose-Hubbard Hamiltonian [106, 108–110]. Here $\hat{\alpha}_k$ ($\hat{\alpha}_k^\dagger$) is the bosonic annihilation (creation) operator, $U$ and $J$ are the interaction strength and the hopping energy, the index $k$ is considered mod $M$, and $\phi$ is the phase factor acquired by a particle that winds around the plaquette once and is periodic with period $2\pi$.

Using Heisenberg equations of motion and substituting $\langle \hat{\alpha}_k \rangle$ and $\langle \hat{\alpha}_k^\dagger \rangle$ with their expectation values, it is possible to obtain for the considered case of $M = 3$:

$$i\dot{\alpha}_1 = U n_1 \alpha_1 - J e^{i\phi/3} \alpha_2 - J e^{-i\phi/3} \alpha_3,$$
$$i\dot{\alpha}_2 = U n_2 \alpha_2 - J e^{i\phi/3} \alpha_3 - J e^{-i\phi/3} \alpha_1, \qquad (5.1)$$
$$i\dot{\alpha}_3 = U n_3 \alpha_3 - J e^{i\phi/3} \alpha_1 - J e^{-i\phi/3} \alpha_2.$$

A sketch of the system is shown in the left-hand side panel of Fig. 5.1. As in Section 1.2, it is possible to cast this system of equations in the Hamiltonian form $i\dot{\boldsymbol{\alpha}} = \mathcal{H}\boldsymbol{\alpha}$ (note that here $\mathcal{H}$ is not a linear operator anymore), where:

$$\mathcal{H} = \begin{pmatrix} Un_1 & -Je^{i\phi/3} & -Je^{-i\phi/3} \\ -Je^{-i\phi/3} & Un_2 & -Je^{i\phi/3} \\ -Je^{i\phi/3} & -Je^{-i\phi/3} & Un_3 \end{pmatrix} = \mathcal{H}^\dagger. \tag{5.2}$$

Note that from now on, when referring to the "Hamiltonian" I will refer to the Hermitian matrix in Eq. 5.2. In the right-hand side of Fig. 5.1 the energy spectrum of $\mathcal{H}$ for the non-interacting case, $U = 0$, is plotted as a function of the phase [106]. However, it is worth emphasizing that as well as the degeneracies at $\phi = 0, \pi$, the energy levels at phases $\phi = \pi/2$ and $3\pi/2$ are equidistant from each other: this will in turn lead to interesting physical consequences, as I will show in Section 5.2.
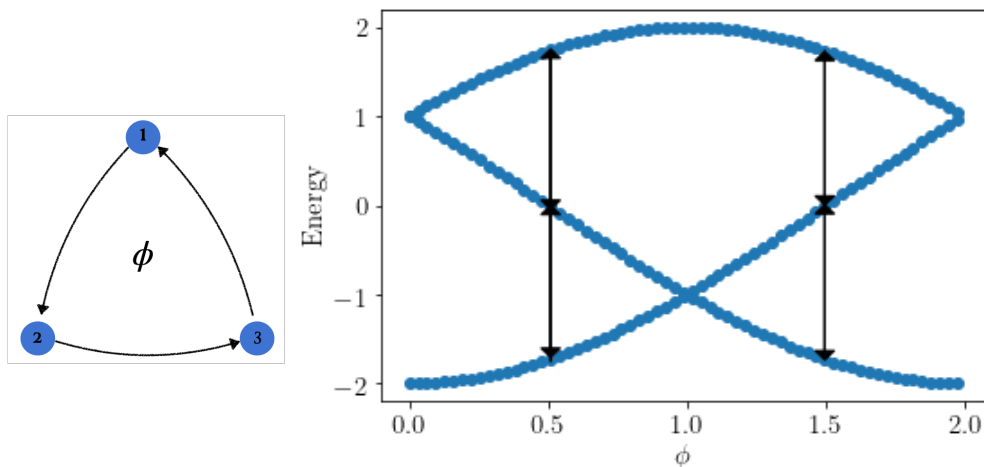


**Figure 5.1:** *Left*: sketch of the 3-site plaquette. *Right*: plot of the spectrum of the Hamiltonian in Eq. 5.2 in the non-interacting case ($U=0$) as $\phi$ (in units of $\pi$) changes from 0 to 2. Note the degeneracies at $\phi = 0$ between the excited states and at $\phi = \pi$ between the ground state and the first excited state. Note also that at $\phi=\pi/2$ and $3\pi/2$ the energies are equally spaced.

Looking at the symmetries of the Hamiltonian in Eq. 5.2, the first thing to observe is that flipping the sign of $J$ is the same as shifting the phase $\phi \to \pi + \phi$. Hence, when looking at quantities that are related to the population (or its expectation value) we expect to find results that are symmetric by flipping the sign of the phase, $\phi$. Moreover, changing

the sign of the interaction, $U \to -U$, corresponds to $\mathcal{H}(\phi) \to -\mathcal{H}(\pi + \phi)$, that simply flips the energy landscape and shifts the phase factor. This means that in order to see what happens to the system when the magnetic flux pierced is $\phi$ and interaction switches from attractive to repulsive (or vice versa), it is sufficient to look at the results for $\pi + \phi$. These symmetries combined with the literature results in Refs. [46, 106, 108, 109], allow for checking the numerical results that are presented in the following section.

## 5.2   Numerical results

The two primary tools of investigation of the results were the Inverse Participation Ratio (IPR) and the chiral current, that I will describe here in turn. For a normalized $N$-component state $\boldsymbol{\alpha} = (\alpha_1, \alpha_2, \ldots \alpha_N)$, the IPR as defined in Refs. [111, 112] is:

$$\text{IPR} = \frac{\sum_{i=1}^{N} |\alpha_i|^4}{\left(\sum_{i=1}^{N} |\alpha_i|^2\right)^2} = \sum_{i=1}^{N} n_i^2; \tag{5.3}$$

this constitutes a measure of the localization of the wave packet over the $N$ sites of the system. Practically speaking if the wave packet is fully localized on a single site it is straightforward to see that $\text{IPR} = 1$, whereas if on each site the amplitude of the wave packet is $\alpha_j = 1/\sqrt{N}$ (equally spread wave packet), $\text{IPR} = 1/N$. As we are dealing with a trimer, $N = 3$. In this chapter I will make use of the time average of the inverse participation ratio, $\langle \text{IPR} \rangle$, that I define as:

$$\langle \text{IPR} \rangle = \left( \frac{1}{T} \int_0^T \text{IPR} \, \mathrm{d}t \right)^{-1} = \langle n_1^2 \rangle + \langle n_2^2 \rangle + \langle n_3^2 \rangle, \tag{5.4}$$

where $\langle \bullet \rangle$ represents the time average of $\bullet$. As it involves expectation values of the population, we expect that $\langle \text{IPR} \rangle$ is symmetric with respect to $\phi = \pi$, and that flipping the sign of the interaction results in shifting $\phi$ by $\pi$.

As for the chiral current $I_{\text{ch}}$, this has been used in Refs. [106, 108, 109] to investigate the chirality of the system. In the semi-classical case under examination here, it is defined

as:

$$I_{\text{ch}} = \frac{1}{2} \sum_{j=1}^{N} I_j, \quad I_j = -iJ(e^{i\phi/3} a_j^* a_{j+1} - e^{-i\phi/3} a_{j+1}^* a_j) \tag{5.5}$$

where again, given the cyclic nature of the system, modulo 3 arithmetic holds when going $3 \rightarrow 1$; the 1/2 factor is to avoid double counting. It is expected that if time reversal symmetry $\mathcal{T}$ is preserved, chiral current yields zero [106]: this is easy to understand, since $\mathcal{T} : i \rightarrow -i$. Moreover, we expect this quantity to be anti-symmetric with respect to $\pi$ since flipping the sign of $J$ corresponds to shifting $\phi \rightarrow \pi + \phi$.

Having stated all the symmetries of the system and of the main observables, and having clarified the parameters of the simulations, we can now look into the outcome of the numerics. Once initialized on a single site[1], $\boldsymbol{\alpha}(t=0) \equiv \boldsymbol{\alpha}_0 = (1,0,0)^{\text{T}}$, the wave function was let to evolve using the system of equations (5.1), for a fixed value of the interaction strength, $U$ measured in units of $J$, and a fixed phase $\phi$. The total time of the simulation was initially set to $T = 30J$, and, since most of the investigated quantities involve time averages, I also performed longer simulations, $T = 80J$, in order to check if anything was being left out by an early stop. As this was not the case, I will only show the plots for the shorter time simulations unless otherwise stated. In all cases, integration was performed so that the initial value of the population $n(0) = 1$ did not change throughout the whole process by more than 1%.

First, I decided to map the parameter space $\{U, \phi\}$ with the averages of the IPR and the chiral current; the results are shown in Fig. 5.2.

These plots show a number of interesting features that will be analyzed in further detail later in this section. Focusing on the $\langle \text{IPR} \rangle$ plot, the first thing to note is the symmetry with respect to $\phi = \pi$, as expected from the aforementioned discussion about the symmetries of the expectation values of the population. In addition to that:

1. for strong interactions, there is a darker area; that means that the system is localized on a single site, $\langle \text{IPR} \rangle \approx 1$. This area of the parameter space will be referred to as

---

[1] Given the structure of the Hamiltonian, the choice of the initial site should have no influence on the final result; this is another check for the goodness of the numerics that was not mentioned in the previous section as it is an obvious one.
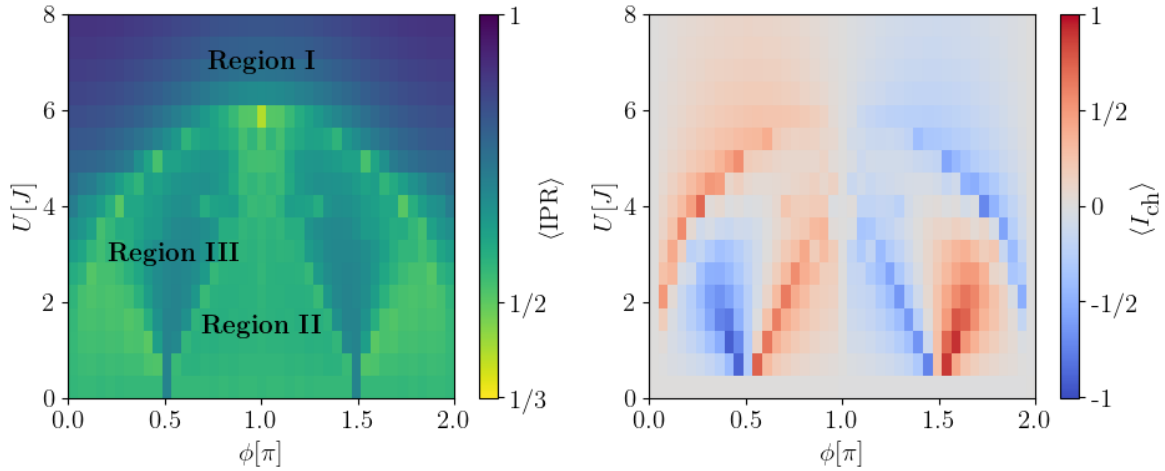
**Figure 5.2:** Plot of the $\langle \text{IPR} \rangle$ (left panel) and $\langle I_{ch} \rangle$ (right panel) for $T = 30J$, both of them showing symmetry ($\langle \text{IPR} \rangle$) and anti-symmetry ($\langle I_{ch} \rangle$) with respect to $\phi = \pi$, as expected. In the $\langle \text{IPR} \rangle$ plot three regions can be distinguished: *I* highly localized with small current, *II* non-localized with (in general) nonzero current and *III* highly localized with nonzero current.

*Region I.*

2. there is a dome shaped area below Region I, where the wave packet on average is spread over two sites: this is what will be called *Region II*. Note that at its apex, at $U \approx 6J$ and $\phi = \pi$, the system is highly delocalized;

3. there are two lung-shaped[2] regions of localization for the wave packet inside region II, that extend down to the non-interacting case; this region of the parameter space is going to be labelled as *Region III*;

Similarly, the chiral current shows anti-symmetry with respect to $\phi = \pi$ (namely $I_{ch}(\phi) = -I_{ch}(-\phi)$), as expected. Moreover:

1. at $\phi = 0, \pi$ the Hamiltonian is $\mathcal{T}$-symmetric, hence the chiral current is zero;

2. in the non-interacting case, the initial state is an equal superposition of the three eigenstates of the Hamiltonian, whose chiral currents add up to zero (*c.f.* Appendix C), hence the net zero chiral current;

3. In region III the current is close to zero, as expected from a localized wave packet.

---

[2]So far this Rorschach test has yield 100% of people seeing this plot agree on the lung shape. Including my mother who, puzzled, asked whether (and why) I was looking at a chest X-ray.

In order to better understand the behavior of the system in the three above-mentioned regions, it is worth looking at the time average of the population on each of the sites, $\langle n_j \rangle$, $j = 1, 2, 3$, shown in Fig. 5.3. The first feature that we observe is that the panels for $\langle n_2 \rangle$ and $\langle n_3 \rangle$ look very similar; in fact they are specular, as a signature of chirality. This is due to the fact that the system of three equations in Eq. 5.1 with the initial condition $(1, 0, 0)^{\mathrm{T}}$ can be cast into a system of two equations [46], in which the two initially-empty sites behave as a single "pseudo-site". The combined interpretation of Figs. 5.2 and 5.3
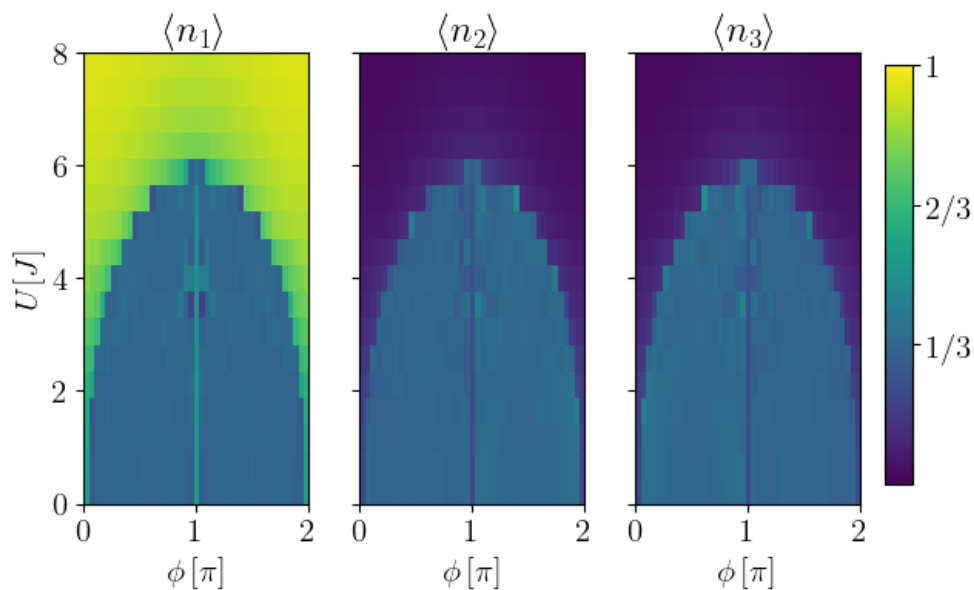


**Figure 5.3:** Plot of the time average of the population on each site, $\langle n_1 \rangle$, $\langle n_2 \rangle$, $\langle n_3 \rangle$ from the left to the right, respectively, for $T = 30J$. Note that all the population is, on average, at the starting site when parameters are in region I (localization regime); there also is a peak of $\langle n_1 \rangle$ around $\phi = \pi$ (as opposed to the valleys in $\langle n_2 \rangle$ and $\langle n_3 \rangle$) showing the dimer-like behavior described in the text.

will guide now the characterization of the above-mentioned three regions.

## 5.2.1 Region I

In all the panels in Fig. 5.3, the area of parameter space corresponding to region I stands out clearly. In fact, there $\langle n_1 \rangle \approx 1$ and consequently both $\langle n_2 \rangle$ and $\langle n_3 \rangle \approx 0$; combining this and the fact that the $\langle \mathrm{IPR} \rangle$ shows a strong localization (namely $\langle \approx 1 \rangle$) and the chiral current is small ($\langle I_{\mathrm{ch}} \rangle \approx 0$), allows us to state that in region I self-trapping takes

place [46], in analogy with what is observed for strong interactions in the dimer case, *c.f.* Chapter 1.2. These intuitions on the dynamic behavior of the system in region I can be
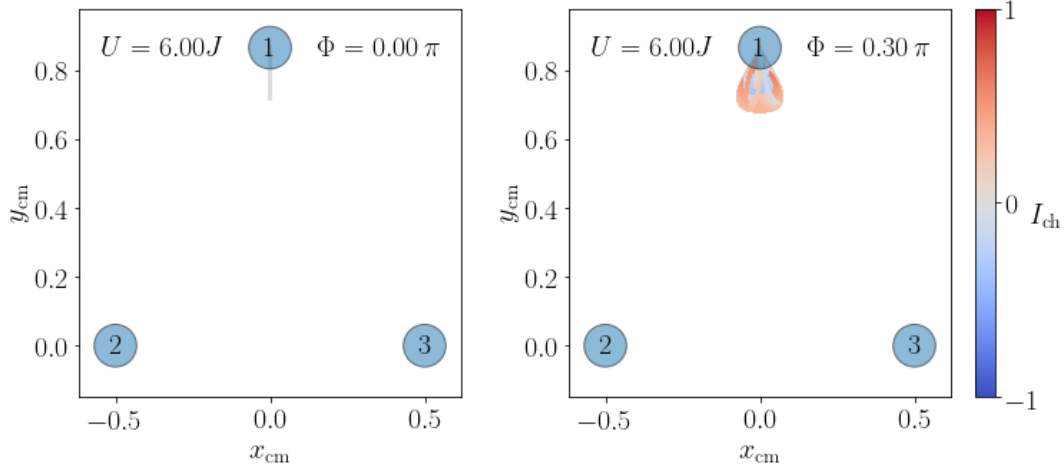


**Figure 5.4:** Plots of the trajectory of the center of mass for values of the parameters picked in Region I, and specified in each plot. Color represents the value of the current. Note that the wave packet never leaves the neighborhood of the site on which it is initialized.

verified by looking at plots of the position of the center of mass of the wave packet in time. Its coordinates can obtained as:

$$x_{\text{cm}} = \frac{1}{2}(n_3 - n_2) \qquad y_{\text{cm}} = \frac{\sqrt{3}}{2}n_1,$$

and the results are shown in Fig. 5.4. Those plots show a sequence of points (close enough to look like a continuous line) each representing the instantaneous position of the center of mass, and color coded according to the value of the current at that specific instant of time: red means counterclockwise circulation, conversely blue means clockwise circulation. The closer the points to the center of the plaquette, the more the wave packet is spread over the three sites; if the center of mass lies on the line connecting two sites, it means that the wave packet is spread only over those two sites. When parameters are chosen from region I the center of mass never leaves the neighborhood of the initial site, and the chiral current oscillates so that it averages to small values, as stated previously.

## 5.2.2 Region II

In the plots of Fig. 5.3, regions II and III do not show up as clearly as region I. Furthermore, the fact that in those areas $\langle n_j \rangle \approx 1/3$ for all the three sites, means that on average the wave packet visits all the sites for the same amount of time. Moreover, the $\langle \text{IPR} \rangle$ averages to $1/2$, that is to say the population occupies on average two sites at a time. In order to better understand what this means, it is worth looking at the plot of the center of mass in Fig. 5.5.
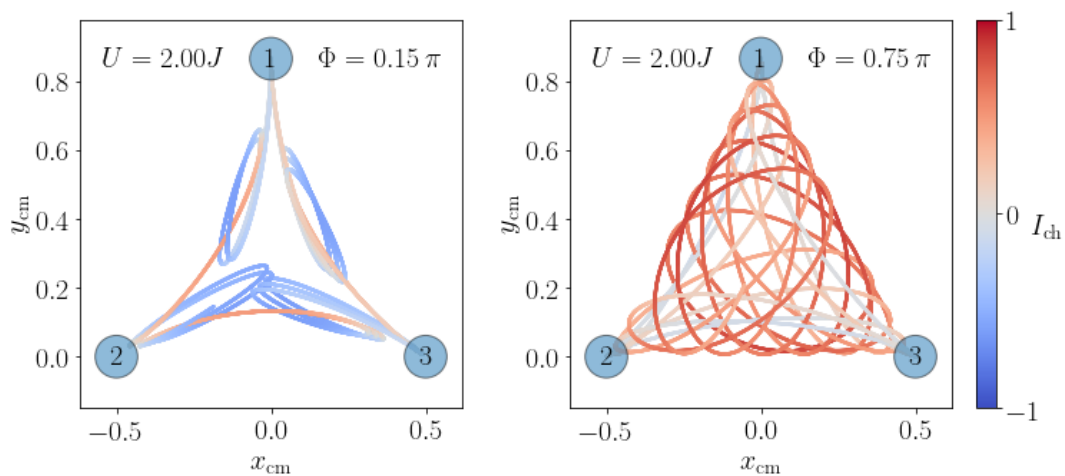


**Figure 5.5:** Plots of the trajectory of the center of mass for values of the parameters picked in Region II, and specified in each plot. Note the Rabi-oscillations and the rotating dimer-like behavior, with two sites behaving as a single pseudo-site.

In this case, the center of mass experiences a dimer-like behavior, in which it oscillates between one site and the other two, that collectively behave as a single pseudo-site. Moreover, from Fig. 5.5 it is clear that this configuration rotates, that is to say all the three sites get to cover the role of the fully occupied site. An interesting qualitative difference between the plots showed in Fig. 5.5 is that for values of the phase $\phi < \pi/2$, the wave packet spends less time being spread over the three sites (left panel), whereas for values of $\phi > \pi/2$ Rabi-oscillations involve more of such spreading (right panel).

Conversely, at $\phi = 0$ and $\pi$ sites 2 and 3 remain combined and always play the role of the pseudo-site. Here, we can investigate the behaviour of the system with the help of the results in Ref. [46]. In this case, the plots of the center of mass trajectories displayed in
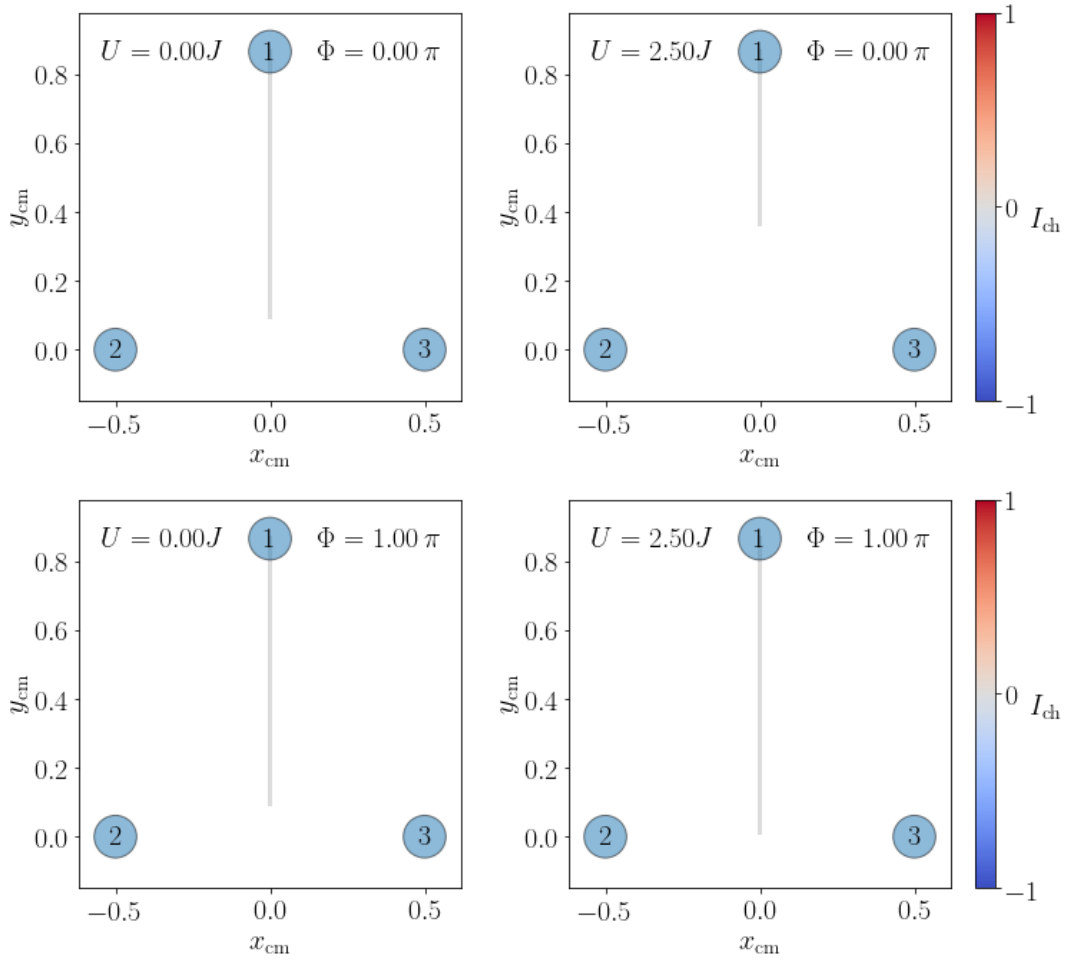
**Figure 5.6:** Plots of the trajectory of the center of mass for values of the parameters picked in Region II at $\phi = 0$ (top row) and $\phi = \pi$ (bottom row) at different values of the interaction specified in each plot. As the system is $\mathcal{T}$-symmetric, current is zero (hence the color does not change). Note that the system behaves as if it was a dimer due to the symmetry of the equations.

Fig. 5.6, exhibit the above-mentioned dimer-like behavior: the system is either localized on a single site, or it is equally spread over the other two, undergoing Rabi-like oscillations; moreover, note that since at $\phi = 0, \pi$, the Hamiltonian is $\mathcal{T}$-symmetric, the net current is zero. It is interesting to note that as in this regime the system behaves like a dimer, for stronger interactions it shows a transition from Rabi-like oscillations to self-trapping, as also described in Ref. [46]. There, the authors investigate the transition from Rabi-like oscillations to self-trapping solving the system in Eq. 5.1 exactly. This is done by considering the fact that the second and third equations of the system (5.1) are identical, and with the same initial conditions. In Ref. [46], the authors obtain for the trimer case

that the transition from Rabi-like oscillations to self-trapping behaves in two different ways depending on the mutual sign of $U$ and $J$, as also shown in Fig. 5.7. If both $U$ and
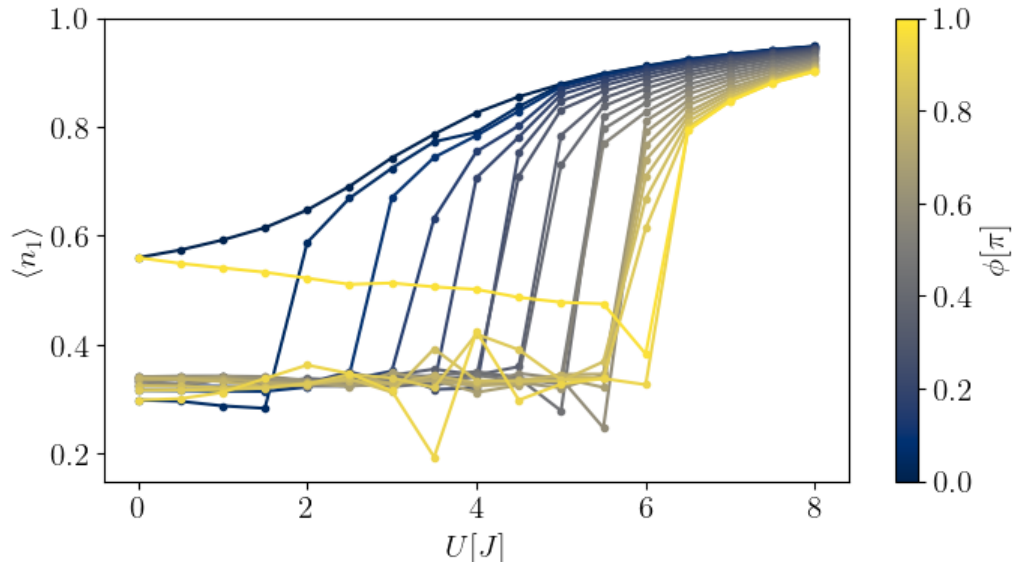


**Figure 5.7:** Plot of the average value of the population on the starting site as a function of the interaction strength, for different values of $\phi$ (color scale) from 0 (darker) to $\pi$ (lighter); lines are a guide to the eye. The behavior for $\phi=0, \pi$ is qualitatively explained in the main text. The difference in the value of $\langle n_1 \rangle$ for $U=0$ is explained in Appendix C.

$J$ have the same sign, there is a sharp transition to the self-trapping regime as $U$ grows larger, at $U=6J$; otherwise, the transition is smooth. Note that in this case the transition happens at a much higher value of the interaction strength than the dimer case. This means that, in order to see an abrupt transition to localization in a three-site plaquette, not only one has to choose attractive interactions, but it also has to be much stronger than the dimer case [46]. In Fig. 5.7 the ratio $U/J$ shows this change of sign at $\phi=\pi$; this can be obtained looking at the Hamiltonian in Eq. 5.2, and considering that it is periodic, $\mathcal{H}(\phi)=\mathcal{H}(\phi + 2\pi)$, so that:

$$-Je^{\pm i\pi/3}=-Je^{\pm i\pi}=J.$$

Finally, note that in Fig. 5.7 also values of $\phi$ between 0 and $\pi$ are considered. Note that for these values of the phase pierced through the plaquette, the average of the population on the initial site has an interesting behavior that might be worth investigating.

### 5.2.3 Region III

Let us finally turn to region III. So far we have found that region I and II of parameter space display a behavior that we have discussed also in the dimer case, namely Rabi-like oscillations and self-trapping. These regimes are characterized by weak localization and non-zero current, and strong localization with small current respectively. In the plots of Fig. 5.2, on the other hand, region III stands out as a region where there is both strong localization, and a non-zero current. As we are investigating a system of non-linear Schrödinger equations a natural suspicion is that the wave packet is behaving like a soliton: a localized wave packet that circulates around the plaquette [108, 109].

Solitons are usually described as waves that propagate at a constant velocity preserving their shape [113]. These properties, due to the mutual cancellation of non-linearity and dispersion effects [113], are actually one of the reasons why solitons have attracted the interest of scientists also in view of possible applications, as Refs. [114, 115] show.

Looking at the plot of the trajectory of the center of mass in Fig. 5.8 it is clear that, independently of the value of the interaction strength, the trajectory of the center of mass lies on an (almost) straight line connecting two sites. This means that the transfer of the population from one site to the other happens in a direct way, *i.e.* the whole population (or at least a large part of it) moves from one site to the other without going through the third site. Note that in the left panel of Fig. 5.8, although the wave packet is localized and winds around the plaquette, in this case one cannot talk about a soliton, since that panel represents the non-interacting regime. Moreover, notwithstanding the net current is zero, the winding is evident. I suspect that what happens is the following: as analytically proved in Appendix C, in the non-interacting regime, the initial state is obtained as an equal superposition of the three eigenstates, whose characteristic currents add up to zero, *c.f.* Fig. C.2. As a consequence, the eigenstate with the largest current associated is the one contributing to the circulation of the center of mass, whereas the remaining two contribute to the net zero current.

This circulation of the wave packet inside the plaquette suggests that the winding of
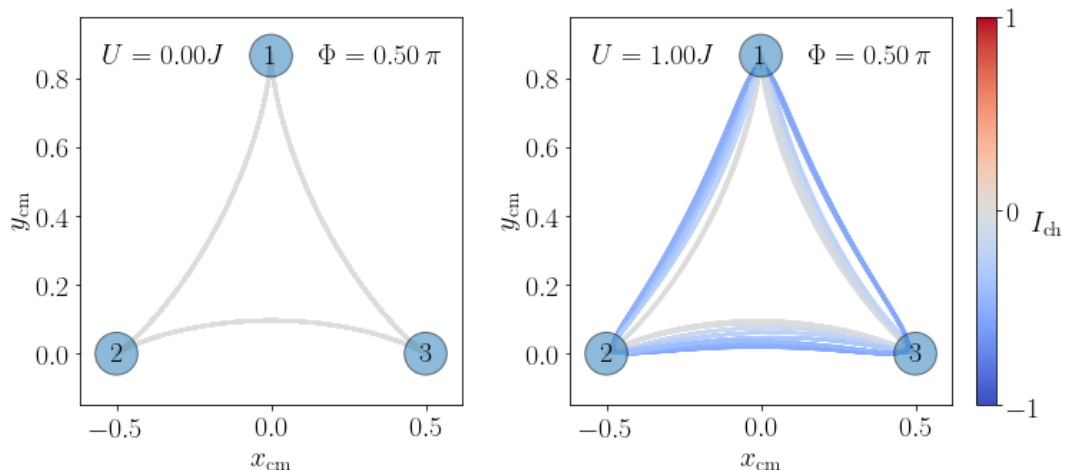
**Figure 5.8:** Plot of the trajectory of the center of mass for different sets of values within region I, specified in each plot. Color represents the value of the current. The center of mass moving on a straight line from one site to the other means direct population transfer from one site to the other, like a soliton on a ring.

the center of mass around the center of the plaquette (that represents the point at which $n_1 = n_2 = n_3$) can be useful to characterize this region. In the frame of reference whose origin lies at the center of the plaquette, the coordinates of the center of mass are $(x, y)$; as we are interested in the winding, it is convenient to consider the polar coordinates in this frame of reference, so that $x = r \cos \theta$ and $y = r \sin \theta$, where $r$ is the distance from the center and $\theta$ the polar angle. We now consider the winding given by:

$$w_{\text{com}} = \left[ \frac{1}{2\pi} \int_0^T \frac{\mathrm{d}\theta}{\mathrm{d}t} \mathrm{d}t \right],$$ (5.6)

where $[\bullet]$ denotes the integer part of $\bullet$ and $\theta = \text{atan}(y/x)$. Taking the derivative of the polar angle leads to $\dot{\theta} = (x\dot{y} - \dot{x}y)/(x^2 + y^2)$. Discretizing this quantity means that at each step labelled by $(n)$, the angle $\theta$ changes by an amount:

$$\Delta\theta^{(n)} = \cos\theta^{(n)}(\sin\theta^{(n+1)} - sin\theta^{(n)}) - (\cos\theta^{(n+1)} - \cos\theta^{(n)})\sin\theta^{(n)}$$

$$= \cos\theta^{(n)}\sin\theta^{(n+1)} - \sin\theta^{(n)}\cos\theta^{(n+1)}$$

$$= \sin\left(\theta^{(n+1)} - \theta^{(n)}\right).$$

A sketch of both the frame of reference of the plaquette and the resulting winding around

its center are shown in Fig. 5.9
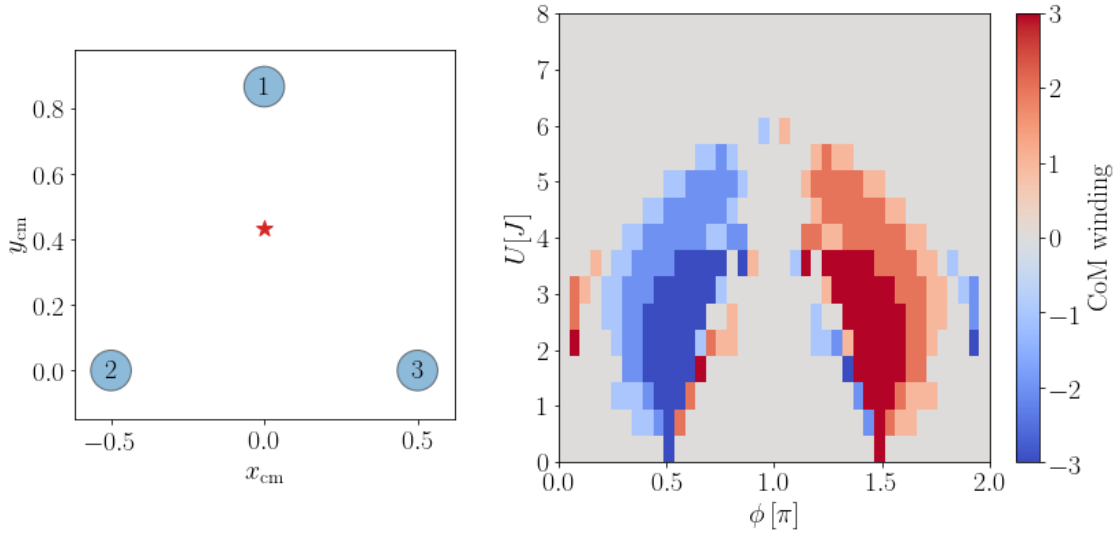


**Figure 5.9:** *Left:* Cartoon of the frame of reference with the origin in the center of the plaquette. *Right:* Plot of the winding of the trajectory of the center of mass around the center of the plaquette. It characterizes very well the regime of direct population transfer in region III.

In this section, I have showed how to characterize the three regions of parameter space using the $\langle \text{IPR} \rangle$ , and the winding around the center of mass of the plaquette. In the next one, I will explain how such a model could be obtained using coupled harmonic oscillators.

## 5.3   Experimental realization and future work

In this final chapter, I presented a minimal model for the exploration of the interplay between interactions and synthetic magnetic fields pierced through a plaquette. With the help of known results from the literature, I set up numerical simulations that yield the known results from Refs. [46,106,108,109], and then investigated so-far unexplored regions of the parameter space. I found that three regimes can be spotted, two of them having an analogy with the dimer case: in region I the time average of the IPR yields a value close to 1, and the chiral current yields small values, meaning that the wave packet is self-trapped in the initial state. In region II the system tends to be more spread, as $\langle \text{IPR} \rangle$ lies around 1/2; in this case I considered the possibility of having the system behaving as a dimer in which two sites behave collectively as one, also due to the symmetries of the

system whose equations can be reduced to the equations for a dimer [46]. This behavior reminds us of the Rabi-like oscillations reviewed in Section 1.2. Finally, in region III the wave packet has a soliton-like behavior, as it looks very well localized on a single site while winding around the plaquette. It is, in fact, the winding of the center of mass of the wave packet around the center of the plaquette that characterizes nicely this region of parameter space, *c.f.* Fig. 5.9.

Clearly, in order to prove that it is a soliton, further investigations are needed. One of the first things to check, would definitely be whether the width of the wave packet changes during the evolution. If on the one hand some of the results in Refs. [108, 109] encourage this view, I am puzzled by the fact that the highly localization regime goes down to the non-interacting regime (*c.f.* the bottom row of Fig. 5.2). Another thing that would be worth investigating is the bright spot at $(\phi, U) \approx (\pi, 6J)$ in the plot of the $\langle \text{IPR} \rangle$ where a delocalization peak appears. Finally, it would be of interest investigating the qualitative difference between the plots in Fig. 5.5 when the parameters have been chosen right outside of region III, from opposite sides.

These results have to undergo the experimental check. As soon as the third harmonic oscillator will be in place, the theory developed in Appendix B [21] can be straightforwardly generalized to reproduce this model. In this case, in fact, the feedback that allows for the simulation of both the complex hopping and the on-site interaction is described in detail, and in the RWA it yields:

$$
F_{kj}^{\text{RWA}} \alpha_j = \begin{cases} \sqrt{2\omega} U |\alpha_k|^2 \alpha_k & \text{for } k = j; \\ \sqrt{2\omega} J e^{i\phi_{jk}} \alpha_j & \text{for } k \neq j \end{cases}
$$

where $\phi_{jk} = -\phi_{kj} = \phi$, $U$ is the interaction strength and $\omega$ the dominant frequency. However, at the state of the art, the setup in Appendix B [21] probably lacks the necessary definition to observe all the features of the plot in Fig. 5.2. This is due to unwanted uncontrolled non-linearities that might add up when the system has to be simulated for such a long time (the plots presented are obtained for $T = 30J$). In any case, once this

issue is tackled, the exploration of the interplay of magnetic field and interactions could be straightforwardly broadened to larger systems.

# Chapter 6

# Conclusion

In this thesis I have started with a review of the known results for systems described by non-Hermitian matrices, where it has been observed that these exhibit real spectra under anti-linear symmetry conditions, the simplest of which to implement is $\mathcal{PT}$-symmetry. I also reviewed the concept of exceptional points, namely points in parameter space where the spectral degeneracy is accompanied by a coalescence of the eigenvectors, which is a characteristic of non-Hermitian Hamiltonians. In contrast to the degeneracy points for Hermitian Hamiltonians, these behave as *imaginary* fictitious monopoles generating a field whose strength grows with the distance. In order to investigate the dynamical features of non-Hermitian Hamiltonians, I introduced a class of minimal 2-site models, called dimers, in which non-Hermitianity was introduced by adding on-site gain and loss and by making the hopping energy asymmetric, in turn. Finally, I introduced the concept of mechanical metamaterials, a flexible and powerful platform that allowed us to simulate the dimer models mentioned, and experimentally explore their dynamics.

In the second chapter, considering the dynamics of a non-Hermitian Hamiltonian with time-dependent parameters, I gave a formulation for the geometric factor $\gamma_n^{\mathrm{G}}$ and observed that, as opposed to its Hermitian counterpart, not only it is a complex number, but its imaginary part is gauge invariant also along open paths in parameter space. I then focused on $\mathcal{PT}$-symmetric systems in which case the adiabatic theorem holds with the

same hypotheses as the Hermitian quantum mechanics: away from spectral degeneracies and for slowly varying Hamiltonians. The consequence of the imaginary part of the geometric factor is the exponential change of the amplitude of the wave function during the evolution of the system in time along an open path in parameter space. In order to probe this result, I considered a non-Hermitian model with balanced on-site gain and loss, and numerically investigated the results theoretically predicted. This $\mathcal{PT}$-symmetric model is widely studied in theory and experiments (*e.g.* in optics and cold atoms setups). Letting the system evolve in time, numerics verified the theoretical predictions made: the square modulus of the wave function shows exponential growth while getting closer to the $\mathcal{PT}$-breaking line and conversely shrinks when moving away from it, also along open paths. Closing the loop in both clockwise and counterclockwise directions, showed two features: the exact specular results, firstly, proves that the factor acquired by the system is actually geometric. Secondly, at the end of the loop, the norm of the system goes back to its initial value, as a consequence of the fact that the trajectory does not enclose any region of broken $\mathcal{PT}$-symmetry.

With this outcome in mind, we joined an experimental group working on the realization of a mechanical metamaterial, and proposed the experimental realization of a $\mathcal{PT}$-symmetric Hamiltonian to investigate the effects of the geometric factor. The experimental platform used is presented in Appendix B, and is made of two harmonic oscillators coupled only via a contactless feedback; we decided to take advantage of its great tunability and flexibility, and experimentally implemented a less commonly realized two-site Hamiltonian, namely the Hatano-Nelson dimer. In Chapter 3 I display the results of a real time measurement of the geometric phase in this non-Hermitian model reproduced using a mechanical metamaterial in the form of a paper. Once the $\mathcal{PT}$-unbroken region was identified, we started exploring the dynamics of the energy (a proxy for *e.g.* the population of a mean field Hamiltonian describing Bose-Einstein condensates or for the intensity of light in a coupled waveguide experiment), and experimentally verified the geometric nature of $\gamma_n^{\mathrm{G}}$ by simulating the adiabatic evolution along closed paths in parameter space

that do not encircle a $\mathcal{PT}$-broken region. Next we introduced a third parameter in the Hamiltonian, and generated closed paths in the three-dimensional parameter space that encircled the $\mathcal{PT}$-broken region. In this case, as expected from the theoretical results, the change in population with respect to its initial value is proportional to the "non-Hermitian flux" generated by the enclosed $\mathcal{PT}$-broken region. This work paved the way towards the exploration of the interplay between non-Hermitianity and interactions, that I explored in Chapter 4.

Also the fourth chapter is presented in the form of a paper, where we reviewed the known dynamical features of the Hatano-Nelson model, and then introduced asymmetric interaction-dependent hopping terms, supporting our numerical and theoretical results with experimental data. In order to gain insight into the interacting Hatano-Nelson model, we also considered a version of it in which the interactions are normalized. The study of its fixed points and of their behavior, allowed for an understanding of an intermediate regime where, depending on the initial conditions, the system showed either stable (with Rabi-like oscillations) or unstable dynamics (with exponential explosion of the population) for a given set of parameters. With this work we lay the foundations for exploring more exotic interactions and systems, using a larger number of harmonic oscillators so that larger lattices could be explored.

A theoretical study investigating the interplay between interactions and magnetic fields is the subject of the fifth (and last) chapter of this thesis. There I consider a minimal model for the exploration of such effects, namely a three-site chain with periodic boundary conditions. I then consider complex hopping terms such that a particle hopping around the triangular plaquette acquires a phase factor; to such a model I add on-site interactions, to explore the combination of these two effects. In order to analyze the results, I used the Inverse Participation Ratio (IPR), that is a measure of the localization of the wave packet, and the chiral current, a measure of the chirality of the system. Analyzing the outcome of the numerical simulations, allowed me to spot three regions of the parameter space. Further investigations led me to state that in two of them, the dynamics of the trimer

resembles the behavior of the dimer with self-trapping and the Rabi-like oscillations, respectively. The third region, where the wave packet is highly localized and shows non-zero chiral current suggests that the wave packet behaves like a soliton circulating around the plaquette. Next, I introduced a new quantity, the winding of the center of mass around the center of the plaquette, that seems to support this intuition, but further analysis is needed in order to confirm this result. Finally, I obtain a formulation of the feedback to be generated and applied to a set of three oscillators in order to experimentally realize this model in the mechanical oscillator discussed, and discuss some future directions for this project to take in the realm of the simulation of topological phenomena.

This thesis paves the way to a number of interesting future research directions. Looking at the short time-scale, investigating the interplay of interactions with synthetic magnetic brought to the observation of a localized wave packet that winds around a plaquette already looking at a minimal model. It would be interesting looking at the existence of such a magnetic soliton using other types of interactions, or maybe density dependent gauges.

Furthermore, the contribution of the non-Hermitian geometric factor and its gauge-invariance along open paths constitute the first step towards the implementation of this effect in real life (*e.g.* sensing), alongside with the vast number of applications of $\mathcal{PT}$-symmetric Hamiltonians (unidirectional invisibility, anomalous wave transportation and guiding). Exploring the interplay of $\mathcal{PT}$-symmetry and interactions is definitely tempting, as $\mathcal{PT}$-symmetric systems are dissipative systems with real spectra and interactions allow the system to dynamically break the $\mathcal{PT}$-symmetry, or even observing stable nonlinear modes in the $\mathcal{PT}$-broken regime. Moreover, notwithstanding the mechanical metamaterial introduced has just seen the light it has already proved its tunability and flexibility in investigating the parameter space of a non-Hermitian Hamiltonian. As soon as this will be scaled up in number, it will be interesting to investigate even more exotic interactions like long distance interactions or density dependent gauges to name a few, together with effects related to the breakdown of the bulk-boundary correspondence, like the so-called non-

Hermitian skin effect and other anomalous dynamical features. Such phenomena could then be brought to a smaller length-scale once lattices of coupled harmonic oscillators are scaled down in size.

# Appendix A

# Hermitian Geometric phase

In this Appendix, I derive a general formulation of the geometric phase in the Hermitian case, following Refs. [3, 4, 116]. After that I will highlight the parallelism between its effects and the physics of magnetic fields following Refs. [4, 117].

Consider a system described by the time-dependent Hamiltonian $\mathcal{H}$, which we shall assume has a non-degenerate energy spectrum at all times. Given the instantaneous orthonormal eigenbasis at time $t$, $\{|\phi_n(t)\rangle\}$ , the generic state can be written as:

$$|\psi(t)\rangle = \sum_n a_n(t)|\phi_n(t)\rangle, \tag{A.1}$$

where the coefficients of the expansion $a_n(t)$ are to be determined. By direct substitution of Eq. A.1 into the time-dependent Schrödinger equation $i\frac{\partial}{\partial t}|\psi(t)\rangle = \mathcal{H}|\psi(t)\rangle$, where $\hbar=1$, one obtains:

$$i\sum_n \left[\dot{a}_n(t)|\phi_n(t)\rangle + a_n(t)\frac{\partial}{\partial t}|\phi_n(t)\rangle\right] = \sum_n a_n(t)\varepsilon_n(t)|\phi_n(t)\rangle. \tag{A.2}$$

Projecting this result on $\langle \phi_k(t)|$ and rearranging the terms:

$$
\begin{aligned}
\dot{a}_k(t) &= -ia_k(t)\varepsilon_k(t) - \sum_n a_n(t) \langle \phi_k(t)| \frac{\partial}{\partial t} |\phi_n(t)\rangle \\
&= a_k(t)\left[ -i\varepsilon_k(t) - \langle \phi_k(t)| \frac{\partial}{\partial t} |\phi_k(t)\rangle \right] - \sum_{n \neq k} a_n(t) \langle \phi_k(t)| \frac{\partial}{\partial t} |\phi_n(t)\rangle ,
\end{aligned}
\tag{A.3}
$$

where in the second equation I simply extracted from the sum the term with $n = k$. Let us focus on the expectation value in the last term; by taking the time derivative of the eigenvalue equation, this can be re-written as:

$$
\langle \phi_k(t)| \frac{\partial}{\partial t} |\phi_n(t)\rangle = \frac{1}{\varepsilon_n - \varepsilon_k} \langle \phi_k(t)|\dot{\mathcal{H}}|\phi_n(t)\rangle ;
\tag{A.4}
$$

this term can be neglected under the hypotheses of the adiabatic theorem, which states that a system prepared in an eigenstate of a slowly varying Hamiltonian, will remain in this eigenstate during the time evolution [3, 4, 116]. We then obtain that in this case:

$$
\dot{a}_k(t) \approx -ia_k(t)\varepsilon_k(t) - a_k(t) \langle \phi_k(t)| \frac{\partial}{\partial t} |\phi_k(t)\rangle ;
$$

with the (reasonable) initial condition that $a_k(0) = 1$, we can integrate this equation to obtain:

$$
a_k(t) = e^{i\gamma_k^{\mathrm{D}}} e^{i\gamma_k^{\mathrm{G}}} ,
$$

where I defined two phases:

$$
\gamma_k^{\mathrm{D}} = -\int_0^t d\tau \, \epsilon_k(\tau),
\tag{A.5}
$$

and:

$$
\gamma_k^{\mathrm{G}}(t) = i \int_0^t d\tau \, \langle \phi_k(\tau)| \frac{\partial}{\partial \tau} |\phi_k(\tau)\rangle .
\tag{A.6}
$$

The quantity in Eq. A.5, is known as dynamic phase (hence the superscript), and it arises from the time evolution of a state under the operator $e^{-i\mathcal{H}t}$; the other phase factor is a feature of the time-dependent Hamiltonian that I will investigate now.

In case the time dependence of the Hamiltonian $\mathcal{H}$ takes place via some parameters, $\mathbf{P}(t)$, $\gamma_k^{\mathrm{G}}$ can be written as:

$$\gamma_k^{\mathrm{G}}(t) = i \int_{P(0)}^{P(t)} \mathrm{d}\mathbf{P} \cdot \langle \phi_k(\mathbf{P}) | \boldsymbol{\nabla}_{\mathbf{P}} | \phi_k(\mathbf{P}) \rangle, \qquad (A.7)$$

that is a line integral to be performed in parameter space along the path connecting $\mathbf{P}(0)$ and $\mathbf{P}(t)$, the initial and final point of the time evolution respectively. Note that the integrand is gauge dependent: as $|\phi_k(\mathbf{P})\rangle \to e^{i\zeta(\mathbf{P})} |\phi_k(\mathbf{P})\rangle$, then the integrand is shifted by $-\boldsymbol{\nabla}_{\mathbf{P}}\zeta(\mathbf{P})$. This means that the overall phase $\gamma_k$ will be affected by an additional term $\zeta(\mathbf{P}(0)) - \zeta(\mathbf{P}(t))$. As there is no restriction in the choice of the path, one can always choose a gauge $\zeta(\mathbf{P})$ such that the accumulated phase along the path connecting $\mathbf{P}(0)$ and $\mathbf{P}(t)$ is cancelled out.

However, if the evolution takes place on a *closed loop* in parameter space, $\mathcal{C}$, things change. In fact, the choice made on the phase of the eigenstates implies that $\zeta(\mathbf{P})$ is single-valued; this in turn means that $\mathbf{P}(0)$ and $\mathbf{P}(T)$ ($T$ being the time needed to go around a loop in parameter space) differ by an integer multiple of $2\pi$, and –more importantly– this quantity *cannot be gauged away* [81], hence this is a physical observable. The gauge-invariant physical quantity

$$\gamma_k^{\mathrm{G}} = \oint_{\mathcal{C}} \mathrm{d}\mathbf{P} \cdot \boldsymbol{\mathcal{A}}_k(\mathbf{P}), \quad \boldsymbol{\mathcal{A}}_k(\mathbf{P}) \doteq i \langle \phi_k(\mathbf{P}) | \boldsymbol{\nabla}_P | \phi_k(\mathbf{P}) \rangle, \qquad (A.8)$$

is a geometric phase (hence the G in the subscript) as it only depends on the geometry of the path traced in parameter space, and not on how fast he system evolves [3, 4, 81, 116]. This factor is known as *Berry phase*, while $\boldsymbol{\mathcal{A}}_k(\mathbf{P})$ is called *Berry vector potential* or *Berry connection* [3, 4, 116]. [1] Given the circulation integral, one may well think of applying Stoke's theorem in parameter space. If $\mathcal{S}_{\mathcal{C}}$ is the surface enclosed by the curve $\mathcal{C}$, the

---

[1]The geometric phase is also known as Pancharatnam phase, or Pancharatnam-Berry phase. In order not to displease anyone, I will try and call it geometric phase as much as I can. To my knowledge, this naming issue does not apply to the Berry vector potential and the Berry connection.

integral in Eq. A.8 is equivalent to the surface integral of the curl of $\langle\phi_k(\mathbf{P})|\boldsymbol{\nabla}_P|\phi_k(\mathbf{P})\rangle$:

$$\boldsymbol{\nabla}_{\mathbf{P}} \times \mathcal{A}(\mathbf{P}) = i\boldsymbol{\nabla}_{\mathbf{P}} \times \langle\phi_k(\mathbf{P})|\boldsymbol{\nabla}_{\mathbf{P}}|\phi_k(\mathbf{P})\rangle\,.$$

Working component-wise on the $k$-th band, suppressing the band index for the sake of notation:

$$\Omega_{\mu\nu}(\mathbf{P}) = \frac{\partial}{\partial P^\mu}\mathcal{A}_\nu(\mathbf{P}) - \frac{\partial}{\partial P^\nu}\mathcal{A}_\mu(\mathbf{P})$$
$$= i\left[\left\langle\frac{\partial\phi(\mathbf{P})}{\partial P^\mu}\bigg|\frac{\partial\phi(\mathbf{P})}{\partial P^\nu}\right\rangle - \left\langle\frac{\partial\phi(\mathbf{P})}{\partial P^\nu}\bigg|\frac{\partial\phi(\mathbf{P})}{\partial P^\mu}\right\rangle\right].$$

This quantity is called *Berry curvature*, and in three dimensions it behaves as if it was the magnetic field in parameter space (this explains why $\mathcal{A}_n$ is referenced to also as Berry vector potential).

At this point, it is worth underlining that because of its definition, the integral of the Berry curvature over a closed manifold is related to the *Chern number*, which is an integer topological quantity. As a further proof of this fact, following Ref. [117] consider a closed path $\mathcal{C}$ and a Berry connection $\mathcal{A}$ on a closed manifold; then one can arbitrary choose the orientation of the path of integration $\mathcal{C}_\pm$ and as a consequence define the geometric phase as:

$$\gamma_\pm = \oint_{\mathcal{C}_\pm} d\mathbf{l} \cdot \mathcal{A}_k = \int_{\mathcal{S}_\pm} d\mathbf{S} \cdot \Omega_k,$$

where $\mathcal{S}$ is the surface enclosed by $\mathcal{C}$, and $\Omega_k = \boldsymbol{\nabla} \times \mathcal{A}_k$ where $n$ is the band index. Since these two phases must be associated to the same state, they must differ by an integer multiple of $2\pi$:

$$\gamma_+ = -\gamma_- + 2\pi\nu, \nu \in \mathbb{Z}.$$

Integrating over the entire manifold means:

$$\int_{\mathcal{S}_{\text{tot}}} \mathrm{d}\mathbf{S} \cdot \Omega^n = \int_{\mathcal{S}_+} \mathrm{d}\mathbf{S} \cdot \Omega^n + \int_{\mathcal{S}_-} \mathrm{d}\mathbf{S} \cdot \Omega^n = 2\pi\nu.$$

Geometric phases naturally appear in a number of problems as a consequence of a closed loop evolution in the parameter space. In what follows, a simple example of its role in the measurement of the velocity is briefly presented, but for an extended and more complete representation of the role of Berry phase in quantum mechanics, please refer to Ref. [81], that I will follow here.

Let us now relax this condition on the slowly varying Hamiltonian, and look at the first order corrections to the state $\psi(t)$. This means expecting that the eigenstates are changing linearly in time (as we are inspecting the first order corrections) as $|\phi_n(t)\rangle \to |\phi_n(t)\rangle + |\delta_n(t)\rangle$; furthermore, we expect corrections to have components along $|\phi_m(t)\rangle$, $m \neq n$. Using the perturbed eigenstates as in $|\psi(t)\rangle = \sum_n a_n(t)(|\phi_n(t)\rangle + |\delta_n(t)\rangle)$ in the time-dependent Schrödinger equation:

$$i\hbar\left[\left(-\frac{i}{\hbar}\epsilon_n(t) - \langle\phi_n(t)|\frac{\partial}{\partial t}|\phi_n(t)\rangle\right)(|\phi_n(t)\rangle + |\delta_n(t)\rangle) + \frac{\partial}{\partial t}(|\phi_n(t)\rangle + |\delta_n(t)\rangle)\right] =$$

$$\epsilon_n(t)\,|\phi_n(t)\rangle + \mathcal{H}\,|\delta_n(t)\rangle\,.$$

By rearranging the terms and considering that $\langle\phi_n(t)|\frac{\partial}{\partial t}|\phi_n(t)\rangle\,|\delta_n(t)\rangle$ and $\partial_t\,|\delta_n(t)\rangle$ are second order corrections, this equation becomes:

$$i\hbar\left[-\frac{i}{\hbar}\epsilon_n(t)\,|\delta_n(t)\rangle - \langle\phi_n(t)|\frac{\partial}{\partial t}|\phi_n(t)\rangle\,|\phi_n(t)\rangle + \frac{\partial}{\partial t}\,|\phi_n(t)\rangle\right] = \mathcal{H}\,|\delta_n(t)\rangle$$

$$i\hbar\left[\frac{\partial}{\partial t} - \langle\phi_n(t)|\frac{\partial}{\partial t}|\phi_n(t)\rangle\right]|\phi_n(t)\rangle = (\mathcal{H} - \epsilon_n(t))\,|\delta_n(t)\rangle\,;$$

using the fact that $i\partial_t = \mathcal{H}$ and projecting on $\langle\phi_m(t)|$, with $m \neq n$, we finally obtain:

$$i\langle\phi_m(t)|\frac{\partial}{\partial t}|\phi_n(t)\rangle = (\epsilon_m(t) - \epsilon_n(t))\langle\phi_m(t)|\delta_n(t)\rangle$$

$$|\delta_n(t)\rangle = i\sum_{m\neq n}\frac{\langle\phi_m(t)|\frac{\partial}{\partial t}|\phi_n(t)\rangle}{\epsilon_m(t) - \epsilon_n(t)}|\phi_m(t)\rangle, \tag{A.9}$$

so that to the first order, the initial state can be written as:

$$|\psi(t)\rangle = e^{i\gamma_n^{\mathrm{D}}} e^{i\gamma_n^{\mathrm{G}}}\left[|\phi_n(t)\rangle - i\sum_{k\neq n}\frac{\langle\phi_k(t)|\partial_t|\phi_m(t)\rangle}{E_n - E_k}|\phi_k(t)\rangle\right]. \tag{A.10}$$

Let us consider a crystal, so that the states are Bloch states that are parametrized by the wave vector, $\mathbf{q}$. Given the velocity operator defined as $\hbar\langle\dot{\mathbf{r}}\rangle = i\langle[\mathcal{H}, \mathbf{r}]\rangle$, in the parameter space $(\mathbf{q}, t)$ we have:

$$\hbar\dot{\mathbf{r}}(\mathbf{q}) = i\, e^{i\mathbf{q}\cdot\mathbf{r}}[\mathcal{H}, \mathbf{r}]e^{-i\mathbf{q}\cdot\mathbf{r}} \equiv \frac{\partial\mathcal{H}}{\partial\mathbf{q}},$$

where the explicit dependence of $\mathcal{H}$ on $\mathbf{q}$ and $t$ is suppressed for the sake of notation. Taking the expectation value of this quantity with respect to the state in Eq. A.10, and using the Schrödinger equation to obtain that $\langle\phi_n|\partial_q H|\phi_m\rangle = (\epsilon_n - \epsilon_m)\langle\partial_q\phi_n|\phi_m\rangle$, one finds for the $n$-th energy level:

$$\hbar v_n(\mathbf{q}) = \frac{\partial E_n(\mathbf{q})}{\partial q} - i\left[\left\langle\frac{\partial\phi_n}{\partial q}\bigg|\frac{\partial\phi_n}{\partial t}\right\rangle - \left\langle\frac{\partial\phi_n}{\partial t}\bigg|\frac{\partial\phi_n}{\partial q}\right\rangle\right] \equiv \frac{\partial E_n(\mathbf{q})}{\partial q} - \hbar\Omega_{qt}^n. \tag{A.11}$$

This result says that velocity is affected by an extra term, called *anomalous velocity*, and that this term is related to the geometric phase $\Omega_{qt}$; moreover, if Eq. A.11 is integrated over the entire Brillouin zone, the second term is the only one contributing.

# Geometric phase and magnetic fields

In the final part of this appendix, I will review an explicative example connecting the physics of geometric phase with the physics of magnetic fields [4,117,118]. This connection can already be spotted from the definition of the Berry curvature, $\boldsymbol{\Omega} = \nabla \times \boldsymbol{\mathcal{A}}$, that resembles the way the magnetic field is defined as the curl of the magnetic vector potential.

Consider a particle with spin $1/2$ in a region of space permeated by a magnetic field, $\mathbf{B}$, that is slowly rotating with frequency $\omega$. If the rotation takes place around the $z$ axis, the magnetic field can be written explicitly component-wise as:

$$\mathbf{B}(t) = B \begin{pmatrix} \sin\theta \cos\omega t \\ \sin\theta \sin\omega t \\ \cos\theta \end{pmatrix},$$

where $\theta$ is the polar angle and $B$ the magnitude of the field.

Assuming that the rotation of the magnetic field is slow enough that the spin of the particle follows the direction of $\mathbf{B}$, the Hamiltonian can be written as $\mathcal{H} = \mu \mathbf{B} \cdot \boldsymbol{\sigma}$, where $\boldsymbol{\sigma} = (\sigma_x, \sigma_y, \sigma_z)^{\mathrm{T}}$ is the spin angular momentum operator and $\mu = \hbar e / 2m$ is the Bohr magneton [4,117]. Explicitly:

$$\mathcal{H}(t) = \mu B \begin{pmatrix} \cos\theta & e^{-i\omega t} \sin\theta \\ e^{-i\omega t} \sin\theta & -\cos\theta \end{pmatrix},$$

with eigenvalues $\varepsilon_\pm = \pm \mu B$ for the spin up and down configurations respectively, and associated eigenstates:

$$|\phi_-(t)\rangle = \begin{pmatrix} e^{-i\omega t} \sin\frac{\theta}{2} \\ -\cos\frac{\theta}{2} \end{pmatrix}, \qquad |\phi_+(t)\rangle = \begin{pmatrix} e^{-i\omega t} \cos\frac{\theta}{2} \\ \sin\frac{\theta}{2} \end{pmatrix}. \qquad (A.12)$$

We can now combine these with the definition of the Berry connection in Eq. A.8 to obtain the geometric phase, observing that the only time dependent parameter in the

Hamiltonian is the azimuthal angle $\varphi \equiv \omega t$. The Berry connection only has one non-zero component, namely:

$$\boldsymbol{\mathcal{A}}_- = \frac{1}{B \sin\theta} \sin^2\frac{\theta}{2}\hat{\varphi}, \qquad \boldsymbol{\mathcal{A}}_+ = \frac{1}{B \sin\theta} \cos^2\frac{\theta}{2}\hat{\varphi};$$

and its curl (evaluated in spherical polar coordinates) is directed along the direction of the magnetic field:

$$\boldsymbol{\Omega}_\pm = \mp\frac{1}{2B^2}\hat{B}. \tag{A.13}$$

Finally, we obtain from Eq. A.8:

$$\gamma_\pm(\mathcal{C}) = \int_0^{2\pi} B \sin\theta \; \mathrm{d}\varphi \; \mathcal{A}_\pm = -\pi(1 \mp \cos\theta) = \mp\frac{1}{2}\Omega_S(\mathcal{C}),$$

where the last equation of this chain expresses the geometric phase in terms of the solid angle $\Omega_S$ subtended by the closed trajectory $\mathcal{C}$, modulo $2\pi$.

The experimental verification of this theoretical prediction of Sir M. V. Berry [37] arrived by two distinct research groups working at the same facility in Grenoble, *c.f.* Refs. [119, 120].

Let us now look at this solution under a different point of view, and in order to do so, let us start noticing that the Hamiltonian is fully described by three parameters, namely $(B, \theta, \varphi(t))$. It then seems legitimate to think of the parameter space as the surface of a sphere of radius $B$. Furthermore, the definition of the Berry curvature $\boldsymbol{\Omega}_\pm$ in Eq. A.13 looks exactly like the magnetic field generated by a fictitious magnetic monopole of charge $\pm 1/2$ placed at the origin of this sphere. Finally, note that the origin of the sphere is where $B = 0$, that in turn means where $\varepsilon_- = \varepsilon_+$ *i.e.* the states are degenerate.

It is now clear the parallelism between the physics described so far and the undergraduate theory on magnetic fields: the point where the eigenstates become degenerate acts as a monopole of charge $1/2$ that generates a field described by the Berry curvature, that is obtained as the curl of the Berry connection, its vector potential, $\boldsymbol{\Omega} = \nabla \times \boldsymbol{\mathcal{A}}$. Evaluating

the flux of this field through a closed surface of contour $\mathcal{C}$ generates the geometric phase, $\gamma$.

In the work presented in Chapter 3, we observed an analogous result for a non-Hermitian Hamiltonian. In fact, also in the case of non-Hermitian geometric phase it is possible to draw this parallelism [39], in which case the monopole is located at the exceptional point (that differ slightly from the degeneracy points, *c.f.* Section 1.1.3), its charge is imaginary and generates a field that grows with the distance from the monopole.

# Appendix B

# Coupled Harmonic oscillators

In co-authoring this paper, together with Hannah Price and Tomoki Ozawa we took care of the "Mapping and Theory Background" section; Ritika Anandwade, Yaashnaa Singhal, Sai Naga Manoj Paladugu, Michael Castle, Shraddha Agrawal, Ellen Carlson, Cait Battle-McDonald and Bryce Gadway were concerned with the experiment realization, the experimental results and the main writing.

# Synthetic Mechanical Lattices with Synthetic Interactions

Ritika Anandwade,[1, *] Yaashnaa Singhal,[1, *] Sai Naga Manoj Paladugu,[1, *]
Enrico Martello,[2, *] Michael Castle,[1] Shraddha Agrawal,[1] Ellen Carlson,[3] Cait
Battle-McDonald,[4] Tomoki Ozawa,[5, †] Hannah M. Price,[2, ‡] and Bryce Gadway[1, §]

[1]*Department of Physics, University of Illinois at Urbana-Champaign, Urbana, IL 61801-3080, USA*
[2]*School of Physics and Astronomy, University of Birmingham,*
*Edgbaston, Birmingham B15 2TT, United Kingdom*
[3]*Department of Physics and Astronomy, Haverford College,*
*370 Lancaster Ave, Haverford, PA 19041-1392, USA*
[4]*Department of Physics, Smith College, Northampton, MA 01063, USA*
[5]*Advanced Institute for Materials Research (WPI-AIMR), Tohoku University, Sendai 980-8577, Japan*
(Dated: July 21, 2021)

Metamaterials based on mechanical elements have been developed over the past decade as a powerful platform for exploring analogs of electron transport in exotic regimes that are hard to produce in real materials. In addition to enabling new physics explorations, such developments promise to advance the control over acoustic and mechanical metamaterials, and consequently to enable new capabilities for controlling the transport of sound and energy. Here, we demonstrate the building blocks of highly tunable mechanical metamaterials based on real-time measurement and feedback of modular mechanical elements. We experimentally engineer synthetic lattice Hamiltonians describing the transport of mechanical energy (phonons) in our mechanical system, with control over local site energies and loss and gain as well as control over the complex hopping between oscillators, including a natural extension to non-reciprocal hopping. Beyond linear terms, we experimentally demonstrate how this measurement-based feedback approach opens the window to independently introducing nonlinear interaction terms. Looking forward, synthetic mechanical lattices open the door to exploring phenomena related to topology, non-Hermiticity, and nonlinear dynamics in non-standard geometries, higher dimensions, and with novel multi-body interactions.

Networks of coupled harmonic oscillators have long served as a foundational model for understanding thermal transport in solids [1], and over the past decade have additionally become a powerful theoretical and experimental platform for exploring topology [2] and its connections to mechanical structures [3–5]. While experiments based on physically coupled oscillators offer powerful capabilities for the realization of artificial materials and the visualization of novel transport phenomena therein [6–18], such physical coupling terms present natural limitations on the Hamiltonians that may be directly engineered. For example, Newton's third law dictates that the direct hopping terms should obey reciprocity, with forward and backward tunneling pathways having equal amplitudes. The position-dependence of spring forces further implies the restriction to realizing only time-reversal invariant hopping Hamiltonians.

While a number of clever approaches have been proposed [19–22] and implemented [6, 7] to circumvent such limitations while maintaining physical coupling between oscillators, one may seek alternative approaches that avoid direct physical connections altogether. In the context of classical electrical or mechanical metamaterials, where mode occupations are on order of the Avogadro

number, one can naturally think about utilizing measurements of the oscillators' properties - *e.g.*, center-of-mass positions and momenta - as a resource for Hamiltonian engineering, with little concern for the disturbance of the natural system dynamics. Indeed, the natural suitability of classical metamaterials for measurement-based feedback has in recent years led to proposals for the realization of designer non-Newtonian systems [23], and even first demonstrations of the engineering of non-reciprocity in robotic mechanical metamaterials of physically coupled rotors [24, 25]. Here, through the measurement of and feedback on a system of otherwise physically disconnected mechanical oscillators, we demonstrate a general approach to engineering nonlinear synthetic lattice Hamiltonians. We experimentally demonstrate the engineering of complex and non-reciprocal hopping terms, complex local site energies, and synthetic quartic nonlinearities, exploring the use of feedback-based control to drive both $\mathcal{PT}$-symmetry breaking and Josephson self-trapping phase transitions in a synthetic double-well. The extension to larger, many-site arrays of synthetically coupled oscillators, incorporating even more exotic synthetic nonlinearities, will enable explorations of novel lattice Hamiltonians with tailored mean-field interactions.

This paper is organized as follows. Section I describes our experimental system and presents an informal discussion of our feedback-based approach to Hamiltonian engineering. In Sec. II, we provide the formal theoretical framework underlying this approach to engineering effective tight-binding models for mechanical oscillators syn-

———————

* These authors contributed equally to this work.
† tomoki.ozawa.d8@tohoku.ac.jp
‡ H.Price.2@bham.ac.uk
§ bgadway@illinois.edu

thetically coupled by measurement-based feedback. In Sec. III, we provide several examples for the engineering of specific Hamiltonian terms, such as local site energies (real and imaginary) and inter-site hopping terms (complex and non-reciprocal), as well as nonlinear interaction terms. For each example, we provide a theoretical derivation for the required feedback forces, as well as an experimental demonstration of the implementation. We summarize our results in Sec. IV.

## I. DESCRIPTION OF THE SYSTEM

As depicted in Fig. 1(a,b), our prototype for a "lattice of synthetically coupled oscillators" consists of modular, large-scale (kg-scale mass) mechanical oscillators. In the absence of applied feedback forces, these oscillators are characterized by nearly identical natural oscillation frequencies $f_0 \sim 3.05$ Hz and quality factors $Q \sim 1000$.

An analog accelerometer (EVAL-ADXL203) is fixed to each oscillator, and we acquire real-time measurements of acceleration $a(t)$ by sending the signals to a common computer. By taking the numerical derivative of the acquired signal, we additionally acquire real-time measurements of the oscillators' jerk $j(t) \equiv \partial a(t)/\partial t$. As the signals come from harmonic oscillators with roughly constant frequencies, we can associate the measured acceleration and jerk signals as proxies for the oscillator position $x(t)$ and momentum $p(t)$ signals, respectively (as the sets of variables $\{a, x\}$ and $\{j, p\}$ have proportional relationships, as we explain in more detail later). We hereafter refer to the input signals as position $\tilde{x}$ and momentum $\tilde{p}$. In experiment, we normalize the $\tilde{x}$ and $\tilde{p}$ signals to the same dimensionless amplitude, reflecting the equipartition of kinetic and potential energy.

Our "synthetic mechanical lattice" approach implements an effective Hamiltonian $\mathcal{H} = H + H_0$ in the oscillator array, where the portion $H$ can be considered as a perturbation to the bare Hamiltonian $H_0$ of the uncoupled, identical oscillators. The modified part of the Hamiltonian, $H$ (the terms of which have frequency scales $\ll f_0$), describes the transport of mechanical energy (phonons) between the oscillators, small shifts to the oscillator frequencies, and any engineered nonlinearities. Roughly speaking, to implement $H$ we apply individual feedback forces to the oscillators that reflect the relationship $F_i \sim -\partial H/\partial \tilde{x}_i$ (cf. Fig. 1(a)). These forces can in principle have almost any dependence on the positions $\tilde{x}_i$ and momenta $\tilde{p}_i$, including higher powers thereof, opening up new possibilities for Hamiltonian engineering [26]. To note, we will develop the framework for this feedback-based control more formally in Sec. II.

We implement these feedback forces magnetically, avoiding any added mechanical contacts. Each oscillator has a dipole magnet attached to a central, cylindrical shaft. The dipole magnet is embedded in a wound coil (gradient solenoid [27], with a higher winding density at its base than at its top). We control the current (between 0 and 2 A) in the coil, which produces an axial magnetic field gradient that in turn creates a force on the oscillator. While there is a fixed direction of current flow, we operate with a nominal offset gradient and control the variations about this offset, thus achieving an effective bi-directional (positive and negative along the axial direction) control of forces.

Figure 1(c) displays the typical real-time measurements acquired for one example experiment, which explores a self-trapped mode in a nonlinear double-well (discussed further later on, in the context of Fig. 7). The measured $\tilde{x}$ (panel **i**) and $\tilde{p}$ (panel **ii**) signals for oscillators 1 (red) and 2 (blue) are shown in panels **i** and **ii**, including zoomed in views over several seconds showing the intra-envelope dynamics. From these primary measurements, we construct a proxy for the local mechanical energy $E_i = (\tilde{x}_i^2 + \tilde{p}_i^2)/2$, as shown in panel **iii**. The local mechanical energy plays a role analogous to the local particle probability density $|\psi_i|^2$ of a wave function $\psi$ under the evolution of the implemented tight-binding Hamiltonian. One may also extract the local phase $\phi_i = \arg(\tilde{x}_i + i\tilde{p}_i)$ at each oscillator, associated with $\arg(\psi_i)$ of the corresponding evolving wave function. To note, the initial linear and quadratic rise of the signals in panels **i**/**ii** and **iii**, respectively, relate to an initial preparation step of 10 s during which a sinusoidal force prepares the respective energy and phases of the two oscillators. In panels **iv** and **v**, we plot further derived experimental quantities relevant to the dynamics in this case of a tunnel-coupled double-well with nonlinear interactions. Panel **iv** depicts the normalized energy imbalance $z = (E_1 - E_2)/(E_1 + E_2)$ and panel **v** depicts the relative oscillator phase $\Delta\phi = \phi_1 - \phi_2$. The trajectories of $z$ and $\Delta\phi$ reflect a self-trapped mode with a trapped population imbalance but a running relative phase.

## II. MAPPING AND THEORY BACKGROUND

The theoretical basis for our synthetic mechanical metamaterial is a mapping which can be made in certain limits from Newton's equations of motion to the Heisenberg equations for a tight-binding quantum Hamiltonian. Such an approach has previously been used, for example, to propose how to simulate a Peierls hopping phase and an effective Harper-Hofstadter model with time-modulated classical coupled harmonic oscillators [19, 20]. In this section, we show how this approach can be applied to implement a wide variety of Hamiltonian terms by subjecting individual and pairs of classical oscillators to weak feedback.

Before entering into details of the mapping, we start by considering the equations of motion for a pair of uncoupled and identical harmonic oscillators:

$$m\dot{x}_i(t) = p_i(t), \qquad \dot{p}_i(t) = -m\omega^2 x_i(t), \qquad (1)$$

where $x_i(t)$ and $p_i(t)$ are position and momentum of an oscillator at time $t$ with the index $i = 1, 2$ running over
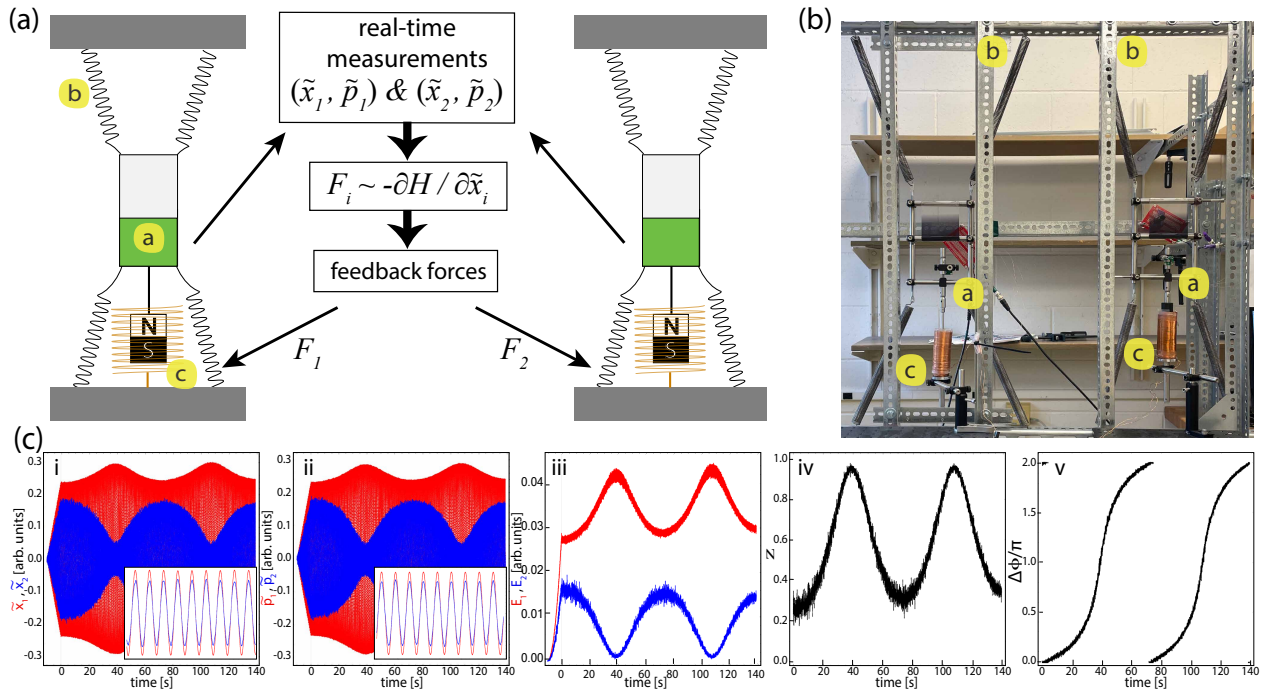
FIG. 1. **Modular mechanical oscillators synthetically coupled by measurement-based feedback.** **(a)** A cartoon depiction of the implemented mechanical oscillators, which feature embedded accelerometers (marked $a$) for the real-time measurement of proxies for position ($\tilde{x}$) and momentum ($\tilde{p}$), a set of four springs (one marked $b$), and a dipole magnet embedded in a gradient solenoid for the application of forces (marked $c$). Real-time feedback forces $F_i$, which depend on the real-time measurements $\tilde{x}_i$ and $\tilde{p}_i$, are used to implement an effective tight-binding Hamiltonian $H$. **(b)** A photograph of the large-scale prototype used to implement the two-site synthetically-coupled mechanical lattice depicted in (a), with letters denoting the same elements. **(c)** Acquired experimental data and processed observables for a two-site system with synthetic hopping and synthetic nonlinearity. Panel **i**: Experimental measurements of $\tilde{x}_1$ (red) and $\tilde{x}_2$ (blue), with inset showing short-time dynamics over several oscillator periods from $t = 0$ to $3$ s. Panel **ii**: Similar plots for the corresponding $\tilde{p}_i$ measurements. Panel **iii**: Constructed proxy for the local mechanical energy, $E_i \propto \tilde{x}_i^2 + \tilde{p}_i^2$, for two coupled masses with synthetic nonlinearity. Panel **iv**: Dynamics of the normalized population imbalance $z = (E_1 - E_2)/(E_1 + E_2)$. Panel **v**: Dynamics of the relative oscillator phase $\Delta\phi = \phi_1 - \phi_2$, where the local oscillator phase is reconstructed from the $\tilde{x}$ and $\tilde{p}$ measurements as $\phi_i = \arg(\tilde{x}_i + i\tilde{p}_i)$.

the two oscillators, $\omega = \omega_1 = \omega_2$ is the angular oscillation frequency and $m = m_1 = m_2$ is the mass. The dot over variables denote the first derivative in time. Below, we often suppress the explicit time-dependence, $(t)$, when it is obvious. For convenience of measurement, it is more natural for us to work with the acceleration, $a_i(t)$, and the jerk, $j_i(t) \equiv \dot{a}_i(t)$, instead of the position and momentum. However, for a harmonic oscillator, these are simply related as

$$a_i(t) = -\omega^2 x_i(t), \qquad j_i(t) = -\frac{\omega^2}{m} p_i(t) \qquad (2)$$

and their equations of motion are

$$\dot{a}_i(t) = j_i(t), \qquad \dot{j}_i(t) = -\omega^2 a_i(t) \qquad (3)$$

suggesting the acceleration as a proxy for the position, and the jerk as a proxy for the momentum. To make this concept clearer in what follows, we shall introduce the notation $X_i \equiv a_i$ and $P_i \equiv j_i$, so that the equations of motion become

$$\dot{X}_i = P_i, \qquad \dot{P}_i = -\omega^2 X_i. \qquad (4)$$

To couple the two oscillators and simulate different effects, we now add feedback to the system such that the equations of motion become

$$\dot{X}_i = P_i, \qquad \dot{P}_i = -\omega^2 X_i + F_i. \qquad (5)$$

where $F_i$ is a function of $(X_1, X_2, P_1, P_2)$. In analogy with the real momentum, this feedback acts as a "force" on the oscillator. Here we present a general recipe, while below, we shall discuss specific examples of $F_i$ that we consider to map to different Hamiltonians. As stated above, the experiment works with normalized effective variables for position and momentum. However, for concreteness, we retain the dimensionality of $X_i$ and $P_i$ and include relevant angular frequency $\omega$ terms below.

To map the above equations to Heisenberg equations, we introduce the classical complex variables [19, 20]:

$$\alpha_i \equiv \sqrt{\frac{\omega}{2}} X_i + i \sqrt{\frac{1}{2\omega}} P_i \qquad (6)$$

in analogy with the annihilation operator of the quantum harmonic oscillator. It can be straightforwardly shown

from this that $|\alpha_i|^2$ then scales with the instantaneous oscillation energy of a given mass. From this, it follows that we can re-express the acceleration and jerk as

$$X_i = \sqrt{\frac{1}{2\omega}}(\alpha_i + \alpha_i^*), \qquad P_i = -i\sqrt{\frac{\omega}{2}}(\alpha_i - \alpha_i^*) \quad (7)$$

and hence the equations of motion are

$$\dot{\alpha}_i = -i\omega\alpha_i + \frac{i}{\sqrt{2\omega}}F_i, \qquad (8)$$

where the feedback term, $F_i$, should also be re-expressed as a function of $(\alpha_1, \alpha_1^*, \alpha_2, \alpha_2^*)$. Note that the complex conjugate of this equation describes the time-evolution of the conjugate variables, $\alpha_i^*$.

In the absence of the feedback, it can be seen from Eq. 8 that the time-dependence of the complex amplitudes is given by $\alpha_i(t) \propto e^{-i\omega t}$ (and similarly $\alpha_i^*(t) \propto e^{i\omega t}$) as expected for harmonic oscillators. Including the feedback naturally modifies the dynamics. However, provided that $\omega$ remains the largest frequency-scale in the problem and that the feedback is sufficiently weak, these dynamical changes will be slow and small compared to the natural oscillations. In this limit, we can assume that the complex amplitudes' fastest time-dependence is still given by $\alpha_i(t) \propto e^{-i\omega t}$ [19, 20], or in other words, that the $\alpha_i$ variables "rotate" with a frequency $\approx \omega$ (while the conjugate variables $\alpha_i^*$ "rotate" with $\approx -\omega$).

Working in this high-frequency limit allows us to apply the "rotating-wave approximation" (RWA) to simplify Eq. 8 [19, 20]. The RWA is an approach well-known from quantum optics, in which only so-called "co-rotating terms" with a frequency $\approx \omega$ are kept in the dynamics. To physically understand the RWA, we can imagine transforming Eq. 8 into a "co-rotating frame" at the natural frequency $\omega$. In this frame, a term $\propto \alpha_i$, for example, varies relatively slowly (due to feedback), while a term $\propto \alpha_i^*$ oscillates rapidly at a frequency $\approx -2\omega$. Terms like the former are "co-rotating" while the latter are "counter-rotating" as they will rapidly average to zero over the timescale for the slow dynamics. In the limit that $\omega \to \infty$, only "co-rotating terms" with a frequency $\approx \omega$ remain important, justifying the RWA assumption that all other terms can be dropped.

Under the condition of high natural frequency and weak feedback, we can therefore re-write Eq. 8 as

$$\dot{\alpha}_i = -i\omega\alpha_i + \sum_j \frac{i}{\sqrt{2\omega}}F_{ij}^{\mathrm{RWA}}\alpha_j , \qquad (9)$$

where $F_i \to \sum_j F_{ij}^{\mathrm{RWA}}\alpha_j$ is the RWA, *i.e.*, where we only keep suitable co-rotating terms in the feedback applied to oscillator $i$. Note that such terms must contain at least one factor of either $\alpha_1$ or $\alpha_2$ (as both oscillators have natural frequency $\omega$), and so we have explicitly factored out $\alpha_j$ in this expression for convenience. In general, $F_i^{\mathrm{RWA}}$ can still be any suitable function of $(\alpha_1, \alpha_1^*, \alpha_2, \alpha_2^*)$, as discussed further below, and so can encode a wide-range of physical effects. Explicit examples are given in the following sections to further illustrate this approximation.

The equation of motion (Eq. 9) can be regarded as the Heisenberg equation of motion derived from a quantum-mechanical Hamiltonian (with $\hbar$ suppressed)

$$\mathcal{H} = \sum_i \omega\hat{\alpha}_i^\dagger\hat{\alpha}_i - \frac{1}{\sqrt{2\omega}}\sum_{i,j}\frac{1}{n_i+1}\hat{\alpha}_i^\dagger\hat{F}_{ij}^{\mathrm{RWA}}\hat{\alpha}_j, \quad (10)$$

where $\hat{\alpha}_i^\dagger$ and $\hat{\alpha}_i$ are creation and annihilation operators for site $i$ obeying bosonic commutation relations. The operator $\hat{F}_{ij}^{\mathrm{RWA}}$ is an operator obtained by replacing $(\alpha_1, \alpha_1^*, \alpha_2, \alpha_2^*)$ in $F_{ij}^{\mathrm{RWA}}$ by $(\hat{\alpha}_1, \hat{\alpha}_1^\dagger, \hat{\alpha}_2, \hat{\alpha}_2^\dagger)$ and moving all the creation operators to the left of the annihilation operators. The factor of $n_i$ is the number of the operators $\alpha_i^\dagger$ appearing in $F_{ij}^{\mathrm{RWA}}$. With the identification $\alpha_i = \langle\hat{\alpha}_i\rangle$ and $\alpha_i^* = \langle\hat{\alpha}_i^\dagger\rangle$, where $\langle\cdot\rangle$ is the quantum mechanical average of the operator with respect to the initial state, the Heisenberg equation of motion for Eq. 10 reduces exactly to Eq. 9 when $\hat{F}_{ij}^{\mathrm{RWA}}$ does not itself contain operators. When $\hat{F}_{ij}^{\mathrm{RWA}}$ does contains operators, this will correspond to inter-particle interactions in the quantum-mechanical language, as discussed further below. In such cases, assuming that the energy in each oscillator is large enough so that we are in the classical limit, we can approximate $\langle\hat{F}_{ij}^{\mathrm{RWA}}\hat{\alpha}_j\rangle \approx F_{ij}^{\mathrm{RWA}}\alpha_j$ such that interaction terms also reduce to the corresponding terms in Eq. 9.

Hence, the dynamics of our synthetic mechanical meta-material can be used to simulate the above general class of quantum mechanical tight-binding Hamiltonians. Note also that although we focus experimentally in this paper on up to two oscillators, the above equations are valid for $n$ identical oscillators, in which case $\mathcal{H}$ will describe an $n$-site Hamiltonian. The generalization to non-identical oscillators is also straightforward, as discussed in Ref. [19], provided that all the natural oscillator frequencies are large enough that the RWA can be applied.

Having reviewed the above general theoretical recipe, we shall now give explicit examples for using feedback to engineer specific types of desired terms in the tight-binding Hamiltonian, both in theory and experiment.

### III. HAMILTONIAN CONTROL EXAMPLES

#### A. Control of Local Site Energy Shifts

As a first example of this theoretical approach, we show how adding weak feedback corresponding to $F_i \propto X_i$ leads to local site energy shifts in the above Hamiltonian mapping. Physically, such a term corresponds in experiment to applying a local feedback which is proportional to the measured acceleration of the given oscillator.

Theoretically, we start by writing the feedback term as

$$F_i = A_{i,i}X_i = \frac{A_{i,i}}{\sqrt{2\omega}}(\alpha_i + \alpha_i^*), \qquad (11)$$
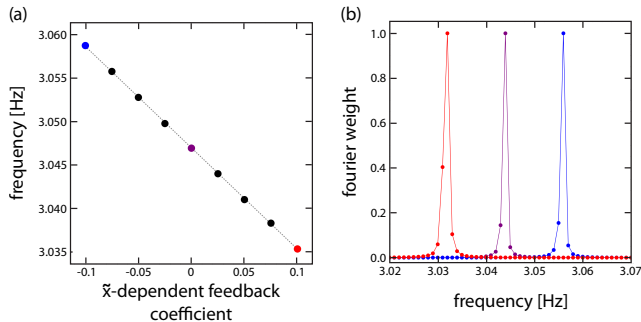
FIG. 2. **Local control of site energy shifts by position-dependent feedback. (a)** Oscillation frequency of an individual oscillator (determined by Fourier analysis of the experimental oscillator dynamics), as a function of the coefficient for the position-dependent feedback force. Error bars (smaller than the data points) represent the standard error of the mean of the fit used to determine the points. **(b)** Scaled power spectra of the Fourier-transformed oscillator position dynamics for three different values of the $\tilde{x}$ feedback coefficient, with colors relating to those of the points in (a).

where $A_{i,i}$ is the (weak) amplitude for the feedback applied to oscillator $i$, which depends on the measurements of $X_i$. (Note that Einstein's index summation convention is not applied here).

Adding a feedback like this means that one of our equations of motion becomes $\dot{P}_i = -(\omega^2 - A_{i,i})X_i$, which is equivalent to having a new effective natural frequency $\tilde{\omega}_i = \sqrt{\omega^2 - A_{i,i}}$. Assuming weak amplitudes for the driving force and taking a Taylor expansion of this expression, we obtain $\tilde{\omega}_i \simeq \omega - A_{i,i}/2\omega$.

Alternatively, this result can be obtained by substituting the applied feedback form into Eq. 8, leading to

$$\dot{\alpha}_i = -i\omega\alpha_i + i\frac{A_{i,i}}{2\omega}(\alpha_i + \alpha_i^*). \qquad (12)$$

Applying the RWA means that we neglect the counter-rotating $\alpha_i^*$ term such that

$$F_{ij}^{\mathrm{RWA}}\alpha_j = \begin{cases} \frac{A_{i,i}}{\sqrt{2\omega}}\alpha_i & \text{for } i = j \\ 0 & \text{for } i \neq j \end{cases} \qquad (13)$$

The Hamiltonian [Eq. 10] then follows directly as

$$\mathcal{H} = \sum_i (\omega + \Delta_i)\hat{\alpha}_i^\dagger\hat{\alpha}_i, \qquad (14)$$

where $\Delta_i = -A_{i,i}/2\omega$. In terms of the tight-binding Hamiltonian, this is interpreted as adding a tunable site energy shift $\Delta_i$ to site $i$ of the lattice, as desired. Physically, this corresponds to a local shift of the corresponding oscillator frequency by an amount $\Delta_i$.

We now demonstrate experimentally this control of local site energies by position-dependent self-feedback. Figure 2 depicts the control of the oscillator frequency, corresponding to site energy shifts in the equivalent tight-binding model, through the application of $\tilde{x}$-dependent

self-feedback. In Fig. 2(a), we plot the experimentally measured oscillator frequency as a function of the applied coefficient of self-feedback. We find a linear relationship between the measured frequency and the applied feedback, consistent with the fact that we are safely in the limit of weak feedback, with the modifications to the bare oscillator frequency at the level of $\lesssim 0.5\%$.

These oscillation frequencies are determined by first depositing mechanical energy into the oscillator over 10 s (by application of a strong oscillating force) and then allowing the oscillator to ring down freely over 100 s. We then perform a numerical Fourier transform of the position data and fit the resulting spectrum to a Lorentzian line shape, extracting the center frequency. Figure 2(b) shows several such experimental line shape curves, with colors corresponding to the data points of the extracted center frequencies in Fig. 2(a).

### B. Local Control of Loss and Gain

Similarly, local feedback can be used to simulate on-site loss and gain. For a tight-binding Hamiltonian, this would correspond to having

$$\mathcal{H} = \sum_i (\omega - i\gamma_i)\hat{\alpha}_i^\dagger\hat{\alpha}_i, \qquad (15)$$

where $\gamma_i$ is real and with $\gamma_i > 0$ and $\gamma_i < 0$ representing local loss and gain, respectively. From this, we can read-off that we require

$$F_{ij}^{\mathrm{RWA}}\alpha_j = \begin{cases} i\gamma_i\sqrt{2\omega}\alpha_i & \text{for } i = j \\ 0 & \text{for } i \neq j \end{cases} \qquad (16)$$
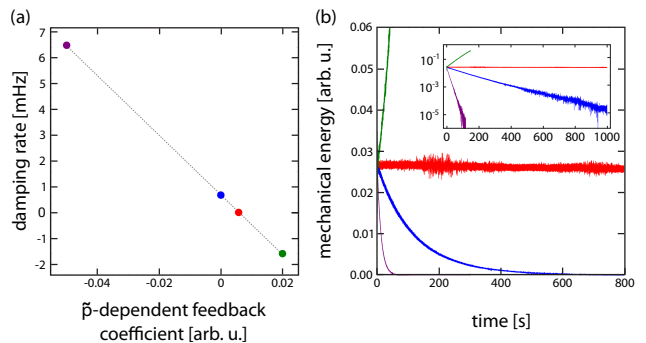


FIG. 3. **Local control of loss and gain by momentum-dependent feedback. (a)** Damping rate of an individual oscillator as a function of the applied coefficient of momentum-dependent feedback. The damping rate $\gamma$ for each point is determined by fitting experimental data sets of the mechanical energy dynamics to an exponential decay $\propto e^{-2(2\pi\gamma t)}$, with negative $\gamma$ values relating to gain. Error bars (smaller than the data points) represent the standard error of the mean of the fit. **(b)** Mechanical energy dynamics for several values of the applied $\tilde{p}$ feedback coefficient. Colors relate to those of the points in (a). Inset: semi-log plot of the same oscillator energy growth/decay curves.
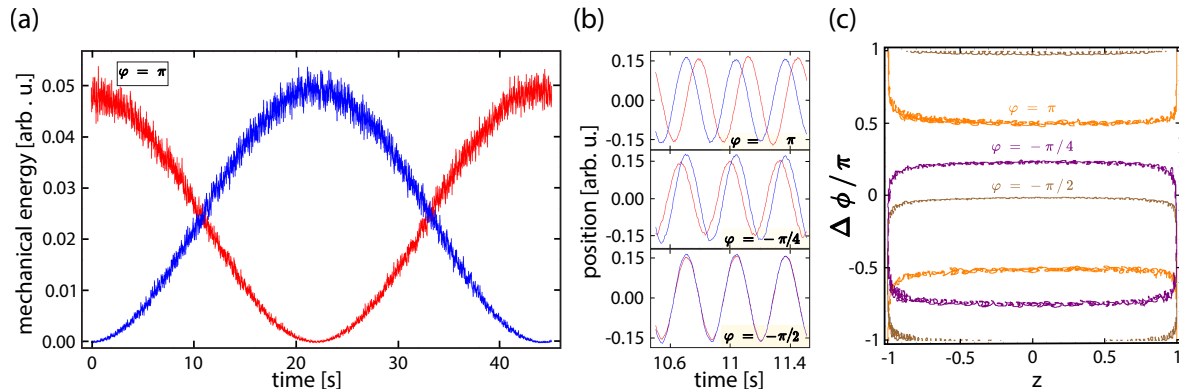
FIG. 4. **Inter-oscillator hopping.** (a) Transfer of mechanical energy between two synthetically coupled oscillators as a function of time for a tunnelling phase $\varphi = \pi$. The red and blue data curves relate to the experimentally measured mechanical energy dynamics of oscillators 1 and 2, respectively. (b) Experimental oscillator position ($\tilde{x}$) dynamics over several oscillation periods, for the cases of tunneling phase values $\varphi = \pi$ (top), $-\pi/4$ (middle), and $-\pi/2$ (bottom). (c) Phase space maps depicting the dynamical trajectories of the measured normalized mechanical energy imbalance $z$ and relative oscillator phase $\Delta\phi$ of the oscillator double-well. The trajectories related to the three tunneling phase values depicted in (b), for $\varphi = \pi$ (orange), $\varphi = -\pi/4$ (purple), and $\varphi = -\pi/2$ (brown). The trajectories reflect data sampled from one period of the mechanical energy dynamics ($\sim 50$ s), with a low-pass filter applied to the plotted data.

It is straightforward to see from Eq. 7 that a suitable choice of feedback is

$$F_i = B_{i,i}P_i = -iB_{i,i}\sqrt{\frac{\omega}{2}}(\alpha_i - \alpha_i^*), \qquad (17)$$

where $\gamma_i = -B_{i,i}/2$, as the unwanted $\alpha_i^*$ term in this expression will be neglected in the RWA. Here, $B_{i,i}$ is the (weak) amplitude for the feedback applied to oscillator $i$, which depends on the measurements of $P_i$. Physically, this corresponds in our setup to local feedback which is proportional to the jerk of the oscillator.

Our control of the local loss and gain terms of a single oscillator (site) is demonstrated in Fig. 3. Figure 3(a) plots the measured rate of mechanical energy damping as a function of the applied coefficient of momentum-dependent self-feedback. We find a very linear relationship between the applied amplitude of feedback and the shift of the measured rate of damping/gain (with a nearly identical slope to that found in Fig. 2(a), owing to our normalization of the dimensionless $\tilde{x}$ and $\tilde{p}$ signals).

The damping rates in Fig. 3(a) are determined as follows. We first excite the oscillator (as in Fig. 2) by sinusoidally driving it near resonance for 10 s, and then allow it to undergo free evolution under the applied feedback for up to 1000 s. We then compute a proxy of the mechanical energy stored in the oscillator, $E = (\tilde{x}^2 + \tilde{p}^2)/2$, as plotted for the four different feedback cases shown in Fig. 3(b). A simple exponential decay curve is fit to the dynamics of the mechanical energy, with negative decay values indicating an exponential gain. Starting from a relatively long decay time of $\sim 200$ s, corresponding to a natural quality factor of nearly 1000, we can introduce greatly enhanced loss or even strong gain through this momentum-dependent feedback. Importantly, for the investigation of unitary dynamics, we can also achieve an

excellent cancellation of the loss/gain terms by the appropriate weak self-feedback (*cf.* red curve in Fig. 3(b)). We note that similar feedback for the enhancement of mechanical quality factors has previously been reported in Ref. [16].

## C. (Complex) Inter-oscillator Hopping

So far, only self-feedback of the form $F_{ij}^{\text{RWA}}\alpha_j \propto \delta_{ij}$ has been taken into consideration and, as a consequence, only on-site phenomena have been investigated. However, if one were to reproduce, for example, a Hamiltonian containing a hopping term like:

$$\mathcal{H} = \sum_i \omega\,\hat{\alpha}_i^\dagger\hat{\alpha}_i - J\sum_{i>j}(e^{i\varphi}\hat{\alpha}_i^\dagger\hat{\alpha}_j + \text{ H.c.}), \qquad (18)$$

then a feedback involving inter-oscillator forces is needed. In the equation above, $J$ is the hopping amplitude, and $\varphi$ is the tunnelling phase that mimics the Peierls phase gained by a charged particle hopping on a tight-binding lattice in the presence of a magnetic vector potential. Hence, the latter may be designed to engineer artificial magnetic fields and topological quantum Hall tight-binding models in larger systems.

In order to realise Eq. 18, we require:

$$F_{ij}^{\text{RWA}}\alpha_j = \begin{cases} 0 & \text{for } i = j \\ \sqrt{2\omega}J\,e^{i\varphi_{j,i}}\alpha_j & \text{for } i \neq j \end{cases}$$

with $\varphi_{j,i} = \varphi$ and $\varphi_{i,j} = -\varphi$. In this case, a possible choice of feedback applied to the $i$-th oscillator depending
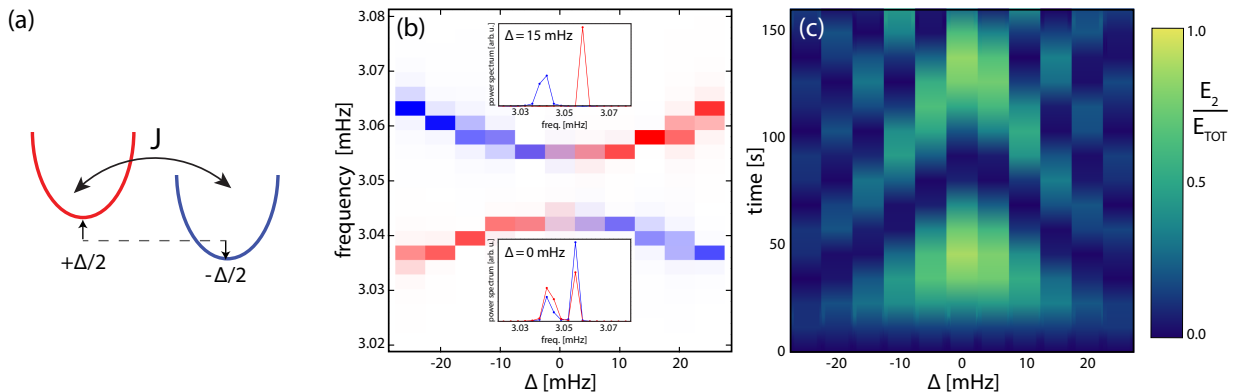
FIG. 5. **Avoided crossing in a biased double-well. (a)** A two-oscillator "double-well" with synthetic hopping $J$ and an inter-well bias $\Delta$. **(b)** Frequency spectra of the two-oscillator system as a function of inter-well bias $\Delta$. Overlaid power spectra of the coupled oscillator dynamics upon initialization of oscillator 1 (red) and oscillator 2 (blue), as determined by a Fourier-transform of the experimental dynamics over 380 s. White regions relate to frequencies with no weight in either oscillator, purple relates to delocalized modes, and red (blue) regions relate modes with weight concentrated in oscillator 1 (2). Insets show the power spectra when initializing in oscillator 1 (red) and 2 (blue) for values of $\Delta = 15$ mHz (top) and $\Delta = 0$ mHz (bottom). **(c)** Population dynamics as a function of $\Delta$. Initializing mechanical energy solely in oscillator 1, the plot shows the experimental dynamics of the mechanical energy appearing in oscillator 2, normalized to the total energy.

on the $j$-th one is:

$$F_i = A_{j,i} X_j + B_{j,i} P_j, \quad i \neq j$$
$$= A_{j,i} \frac{1}{\sqrt{2\omega}} (\alpha_j + \alpha_j^*) - i B_{j,i} \sqrt{\frac{\omega}{2}} (\alpha_j - \alpha_j^*).$$

Hence, one needs to set $A_{j,i} = 2J\omega\cos\varphi_{j,i}$ and $B_{j,i} = -2J\sin\varphi_{j,i}$. Experimentally, this can be realised by measuring both jerk and acceleration from one oscillator, and applying a commensurate feedback to the other. Note that for a system with many oscillators, the hopping amplitudes and phases can be chosen to have arbitrary spatial dependence so as to encode the desired lattice geometry, connectivity and gauge fields.

In experiment, working with normalized measurements for $\tilde{x}$ and $\tilde{p}$, the application of conjugate forces for the implementation of complex hopping is relatively straightforward. We demonstrate this control in Fig. 4. Figure 4(a) plots the dynamics of the mechanical energy stored in oscillator 1 (red) and oscillator 2 (blue) as a function of evolution time under the applied inter-oscillator feedback. Prior to the plotted dynamics, we again include an initialization step during which energy is deposited into oscillator 1 by a sinusoidal drive. High-visibility Rabi oscillations are observed in the mechanical energy dynamics, with energy flowing from oscillator 1 to oscillator 2, and back. As noted by the inset, these dynamics occur for a tunneling phase of $\varphi = \pi$.

To see the consequence of the imposed tunneling phase $\varphi$, we need only look at the traces of either $\tilde{x}$ or $\tilde{p}$ for the two oscillators, which provide information about the *relative phase* of the oscillators. Figure 4(b) shows the dynamics of the position signals of the two oscillators, with a zoom in on the time (near 10 s) at which the two oscillators first have nearly equal mechanical energies. For the case of $\varphi = \pi$, we have a position-dependent

force, and the two signals are out of phase by $\pi/2$, similar to the usual physical scenario of coupled oscillating masses. However, unlike the usual case, we find that as energy moves from oscillator 1 to 2, the $\tilde{x}_2$ signal actually leads the $\tilde{x}_1$ signal, whereas it would normally lag for a physical spring. This reflects our implementation of a $\pi$ tunneling phase. The lower two panels indicate the consequence of introducing a momentum-dependence to the inter-oscillator coupling. In particular, for $\varphi = -\pi/2$, the coupling terms become fully momentum-dependent, leading to dynamics in which the oscillators swing in phase as energy is transferred, signaling a concomitant change to the phase structure of the system's eigenstates.

To note, there are slight differences in the relative amplitudes of the red and blue curves during this time window for the three different panels of Fig. 4(b), relating to slightly different hopping rates for the different $\varphi$ values. This stems from the presence of a small *natural* coupling between the oscillators, which do in fact share a common physical support apparatus for convenience. To avoid such effects, one can simply actively cancel such natural contributions prior to adding synthesized hopping (which is done later for the probing of non-reciprocal hopping in Fig. 6). Here, by working with synthesized coupling terms that are much larger than the natural coupling, we simply work above it and tolerate a small $\varphi$-dependence to the hopping rate.

Figure 4(c) depicts more comprehensively how the relative phase and mechanical energy of the oscillators evolve throughout the dynamics. Taking advantage of the ability to simultaneously measure both the $\tilde{x}$ and $\tilde{p}$ signals at all sites, we reconstruct both the normalized energy imbalance of the two oscillators, $z = (E_1 - E_2)/(E_1 + E_2)$, as well as the relative phase between them, $\Delta\phi = \phi_1 - \phi_2$, where we simply determine the energies and phases of

the oscillators as $E = (\tilde{x}^2 + \tilde{p}^2)/2$ and $\phi = \arg(\tilde{x} + i\tilde{p})$. The evolution of $z$ and $\Delta\phi$ under the system evolution maps out the phase-space dynamics of this simple two-mode system. For the case of hopping with equal site energies, these dynamics should map out trajectories as shown in Fig. 4(c), with full oscillations between $z = \pm 1$, and with the curves centered about a $\Delta\phi$ value determined directly by the tunneling phase $\varphi$. In an analogous description in terms of an effective Bloch sphere (with the energy initiated at site 1 relating to a state vector initially aligned along $+z$), these trajectories simply relate to the paths traversed in a response to different applied tunneling "torque" vectors lying (at azimuthal angles $\varphi$) in the equatorial plane.

We now integrate our demonstrated control over site energy terms with this control over inter-site hopping. In particular, we investigate how the frequency spectrum of this two-oscillator system evolves as we add a variable inter-site frequency offset $\Delta$ (applied as equal amplitude shifts of $\pm\Delta/2$ to oscillators 1 and 2, respectively) while keeping a fixed inter-oscillator hopping rate $J$, as depicted in Fig. 5(a). Similar to Fig. 2, we obtain these frequency spectra by looking at the dynamics and performing a numerical Fourier transform. Figure 5(b) shows this spectrum, with the canonical avoided crossing encountered near $\Delta = 0$ as the modes of the two oscillators hybridize due to the engineered hopping. To note, the color indexing of Fig. 5(b) reflects the weight of the response at a given frequency that is found to relate to energy in oscillator 1 (red) and oscillator 2 (blue). Specifically, we investigate the dynamical evolution following the initialization of energy at site 1 or 2, yielding distinct Fourier spectra as depicted in red and blue, respectively. One sees that for large $\Delta$ the eigenmodes are nearly localized to the individual oscillators, while they are near-evenly delocalized near resonance. Finally, in Fig. 5(c), starting with energy in oscillator 1, we plot the dynamical evolution of the normalized energy in oscillator 2 as a function of $\Delta$. This Chevron Rabi pattern relates to high-visibility oscillations near $\Delta = 0$, with faster and lower-amplitude oscillations for larger values of the site-to-site frequency mismatch.

### D. Non-reciprocal Inter-oscillator Hopping

Going further, one advantage of using feedback to engineer inter-oscillator hopping terms is that it is straightforward to realise non-reciprocal couplings. Non-reciprocal Hamiltonians [28] naturally host chiral phenomena, and are intimately connected to the physics of non-Hermitian mechanics [29]. While non-reciprocity would be challenging to access in physical systems governed by Newtonian mechanics – where forces come in equal and opposite pairs – it can effectively be engineered in active matter [24, 25, 30] and in systems featuring dissipation [31]. Here, as we show, it can be engineered at will in synthetically coupled mechanical networks.

We consider the following Hamiltonian:

$$\mathcal{H} = \sum_i \omega \, \hat{a}_i^\dagger \hat{a}_i - \sum_{i>j} [(J + \delta J)e^{i\varphi}\hat{a}_i^\dagger \hat{a}_j + (J - \delta J)e^{-i\varphi}\hat{a}_j^\dagger \hat{a}_i],$$

where the change in the hopping amplitude $J \to J \pm \delta J$ [cf. $\mathcal{H}$ in Eq. 18] represents a non-reciprocal inter-oscillator coupling. This type of non-reciprocal coupling is well-known from the Hatano-Nelson model [32–34], and it not only selects a preferential direction of hopping, but more importantly causes this Hamiltonian to become non-Hermitian ($\mathcal{H}^\dagger \neq \mathcal{H}$). Note that for $|\delta J/J| < 1$, this Hamiltonian is $\mathcal{PT}$-symmetric and its eigenvalues are real. Conversely, if $|\delta J/J| > 1$, the $\mathcal{PT}$-symmetry of the system is broken and the energies become complex. At $|\delta J/J| = 1$ the energy levels coalesce in an exceptional point and the $\mathcal{PT}$ phase transition takes place. Explicitly, the non-reciprocal double-well (with coupled left and right modes, $|L\rangle$ and $|R\rangle$) possesses eigenmodes $\pm\sqrt{J^2 - \delta J^2}/(\delta J - J)|L\rangle + |R\rangle$ (up to normalization factors), having eigenfrequencies $\pm\sqrt{J^2 - \delta J^2}$, respectively.

Following the earlier discussed procedure, it is straightforward to obtain the new definitions for $A_{j,i}$ and $B_{j,i}$:

$$A_{1,2} = 2(J + \delta J)\,\omega\cos\varphi \quad \text{and} \quad B_{1,2} = -2(J + \delta J)\sin\varphi,$$
$$A_{2,1} = 2(J - \delta J)\,\omega\cos\varphi \quad \text{and} \quad B_{2,1} = 2(J - \delta J)\sin\varphi;$$

with analogous physical meaning as before. Because each of these force terms are added by hand, non-reciprocal hoppings are as natural to engineer in this setting as reciprocal ones.

In Fig. 6 we experimentally demonstrate the ability to engineer non-reciprocal hopping terms (depicted in the cartoon of Fig. 6(a)), driving this two-site system across a $\mathcal{PT}$ symmetry-breaking phase transition. To note, while in the earlier data (Figs. 2-5) there existed an additional, small contribution to the hopping due to physical coupling (via the shared support structure), for this data we take care to first actively cancel, via feedback, the physical coupling (scale $\lesssim$ 1 mHz) prior to introducing our synthetic coupling forces.

For a fixed value of $J \approx 2\pi \times 8.4$ mHz, we introduce a tunable hopping asymmetry $\delta J$. Figure 6(b) shows the dynamics of the measured oscillator energies, beginning with energy residing in oscillator 1, for values of $\delta J = J/8$ (top) and $7J/8$ (bottom). Unlike in the case of reciprocal hopping terms, the total mechanical energy is not fixed throughout these dynamics, even in the $\mathcal{PT}$-symmetric phase. As energy flows from oscillator 1 to 2, the energy of the system grows. The difference of scale of the two panels of Fig. 6(b) reflects the fact that this growth in energy becomes more pronounced for larger values of $\delta J$ approaching the $\mathcal{PT}$ symmetry-breaking phase transition. As stated above, the eigenstates of the system in the $\mathcal{PT}$-symmetric regime similarly reflect an asymmetry between left and right modes, which for larger lattices gives rise to the non-Hermitian skin effect [35]. One
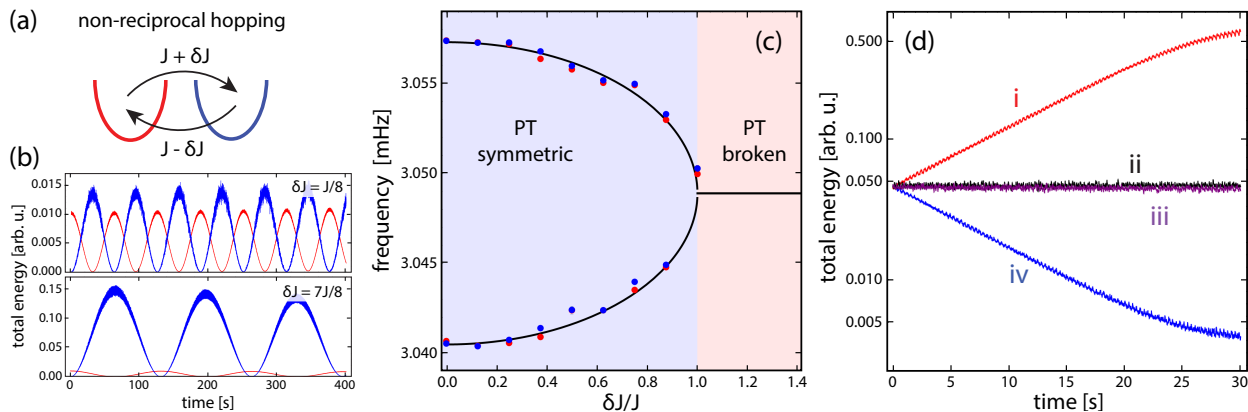
FIG. 6. **Non-reciprocal hopping and PT symmetry breaking (a)** Two oscillators coupled with non-reciprocal hopping terms, $J \pm \delta J$. **(b)** Experimental population dynamics, starting with all energy in the first oscillator, for $\delta J/J = 0.125$ and $\delta J/J = 0.875$. **(c)** Fit-extracted peak locations of the power spectra based on experimental dynamics when starting with all energy in oscillator 1 (red dots) and with all energy in oscillator 2 (blue dots). The solid lines relate to the expected real eigenspectrum for $f_0 = 3.0489$ Hz and $J = 2\pi \times 8.4$ mHz. Error bars, which are smaller than the points, relate to the standard error of the fits to two Gaussian peaks. **(d)** Experimental total energy ($E_1 + E_2$) dynamics for excitation of eigenmodes in the case of fully asymmetric hopping (i and iv, with $J = 0$) and fully symmetric hopping (ii and iii, with $\delta J = 0$). For the symmetric case, the initial states relate to the two oscillators having equal energy and an initial relative oscillator phase of 0 (ii) and $\pi$ (iii). For the asymmetric case, the initial states relate to the two oscillators having equal energy and an initial relative oscillator phase of $\pi/2$ (i) and $-\pi/2$ (iv).

additionally finds a clear difference in the rate of population exchange (Rabi) dynamics observed in these two cases, with the dynamics slowing down appreciably as $\delta J/J$ approaches 1. This slow-down of the dynamics reflects a change to the eigenspectrum of the system, with the real eigenvalues coalescing at an exceptional point at $\delta J = J$, then transforming into imaginary eigenenergies, reflecting modes that undergo pure exponential decay or gain (ignoring the intra-envelope $\tilde{x}$ or $\tilde{p}$ dynamics at the bare frequency $\omega$).

We can again directly investigate this frequency response of the system upon approaching the $\mathcal{PT}$-breaking phase transition by simply Fourier-transforming the oscillation dynamics (taken over 400 s) and extracting a peak or peaks in the resulting power spectrum. We perform this analysis for both the cases of starting in oscillator 1 (red points) and oscillator 2 (blue points) and plot the resulting resonance values in Fig. 6(c). We perform this analysis solely in the $\mathcal{PT}$ symmetric regime (and up to $\delta J = J$), but find a clear closing of the energy gap in the system as the $\mathcal{PT}$ phase transition is approached. The measured frequency resonance values are in good agreement with the plotted theory curve, which relates to the form $f_0 \pm (J/2\pi)\sqrt{1 - (\delta J/J)^2}$ with $f_0 = 3.0489$ Hz and $J = 2\pi \times 8.4$ mHz.

To gain insight into the structure of the eigenmodes in the $\mathcal{PT}$-broken region, we seek to prepare these eigenmodes directly and observe their evolution. Figure 6(d) contrasts the behavior of prepared eigenmodes in the purely reciprocal case (curves ii and iii) to those in the purely non-reciprocal case (i and iv). In the reciprocal case ($\delta J = 0$, $J \approx 2\pi \times 8.4$ mHz), we prepare both in-

phase and out-of-phase eigenmodes of the coupled two-oscillator system, by initially driving the two oscillators (to deposit mechanical energy) with a controlled phase difference, to result in equal-energy superposition states with relative phases of 0 (ii) and $\pi$ (iii). We plot, in Fig. 6(d), the dynamics of the total energy $E = E_1 + E_2$ for these two cases, observing no appreciable variation in this reciprocal hopping scenario.

For the purely non-reciprocal case ($J = 0$, $\delta J \approx 2\pi \times 8.4$ mHz), the eigenstate structure is maximally distinct to the reciprocal case, yielding equal-energy superposition states with relative phases of $\pm\pi/2$. Using the same general initialization procedure, we prepare these eigenmodes of the non-reciprocal double-well, and we indeed observe distinct dynamics of the total energy, resulting in an exponential growth of the mode with relative phase $\pi/2$ (i) and an exponential attenuation of the mode with relative phase $-\pi/2$ (iv), at least up until the scale at which uncontrolled nonlinearities modify this picture.

### E. Synthetic Interactions

Finally, it is worth considering the outcome of weak non-linear feedback, as this is a way to simulate mean-field interactions in the Hamiltonian mapping. In the context of classical emulation experiments, this feedback based approach has connections to recent proposals and realizations in photonic [36] and electronic [37] networks. As an example of how feedback can introduce synthetic interactions, consider an energy-dependent feedback $F_i = (A_{i,i}X_i^2 + B_{i,i}P_i^2)X_i$. In this case, a measure
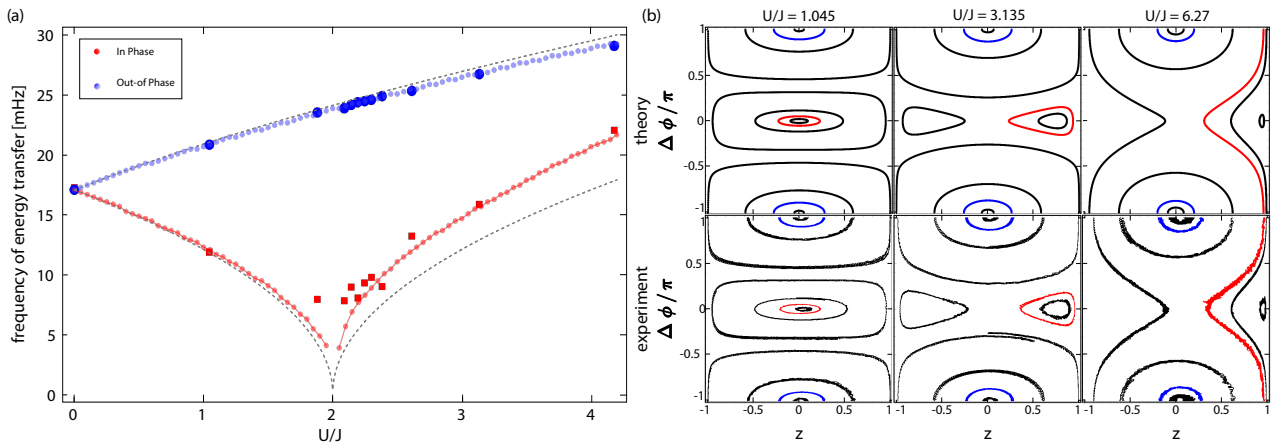
FIG. 7. **Eigenmodes and phase-space dynamics of a two-oscillator system with synthetic interactions. (a)** Mode frequencies for a double-well system with synthetic Hartree-like local interactions, implemented via self-feedback forces $F_i \propto E_i \tilde{x}_i$, where $E_i$ is the total mechanical energy in mode $i$. The frequencies are determined by fits to the experimental population imbalance dynamics of in-phase ($\Delta\phi = 0$) and out-of-phase ($\Delta\phi = \pi$) modes with an initial population imbalance $z = 0.3$. The out-of-phase mode stiffens with increasing $U/J$, while the in-phase mode softens across the self-trapping transition at $U/J \sim 2$. The dark blue circles (dark red squares) relate to experimental data, the light blue (red) points relate to numerical simulations, and the light gray dashed lines relate to the approximate analytical expressions described in the text. **(b)** Phase-space maps of the experimental dynamics of the relative oscillator phase $\Delta\phi$ and normalized energy imbalance $z$, for $U/J \approx 1$, 3, and 6. To note, small residual loss and/or gain terms leads to slightly disconnected trajectories in the experimental panels.

related to the "energy" of the system is used to create a non-linear on-site potential. By substituting the results in Eq. 7 into the form of the feedback, we have

$$F_i = \left[ \tilde{A}_{i,i}(\alpha_i + \alpha_i^*)^2 - \tilde{B}_{i,i}(\alpha_i - \alpha_i^*)^2 \right](\alpha_i + \alpha_i^*)$$
$$= \Omega_{-,i}(\alpha_i^3 + \alpha_i^{*3} + \alpha_i^2\alpha_i^* + \alpha_i^{*2}\alpha_i)$$
$$+ \Omega_{+,i}(\alpha_i^2\alpha_i^* + \alpha_i^{*2}\alpha_i),$$

where $2\omega\tilde{A}_{i,i} = A_{i,i}$, $2\tilde{B}_{i,i} = B_{i,i}$ and $\Omega_{\pm,i} = \tilde{A}_{i,i} \pm \tilde{B}_{i,i}$. When applying the RWA one should be careful in neglecting terms, since also the contribution from terms like $\alpha_i^3$ and $\alpha_i^{*2}\alpha_i$ can be discarded. In the former case, we have a much faster co-rotating wave, while in the latter case the net contribution in terms of frequency is $\approx e^{-i\omega t}$, which is counter-rotating with frequency $\approx 2\omega$ in the rotating frame. We are then left with:

$$F_{ij}^{\text{RWA}}\alpha_j = \begin{cases} 2\tilde{A}_{i,i}\,|\alpha_i|^2\alpha_i & \text{for } i = j \\ 0 & \text{for } i \neq j \end{cases}$$

Then the Hamiltonian in Eq. 10 follows as:

$$\mathcal{H} = \sum_i \omega\hat{\alpha}_i^\dagger\hat{\alpha}_i - \sum_i U_i\hat{\alpha}_i^\dagger\hat{\alpha}_i^\dagger\hat{\alpha}_i\hat{\alpha}_i, \quad U_i = \tilde{A}_{i,i}/\sqrt{2\omega},$$

where the second term is the on-site interaction. When written in terms of the equation of motion, Eq. 9, after replacing operators by c-numbers, features a term that reflects a local (diagonal, Hartree) mean-field interaction.

We now implement this local mean-field interaction in our two-oscillator double-well, with a common value of the nonlinear $U$ term applied to each oscillator. Here,

the term $U$ describes a local angular frequency shift due to mean-field nonlinearity, where the scale is such that it represents the shift that would be experienced by a given oscillator when all of the mechanical energy resides in said oscillator (with total mechanical energy approximately conserved in the following scenarios we explore). We calibrate the $U$ term for each oscillator by directly measuring the oscillator frequency in an uncoupled configuration for several values of the nonlinear feedback coefficient as well as several values of the mechanical energy. To note, while the engineered variations of the quartic nonlinearity are indeed found to be linearly tunable by application of feedback force terms $\propto (\tilde{x}_i^2 + \tilde{p}_i^2)\tilde{x}_i$, our calibrations additionally account for *natural* contributions to the oscillator nonlinearity due to the physical properties of the springs. For example, to achieve a "non-interacting" scenario, we in fact first cancel the relatively weak quartic nonlinearities that occur naturally due to the physical properties of our springs. Controlled nonlinear terms are then added to this "non-interacting" starting point. To note, this cancellation was performed for the study presented earlier in Fig. 6, and for all studies presented hereafter.

We now use our ability to apply a tunable nonlinearity to a tunnel-coupled system to explore the self-trapping phase transition of the canonical Josephson double-well [38, 39]. This mean-field model describing interacting bosonic excitations in a coherently coupled two-mode system is ubiquitous, describing physical systems ranging from polariton fluids [40] to cold atomic gases [41–44] to classical photonics [45–48]. Working with a fixed hopping $J \approx -2\pi \times 8.4$ mHz, we plot in

Fig. 7(a) the mode spectrum of this double-well system as we tune the nonlinear $U$ term. Specifically, we present the measured frequency dependence of prepared in-phase ($\Delta\phi = 0$) and out-of-phase ($\Delta\phi = \pi$) superposition modes, each having a small initial inter-well energy imbalance of $z = 0.3$. Similar to before, the relative phase $\Delta\phi$ and energy imbalance $z$ of the initial state is controlled by the relative amplitudes and phases of the applied sinusoidal drives during an initial preparation time step. Here, we determine the mode frequencies of the system by simply taking the inverse of the time separation between local extrema of the $z$ dynamics.

Specifically, in Fig. 7(a) we show how the measured in-phase and out-of-phase mode frequencies evolve as we tune the ratio of $U/J$ across the expected self-trapping phase transition at $U = 2J$. For zero quartic nonlinearity, we find excellent agreement between the measured frequencies of the in-phase and out-of-phase modes. Upon adding a weak $U$ term, however, these modes undergo radically different responses. The out-of-phase or $\pi$ mode becomes stiffened, seeing its frequency increase directly as $U$ is increased. The in-phase mode, in contrast, acquires a decreased mode frequency, leading to very slow dynamics near $U = 2J$. Beyond $U = 2J$, the frequency of the in-phase mode begins to increase, approaching that of the stiffened $\Delta\phi = \pi$ mode.

This observed difference in the modal frequency response – that the $\pi$ mode is continuously stiffened for increasing $U$, while the 0-phase mode undergoes mode-softening – is completely in line with the expected response associated with the Josephson double-well [49] and its supported dynamical self-trapping phase transition [38, 39]. Our measured mode frequencies are in fair agreement with approximate analytical forms for the 0-phase (plasma) mode and $\pi$ mode oscillation frequencies (Eqs. 4.7 and 4.10 of Ref. [38], respectively), which we plot as dashed black lines. We note some disagreement between our data and these analytical formulae, however, which is expected as these expressions are strictly valid only near $z = 0$. We find considerably better agreement between our data and the frequencies predicted by numerical simulations of an ideal Josephson double well for our given initial $z$ value of 0.3, plotted as the connected-dot curves of Fig. 7(a).

There exist further distinctions between the response of these two modes beyond their frequency behavior. Specifically, while the frequencies of the in-phase mode are similarly small on either side of the mode-softening encountered at $U = 2J$, we find that there are net swings of the energy imbalance $z$ for values $U < 2J$, *i.e.*, $z$ changes sign during the dynamics. In contrast, for $U > 2J$ we find that the excess mechanical energy becomes *self-trapped* to the oscillator in which it is initiated. This self-trapping transition of the in-phase mode reflects a drastic modification of the phase space portraits describing this system, as a separatrix moves through the phase space for increasing $U/J$ [38, 39].

We now examine this behavior in Fig. 7(b) by mapping out the phase space portraits for several values of $U/J$, utilizing the same approach as in Fig. 4(c). The out-of-phase modes, indicated by the blue trajectories, remain relatively unaffected in the three phase-space portraits for $U/J$ values of $\sim1$, 3, and 6. In contrast, trajectories starting near the unstable fixed point at $z = 0$ and $\Delta\phi = 0$ are significantly altered by the introduction of nonlinear $U$ term. These trajectories first become self-trapped in both relative phase $\Delta\phi$ and energy imbalance $z$ for moderate $U$ values just beyond the self-trapping transition (*i.e.*, for $U \sim 3J$). For still larger values, we encounter a different form of self-trapped mode, having $z$ values confined to either side of $z = 0$ but experiencing a running relative phase $\Delta\phi$. These results, in excellent agreement with theory, demonstrate how the incorporation of real-time measurements can enable both the implementation of synthetic interactions as well as visualization of the resulting nonlinear dynamics.

While the mean-field Josephson model with uniform interactions is naturally realized by a range of physical systems, our general approach to engineering synthetic nonlinearities allows for the extension to more intricate forms of interactions. As one simple demonstration of this, we examine in Fig. 8 the phase-space dynamics of a double-well system under the application of a well-dependent interaction term $U_1 = -U_2 = 2.2J$. We again start from different points in phase space (indicated by the colored disks) and study the phase-space dynamics of $z$ and $\Delta\phi$. Compared to the double-well with uniform quartic nonlinearity, the phase space map is significantly altered, showing two distinct self-trapped regions at relative phases of $\Delta\phi = 0$ and $\pi$. We again find excellent agreement between the observed trajectories and those predicted by theory.

### F.  Additional Possible Terms

Having given specific examples of the terms that we experimentally engineer in this work, we now briefly highlight, from a theoretical view-point, some general considerations for the type of terms that could be accessible with this approach [*cf.* Eq. 10]. Firstly, an advantage of using feedback to engineer the system is that the resulting Hamiltonian can be arbitrarily long-ranged or spatially-structured when it is scaled up to include more oscillators. For example, there are no fundamental theoretical constraints on the range or type of interactions and couplings that are possible between different oscillators, which allows for, in principle, arbitrary network connectivity and nonlinearities, provided that the feedback is weak.

Secondly, we have assumed above that the form of the feedback is time-independent, such that the resulting Hamiltonian is also time-independent. However, this is not required for the RWA to hold so long as the natural frequency, $\omega$, remains the largest frequency scale in the problem. This allows, *e.g.*, for the investigation of
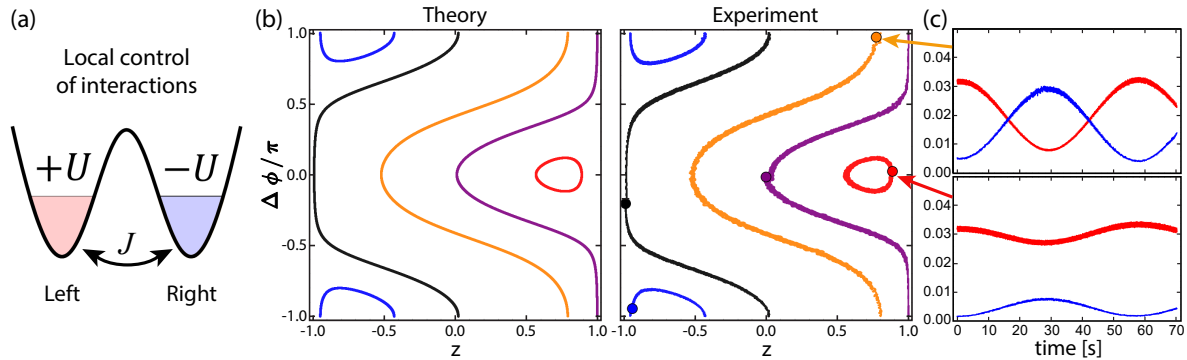
FIG. 8. **Phase-space dynamics in a two-oscillator system with oscillator-dependent interactions. (a)** Cartoon depiction of two-oscillator system mimicking a tunnel-coupled double well with well-dependent nonlinear interactions. **(b)** Left: theoretical phase-space portrait of relative phase and population in the double-well for $U = 2.2J$, revealing self-trapped trajectories (blue and red) and modes with full population swings (orange). Right: experimental phase-space dynamics starting from different initial conditions (indicated by colored circles). **(c)** Dynamics of the measured mechanical energy in the left and right oscillators (shown as red and blue signals, respectively, with arbitrary units), for the indicated experimental trajectories.

time-modulated Hamiltonians, to introduce still further control for engineering effective models [19, 20] or for the investigation of Floquet or stroboscopic Hamiltonians for their own sake [50, 51]. Alternatively, slow variations of the feedback parameters can enable the exploration of adiabatic geometric response and dynamical phase transitions, as well as the population and exploration of system eigenstates by Hamiltonian annealing.

Thirdly, as discussed above, the RWA reduces the feedback to $F_i \rightarrow \sum_j F_{ij}^{\text{RWA}} \alpha_j$ by only keeping co-rotating terms with a frequency $\approx \omega$ in the lab-frame. In general, such terms must have the number of $\alpha$ factors being one greater than the number of $\alpha^*$ factors, as any other combinations should average to zero in the $\omega \rightarrow \infty$ limit. This in turn means that in the RWA Hamiltonian [Eq. 10] the only terms present will contain equal numbers of $\alpha$ and $\alpha^*$ variables. In the language of quantum creation and annihilation operators, this corresponds to Hamiltonians which conserve the total number of particles in the system, but do not necessarily constrain the local particle number or the energy of the system. This therefore allows for many other types of terms, such as correlated hopping terms in which, for example, two particles hop at once. Considering only two-body (quartic) interactions, the degree of control afforded by this approach should have direct applications in the engineering of interacting Hamiltonians with exotic forms [52] or fine-tuned symmetries [53, 54]. This approach even allows for the direct engineering of Hamiltonians dominated by beyond-quartic terms [55], which could enable the realization of exotic phases requiring higher-order interactions, without complications due to the presence of lower-order terms [56].

### G. Beyond the RWA

Finally, it is worth noting that the RWA is strictly valid for weak feedback in the limit that $\omega \rightarrow \infty$. In general, there will be corrections to the RWA coming from the coupling between the $\alpha$ and $\alpha^*$ variables in the dynamical equations [*cf.* Eq. 8]. For example, as discussed in Refs. [19, 20], this can lead to corrections such as, at lowest order, an overall shift to the resonance frequency, which is a classical analogue of the Bloch-Siegert shift.

At even lower frequencies or for stronger feedback, the RWA cannot be applied and counter-rotating feedback terms, such as those linearly-dependent only on $\alpha_i^*$, should not be neglected. In such cases, by a similar line of reasoning to that above, the system can be mapped to a tight-binding Hamiltonian that now does not conserve the total particle number. As is well-known, such particle-non-conserving terms in bosonic Hamiltonians can lead to parametric instabilities, as recently studied, for example, in topological models [19, 20, 57–59].

### IV. CONCLUSION

We have presented a general recipe for engineering synthetic lattice tight-binding models, featuring both linear and nonlinear terms, based on the real-time measurement of and feedback on arrays of isolated mechanical oscillators. We have experimentally demonstrated the basic elements of this approach, including the control of real and imaginary site energies, complex and non-reciprocal inter-site hopping terms, and engineered nonlinear interactions. The presented approach is general, directly applicable to classical emulators based on mechanics or electronics and photonics [60], but also intimately related to recent ideas for the steering of quantum systems into new

many-body phases via measurement-based feedback [61–64]. Looking forward, as this approach is expanded to many-site arrays of classical oscillators, the ability to synthesize near-arbitrary mean-field lattice Hamiltonians will open up new opportunities for exploring exotic transport phenomena in a highly accessible laboratory setting. More generally, the incorporation of measurement-aided approaches promises to expand our capabilities for synthetic lattice and synthetic dimensions [65] engineering.

## V.   ACKNOWLEDGEMENTS

[1] P. Debye, Annalen der Physik **344**, 789 (1912).

[2] S. D. Huber, Nature Physics **12**, 621 (2016).

[3] C. L. Kane and T. C. Lubensky, Nature Physics **10**, 39 (2014).

[4] X. Mao and T. C. Lubensky, Annual Review of Condensed Matter Physics **9**, 413 (2018).

[5] G. Ma, M. Xiao, and C. T. Chan, Nature Reviews Physics **1**, 281 (2019).

[6] R. Süsstrunk and S. D. Huber, Science **349**, 47 (2015).

[7] L. M. Nash, D. Kleckner, A. Read, V. Vitelli, A. M. Turner, and W. T. M. Irvine, Proceedings of the National Academy of Sciences **112**, 14495 (2015).

[8] D. J. Apigo, K. Qian, C. Prodan, and E. Prodan, Phys. Rev. Materials **2**, 124203 (2018).

[9] E. Prodan and C. Prodan, Phys. Rev. Lett. **103**, 248101 (2009).

[10] R. Süsstrunk and S. D. Huber, Proceedings of the National Academy of Sciences **113**, E4767 (2016).

[11] V. Peri, Z.-D. Song, M. Serra-Garcia, P. Engeler, R. Queiroz, X. Huang, W. Deng, Z. Liu, B. A. Bernevig, and S. D. Huber, Science **367**, 797 (2020).

[12] W. Deng, X. Huang, J. Lu, V. Peri, F. Li, S. D. Huber, and Z. Liu, Nature Communications **11**, 3227 (2020).

[13] G. Salerno, A. Berardo, T. Ozawa, H. M. Price, L. Taxis, N. M. Pugno, and I. Carusotto, New Journal of Physics **19**, 055001 (2017).

[14] W. Cheng, E. Prodan, and C. Prodan, Phys. Rev. Lett. **125**, 224301 (2020).

[15] K. Qian, L. Zhu, K. H. Ahn, and C. Prodan, Phys. Rev. Lett. **125**, 225501 (2020).

[16] I. H. Grinberg, M. Lin, C. Harris, W. A. Benalcazar, C. W. Peterson, T. L. Hughes, and G. Bahl, Nature Communications **11**, 974 (2020).

[17] Y. Barlas and E. Prodan, Phys. Rev. B **98**, 094310 (2018).

[18] M. Serra-Garcia, V. Peri, R. Süsstrunk, O. R. Bilal, T. Larsen, L. G. Villanueva, and S. D. Huber, Nature **555**, 342 (2018).

[19] G. Salerno, T. Ozawa, H. M. Price, and I. Carusotto, Phys. Rev. B **93**, 085105 (2016).

[20] G. Salerno and I. Carusotto, EPL (Europhysics Letters) **106**, 24002 (2014).

[21] Y.-T. Wang, P.-G. Luan, and S. Zhang, New Journal of Physics **17**, 073031 (2015).

[22] N. P. Mitchell, L. M. Nash, D. Hexner, A. M. Turner, and W. T. M. Irvine, Nature Physics **14**, 380 (2018).

[23] L. Sirota, R. Ilan, Y. Shokef, and Y. Lahini, Phys. Rev. Lett. **125**, 256802 (2020).

[24] M. Brandenbourger, X. Locsin, E. Lerner, and C. Coulais, Nature Communications **10**, 4608 (2019).

[25] A. Ghatak, M. Brandenbourger, J. van Wezel, and C. Coulais, Proceedings of the National Academy of Sciences  (2020), 10.1073/pnas.2010580117.

[26] Here we consider only instantaneous dependencies, but this approach also allows for time-retarded interactions.

[27] R. Pouladian-Kari, Measurement Science and Technology **1**, 1377 (1990).

[28] M. Fruchart, R. Hanai, P. B. Littlewood, and V. Vitelli, Nature **592**, 363 (2021).

[29] Y. Ashida, Z. Gong, and M. Ueda, Advances in Physics **69**, 249 (2020).

[30] S. Shankar, A. Souslov, M. J. Bowick, M. C. Marchetti, and V. Vitelli, "Topological active matter,"  (2020), arXiv:2010.00364 [cond-mat.soft].

[31] W. Gou, T. Chen, D. Xie, T. Xiao, T.-S. Deng, B. Gadway, W. Yi, and B. Yan, Phys. Rev. Lett. **124**, 070402 (2020).

[32] N. Hatano and D. R. Nelson, Phys. Rev. Lett. **77**, 570 (1996).

[33] N. Hatano and D. R. Nelson, Phys. Rev. B **56**, 8651 (1997).

[34] N. Hatano and D. R. Nelson, Phys. Rev. B **58**, 8384 (1998).

[35] S. Liu, R. Shao, S. Ma, L. Zhang, O. You, H. Wu, Y. J. Xiang, T. J. Cui, and S. Zhang, Research **2021**, 5608038 (2021).

[36] C. W. Duncan, M. J. Hartmann, R. R. Thomson, and P. Öhberg, The European Physical Journal D **74**, 84 (2020).

[37] Y. Hadad, J. C. Soric, A. B. Khanikaev, and A. Alù, Nature Electronics **1**, 178 (2018).

[38] S. Raghavan, A. Smerzi, S. Fantoni, and S. R. Shenoy, Phys. Rev. A **59**, 620 (1999).

[39] B. Juliá-Díaz, D. Dagnino, M. Lewenstein, J. Martorell, and A. Polls, Phys. Rev. A **81**, 023615 (2010).

[40] M. Abbarchi, A. Amo, V. G. Sala, D. D. Solnyshkov, H. Flayac, L. Ferrier, I. Sagnes, E. Galopin, A. Lemaître, G. Malpuech, and J. Bloch, Nature Physics **9**, 275 (2013).

[41] M. Albiez, R. Gati, J. Fölling, S. Hunsmann, M. Cristiani, and M. K. Oberthaler, Phys. Rev. Lett. **95**, 010402 (2005).

[42] S. Levy, E. Lahoud, I. Shomroni, and J. Steinhauer, Nature **449**, 579 (2007).

[43] T. Anker, M. Albiez, R. Gati, S. Hunsmann, B. Eiermann, A. Trombettoni, and M. K. Oberthaler, Phys. Rev. Lett. **94**, 020403 (2005).

[44] T. Zibold, E. Nicklas, C. Gross, and M. K. Oberthaler, Phys. Rev. Lett. **105**, 204101 (2010).

[45] R. Y. Chiao, E. Garmire, and C. H. Townes, Phys. Rev. Lett. **13**, 479 (1964).

[46] A. Hasegawa and F. Tappert, Applied Physics Letters **23**, 142 (1973).

[47] L. F. Mollenauer, R. H. Stolen, and J. P. Gordon, Phys. Rev. Lett. **45**, 1095 (1980).

[48] A. W. Snyder, D. J. Mitchell, L. Poladian, and F. Ladouceur, Opt. Lett. **16**, 21 (1991).

[49] However, the roles of the two modes are reversed, as we operate with a negative $J$ value (effectively a $\pi$ tunneling phase). In the canonical bosonic Josephson junction [38], the out-of-phase $\pi$-mode undergoes mode-softening while the in-phase plasma mode is purely stiffened.

[50] M. Bukov, L. D'Alessio, and A. Polkovnikov, Advances in Physics **64**, 139 (2015).

[51] G. Casati and L. Molinari, Progress of Theoretical Physics Supplement **98**, 287 (1989).

[52] P. Matus, K. Giergiel, and K. Sacha, Phys. Rev. A **103**, 023320 (2021).

[53] M. Pretko, Phys. Rev. B **100**, 245103 (2019).

[54] A. Mil, T. V. Zache, A. Hegde, A. Xia, R. P. Bhatt, M. K. Oberthaler, P. Hauke, J. Berges, and F. Jendrzejewski, arXiv:1909.07641 (2019).

[55] F. Petiziol, M. Sameti, S. Carretta, S. Wimberger, and F. Mintert, "Quantum simulation of three-body interactions in weakly driven quantum systems," (2020), arXiv:2011.03399 [quant-ph].

[56] M. F. Lapa, J. C. Y. Teo, and T. L. Hughes, Phys. Rev. B **93**, 115131 (2016).

[57] R. Shindou, R. Matsumoto, S. Murakami, and J.-i. Ohe, Phys. Rev. B **87**, 174427 (2013).

[58] V. Peano, M. Houde, C. Brendel, F. Marquardt, and A. A. Clerk, Nature Communications **7**, 10779 (2016).

[59] G. Engelhardt and T. Brandes, Phys. Rev. A **91**, 053621 (2015).

[60] T. Ozawa, H. M. Price, A. Amo, N. Goldman, M. Hafezi, L. Lu, M. C. Rechtsman, D. Schuster, J. Simon, O. Zilberg, and I. Carusotto, Rev. Mod. Phys. **91**, 015006 (2019).

[61] H. M. Hurst and I. B. Spielman, Phys. Rev. A **99**, 053612 (2019).

[62] H. M. Hurst, S. Guo, and I. B. Spielman, Phys. Rev. Research **2**, 043325 (2020).

[63] M. H. Muñoz Arias, P. M. Poggi, P. S. Jessen, and I. H. Deutsch, Phys. Rev. Lett. **124**, 110503 (2020).

[64] M. H. Muñoz Arias, I. H. Deutsch, P. S. Jessen, and P. M. Poggi, Phys. Rev. A **102**, 022610 (2020).

[65] T. Ozawa and H. M. Price, Nat. Rev. Phys. **1**, 349 (2019).

# Appendix C

# Analytics for the non-interacting case

In this appendix, the analytics for the trimer in Chapter 5 are carried out.

As shown in Fig. 5.2, the localization spotted in the lung-shaped region discussed in Sec. 5.2 extends down to the non-interacting case, $U = 0$. As this phenomenon happens at $\phi = \pi/2$, that is to say where the eigenenergies are equally spaced, we may expect that the equal level spacing can explain this phenomenon in the non interacting case. In order to confirm this intuition, analytics will be carried out in the following for the case of $\phi \in ]0, \pi[$, as the same results apply, with minor changes, to the other half of the parameter space.

The eigenvectors of the Hamiltonian in Eq. 5.2 for $\phi \in ]0, \pi[$ are:

$$v_- = \frac{1}{\sqrt{3}} \begin{pmatrix} 1 \\ 1 \\ 1 \end{pmatrix}, \quad v_0 = \frac{1}{\sqrt{3}} \begin{pmatrix} -e^{i\pi/3} \\ -e^{-i\pi/3} \\ 1 \end{pmatrix} \quad v_+ = \frac{1}{\sqrt{3}} \begin{pmatrix} -e^{-i\pi/3} \\ -e^{i\pi/3} \\ 1 \end{pmatrix}$$

to which the energies $\varepsilon_-$, $\varepsilon_0$, $\varepsilon_+$ are associated, representing the energy of the ground state, and the first and second excited states, respectively.

Up to an overall phase factor, the initial state $(1, 0, 0)^{\mathrm{T}}$ can be written as the following

linear combination of the eigenvectors:

$$|\alpha(t=0)\rangle = \frac{1}{\sqrt{3}}\left(|v_-\rangle - e^{-i\pi/3}|v_0\rangle - e^{i\pi/3}|v_+\rangle\right),$$

then, the time evolution is described by:

$$|\alpha(t)\rangle = \frac{1}{\sqrt{3}}\left(e^{-i\varepsilon_- t}|v_-\rangle - e^{-i\varepsilon_0 t}e^{-i\pi/3}|v_0\rangle - e^{-i\varepsilon_+ t}e^{i\pi/3}|v_+\rangle\right), \qquad \text{(C.1)}$$

that will be used to evaluate the $\langle\text{IPR}\rangle$ as described in Eq. 5.4.

Let us consider $\phi \neq \pi/2$; the first step in order to determine the time average of the IPR as defined in Eq. 5.4 is evaluating $n_i = |\alpha_i|^2$; for the site initialy loaded it yields:

$$\begin{aligned}
n_1 &= \left|\frac{1}{\sqrt{3}}\left(\frac{1}{\sqrt{3}}e^{-i\varepsilon_- t} + \frac{1}{\sqrt{3}}e^{-i\varepsilon_0 t - i\pi/3} + \frac{1}{\sqrt{3}}e^{-i\varepsilon_+ t + i\pi/3}\right)\right|^2 \\
&= \frac{1}{9}\Big|\cos\varepsilon_- t + \cos(\varepsilon_0 t - i\pi/3) + \cos(\varepsilon_+ t + i\pi/3) \\
&\quad - i\sin\varepsilon_- t - i\sin(\varepsilon_0 t - i\pi/3) - i\sin(\varepsilon_+ t + i\pi/3)\Big|^2.
\end{aligned}$$

Before expanding this square and evaluating the expectation value of $n_1$, the following short notation is introduced: instead of writing $\cos(\bullet)$ or $\sin(\bullet)$, I will make use of the short notation $c_\nu$ and $s_\nu$, and $\nu = -$, $0$, $+$ to indicate the argument of the trigonometric functions, respectively $\varepsilon_- t$, $\varepsilon_0 t - \pi/3$ and $\varepsilon_+ t + \pi/3$. By doing so, this last equation reads:

$$\begin{aligned}
n_1 &= \frac{1}{9}|c_- + c_0 + c_+ - is_- - is_0 - is_+|^2 \\
&= \frac{1}{9}(3 + 2c_-c_0 + 2c_-c_+ + 2c_0c_+ - 2s_-s_0 - 2s_-s_+ - 2s_0s_+).
\end{aligned} \qquad \text{(C.2)}$$

We now want to find the time averate of $n_1$ and of $n_1^2$ to check the numerical results in Section 5.2. As the time average of a generic time-dependent quantity $x(t)$ is defined as $\langle n_1\rangle \equiv \int_0^T \mathrm{d}(t)\, n_1(t)/T$, we obtain for an asymptotically long time $T \to \infty$ that $\langle n_1\rangle = 1/3$, that matches the numerical results in Fig. 5.3. When working through the same steps for $n_2$ and $n_3$ the result is exactly the same with a slightly different encoding of the subscripts

$-$, 0, $+$. Evaluating $n_1^2$ yields:

$$n_1^2 = \frac{1}{81}\left(9 + 4c_-^2 c_0^2 + 4c_0^2 c_+^2 + 4c_-^2 c_+^2 + 4s_-^2 s_0^2 + 4s_0^2 s_+^2 + 4s_-^2 s_+^2 + \dots\right)$$

where the dots indicate terms that have odd powers of cos and sin, that average to 0 over long times. Using that:

$$\langle c^4 \rangle = \langle s^4 \rangle = \frac{3}{8}; \quad \langle c_\mu^2 s_\nu^2 \rangle = \langle c_\mu^2 c_\nu^2 \rangle = \langle s_\mu^2 s_\nu^2 \rangle = \frac{1}{4};$$

where $\mu, \nu = -, 0, +$, we find that the time average for the square of the populations $\langle n_i^2 \rangle$ yields the same result for the threesites, namely 15/81. It follows that IPR $= 27/15 \approx 1.8$.

We now investigate what happens right at $\pi/2$: where the zero of the energy can be chosen in such a way that $\varepsilon_0 = 0$ and $\varepsilon_- = -\varepsilon_+ \equiv \varepsilon$. Because of this equal spacing between the energy values, the calculation changes slightly, as can be immediately seen by comparing Eq. C.2 with:

$$\begin{aligned} n_1 &= \left|\frac{1}{\sqrt{3}}\left(\frac{1}{\sqrt{3}}e^{-i\varepsilon t} + \frac{1}{\sqrt{3}}e^{-i\pi/3} + \frac{1}{\sqrt{3}}e^{i\varepsilon t + i\pi/3}\right)\right|^2 \\ &= \frac{1}{9}|1 + 2\sin\varepsilon t + \pi/6|^2. \end{aligned}$$

Also in this case, the results for $n_2$ and $n_3$ are completely analogous (in which case it is convenient to factor out $e^{-i\pi/6}$ and $e^{-i\pi/3}$, respectively), and the evaluation of the time average yields 1/3 in all the three cases, as expected from the results in Fig. 5.3. Taking the square of these quantities and evaluating the time average, one obtains straightforwardly that $\langle n_1^2 \rangle = \langle n_2^2 \rangle = \langle n_3^2 \rangle = 19/81$, hence the $\langle$IPR$\rangle$ yields $57/81 \approx 0.70$.

Finally, when $\phi = 0$ using the Gram-Schmidt algorithm, the basis vectors can be written as:

$$v_- = \frac{1}{\sqrt{3}}\begin{pmatrix} 1 \\ 1 \\ 1 \end{pmatrix}, \quad v_0 = \frac{1}{\sqrt{2}}\begin{pmatrix} -1 \\ 0 \\ 1 \end{pmatrix} \quad v_+ = \frac{1}{\sqrt{6}}\begin{pmatrix} -1 \\ 2 \\ -1 \end{pmatrix}.$$

| flux | numerics | analytics |
|------|----------|-----------|
| $\phi \neq \pi/2,\, 3\pi/2$ | $\sim 0.51$ | 0.55 |
| $\phi = 0$ | $\sim 0.48$ | 0.55 |
| $\phi = \pi/2$ | $\sim 0.64$ | 0.70 |
| $\phi = \pi$ | $\sim 0.48$ | 0.55 |
| $\phi = 3\pi/2$ | $\sim 0.64$ | 0.70 |

**Table C1:** Values of the $\langle \mathrm{IPR} \rangle$ for both the numerics and the analytics. Note that at $\phi = \pi/2$ the wave packet is more localized (lower $\langle \mathrm{IPR} \rangle$ ) than for other values. These results agree with the numerics in the non-interacting case (*c.f.* Figs. 5.2 and 5.3).

Then, setting the zero of the energy at the first excited state (degenerate with the second excited state), $\varepsilon_+ = \varepsilon_0 = 0$ and re-labeling $\varepsilon_- = \varepsilon$, the state describing the time evolution of the system at $\phi = 0$, $\left| \alpha^{(0)}(t) \right\rangle$ can be written as:

$$\left| \alpha^{(0)}(t) \right\rangle = \frac{1}{\sqrt{3}} e^{-i\epsilon t} \left| v_- \right\rangle - \frac{1}{\sqrt{2}} \left| v_0 \right\rangle - \frac{1}{\sqrt{6}} \left| v_+ \right\rangle .$$

Following the same procedure as before, there is a difference: on average, the population is not equally spread over the three sites, $\langle n_1 \rangle = 5/9$ and $\langle n_2 \rangle = \langle n_3 \rangle = 2/9$. This is due to the uneven distribution of the initial wave packet on the three sites as one can see when comparing this last equation with Eq. C.1. Anyway the $\langle \mathrm{IPR} \rangle$ yields the same result as before, $15/27 \approx 0.55$.

A completely analogous result is obtained in the $\phi = \pi$ case.

These results not only confirm the qualitatively behaviour of the system in the non-interacting case (*c.f.* Figs. 5.2 and 5.3), but also yield the same numerical value as the simulations, as summarized in Table C1, where the result of the calculations made for $\phi$ up to $2\pi$ are listed.

Furthermore, the plot in Fig. C.1 represents the slice at $U = 0$ of the plot of the $\langle \mathrm{IPR} \rangle$ in the left panel of Figs. 5.2.
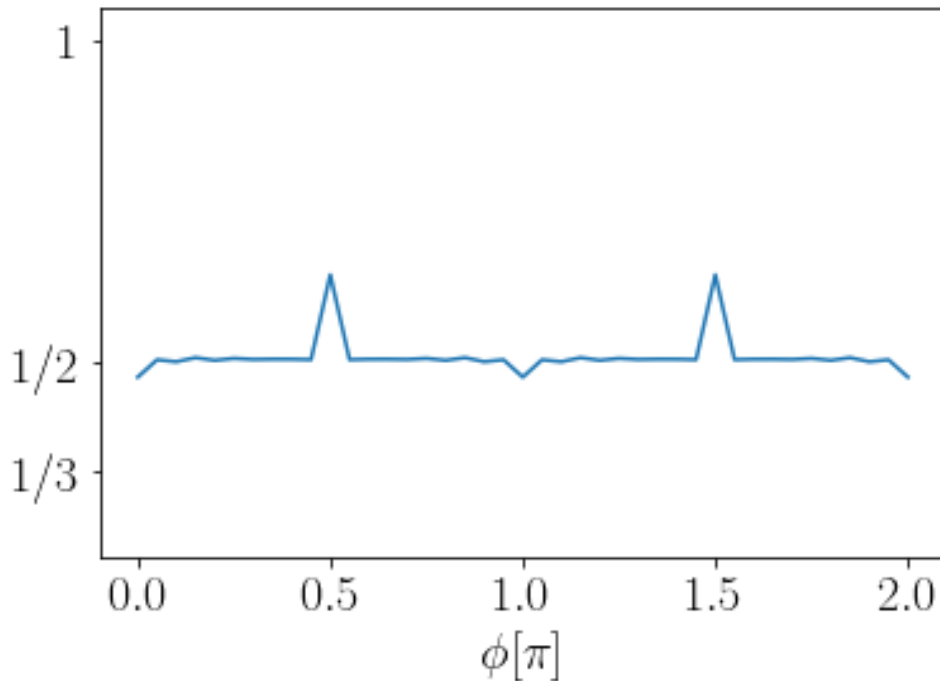
**Figure C.1:** Plot of $\langle \text{IPR} \rangle$ (Eq. 5.4) in the non-interacting case, $U = 0$ as a function of the phase pierced through the plaquette. The peaks in $\langle \text{IPR} \rangle$ appear as expected at $\phi = \pi/2$ and $3\pi/2$, in agreement with the numerics as explained in the text. Line is a guide to the eye.

Finally, a note on the current. As mentioned in Sec. 5.2, in the non-interacting case the chiral current averages to zero, *c.f.* Fig. 5.2. This phenomenon is due to the initial state being in an equal superposition of the three eigenstates, each of them contributing with a chiral current that is characteristic [109].

Interestingly, the sum of the chiral currents characterizing the eigenstates is zero, as shown in Fig. C.2 where the currents associated with the eigenstates are plotted versus the phase pierced through the plaquette. Their sum is plotted as the dotted line that is always zero, explaining the behavior of the current shown in Fig. 5.2.
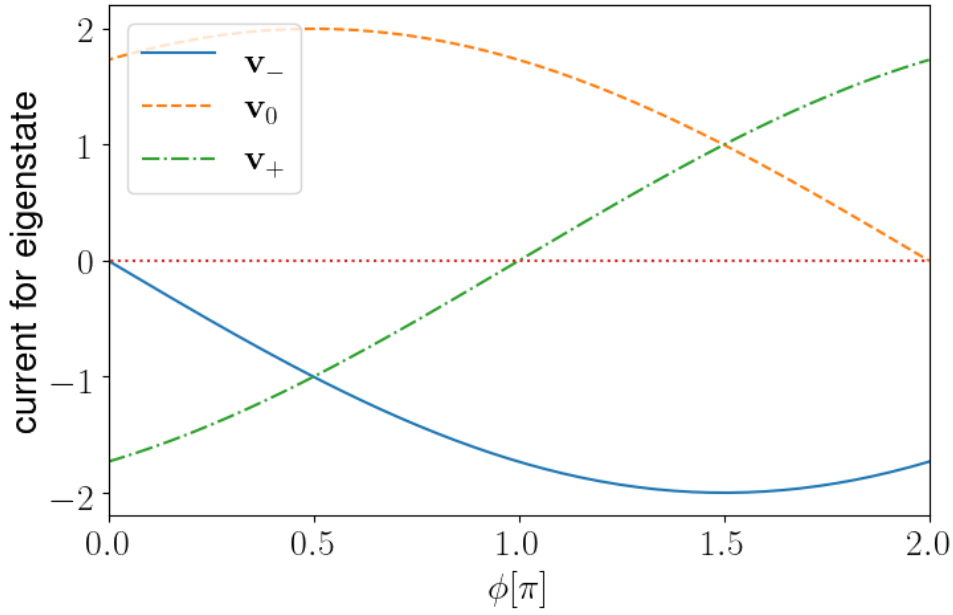
**Figure C.2:** Plot of the currents characterizing the eigenstates of the Hamiltonian for different values of the phase pierced through the plaquette: the blue solid line represents the current associated with the ground state, the dashed line the current associated with the first excited state, and the dash-dotted line is the current associated with the second excited state. The dotted line represent their sum, that is constantly zero.

# Bibliography

[1] Yaashnaa Singhal, Enrico Martello, Shraddha Agrawal, Tomoki Ozawa, Hannah Price, and Bryce Gadway. Measuring the adiabatic non-hermitian berry phase in feedback-coupled oscillators. *arXiv preprint arXiv:2205.02700*, 2022.

[2] Enrico Martello, Yaashnaa Singhal, Bryce Gadway, Tomoki Ozawa, and Hannah M Price. Coexistence of stable and unstable population dynamics in a nonlinear non-hermitian mechanical dimer. *arXiv preprint arXiv:2302.03572*, 2023.

[3] Ramamurti Shankar. *Principles of quantum mechanics*. Springer Science & Business Media, 2012.

[4] Jun John Sakurai and Jim Napolitano. *Modern quantum mechanics*. Pearson Higher Ed, second edition, 2011.

[5] Dorje C Brody. Biorthogonal quantum mechanics. *Journal of Physics A: Mathematical and Theoretical*, 47(3):035305, 2013.

[6] Patrick Dorey, Clare Dunning, and Roberto Tateo. A reality proof in pt-symmetric quantum mechanics. *Czechoslovak journal of physics*, 54(1):35–41, 2004.

[7] Zongping Gong, Yuto Ashida, Kohei Kawabata, Kazuaki Takasan, Sho Higashikawa, and Masahito Ueda. Topological phases of non-hermitian systems. *Phys. Rev. X*, 8:031079, Sep 2018.

[8] Ananya Ghatak and Tanmoy Das. New topological invariants in non-Hermitian systems. *Journal of Physics: Condensed Matter*, 31(26):263001, 2019.

[9] Carl M Bender and Stefan Boettcher. Real spectra in non-hermitian hamiltonians having p t symmetry. *Physical review letters*, 80(24):5243, 1998.

[10] Ramy El-Ganainy, Konstantinos G Makris, Mercedeh Khajavikhan, Ziad H Musslimani, Stefan Rotter, and Demetrios N Christodoulides. Non-hermitian physics and PT symmetry. *Nature Physics*, 14(1):11–19, 2018.

[11] Carl M Bender, MV Berry, and Aikaterini Mandilara. Generalized pt symmetry and real spectra. *Journal of Physics A: Mathematical and General*, 35(31):L467, 2002.

[12] Yuto Ashida, Zongping Gong, and Masahito Ueda. Non-hermitian physics. *Advances in Physics*, 69(3):249–435, 2020.

[13] Ali Mostafazadeh. Pseudo-hermiticity versus pt symmetry: the necessary condition for the reality of the spectrum of a non-hermitian hamiltonian. *Journal of Mathematical Physics*, 43(1):205–214, 2002.

[14] Konstantinos G Makris, R El-Ganainy, DN Christodoulides, and Ziad H Musslimani. Beam dynamics in p t symmetric optical lattices. *Physical Review Letters*, 100(10):103904, 2008.

[15] Christian E Rüter, Konstantinos G Makris, Ramy El-Ganainy, Demetrios N Christodoulides, Mordechai Segev, and Detlef Kip. Observation of parity–time symmetry in optics. *Nature physics*, 6(3):192–195, 2010.

[16] A. Guo, G. J. Salamo, D. Duchesne, R. Morandotti, M. Volatier-Ravat, V. Aimez, G. A. Siviloglou, and D. N. Christodoulides. Observation of $\mathcal{PT}$-symmetry breaking in complex optical potentials. *Phys. Rev. Lett.*, 103:093902, Aug 2009.

[17] ZH Musslimani, Konstantinos G Makris, Ramy El-Ganainy, and Demetrios N Christodoulides. Optical solitons in p t periodic potentials. *Physical Review Letters*, 100(3):030402, 2008.

[18] Ching Hua Lee, Stefan Imhof, Christian Berger, Florian Bayer, Johannes Brehm, Laurens W Molenkamp, Tobias Kiessling, and Ronny Thomale. Topolectrical circuits. *Communications Physics*, 1(1):39, 2018.

[19] Steven A Cummer, Johan Christensen, and Andrea Alù. Controlling sound with acoustic metamaterials. *Nature Reviews Materials*, 1(3):1–13, 2016.

[20] Ananya Ghatak, Martin Brandenbourger, Jasper van Wezel, and Corentin Coulais. Observation of non-Hermitian topology and its bulk-edge correspondence in an active mechanical metamaterial. *Proceedings of the National Academy of Sciences*, 117(47):29561–29568, 2020.

[21] Ritika Anandwade, Yaashnaa Singhal, Sai Naga Manoj Paladugu, Enrico Martello, Michael Castle, Shraddha Agrawal, Ellen Carlson, Cait Battle-McDonald, Tomoki Ozawa, Hannah M Price, et al. Synthetic mechanical lattices with synthetic interactions. *arXiv preprint arXiv:2107.09649*, 2021.

[22] Li Xin, Yu Siyuan, Liu Harry, Lu Minghui, and Chen Yanfeng. Topological mechanical metamaterials: A brief review. *Current Opinion in Solid State and Materials Science*, 24(5):100853, 2020.

[23] Constantinos Valagiannopoulos. Multistability in coupled nonlinear metasurfaces. *IEEE Transactions on Antennas and Propagation*, 70(7):5534–5540, 2022.

[24] Yertay Zhiyenbayev, Yannis Kominis, Constantinos Valagiannopoulos, Vassilios Kovanis, and Anastasios Bountis. Enhanced stability, bistability, and exceptional points in saturable active photonic couplers. *Physical Review A*, 100(4):043834, 2019.

[25] Stefano Longhi. Half-spectral unidirectional invisibility in non-Hermitian periodic optical structures. *Optics letters*, 40(23):5694–5697, 2015.

[26] Romain Fleury, Dimitrios Sounas, and Andrea Alu. An invisible acoustic sensor based on parity-time symmetry. *Nature communications*, 6(1):1–7, 2015.

[27] Jan Carl Budich and Emil J Bergholtz. Non-hermitian topological sensors. *Physical Review Letters*, 125(18), 2020.

[28] Mohammad H Teimourpour, Li Ge, Demetrios N Christodoulides, and Ramy El-Ganainy. Non-hermitian engineering of single mode two dimensional laser arrays. *Scientific reports*, 6(1):33253, 2016.

[29] Carl M Bender. Making sense of non-Hermitian Hamiltonians. *Reports on Progress in Physics*, 70(6):947–1018, may 2007.

[30] Carl M Bender. *PT symmetry: In quantum and classical physics*. World Scientific, 2019.

[31] WD Heiss. The physics of exceptional points. *Journal of Physics A: Mathematical and Theoretical*, 45(44):444016, 2012.

[32] Mohammad-Ali Miri and Andrea Alù. Exceptional points in optics and photonics. *Science*, 363(6422), 2019.

[33] Rosie Hayward and Fabio Biancalana. Complex berry phase dynamics in $\mathcal{PT}$-symmetric coupled waveguides. *Phys. Rev. A*, 98:053833, Nov 2018.

[34] P Wang, KL Zhang, and Z Song. Transition from degeneracy to coalescence: Theorem and applications. *Physical Review B*, 104(24):245406, 2021.

[35] Ali Mostafazadeh. Spectral singularities of complex scattering potentials and infinite reflection and transmission coefficients at real energies. *Physical review letters*, 102(22):220402, 2009.

[36] Stefano Longhi. PT-symmetric laser absorber. *Physical Review A*, 82(3):031801, 2010.

[37] Michael Victor Berry. Quantal phase factors accompanying adiabatic changes. *Proceedings of the Royal Society of London. A. Mathematical and Physical Sciences*, 392(1802):45–57, 1984.

[38] Alexander I Nesterov and F Aceves de la Cruz. Complex magnetic monopoles, geometric phases and quantum evolution in the vicinity of diabolic and exceptional points. *Journal of Physics A: Mathematical and Theoretical*, 41(48):485304, 2008.

[39] Rosie Hayward and Fabio Biancalana. Monopole-antimonopole instability in non-hermitian coupled waveguides. *Phys. Rev. A*, 101:043846, Apr 2020.

[40] S. Raghavan, A. Smerzi, S. Fantoni, and S. R. Shenoy. Coherent oscillations between two weakly coupled bose-einstein condensates: Josephson effects, $\pi$ oscillations, and macroscopic quantum self-trapping. *Phys. Rev. A*, 59:620–633, Jan 1999.

[41] Augusto Smerzi, Stefano Fantoni, Stefano Giovanazzi, and SR Shenoy. Quantum coherent atomic tunneling between two trapped bose-einstein condensates. *Physical Review Letters*, 79(25):4950, 1997.

[42] E. M. Graefe, H. J. Korsch, and A. E. Niederle. Mean-field dynamics of a non-hermitian bose-hubbard dimer. *Phys. Rev. Lett.*, 101:150408, Oct 2008.

[43] Eva-Maria Graefe, Hans Jürgen Korsch, and Astrid Elisa Niederle. Quantum-classical correspondence for a non-Hermitian Bose-Hubbard dimer. *Phys. Rev. A*, 82:013629, Jul 2010.

[44] Amos Hardy and William Streifer. Coupled mode theory of parallel waveguides. *Journal of lightwave technology*, 3(5):1135–1146, 1985.

[45] DN Christodoulides and RI Joseph. Discrete self-focusing in nonlinear arrays of coupled waveguides. *Optics letters*, 13(9):794–796, 1988.

[46] M. I. Molina and G. P. Tsironis. Dynamics of self-trapping in the discrete nonlinear schrödinger equation. *Physica D: Nonlinear Phenomena*, 65(3):267–273, 1993.

[47] VM Kenkre and DK Campbell. Self-trapping on a dimer: time-dependent solutions of a discrete nonlinear schrödinger equation. *Physical Review B*, 34(7):4959, 1986.

[48] Hamidreza Ramezani, Tsampikos Kottos, Ramy El-Ganainy, and Demetrios N Christodoulides. Unidirectional nonlinear pt-symmetric optical structures. *Physical Review A*, 82(4):043803, 2010.

[49] Marco Abbarchi, A Amo, VG Sala, DD Solnyshkov, H Flayac, L Ferrier, I Sagnes, E Galopin, A Lemaître, G Malpuech, et al. Macroscopic quantum self-trapping and josephson oscillations of exciton polaritons. *Nature Physics*, 9(5):275–279, 2013.

[50] Antonio Barone and Gianfranco Paterno. *Physics and applications of the Josephson effect*, volume 1. Wiley Online Library, 1982.

[51] Michael Albiez, Rudolf Gati, Jonas Fölling, Stefan Hunsmann, Matteo Cristiani, and Markus K Oberthaler. Direct observation of tunneling and nonlinear self-trapping in a single bosonic josephson junction. *Physical review letters*, 95(1):010402, 2005.

[52] Eva-Maria Graefe. Stationary states of a PT symmetric two-mode Bose–Einstein condensate. *Journal of Physics A: Mathematical and Theoretical*, 45(44):444015, 2012.

[53] Naomichi Hatano and David R. Nelson. Localization transitions in non-Hermitian quantum mechanics. *Phys. Rev. Lett.*, 77:570–573, Jul 1996.

[54] Naomichi Hatano and David R. Nelson. Vortex pinning and non-Hermitian quantum mechanics. *Phys. Rev. B*, 56:8651–8673, Oct 1997.

[55] Naomichi Hatano and David R. Nelson. Non-Hermitian delocalization and eigenfunctions. *Phys. Rev. B*, 58:8384–8390, Oct 1998.

[56] Tony E. Lee. Anomalous edge state in a non-hermitian lattice. *Phys. Rev. Lett.*, 116:133903, Apr 2016.

[57] Emil J. Bergholtz, Jan Carl Budich, and Flore K. Kunst. Exceptional topology of non-hermitian systems. *Rev. Mod. Phys.*, 93:015005, Feb 2021.

[58] Bo Peng, Şahin Kaya Özdemir, Fuchuan Lei, Faraz Monifi, Mariagiovanna Gianfreda, Gui Lu Long, Shanhui Fan, Franco Nori, Carl M Bender, and Lan Yang. Parity–time-symmetric whispering-gallery microcavities. *Nature Physics*, 10(5):394–398, 2014.

[59] Freek Ruesink, Mohammad-Ali Miri, Andrea Alu, and Ewold Verhagen. Nonreciprocity and magnetic-free isolation based on optomechanical interactions. *Nature communications*, 7(1):1–8, 2016.

[60] Kejie Fang, Jie Luo, Anja Metelmann, Matthew H Matheny, Florian Marquardt, Aashish A Clerk, and Oskar Painter. Generalized non-reciprocity in an optomechanical circuit via synthetic magnetism and reservoir engineering. *Nature Physics*, 13(5):465–471, 2017.

[61] Sebastian Weidemann, Mark Kremer, Tobias Helbig, Tobias Hofmann, Alexander Stegmaier, Martin Greiter, Ronny Thomale, and Alexander Szameit. Topological funneling of light. *Science*, 368(6488):311–314, 2020.

[62] Motohiko Ezawa. Non-hermitian boundary and interface states in nonreciprocal higher-order topological metals and electrical circuits. *Phys. Rev. B*, 99:121411, Mar 2019.

[63] Motohiko Ezawa. Electric-circuit simulation of the schrödinger equation and non-hermitian quantum walks. *Phys. Rev. B*, 100:165419, Oct 2019.

[64] Shuo Liu, Ruiwen Shao, Shaojie Ma, Lei Zhang, Oubo You, Haotian Wu, Yuan Jiang Xiang, Tie Jun Cui, and Shuang Zhang. Non-hermitian skin effect in a non-hermitian electrical circuit. *Research*, 2021, 2021.

[65] Robert C Hilborn. *Chaos and nonlinear dynamics: an introduction for scientists and engineers*. Oxford University Press on Demand, 2000.

[66] Massimo Cencini, Fabio Cecconi, and Angelo Vulpiani. *Chaos: from simple models to complex systems*, volume 17. World Scientific, 2009.

[67] Yi-Piao Wu, Guo-Qing Zhang, Cai-Xia Zhang, Jian Xu, and Dan-Wei Zhang. Interplay of nonreciprocity and nonlinearity on mean-field energy and dynamics of a bose-einstein condensate in a double-well potential. *Frontiers of Physics*, 17(4):1–10, 2022.

[68] N. David Mermin and Herbert Wagner. Absence of ferromagnetism or antiferromagnetism in one-or two-dimensional isotropic Heisenberg models. *Physical Review Letters*, 17(22):1133, 1966.

[69] J. B. Pendry. Negative refraction makes a perfect lens. *Phys. Rev. Lett.*, 85:3966–3969, Oct 2000.

[70] Andrew A. Houck, Jeffrey B. Brock, and Isaac L. Chuang. Experimental observations of a Left-Handed Material that obeys Snell's law. *Phys. Rev. Lett.*, 90:137401, Apr 2003.

[71] Zhengyou Liu, Xixiang Zhang, Yiwei Mao, Y. Y. Zhu, Zhiyu Yang, C. T. Chan, and Ping Sheng. Locally resonant sonic materials. *Science*, 289(5485):1734–1736, 2000.

[72] Nicholas Fang, Dongjuan Xi, Jianyi Xu, Muralidhar Ambati, Werayut Srituravanich, Cheng Sun, and Xiang Zhang. Ultrasonic metamaterials with negative modulus. *Nature materials*, 5(6):452–456, 2006.

[73] Yiqun Ding, Zhengyou Liu, Chunyin Qiu, and Jing Shi. Metamaterial with simultaneously negative bulk modulus and mass density. *Phys. Rev. Lett.*, 99:093904, Aug 2007.

[74] Roman Süsstrunk and Sebastian D. Huber. Observation of phononic helical edge states in a mechanical topological insulator. *Science*, 349(6243):47–50, 2015.

[75] Lisa M. Nash, Dustin Kleckner, Alismari Read, Vincenzo Vitelli, Ari M. Turner, and William T. M. Irvine. Topological mechanics of gyroscopic metamaterials. *Proceedings of the National Academy of Sciences*, 112(47):14495–14500, 2015.

[76] Sebastian D Huber. Topological mechanics. *Nature Physics*, 12(7):621–623, 2016.

[77] James Utama Surjadi, Libo Gao, Huifeng Du, Xiang Li, Xiang Xiong, Nicholas Xuanlai Fang, and Yang Lu. Mechanical metamaterials and their engineering applications. *Advanced Engineering Materials*, 21(3):1800864, 2019.

[78] Martin Brandenbourger, Xander Locsin, Edan Lerner, and Corentin Coulais. Nonreciprocal robotic metamaterials. *Nature Communications*, 10(1), Oct 2019.

[79] Han Zhao, Xingdu Qiao, Tianwei Wu, Bikashkali Midya, Stefano Longhi, and Liang Feng. Non-hermitian topological light steering. *Science*, 365(6458):1163–1166, 2019.

[80] Navot Silberstein, Jan Behrends, Moshe Goldstein, and Roni Ilan. Berry connection induced anomalous wave-packet dynamics in non-hermitian systems. *Phys. Rev. B*, 102:245147, Dec 2020.

[81] Di Xiao, Ming-Che Chang, and Qian Niu. Berry phase effects on electronic properties. *Rev. Mod. Phys.*, 82:1959–2007, Jul 2010.

[82] Pierre Delplace, JB Marston, and Antoine Venaille. Topological origin of equatorial waves. *Science*, 358(6366):1075–1077, 2017.

[83] Pierre Delplace and Antoine Venaille. From the geometry of Foucault pendulum to the topology of planetary waves. *arXiv preprint arXiv:2006.08488*, 2020.

[84] Julio C Gutiérrez-Vega. Pancharatnam–berry phase of optical systems. *Optics letters*, 36(7):1143–1145, 2011.

[85] Michael Berry et al. Anticipations of the geometric phase. *Physics Today*, 43(12):34–40, 1990.

[86] G Nenciu and G Rasche. On the adiabatic theorem for nonself-adjoint Hamiltonians. *Journal of Physics A: Mathematical and General*, 25(21):5741, 1992.

[87] David Viennot, Arnaud Leclerc, Georges Jolicard, and John P Killingbeck. Consistency between adiabatic and non-adiabatic geometric phases for non-self-adjoint hamiltonians. *Journal of Physics A: Mathematical and Theoretical*, 45(33):335301, 2012.

[88] Arnaud Leclerc, David Viennot, and Georges Jolicard. The role of the geometric phases in adiabatic population tracking for non-hermitian hamiltonians. *Journal of Physics A: Mathematical and Theoretical*, 45(41):415201, 2012.

[89] S Ibáñez and JG Muga. Adiabaticity condition for non-hermitian hamiltonians. *Physical Review A*, 89(3):033403, 2014.

[90] G Dattoli, R Mignani, and A Torre. Geometrical phase in the cyclic evolution of non-hermitian systems. *Journal of Physics A: Mathematical and General*, 23(24):5795, 1990.

[91] G Dattoli, A Torre, and R Mignani. Non-Hermitian evolution of two-level quantum systems. *Physical Review A*, 42(3):1467, 1990.

[92] Huitao Shen, Bo Zhen, and Liang Fu. Topological band theory for non-hermitian hamiltonians. *Phys. Rev. Lett.*, 120:146402, Apr 2018.

[93] Robert S Whitney, Yuriy Makhlin, Alexander Shnirman, and Yuval Gefen. Geometric nature of the environment-induced berry phase and geometric dephasing. *Physical review letters*, 94(7):070407, 2005.

[94] Simon Lieu. Topological phases in the non-hermitian su-schrieffer-heeger model. *Physical Review B*, 97(4):045106, 2018.

[95] S. Longhi. Bloch oscillations in complex crystals with $\mathcal{PT}$ symmetry. *Phys. Rev. Lett.*, 103:123601, Sep 2009.

[96] Joseph Schindler, Ang Li, Mei C. Zheng, F. M. Ellis, and Tsampikos Kottos. Experimental study of active LRC circuits with $\mathcal{PT}$ symmetries. *Phys. Rev. A*, 84:040101, Oct 2011.

[97] S. Bittner, B. Dietz, U. Günther, H. L. Harney, M. Miski-Oglu, A. Richter, and F. Schäfer. $\mathcal{PT}$ symmetry and spontaneous symmetry breaking in a microwave billiard. *Phys. Rev. Lett.*, 108:024101, Jan 2012.

[98] Lev Davidovich Landau and Evgenii Mikhailovich Lifshitz. *Course of theoretical physics*, volume 1. Elsevier, 2013.

[99] Grazia Salerno and Iacopo Carusotto. Dynamical decoupling and dynamical isolation in temporally modulated coupled pendulums. *EPL (Europhysics Letters)*, 106(2):24002, 2014.

[100] Grazia Salerno, Tomoki Ozawa, Hannah M. Price, and Iacopo Carusotto. Floquet topological system based on frequency-modulated classical coupled harmonic oscillators. *Phys. Rev. B*, 93:085105, Feb 2016.

[101] K von Klitzing, G Dorda, and M Pepper. New method for high-accuracy determination of the fine-structure constant based on quantized Hall resistance. *Phys. Rev. Lett.*, 45:494–497, August 1980.

[102] R. B. Laughlin. Anomalous quantum hall effect: An incompressible quantum fluid with fractionally charged excitations. *Phys. Rev. Lett.*, 50:1395–1398, May 1983.

[103] Douglas R. Hofstadter. Energy levels and wave functions of bloch electrons in rational and irrational magnetic fields. *Phys. Rev. B*, 14:2239–2249, Sep 1976.

[104] Steven M Girvin. The quantum hall effect: novel excitations and broken symmetries. In *Aspects topologiques de la physique en basse dimension. Topological aspects of low dimensional systems: Session LXIX. 7–31 July 1998*, pages 53–175. Springer, 2002.

[105] Y-J Lin, Rob L Compton, Karina Jiménez-García, James V Porto, and Ian B Spielman. Synthetic magnetic fields for ultracold neutral atoms. *Nature*, 462(7273):628–632, 2009.

[106] Pedram Roushan, Charles Neill, Anthony Megrant, Yu Chen, Ryan Babbush, Rami Barends, Brooks Campbell, Zijun Chen, Ben Chiaro, Andrew Dunsworth, et al. Chiral ground-state currents of interacting photons in a synthetic magnetic field. *Nature Physics*, 13(2):146–151, 2017.

[107] A. V. Poshakinskiy and A. N. Poddubny. Phonoritonic crystals with a synthetic magnetic field for an acoustic diode. *Phys. Rev. Lett.*, 118:156801, Apr 2017.

[108] Geva Arwas, Amichay Vardi, and Doron Cohen. Triangular bose-hubbard trimer as a minimal model for a superfluid circuit. *Physical Review A*, 89(1):013601, 2014.

[109] Geva Arwas, Amichay Vardi, and Doron Cohen. Superfluidity and chaos in low dimensional circuits. *Scientific reports*, 5(1):13433, 2015.

[110] B Andrei Bernevig and Taylor L Hughes. *Topological insulators and topological superconductors*. Princeton university press, 2013.

[111] Bernhard Kramer and Angus MacKinnon. Localization: theory and experiment. *Reports on Progress in Physics*, 56(12):1469, 1993.

[112] Sebabrata Mukherjee and Mikael C Rechtsman. Observation of Floquet solitons in a topological bandgap. *Science*, 368(6493):856–859, 2020.

[113] Thierry Dauxois and Michel Peyrard. *Physics of solitons*. Cambridge University Press, 2006.

[114] Alwyn Scott. Waves called solitons: Concepts and experiments, 2001.

[115] Zhigang Chen, Mordechai Segev, and Demetrios N Christodoulides. Optical spatial solitons: historical overview and recent advances. *Reports on Progress in Physics*, 75(8):086401, 2012.

[116] Giuseppe Nardulli. *Meccanica Quantistica II, Applicazioni*, volume 2. FrancoAngeli, 2001.

[117] Hannah M Price. Lecture notes on topological phases of matter.

[118] Barry R Holstein. The adiabatic theorem and berry's phase. *American Journal of Physics*, 57(12):1079–1084, 1989.

[119] T Bitter and D Dubbers. Manifestation of berry's topological phase in neutron spin rotation. *Physical review letters*, 59(3):251, 1987.

[120] DJ Richardson, AI Kilvington, K Green, and SK Lamoreaux. Demonstration of berry's phase using stored ultracold neutrons. *Physical review letters*, 61(18):2030, 1988.